Wave Propagation on Multiple Scales along Rough Thin-Elastic Solids

Sebastian Rupprecht

Universität
Augsburg
University

Augsburg 2017

Wave Propagation on Multiple Scales along Rough Thin-Elastic Solids

Sebastian Rupprecht

Dissertation

zur Erlangung des akademischen Grades
Dr. rer. nat.

eingereicht an der
Mathematisch-Naturwissenschaftlich-Technischen Fakultät
der Universität Augsburg

von
Sebastian Rupprecht

Augsburg, Oktober 2017

Erstgutachter: Prof. Dr. Malte Peter
Zweitgutachter: Dr. Luke Bennetts
Datum der mündlichen Prüfung: 20.12.2017

„Mathematik setzt ins Verhältnis, gibt Maß und Zahl und ist völlig logisch. Aber warum die Welt so ist, wie sie ist, das kann die Mathematik auch nicht erklären. Natürlich kann man die Sonnenstrahlung berechnen, man kann sie genau messen, aber was daraus wird: Das Leben auf der Erde, der Sauerstoff zum Atmen, die Wärme auf unserer Haut, davon wissen die Gleichungen nichts. Ich bin mir ganz sicher: Mutter Natur schmunzelt, wenn sie immer wieder sieht, wie wir versuchen, alles mögliche zu berechnen, denn sie weiß, es kommt ein Zauber, ein Geheimnis hinzu, das sich in keiner Zahl und keiner Formel ausdrücken lässt.“

Prof. Dr. Harald Lesch

Abstract

Waves attenuate with distance travelled into rough and randomly disordered media. This is reminiscent of the wave localisation phenomenon, which is a product of wave scattering and occurs in many branches of wave science. Wave localisation refers here to exponential attenuation (on average) of waves in rough media. In this work, the attenuation of waves travelling along rough solids is studied in the setting of strings, beams and floating plates.

Two methods for computing the complex-valued effective wavenumber of a rough beam in the context of linear time-harmonic theory are presented. The roughness of the beam is modelled as a continuous random process of known characteristic length and root-mean-square amplitude for either the beam properties (beam mass or beam rigidity) or beam thickness. The first method is based on a random sampling method, with the effective wave field calculated as the mean of a large ensemble of wave fields for individual realisations of the roughness. The individual wave fields are calculated using a step approximation, which is validated for deterministic problems of mass and rigidity variations via comparison to results produced by an integral-equation approach. The second method assumes a splitting of the length scale of the fluctuations and an observation scale, employing a multiple-scale approximation of the beam deflection to derive analytical expressions for the effective attenuation rate and phase change. Numerical comparisons show agreement of the results of the random sampling method and the multiple-scale approximation for a wide range of parameters in the small roughness-amplitude regime. It is shown that the effective wavenumbers only differ by a real constant between the cases of varying beam mass and rigidity.

The numerical and semi-analytical methods are extended to describe the attenuation of water waves in a two-dimensional fluid domain, which has its surface covered by a rough thin elastic plate and is of finite depth. The plate roughness is modelled with similar properties as for the in-vacuo beam problem. The numerical method is based on an approximation of the full-linear solution in the fluid domain, the semi-analytical method uses a multiple-scale expansion of the velocity potential, from which an equation can be derived describing the attenuation of the effective wave field. The results obtained via the numerical method validate the multiple-scale approach for small-amplitude plate roughness. However, individual wave fields attenuate significantly slower that effective wave fields for the in-vacuo beam and floating plate problems.

Localisation of individual wave fields is shown for strings with continuous density variations for large roughness amplitudes, for which multiple-scale approaches are not valid anymore. Individual and effective wave fields show similar attenuation behaviour in this large roughness-amplitude regime, and a connection between strings with continuous roughness profile and beaded strings is established. Finally, a beam with periodically located notches is presented and our numerical method is modified to simulate wave propagation in the time domain. It is shown that introducing disorder into the notch depths leads to localisation in the audible frequency range.

Key words: Random media, wave attenuation, effective wave field, multiple-scale approach, thin-elastic solids, beam in vacuo, floating plate, inhomogeneous string, localisation

Acknowledgements

There are a number of people to whom I want to express my gratitude and would like to acknowledge their contributions toward this dissertation.

Firstly, I would like to thank my PhD supervisors, Prof. Dr. Malte Peter and Dr. Luke Bennetts, for their support, encouragement and guidance. They taught me invaluable lessons during my time at the University of Augsburg and the University of Adelaide, answered my questions, or helped me in finding the right path to the answers, and provided valuable ideas and techniques for my research. I am deeply grateful for the given opportunities to attend conferences around the world, and widen my professional and cultural horizon.

The financial support from the Australian government, through an Endeavour Research Fellowship in 2016/2017, is gratefully acknowledged, and I would like to thank Prof. Dr. Anthony Roberts from the University of Adelaide to assume my supervision temporarily during my Endeavour Research Fellowship. I am indebted to Dr. Hyuck Chung as well for the financial support for my research visit at Auckland University of Technology and the great collaboration with him. I would like to thank all residents and members of staff at the Kathleen Lumley College, who contributed to an utmost fulfilling academic and social environment, and made my time in Adelaide to a wonderful and unforgettable experience. It has been a pleasure to live with so many fantastic people from all continents with a great variety of professional and cultural backgrounds, and learn from them.

I would like to thank the staff from the School of Mathematics at the University of Adelaide and my home institution for providing me with all I needed and asked for, who took work out of my hands and helped me to focus on my research, and made it possible to perform my computations using high performance computing facilities. My thanks go to my dear colleagues, fellows and friends from the University of Augsburg and University of Adelaide for standing by my side during my PhD.

I would like to express my special appreciation to my friends, who have always believed in me — as opposed to me. They often reminded me that there is a life outside research and provided much welcome relief from the world of mathematics — I have been enjoying and will enjoy every moment with you. Grand gratitude is directed to my family for their enduring love and support. To my grandfather, who had been with me until my PhD journey began: I am eternally grateful for all the unforgettable moments and memories, and thank you for creating footsteps for me to follow.

And finally, I especially want to thank Denise, who has supported me throughout my PhD with her unconditional love, patience and good-heartedness.

Contents

CHAPTER 1

Introduction

Wave propagation through rough media has long been a topic of interest, e.g. in acoustics and electromagnetics, see e.g. Sheng 2006. In the last twenty years, the interest in wave interaction with very large floating structures grew considerably, such as floating landing platforms and offshore structures, which serve e.g. in the offshore oil and gas production. Motivation for research in this area can be found in Kashiwagi 2000 and Watanabe et al. 2004, and an overview over future projects and applications is given by Lamas-Pardo et al. (2015). Such very large floating structures with large horizontal dimension compared to their vertical extent bend under incident waves, see Evans and Porter 2007. To understand the influence of varying thickness profiles, imperfections and the construction of these structures with different materials on their interaction with water waves, profile variations have to be taken into account and studied. The research on such very large floating structures is closely connected to modelling interactions of ocean waves with sea ice, which exhibits non-homogeneities naturally due to cracks, pressure ridges or property and thickness variations, see Squire 2008. Studying wave attenuation along a long beam in vacuo plays an important role in understanding the effects of property and thickness variations. This simpler in-vacuo beam problem has the same key features as the more complex floating plate problem.

Beam models serve, of course, not only as simplified models, but they have been playing a fundamental role in engineering in the last centuries and enabled generations of engineers to solve a variety of construction problems, see e.g. Carrera et al. 2015. A beam is a structure with one dimension much larger than the others and is designed to bear loads transverse to its longitudinal axis. Hence, the deflections occur mainly transverse to the longitudinal axis and the corresponding dynamic beam motion is called the flexural motion, see Doyle 1997. Models for wave propagation along elastic beams are often based on homogeneous beam assumptions, i.e. constant material properties and constant thickness. Wave propagation in a uniform beam is well understood and an extensive study of beams, plates and corresponding vibration analysis can be found in Timoshenko and Woinowsky-Krieger 1959, Mindlin 1951, and Hagedorn and DasGupta 2007. However, the assumption of homogeneous beam properties may not hold and the wave-propagation characteristics over large distances may be affected by the plate roughness causing attenuation of the waves. In Ch. 2, we model flexural wave propagation along a long, thin-elastic beam and study the influence of random fluctuations of the material density, the beam rigidity and the beam thickness (which leads to both varying material density and rigidity). The fluctuations shall be continuous and are incorporated as a function of the longitudinal coordinate via a continuous random process. We model the rough, thin-elastic beams using Euler–Bernoulli beam theory. In this beam theory, effects of bending moment of the beam are taken into account and we assume small shear forces only such that shear deformation can be neglected.

In the case of random media, the effective wave field, i.e. the mean wave field with respect to an ensemble of individual realisations, is often the quantity of interest, in particular the effective wavenumber is of primary interest to describe the attenuation of the wave field, which occurs due to the variations in the beam properties and its thickness. However, computation of the effective wave field and/or effective wavenumber can be numerically intensive and an analytical method is desirable. In general, analytical solutions cannot be found for problems involving complex geometry. In our problem formulation with a prescribed random process describing the profile fluctuations, an analytical method can be derived. The analytical method describes the modulation of the wave propagating along a rough thin-elastic Euler–Bernoulli beam encountering random variations of the beam mass density, rigidity and thickness using a multiple-scale approximation. Analytical methods allow to extract qualitative aspects like dependence on parameters and asymptotic behaviour of the problem and its solution, which might be hard to discover with numerical methods, see Hagedorn and DasGupta 2007. However, to validate the analytical method and its predictions for the attenuation coefficients and phase changes, which are provided as the imaginary and real component of the effective wavenumber, respectively, a numerical method is used. Instead of using boundary element or finite element simulations, which can be applied to solid structures with non-simple shapes, see e.g. Chaves et al. 1999 for boundary element formulations and Reddy 2002 for finite element formulations, we present a numerical method, which is based on a step approximation of the underlying continuous roughness fluctuations, and which allows to compare results for individual and effective wave fields. To obtain effective wave fields as the average of individual wave fields in the numerical method, wave fields have to be calculated for a sufficiently large number of randomly generated roughness profiles using a Monte Carlo algorithm.

After a detailed analysis of wave propagation along a thin-elastic beam in vacuo with continuous roughness profile, we extend this model to a rough thin-elastic plate floating on water in Ch. 3. As mentioned before, this problem setting has in particular applications in modelling interactions of ocean waves with man-made very large floating structures as well as sea ice (which are related closely and have been subject of extensive research). The interaction of ocean waves with sea ice in marginal ice zones plays an important role in our global climate. A marginal ice zone is an immense area in the polar regions consisting of a huge number of ice floes separating continuous ice from the open ocean, and is formed by ocean waves, which break the sea ice, see Wadhams et al. 1986. Simultaneously, the formed marginal ice zone prevents the continuous ice from being broken further, since the ice floes scatter the incoming ocean waves and the extent of marginal ice zones is consequently controlled by these processes. Sizes of ice floes in the marginal ice zone vary from a few metres to hundreds of metres in diameter, see Dixon and Squire 2000. The sizes are typically determined by the wavelengths of the incoming ocean waves, which range up to several hundreds of metres. Ice floes tend to be of sizes between a quarter and half a wavelength of the waves which induce the breaking, see e.g. Meylan 2003. Small ice floes are induced by short waves, which are incident on the marginal ice zone close to the open ocean, and their energy is scattered, hence small ice floes are present in this outer area of the marginal ice zone. With increasing distance from the open ocean, fewer short waves are present due to scattering in the outer marginal ice zone and the diameters of the ice floes increase. Incident waves with large wavelengths can pass the outer areas of the marginal ice zone nearly unimpeded and travel towards the continuous ice. Hence, very long ice floes close to the continuous ice play a crucial role of preventing the continuous ice from being broken by scattering a significant amount of energy of these long waves. The wave energy attenuates exponentially with distance travelled into the marginal ice zone, see e.g. Meylan et al. 2014. The topic of wave interaction in the marginal ice zones attracted huge research interest in the last decades and the approaches are too numerous to list them here. We refer the reader to Squire 2007, 2010 and Broström and Christensen 2008, who gave an extensive overview over literature, models and conducted experiments in this area.

It is our aim to model and determine the attenuation of the long water waves, which already traversed the outer marginal ice zone, by these very large floating ice floes, which exist close to the continuous sea ice. For this, it is physically important to include thickness variations of the ice floes, which has significant impact on the scattering and attenuation behaviour, see e.g. Bennetts and Squire 2012. Since two length scales exist for this problem, which are important to describe the attenuation behaviour analytically, we adopt a multiple-scale approximation, which is based on the multiple-scale approximation for the in-vacuo beam problem. The small scale describes locally the thickness variations, which are modelled to be continuous, and the large scale is the observations scale, on which attenuation is observable. A solution for the equation describing the amplitude on the large scale is sought, which naturally depends on the small-scale behaviour. Since those very large ice floes are only between 1 m and 2 m thick, their rigidity is relatively small and they undergo flexural bending for large wavelengths. Hence, we model those ice floes of variable thickness as elastic Euler–Bernoulli plates floating on water, see e.g. Meylan 2002. The model of a long, rough thin-elastic plate floating on water is an extension of the problem for wave propagation along a long, rough thin-elastic beam in vacuo. This extension introduces a vertical dimension to the problem, and a 5th-order boundary condition at the interface of water and the elastic plate has to be satisfied. The plate roughness is modelled by small-amplitude, continuous variations in the plate thickness along the longitudinal x-axis and is assumed to be uniform in the other horizontal direction. Variations in the plate mass and plate rigidity can easily be incorporated as well and are studied for comparison. Due to the uniformity along the horizontal y-axis, the problem is two-dimensional, hence the problem is set in a two-dimensional fluid domain, which has its surface covered by an elastic plate. To validate the (semi-)analytical multiple-scale method for the velocity potential in the floating plate problem describing the effective wave field, the numerical method for the in-vacuo beam problem is extended to deal with this more complicated problem. Similar to the study by Evans and Porter (2007), we expect qualitative features of the in-vacuo beam problem to appear in the floating plate problem again.

Scattering and wave-localisation phenomena occur in many branches of wave science for incident waves propagating through rough and randomly disordered media. The phenomena have been studied extensively in the past, in particular for one-dimensional random media. We take advantage of the previous work and consider wave propagation along one-dimensional strings in Ch. 4, which (in contrast to beams) do not transmit or resist bending moment and shear stress, see e.g. Hagedorn and DasGupta 2007, and no evanescent waves occur. The motivation for this investigation is mostly derived from the results of the in-vacuo beam problem as well as the floating plate problem, and we hope to get a deeper understanding of the observed features in this simpler setting, for which higher-order conditions do not have to be taken into account anymore. In the literature, inhomogeneities are incorporated into strings via (continuously) varying density and (discrete) beads located on the string, but wave propagation along strings with continuous and discrete inhomogeneities has been studied only separately to the knowledge of the author. A literature overview over strings with either continuous or discrete inhomogeneities as well as fundamental and relevant scattering and localisation results is given in Ch. 4.

Our goal in Ch. 4 is to establish a connection between the continuous and discrete problem. For this, it is necessary to study the respective problems first. After analysing wave propagation along strings with continuously varying density, which exhibits a similar fluctuation profile as for the previous problems, we focus on the problem of a string beaded with point scatterers, for which the Helmholtz equation is satisfied between the scatterers. We study wave propagation along a perturbed periodic array of point scatterers, i.e. randomness is here incorporated as positional disorder from the underlying periodic arrangement of the scatterers, for which the dispersion relation is well known. The setting is called periodic if the discrete point scatterers are identical and mounted to the string with regular spacings, see e.g. Langley 1995. Periodic structures have the advantage that they can be analysed (computationally efficiently) by considering one periodic unit only, see e.g. Bardell et al. 1996. We analyse the influence of positional disorder from the underlying periodic setting for a broad regime of scattering strengths. The transition from a periodic to a disordered setting gives insight into fundamental scattering properties, which might be essential for understanding more complex problem formulations and applications. To establish a connection between the continuous and the discrete problem, the (continuous) roughness profile in the continuous problem is clustered into humps and their statistical properties are transferred to the discrete problem, assigning the scattering strength of the discrete scatterers and the positional disorder.

Finally, we consider wave propagation along beams in vacuo with periodic discrete scatterers in Ch. 5. The discrete scatterers are realised as notches along the beam, where the notch lengths are of the order of the wavelengths, and the distance between adjacent notches is uniform and chosen to be the same as the notch lengths. Periodic beam structures have been studied numerously with different analytical approaches and are well understood, e.g.

simple periodic beams supported at periodic intervals are studied by Miles (1956), and Bobrovnitskii and Maslov (1966). Bardell et al. (1996) extended the periodically supported beam model and studied wave propagation along a periodic beam with identical, but non-symmetric periods, which has applications e.g. in aeronautical and marine construction due to lightening holes and suchlike along beams. It was shown that the periodic asymmetry could be used to design structures with minimum vibration response. For a sufficiently large number of periodic units along the beam, wave propagation along the beam typically shows a pass- and stopband behaviour. While passbands are frequency ranges, for which waves with these frequencies are not attenuated and energy is transmitted along the structure, stopbands are frequency ranges, for which no energy is transmitted and the waves are fully attenuated, see Langley 1995. In this work, we consider a finite number of periodically located notches along a beam with otherwise uniform geometry. In contrast to Hodges and Woodhouse 1989a,b, who showed localisation of vibrations in a bending beam for irregular spacing between discrete scatterers, we focus on irregular notch depths. It is our goal to investigate the effects of notch depth variations on the pass- and stopbands, and to achieve minimum transmission and localisation of waves in the audible frequency range along the notched beam.

Guided wave propagation in beams with structural defects attracted significant attention in the last decades. Damages and defects such as cracks in structures can have severe consequences in a wide range of infrastructures. Since vibrations in structures are affected by cracks, they can be used to detect cracks, and identify their location and severity. Ultrasonic guided waves are easy to generate and can be used for global structure inspections, therefore ultrasonic guided waves are commonly used in structural health monitoring to examine structures and find damages at an early stage, see He and Ng 2017. Due to their widespread use in structures, vibrations in beams with defects have been studied widely. A good overview over ultrasonic guided waves in beams and solid media can be found in Rose 2014. Typically in these studies, Lamb waves are generated at one beam end using piezoelectric transducers, which we adapt for our simulations. For waves with frequencies in the audible range, we do not have to deal with a variety of wave modes propagating along the beam, since only S0 and A0 modes, i.e. symmetric and anti-symmetric Lamb modes of the lowest-order, respectively, exist in this frequency regime, see Behzad et al. 2013, who used this feature for waves with frequencies in the low ultrasonic range propagating along beams with a single step. The numerical method, which is introduced in Ch. 2 and used for solving the time-harmonic problems, is extended to describe wave propagation in the time domain. In analogy to Montiel et al. 2012, the Fourier transform is applied, which makes it possible to calculate dynamic wave propagation along the notched beam for waves with a frequency spectrum directly from the frequency-domain solutions calculated with our numerical method. This serves as the theoretical foundation for experiments, which have to be conducted to show localisation of waves in the audible frequency range travelling along beams with discrete notches of disordered depths.

CHAPTER 2

Wave attenuation along a rough thin-elastic beam

The effective wave field, i.e. the mean wave field with respect to an ensemble of individual realisations, is often the quantity of interest in wave scattering problems. However, computation of the effective wave field and/or effective wavenumber can be a numerically intensive task. The roughness is often assumed to originate from inclusions or discrete variations of the medium properties, which induces non-smooth fluctuations. Several approaches for simulating responses of beams with discontinuities can be found in the literature, e.g. Failla and Santini (2007) dealt with Euler–Bernoulli beams with discontinuities in the shear force and bending moment due to applied point forces and moments, Biondi and Caddemi (2005) proposed closed-form solutions for Euler–Bernoulli beams with flexural stiffness and slope discontinuities, requiring the knowledge of boundary conditions only, Yavari et al. (2001) applied distribution theory to study beams with discontinuities in its slope and mechanical properties. For Euler–Bernoulli plates, Weaver (1997, 1998) studied multiple scattering at point scatterers, Evans and Porter (2007) discussed scattering by a finite number of point scatterers, which are located arbitrarily in an infinite plate, and Dixon and Squire (2000) used a coherent-potential approximation to describe flexural waves scattered by (discrete) random variations in density, for which the analysis is similar, but less complex than for random variations in Young's modulus and the plate thickness. However, these methods cannot be applied to problems involving continuously varying thickness and material properties, which we focus on in this chapter. For continuous thickness variations, Beran (1994) studied flexural waves in a plate strip with random density fluctuations using a statistical modal analysis, and Chaves et al. (1999) extended the existing plate bending boundary element method formulations, see e.g. Gospodinov and Ljutskanov 1982, to incorporate plate thickness or stiffness variations, which is a numerically expensive method. A different method is shown by Bilbao (2004), who used a digital waveguide network method to simulate a signal along a beam with varying thickness, a method which has been used widely with the aim of synthesising musical sound. For our investigations of wave propagation along a long, rough beam with continuous variations, we derive and present a numerical method as well as an analytical method.

In our problem formulation, the continuous fluctuations are defined by a Gaussian autocorrelation function with a prescribed characteristic length, l_{G}, and root-mean-square (roughness) amplitude, ϵ, also referred to as the roughness amplitude. Gaussian autocorrelated random processes are widely used to model rough surfaces for isotropic and homogeneous media, see Tsang et al. 2000, and are characterised with their mean and covariance function only. More specifically, we consider the one-dimensional problem of linear wave propagation along an infinitely long thin-elastic beam in vacuo. The underlying differential equation is of fourth order, making the problem considerably more difficult than related problems of second order, e.g. in standard acoustics of membrane problems. The roughness is a long patch of either rapidly fluctuating mass or rigidity. This corresponds to the roughness entering in the coefficients of the differential operator at zeroth or second order, respectively. For a uniform beam, the wavenumber is real, but the effective wavenumber for a rough beam is complex, with the imaginary component causing the effective wave field to attenuate over the rough interval. The two quantities of interest are the effective phase change and the effective attenuation coefficient (constituting the deviation of real part of the effective wavenumber from the wavenumber of the underlying wave forcing and the imaginary part of the effective wavenumber, respectively). The effective wavenumber or its change from the wavenumber of the underlying uniform medium, $\bar{k}$, is sought and the numerical method and analytical method are applied to obtain the effective wavenumber.

Analytic theories for scattering problems include (i) asymptotic theories, often for long waves compared to the length scale associated with the roughness (homogenisation limit, e.g. Kohn and Vogelius (1984) considered effective plate equations for vanishing plate thickness and rapidly varying fluctuations), (ii) perturbations from an underlying periodic setting (as discussed for a one-dimensional acoustics problem by Maurel et al. (2010)) and (iii) closure assumptions (e.g. as mentioned before the coherent potential approximation, see e.g. Dixon and Squire 2000). Analytic solution methods have predominantly been developed for problems in which the roughness originates from discrete scatterers (inclusions or variations in the medium) and it is common to use analytic theories known as Foldy's method or the quasi-crystalline approximation, as described by Linton and Martin (2005) for a two-dimensional acoustics problem. Direct numerical computations, in which the effective wave field is calculated as the mean of a large ensemble of wave fields for randomly generated realisations of the roughness, are typically based on addition theorems, such as Graf's formulae in two-dimensions. Often, they employ the fast multipole method (see e.g. Gimbutas and Greengard 2013) or other domain decomposition methods (see e.g. Montiel et al. 2015) to accelerate computations for large numbers of scatterers. The numerical methods capture the effective wave field up to an arbitrary degree of accuracy, but rely on e.g. least-squares fitting to extract the effective wavenumber.

We derive a numerical method for our problem formulation, which is based on a version of the step approximation outlined by Bennetts et al. (2015) for a water-wave problem. In this approach, each individual realisation of the continuous rough profile is replaced by discrete steps, permitting the individual wave fields to be calculated via an efficient iterative scheme. The effective wave field is then computed by averaging a large ensemble of realisations, and the components of the effective wavenumber are extracted by least-squares fits. We validate the wave field produced by the step approximation for a deterministic problem, by comparing it to the wave field obtained via an integral equation approach.

Our analytical method is based on a multiple-scale approximation, similar to the approach of Kawahara (1976) (again, for a water-wave problem). A separation of scales is assumed, where the local scale is of the order of the wavelength as well as the characteristic length. The observation scale, L_{ob}, over which effective properties are sought, is assumed much larger, $L_{\mathrm{ob}} = l_{\mathrm{G}}/\epsilon^2$, with $\epsilon \ll 1$. The dependent quantities are then assumed to have a two-scale expansion in ϵ and individual problems are found to be satisfied by each term in the expansion. Passage to mean quantities allows us to derive an analytical expression for the complex-valued effective wavenumber.

The chapter is organised as follows: We introduce the problem formulation and derive the governing Euler–Bernoulli beam equation in Sec. 2.1. The step-approximation method to solve the problem for beams with varying properties is described in Sec. 2.2 and validated using integral equation approaches for deterministic mass and rigidity variations, which are prescribed with deterministic humps, in Sec. 2.3. For the problem of deterministic rigidity variations, different discretisation schemes in the step-approximation method are examined. Before we focus on the problem of beams with rough profiles, we present the underlying random process and the generation of rough profile realisations in Sec. 2.4. The random-sampling method, which is essential to generate effective wave fields, is presented in Sec. 2.5 together with the technique to measure the attenuation of wave fields. The problems of wave propagation along beams with continuously varying mass, beams with continuously varying rigidity and beams with continuously varying thickness are posed in Secs. 2.6–2.8 and multiple-scale methods for the respective problems are derived. Numerical results are given, comparing the results obtained via the analytical and the numerical approach, and we discuss their advantages and disadvantages. Moreover, the relation of the effective wave field and wave fields for individual realisations of the roughness is discussed. A summary and discussion of the results of the chapter are given in Sec. 2.9. Results of this chapter were partially published in Rupprecht et al. 2017.

2.1 Problem formulation

We consider an infinitely long thin beam in vacuo. The problem is one-dimensional in the horizontal coordinate x, which allows us to describe the beam via the Euler–Bernoulli beam equation, assuming that no deformations occur in the plane of the beam cross-section and that during deformation, the cross-section remains plane and normal to the deformed axis of the beam, see e.g. Bauchau and Craig 2009. One way to derive the dynamic Euler–Bernoulli beam equation is based on a variational principle leading to the Euler–Lagrange equation, see e.g. Debnath 2012. In the following, we briefly derive the dynamic Euler–Bernoulli beam equation using a simple physical force balance ansatz, see Alexander 2014. We consider transverse deflection along a beam, which is exposed to an external force, and the beam deflection is $\mathcal{U}(x,t)$. $f(x,t)$ describes the external force per unit length of the beam. The bending moment and the shear force along the beam are denoted with $M(x,t)$ and $V(x,t)$, respectively. For our derivation, we concentrate on a beam element of length Δx. Then, the inertia force, which acts on this beam element, is given by

$$\rho A(x)\Delta x \frac{\partial^2 \mathfrak{U}(x,t)}{\partial t^2},$$

where ρ is the beam's mass density and $A(x)$ is the cross-sectional area of the beam. The inertia force is balanced in vertical direction with

$$-(V + \Delta V) + f(x,t)\Delta x + V = \rho A(x)\Delta x \frac{\partial^2 \mathfrak{U}(x,t)}{\partial t^2}. \tag{2.1}$$

The situation for the beam section of length Δx is shown schematically in Fig. 2.1.

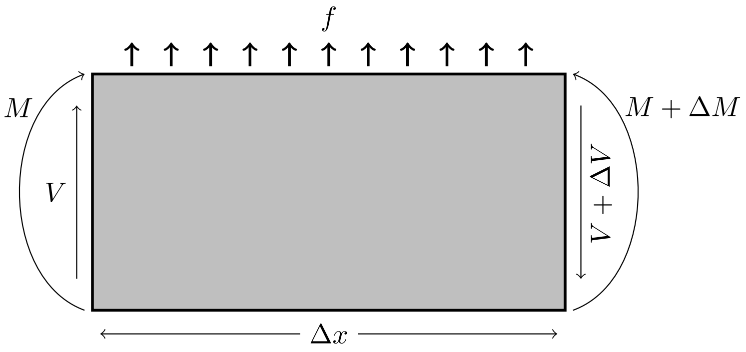

Figure 2.1: Diagram of a beam section of length Δx and adjoining forces under transversal deflection

Furthermore, balancing the moments in the beam section yields

$$(M + \Delta M) - (V + \Delta V)\Delta x + f(x,t)\Delta x \frac{\Delta x}{2} - M = 0. \tag{2.2}$$

When we consider the infinitesimal transition $\Delta x \to 0$, i.e.

$$\Delta V = \frac{\partial V}{\partial x}\Delta x \quad \text{and} \quad \Delta M = \frac{\partial M}{\partial x}\Delta x,$$

and neglect higher-order terms under the assumption of small deformations only, Eqns. (2.1) and (2.2) become

$$-\frac{\partial V(x,t)}{\partial x} + f(x,t) = \rho A(x) \frac{\partial^2 \mathfrak{U}(x,t)}{\partial t^2}, \tag{2.3a}$$

$$\frac{\partial M(x,t)}{\partial x} - V(x,t) = 0. \tag{2.3b}$$

Combining Eqns. (2.3), we obtain

$$-\frac{\partial^2 M(x,t)}{\partial x^2} + f(x,t) = \rho A(x) \frac{\partial^2 \mathfrak{U}(x,t)}{\partial t^2}. \tag{2.4}$$

We also know from classical beam theory, see e.g. Doyle 1997, that the bending moment is of the form

$$M(x,t) = EI(x)\frac{\partial^2 \mathcal{U}(x,t)}{\partial x^2}, \tag{2.5}$$

where E denotes the Young's modulus and I the moment of inertia of the beam cross section. Young's modulus is a material constant describing the linear relation between tension and strain during an elastic deformation of a solid, see e.g. Ashby and Jones 2011. Combining Eqn. (2.4) and Eqn. (2.5) gives the dynamic Euler–Bernoulli beam equation, which describes the transverse deflection of a non-uniform beam with external force f,

$$\frac{\partial^2}{\partial x^2}\left(EI(x)\frac{\partial^2 \mathcal{U}(x,t)}{\partial x^2}\right) + \rho A(x)\frac{\partial^2 \mathcal{U}(x,t)}{\partial t^2} = f(x,t). \tag{2.6}$$

The product of Young's modulus and the moment of inertia of the beam cross section, $EI(x)$, describes the beam rigidity and will be taken together in the following as b. Furthermore, the product of mass density and cross-sectional area, $\rho A(x)$, appearing in Eqn. (2.6), is the mass per unit length. We will denote the mass per unit length as g and refer to it for the sake of brevity as mass only in the following. Together we have

$$b(x) := EI(x), \tag{2.7a}$$

$$g(x) := \rho A(x). \tag{2.7b}$$

We treat problems in which the beams are not subject to external forces, hence $f \equiv 0$ and the right-hand side of Eqn. (2.6) vanishes.

Also, we focus on time-harmonic waves with single angular frequency travelling along the beam. The superposition principle, which plays an important role in the theory of linear waves, allows us in the setting of our linear model to express solutions of problems for waves with non-single frequencies as superposition of solutions for single frequencies, see e.g. Billingham and King 2001. Focusing on time-harmonic waves with a single angular frequency ω, we can study the steady-state behaviour of the beam deflection, $\mathcal{U}(x)$, and its spatial part, $u(x)$, fulfils

$$\mathcal{U}(x,t) = \operatorname{Re}\left\{u(x)\mathrm{e}^{-\mathrm{i}\omega t}\right\}, \tag{2.8}$$

where i denotes the imaginary unit, and it satisfies the linear thin-beam equation

$$\frac{\partial^2}{\partial x^2}\left(b(x)\frac{\partial^2 u(x)}{\partial x^2}\right) - \alpha g(x)u(x) = 0, \qquad x \in (-\infty,\infty), \tag{2.9}$$

where $\alpha = \omega^2$ is the angular frequency squared. The wavenumber is then given by

$$k(x) = \left(\frac{\alpha g}{b}\right)^{1/4}. \tag{2.10}$$

We consider right-travelling waves of unit-amplitude coming from $x \to -\infty$ and study their attenuation along thin, elastic beams, which exhibit roughness in either their mass, rigidity or thickness over a long interval.

2.2 Step-approximation method

To solve the problem of wave propagation along a thin, elastic beam with a general roughness profile (varying mass, varying rigidity or varying thickness, here), we have to use a numerical solution procedure. We use a method, which is based on the approximation of the underlying roughness profile by piecewise constant function, the so-called step-approximation method.

Since we are interested in the impact of the beam roughness on wave propagation along very long beams, it is reasonable to neglect the boundaries and consider an infinitely long beam. For this, the roughness shall extend over a long, finite interval $x \in (0,L)$ and be constant in the surrounding intervals $(-\infty, 0)$ and (L,∞). In each of the problems, i.e. varying mass, varying rigidity and varying thickness problems, the roughness profile (beam mass, beam rigidity and beam thickness, respectively) is approximated by a piece-wise constant function on $M \gg 1$ sub-intervals, with $(-\infty, 0)$ and (L,∞) the 0th and $(M+1)$th sub-intervals, respectively. In Fig. 2.2 we can see an example realisation of a continuous varying mass profile, $g(x)$, fluctuating about the mean mass $\bar{g}$, and a corresponding step approximation of the profile.

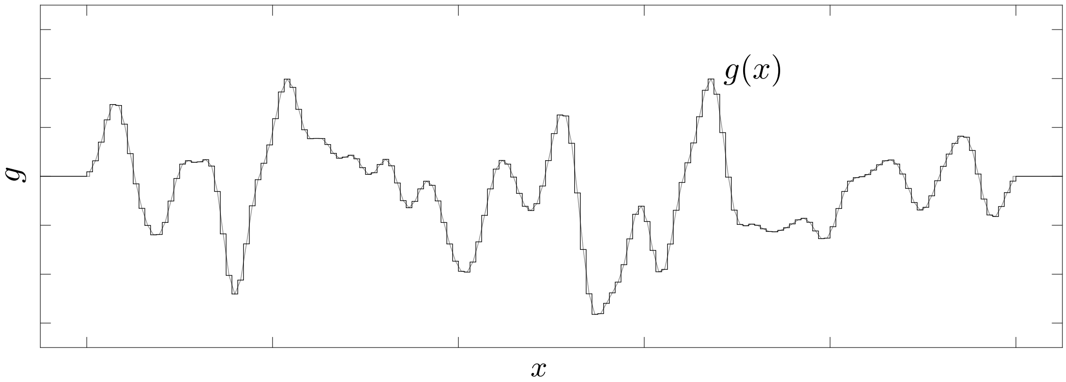

Figure 2.2: Example realisation of continuous roughness profile (grey curve) and corresponding step approximation with four sub-intervals per correlation length (black) for varying mass problem

We denote the value of the mass in the mth sub-interval as g_m, and set it to be equal to the value of the corresponding continuous mass profile at the mid-point. The wavenumber in the mth sub-interval is then given by $k_m = (\alpha g_m/b)^{\frac{1}{4}}$. The mean wavenumber corresponding to the mean mass $\bar{g}$, which is the constant beam mass in the semi-infinite intervals, is denoted with $\bar{k} = (\alpha \bar{g}/b)^{\frac{1}{4}}$. This procedure can be easily transferred to the problems of varying rigidity and varying thickness. For the problem of varying beam rigidity, the method is applied in an identical fashion but for the step approximation of the rigidity profile, $b(x)\,(0 < x < L)$, and for the problem of varying beam thickness for the thickness profile, $h(x)\,(0 < x < L)$.

In the mth sub-interval, the wave field can be expressed as

$$u_m(x) = a_m^{(0)}\,\mathrm{e}^{\mathrm{i}k_m x} + a_m^{(1)}\,\mathrm{e}^{-k_m x} + b_m^{(0)}\,\mathrm{e}^{-\mathrm{i}k_m x} + b_m^{(1)}\,\mathrm{e}^{k_m x}. \tag{2.11}$$

The wave amplitudes $a_m^{(0)}$ and $b_m^{(0)}$ correspond to right- and left-travelling waves, respectively, and $a_m^{(1)}$ and $b_m^{(1)}$ correspond to right- and left-decaying evanescent waves. The motion is forced by a unit-amplitude incident wave propagating in the positive x-direction from $x \to -\infty$, which is set via $a_0^{(0)} = 1$ and $a_0^{(1)} = b_{M+1}^{(0)} = b_{M+1}^{(1)} = 0$.

When discretising the rough interval of the infinitely long beam with the step approximation into M sub-intervals, the scattering interfaces are located at x_m, $m = 0, 1, \ldots, M$, with $x_0 = 0$ and $x_M = L$. Since the Euler–Bernoulli beam Eqn. (2.9) has to be satisfied along the whole interval $(-\infty,\infty)$, we can pose the following one-dimensional weak formulation for an arbitrary square-integrable test function φ with square-integrable derivatives of first and second order to characterise the continuity conditions at each scattering interface,

$$\int_{-\infty}^{\infty} \left[\partial_x^2\big(b(x)\,\partial_x^2 u(x)\big) - \alpha\, g(x)\, u(x)\right] \varphi \,\mathrm{d}x = 0, \tag{2.12}$$

where the notation $\partial_x = \frac{\partial}{\partial x}$ is used for convenience. Eqn. (2.12) has to hold in every sub-interval (and ambient semi-infinite interval), hence

$$\int_{x_m}^{x_{m+1}} \left[\partial_x^2\big(b(x)\,\partial_x^2 u(x)\big) - \alpha\, g(x)\, u(x)\right] \varphi \,\mathrm{d}x = 0 \tag{2.13}$$

for $m = 0, 1, \ldots, M-1$. Using the linearity of the integral and integration by parts then yields

$$\begin{aligned} \int_{x_m}^{x_{m+1}} b(x)\partial_x^2 u(x)\partial_x^2\varphi \,\mathrm{d}x - \left[b(x)\partial_x^2 u(x)\partial_x\varphi\right]_{x_m}^{x_{m+1}} + \\ + \left[\partial_x\big(b(x)\partial_x^2 u(x)\big)\varphi\right]_{x_m}^{x_{m+1}} - \int_{x_m}^{x_{m+1}} \alpha g(x)u(x)\varphi \,\mathrm{d}x = 0. \end{aligned} \tag{2.14}$$

In order to satisfy the Euler–Bernoulli beam Eqn. (2.9), the following continuity conditions at each scattering interface, located at $x = x_m$, $m = 0, 1, \ldots, M$, arise as natural boundary conditions from the weak formulation in Eqn. (2.14) for arbitrary φ,

$$\langle\langle b(x)\partial_x^2 u(x)\rangle\rangle_{x=x_m} = 0, \tag{2.15a}$$

$$\langle\langle \partial_x\big(b(x)\partial_x^2 u(x)\big)\rangle\rangle_{x=x_m} = 0, \tag{2.15b}$$

where $\langle\langle\,\cdot\,\rangle\rangle_{x=\tilde{x}}$ denotes the jump of the included quantity at $x = \tilde{x}$. The first condition is the continuity of the bending moment, the second the continuity of the shear stress. As essential boundary conditions, which ensures the validity of Eqn. (2.14), we apply the continuity of the beam deflection and its slope at the scattering interfaces $x = x_m$, $m = 0, 1, \ldots, M$,

$$\langle\langle u(x) \rangle\rangle_{x=x_m} = 0, \tag{2.15c}$$

$$\langle\langle \partial_x u(x) \rangle\rangle_{x=x_m} = 0. \tag{2.15d}$$

The continuity conditions of deflection (Eqn. (2.15c)), deflection slope (Eqn. (2.15d)), bending moment (Eqn. (2.15a)) and shear stress (Eqn. (2.15b)) are used to couple the wave fields in adjacent sub-intervals. These continuity conditions are applied at the jumps between the finite sub-intervals within the rough interval, and the jumps at the ends of the rough interval and the surrounding semi-infinite intervals, i.e. at $x = 0,\ L$. In the following, an iterative algorithm is presented, which is used to calculate the amplitudes $a_m^{(0)}$ and $a_m^{(1)}$ $(m = 1, \ldots, M + 1)$, and $b_m^{(0)}$ and $b_m^{(1)}$ $(m = 0, \ldots, M)$ for a given roughness realisation.

The Sommerfeld radiation condition is satisfied in all problem formulations in this chapter, which is described by Sommerfeld (1949) as *"the sources must be sources, not sinks of energy. The energy which is radiated from the sources must scatter to infinity; no energy may be radiated from infinity into [...] the field."*, i.e. the wave field far away from the roughness interval $(0,L)$ in the far field consists of only the outgoing and the incident waves, and the respective problems are well-defined.

To calculate the wave field in the whole domain, we derive an iterative algorithm, which is based on a solution procedure for multiple rows of circular ice floes, presented by Bennetts and Squire (2009). Before we devote ourselves to the final iterative algorithm, we firstly focus on the interaction of incident waves with a single interface at adjacent sub-intervals. We begin our investigation with a single interface at $x = 0$, connecting the semi-infinite intervals to the left and right of the origin.

Without loss of generality, we consider waves of unit-amplitude incident on the interface at $x = 0$, which are of the form

$$\begin{aligned} \mathbf{u}_{\mathrm{inc}_-}^{(0)} &= \mathrm{e}^{\mathrm{i}\boldsymbol{\Lambda}_0 x}\mathbf{I}_0, & \qquad \mathbf{u}_{\mathrm{inc}_+}^{(0)} &= \mathrm{e}^{-\mathrm{i}\boldsymbol{\Lambda}_1 x}\mathbf{I}_0, \\ \mathbf{u}_{\mathrm{inc}_-}^{(1)} &= \mathrm{e}^{\mathrm{i}\boldsymbol{\Lambda}_0 x}\mathbf{I}_1, & \qquad \mathbf{u}_{\mathrm{inc}_+}^{(0)} &= \mathrm{e}^{-\mathrm{i}\boldsymbol{\Lambda}_1 x}\mathbf{I}_1, \end{aligned}$$

where $\mathbf{I}_n$, $n = 0{,}1$, depicts the first and second column of the two-dimensional identity matrix, respectively, and the diagonal matrices $\boldsymbol{\Lambda}_0$ and $\boldsymbol{\Lambda}_1$ contain the wavenumbers in the intervals left and right to the interface, respectively,

$$\boldsymbol{\Lambda}_0 = \begin{pmatrix} k_0 & 0 \\ 0 & -k_0 \end{pmatrix} \quad \text{and} \quad \boldsymbol{\Lambda}_1 = \begin{pmatrix} k_1 & 0 \\ 0 & -k_1 \end{pmatrix}. \tag{2.17}$$

Hence, $\mathrm{e}^{\mathrm{i}\boldsymbol{\Lambda}_0 x}$ and $\mathrm{e}^{-\mathrm{i}\boldsymbol{\Lambda}_1 x}$ are the diagonal matrices containing the phases for the right-going waves left to the interface and for the left-going waves right to the interface, respectively,

$$\mathrm{e}^{\mathrm{i}\boldsymbol{\Lambda}_0 x} = \begin{pmatrix} \mathrm{e}^{\mathrm{i}k_0 x} & 0 \\ 0 & \mathrm{e}^{-k_0 x} \end{pmatrix} \quad \text{and} \quad \mathrm{e}^{-\mathrm{i}\boldsymbol{\Lambda}_1 x} = \begin{pmatrix} \mathrm{e}^{-\mathrm{i}k_1 x} & 0 \\ 0 & \mathrm{e}^{k_1 x} \end{pmatrix}. \tag{2.18}$$

Using the phase matrices in Eqn. (2.18), the wave field from Eqn. (2.11) for the semi-infinite interval to the left and the first sub-interval can be expressed in matrix-notation as

$$u_0(x) = \mathbb{1}_2^{\mathrm{T}} \mathrm{e}^{\mathrm{i}\boldsymbol{\Lambda}_0 x} \mathbf{A}_0 + \mathbb{1}_2^{\mathrm{T}} \mathrm{e}^{-\mathrm{i}\boldsymbol{\Lambda}_0 x} \mathbf{B}_0, \tag{2.19a}$$

$$u_1(x) = \mathbb{1}_2^{\mathrm{T}} \mathrm{e}^{\mathrm{i}\boldsymbol{\Lambda}_1 x} \mathbf{A}_1 + \mathbb{1}_2^{\mathrm{T}} \mathrm{e}^{-\mathrm{i}\boldsymbol{\Lambda}_1 x} \mathbf{B}_1, \tag{2.19b}$$

where $\mathbb{1}_2$ is the two-dimensional one-vector and the two-dimensional vectors $\mathbf{A}_0$, $\mathbf{A}_1$ and $\mathbf{B}_0$, $\mathbf{B}_1$ contain the wave amplitudes of the right- and left-going waves, respectively, in the zeroth and first interval, i.e.

$$\mathbf{A}_0 = \begin{pmatrix} a_0^{(0)} \\ a_0^{(1)} \end{pmatrix}, \ \mathbf{A}_1 = \begin{pmatrix} a_1^{(0)} \\ a_1^{(1)} \end{pmatrix} \quad \text{and} \quad \mathbf{B}_0 = \begin{pmatrix} b_0^{(0)} \\ b_0^{(1)} \end{pmatrix}, \ \mathbf{B}_1 = \begin{pmatrix} b_1^{(0)} \\ b_1^{(1)} \end{pmatrix}. \tag{2.20}$$

Considering the incident waves from Eqns. (2.16), the solutions for the incident waves from the left, $\mathbf{u}_{\mathrm{inc}_-}^{(0)}$ and $\mathbf{u}_{\mathrm{inc}_-}^{(1)}$, can be expressed as

$$\mathbf{u}_-^{(n)} = \begin{cases} \mathbf{u}_{\mathrm{inc}_-}^{(n)} + \mathrm{e}^{-\mathrm{i}\boldsymbol{\Lambda}_0 x}\, \mathbf{R}_-^{(n)}, & x \le 0, \\ \mathrm{e}^{\mathrm{i}\boldsymbol{\Lambda}_1 x}\, \mathbf{T}_-^{(n)}, & x \ge 0, \end{cases} \quad n = 0, 1, \tag{2.21a}$$

where $\mathbf{R}_-^{(n)}$ and $\mathbf{T}_-^{(n)}$ denote the two-dimensional vectors of reflection and transmission coefficients, respectively. The reflection and transmission coefficients with subscript "$-$" describe the reflection and transmission of right-going waves incident on the scattering interface from the left. Those values can be directly calculated via the boundary conditions in Eqns. (2.15). Analogously, for the incident waves from the right, $\mathbf{u}_{\mathrm{inc}_+}^{(0)}$ and $\mathbf{u}_{\mathrm{inc}_+}^{(1)}$, we obtain

$$\mathbf{u}_+^{(n)} = \begin{cases} \mathrm{e}^{-\mathrm{i}\boldsymbol{\Lambda}_0 x}\, \mathbf{T}_+^{(n)}, & x \le 0, \\ \mathbf{u}_{\mathrm{inc}_+}^{(n)} + \mathrm{e}^{\mathrm{i}\boldsymbol{\Lambda}_1 x}\, \mathbf{R}_+^{(n)}, & x \ge 0, \end{cases} \quad n = 0, 1. \tag{2.21b}$$

Here, the vectors $\mathbf{R}_+^{(n)}$ and $\mathbf{T}_+^{(n)}$ describe the reflection and transmission from left-going waves incident on the scattering interface from the right.

The two-dimensional solution vectors $\mathbf{u}_\pm^{(n)}$, $n = 0,\ 1$, contain the propagating as well as the evanescent part of the solution for the respective incident waves of unit-amplitude. To describe the wave interactions between adjacent intervals with incident waves of amplitude $\mathbf{A}_0$ (from the left) and $\mathbf{B}_1$ (from the right), the solutions in Eqn. (2.21a) and Eqn. (2.21b) are expressed in terms of the incident amplitudes, which yields

$$\mathbf{u} = \begin{pmatrix} \mathbf{u}_-^{(0)} & \mathbf{u}_-^{(1)} \end{pmatrix} \mathbf{A}_0 + \begin{pmatrix} \mathbf{u}_+^{(0)} & \mathbf{u}_+^{(1)} \end{pmatrix} \mathbf{B}_1. \tag{2.22}$$

Hence, the one-dimensional (complex) wave field is again obtained by

$$u = \mathbb{1}_2^{\mathrm{T}} \mathbf{u}. \tag{2.23}$$

The two-dimensional vectors, which contain the reflection and transmission coefficients, can be merged to 2 × 2-matrices describing the full reflection and transmission behaviour for left- and right-going waves, i.e.

$$\mathbf{R}_\pm = \begin{pmatrix} \mathbf{R}_\pm^{(0)} & \mathbf{R}_\pm^{(1)} \end{pmatrix} \quad \text{and} \quad \mathbf{T}_\pm = \begin{pmatrix} \mathbf{T}_\pm^{(0)} & \mathbf{T}_\pm^{(1)} \end{pmatrix}. \tag{2.24}$$

The square matrices $\mathbf{R}_\pm$ and $\mathbf{T}_\pm$ can be combined into a single matrix $\mathbf{S}$,

$$\mathbf{S} := \begin{pmatrix} \mathbf{R}_- & \mathbf{T}_+ \\ \mathbf{T}_- & \mathbf{R}_+ \end{pmatrix}, \tag{2.25}$$

the so-called scattering matrix. Comparing Eqns. (2.19), (2.21), (2.22) together with Eqn. (2.23), it is observable that we can write the outgoing waves with amplitudes $\mathbf{B}_0$ and $\mathbf{A}_1$ in terms of the incoming waves with amplitudes $\mathbf{A}_0$ and $\mathbf{B}_1$ with the help of the scattering matrix $\mathbf{S} \in \mathbb{C}^{4\times4}$,

$$\begin{pmatrix} \mathbf{B}_0 \\ \mathbf{A}_1 \end{pmatrix} = \underbrace{\begin{pmatrix} \mathbf{R}_- & \mathbf{T}_+ \\ \mathbf{T}_- & \mathbf{R}_+ \end{pmatrix}}_{=\mathbf{S}} \begin{pmatrix} \mathbf{A}_0 \\ \mathbf{B}_1 \end{pmatrix}. \tag{2.26}$$

Fig. 2.3 schematically shows the scattering of the incident waves with amplitudes $\mathbf{A}_0$ and $\mathbf{B}_1$, and the resulting scattered waves with amplitudes $\mathbf{A}_1$ and $\mathbf{B}_0$. These vectors contain the respective entries from Eqn. (2.11) for $m = 0, 1$.

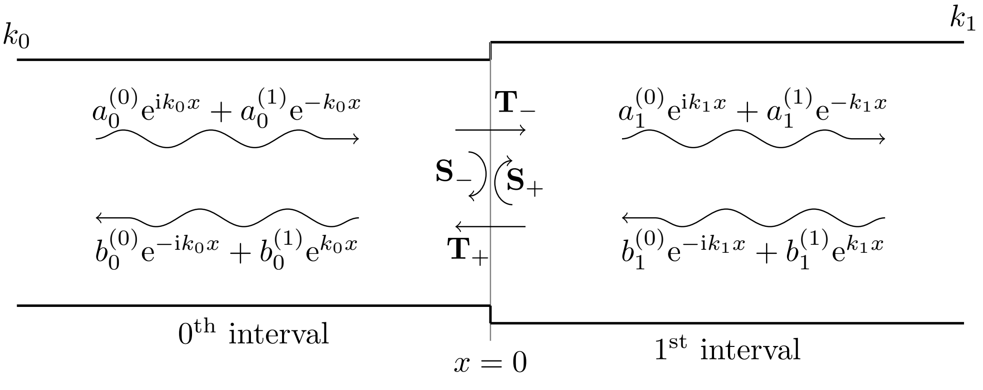

Figure 2.3: Scheme of wave interaction in adjacent intervals

Instead of relating the outgoing waves in respect of the incoming waves, we can equivalently write the wave amplitudes to the right of the scattering interface, $\mathbf{A}_1$ and $\mathbf{B}_1$, in terms of the waves amplitudes to the left of the scattering interface, $\mathbf{A}_0$ and $\mathbf{B}_0$, which gives the transfer matrix $\mathbf{P} \in \mathbb{C}^{4\times 4}$,

$$\begin{pmatrix} \mathbf{A}_1 \\ \mathbf{B}_1 \end{pmatrix} = \mathbf{P} \begin{pmatrix} \mathbf{A}_0 \\ \mathbf{B}_0 \end{pmatrix}. \tag{2.27}$$

The transfer matrix $\mathbf{P}$ can be calculated from the scattering matrix $\mathbf{S}$ with

$$\mathbf{P} = \begin{pmatrix} \mathbf{T}_+ - \mathbf{R}_+ \mathrm{inv}\left(\mathbf{T}_-\right)\mathbf{R}_- & \mathbf{R}_+ \mathrm{inv}\left(\mathbf{T}_-\right) \\ -\mathrm{inv}\left(\mathbf{T}_-\right)\mathbf{R}_- & \mathrm{inv}\left(\mathbf{T}_-\right) \end{pmatrix}. \tag{2.28}$$

Similarly, once the transfer matrix is known, we can directly derive the scattering matrix $\mathbf{S}$. Writing the outgoing waves in terms of the incoming waves (or the waves to the right of the scattering interface in terms of the waves to the left of the scattering interface) is an important step towards the iterative algorithm for multiple scattering interfaces. This approach is useful for combining interactions of multiple scatterers since it avoids the use of large matrices describing the interactions (and the solution of large systems).

It is clear that the solution also satisfies the Sommerfeld radiation condition in the far-fields, since it yields

$$u(x) \sim \begin{cases} a_0^{(0)} \mathrm{e}^{\mathrm{i}k_0 x} + b_0^{(0)} \mathrm{e}^{-\mathrm{i}k_0 x}, & x \to -\infty, \\ a_1^{(0)} \mathrm{e}^{\mathrm{i}k_1 x} + b_1^{(0)} \mathrm{e}^{-\mathrm{i}k_1 x}, & x \to \infty. \end{cases} \tag{2.29}$$

After the derivation of the scattering and transfer matrices for a single scattering interface, we now proceed to the problem of $M+1$ scattering interfaces, which arise at x_m, $m = 0, 1, \ldots, M$, when dividing the rough interval into M sub-intervals. Let us consider the sub-intervals adjacent to the $(m+1)$th scattering interface at x_m. For $m = 0, \ldots, M$, we can write the full solution in the mth and $(m+1)$th interval as

$$\mathbf{u}_m(x) = \mathrm{e}^{\mathrm{i}\boldsymbol{\Lambda}_m (x - x_m)} \mathbf{A}_m^- + \mathrm{e}^{-\mathrm{i}\boldsymbol{\Lambda}_m (x - x_m)} \mathbf{B}_m^-, \qquad x_{m-1} \le x \le x_m, \tag{2.30a}$$

$$\mathbf{u}_{m+1}(x) = \mathrm{e}^{\mathrm{i}\boldsymbol{\Lambda}_{m+1} (x - x_m)} \mathbf{A}_m^+ + \mathrm{e}^{-\mathrm{i}\boldsymbol{\Lambda}_{m+1} (x - x_m)} \mathbf{B}_m^+, \quad x_m \le x \le x_{m+1}, \tag{2.30b}$$

where the amplitudes of the right-travelling waves, $\mathbf{A}_m^\pm$, and the amplitudes of the left-travelling waves, $\mathbf{B}_m^\pm$, are normalised with respect to the interface at x_m. The superscripts in the amplitude notation denote the affiliation to waves to the left $(-)$ and to the right $(+)$ of the $(m+1)$th scattering interface. (Note, that in contrast to the representation in Eqn. (2.20), the vectors $\mathbf{A}_m^\pm$ and $\mathbf{B}_m^\pm$ do not contain the wave amplitudes from Eqn. (2.11) anymore, but their equivalents normalised to the respective scattering interface.) For the first and $(M+1)$th scattering interface in the representation in Eqn. (2.30), the limits denoted with x_{-1} and x_{M+1} disappear, which gives the solution in the semi-infinite intervals.

Applying the continuity conditions from Eqns. (2.15) at all scattering interfaces x_m,

$m = 0, \ldots, M$, we obtain the scattering and transfer matrices,

$$\begin{pmatrix} \mathbf{B}_m^- \\ \mathbf{A}_m^+ \end{pmatrix} = \underbrace{\begin{pmatrix} \mathbf{R}_m^{(-)} & \mathbf{T}_m^{(+)} \\ \mathbf{T}_m^{(-)} & \mathbf{R}_m^{(+)} \end{pmatrix}}_{\mathbf{S}_m} \begin{pmatrix} \mathbf{A}_m^- \\ \mathbf{B}_m^+ \end{pmatrix} \tag{2.31a}$$

and

$$\begin{pmatrix} \mathbf{A}_m^+ \\ \mathbf{B}_m^+ \end{pmatrix} = \mathbf{P}_m \begin{pmatrix} \mathbf{A}_m^- \\ \mathbf{B}_m^- \end{pmatrix}, \tag{2.31b}$$

where the 2×2-matrices $\mathbf{R}_m^{(\pm)}$ and $\mathbf{T}_m^{(\pm)}$ are the reflection and transmission matrices describing the full reflection and transmission behaviour for left- and right-going waves at the $(m+1)$th scattering interface, which is located at $x = x_m$.

The scattering and transfer matrices in Eqns. (2.31) provide the basis for the iterative algorithm in the following since they allow us to relate wave amplitudes beyond adjacent intervals. Even though we set up the solution framework with the scattering and transfer matrices, we lack of knowledge of the amplitudes in the inner sub-intervals. Note that from our problem setting, we only have information about the incident waves from the semi-infinite interval to the left of the first scattering interface, $\mathbf{A}_0^-$, and the semi-infinite interval to the right of the $(M+1)$th scattering interface, $\mathbf{B}_{M+1}^+$. We have an incident wave of unit-amplitude coming from $x \to -\infty$ only, i.e.

$$\mathbf{A}_0^- = \mathbf{I}_0 \quad \text{and} \quad \mathbf{B}_{M+1}^+ = \mathbf{0}.$$

We can reduce the number of unknowns appearing in the full solution in Eqn. (2.30) significantly by equating the two expressions which appear for each of the inner sub-intervals, i.e. we can express the amplitudes corresponding to the right of the mth and to the left of the $(m+1)$th scattering interface with each other for both left- and right-travelling waves by

$$\mathbf{A}_{m+1}^- = \mathrm{e}^{\mathrm{i}\mathbf{\Lambda}_{m+1} l_{m+1}}\, \mathbf{A}_m^+, \tag{2.32a}$$

$$\mathbf{B}_{m+1}^- = \mathrm{e}^{-\mathrm{i}\mathbf{\Lambda}_{m+1} l_{m+1}}\, \mathbf{B}_m^+ \tag{2.32b}$$

for $m = 0, 1, \ldots, M$, where the 2×2-matrix

$$\mathrm{e}^{\mathrm{i}\mathbf{\Lambda}_m l_m} = \begin{pmatrix} \mathrm{e}^{\mathrm{i}k_m l_m} & 0 \\ 0 & \mathrm{e}^{-k_m l_m} \end{pmatrix} \tag{2.33}$$

describes the phase changes due to the distance between adjacent scattering interfaces, $l_m = x_m - x_{m-1}$.

With the approach above, we can calculate the wave interactions in adjacent sub-intervals. However, we cannot calculate the full solution yet, since we do not know the incident waves in the inner sub-intervals. One apparent advantage of the scattering/transfer matrices is their feature that applying it iteratively to all $M+1$ scattering interfaces whilst taking the phase changes into account, we can easily calculate $\mathbf{B}_0^-$ and $\mathbf{A}_{M+1}^+$, which give us the total reflected and transmitted wave field, hence we can deduce how much energy is reflected and transmitted.

Generally, we can merge transfer matrices with this and relate wave fields which are not necessarily adjacent anymore. For this, consider the transfer matrix $\mathbf{P}_m$, which describes the wave interaction at the $(m+1)$th scattering interface. Writing the phase changes arising in the $(m+1)$th sub-interval from Eqns. (2.32) as

$$\mathbf{X}_{m+1} = \begin{pmatrix} \mathrm{e}^{\mathrm{i}\boldsymbol{\Lambda}_{m+1} l_{m+1}} & 0 \\ 0 & \mathrm{e}^{-\mathrm{i}\boldsymbol{\Lambda}_{m+1} l_{m+1}} \end{pmatrix}, \tag{2.34}$$

we can relate the wave fields in the mth and $(m+2)$th sub-interval to each other with $\mathbf{P}_{m,m+1}$,

$$\begin{aligned} \begin{pmatrix} \mathbf{A}_{m+1}^+ \\ \mathbf{B}_{m+1}^+ \end{pmatrix} &= \mathbf{P}_{m+1} \begin{pmatrix} \mathbf{A}_{m+1}^- \\ \mathbf{B}_{m+1}^- \end{pmatrix} \\ &= \mathbf{P}_{m+1}\mathbf{X}_{m+1} \begin{pmatrix} \mathbf{A}_{m}^+ \\ \mathbf{B}_{m}^+ \end{pmatrix} \\ &= \underbrace{\mathbf{P}_{m+1}\mathbf{X}_{m+1}\mathbf{P}_m}_{=:\mathbf{P}_{m,m+1}} \begin{pmatrix} \mathbf{A}_{m}^- \\ \mathbf{B}_{m}^- \end{pmatrix}. \end{aligned} \tag{2.35}$$

We can generalise this procedure to the transfer matrix $\mathbf{P}_{p,q}$, which relates the wave fields in the pth and qth sub-interval $(0 \leq p < q \leq M)$,

$$\begin{pmatrix} \mathbf{A}_{q}^+ \\ \mathbf{B}_{q}^+ \end{pmatrix} = \mathbf{P}_{p,q} \begin{pmatrix} \mathbf{A}_{p}^- \\ \mathbf{B}_{p}^- \end{pmatrix}. \tag{2.36}$$

Analogously to Eqn. (2.35), the interaction at the $(q+1)$th scattering interface can be additionally taken into account, using $\mathbf{X}_{q+1}$, which describes the phase change between the qth and $(q+1)$th scattering interface, and the transfer matrix for the scattering interface at $x = x_{q+1}$ only, $\mathbf{P}_{q+1}$. This gives for $\mathbf{P}_{p,q+1}$ the relation

$$\mathbf{P}_{p,q+1} = \mathbf{P}_{q+1}\mathbf{X}_{q+1}\mathbf{P}_{p,q}. \tag{2.37}$$

As we have already seen in Eqns. (2.31), every scattering matrix has a transfer matrix, and vice versa. This also holds for the merged transfer matrices $\mathbf{P}_{p,q}$ and we can write the corresponding scattering matrix, which describes the wave interaction between the scattering interfaces at $x = x_p$ and $x = x_q$, $\mathbf{S}_{p,q}$, as

$$\begin{pmatrix} \mathbf{B}_p^- \\ \mathbf{A}_q^+ \end{pmatrix} = \underbrace{\begin{pmatrix} \mathbf{R}_{p,q}^{(-)} & \mathbf{T}_{p,q}^{(+)} \\ \mathbf{T}_{p,q}^{(-)} & \mathbf{R}_{p,q}^{(+)} \end{pmatrix}}_{=:\mathbf{S}_{p,q}} \begin{pmatrix} \mathbf{A}_p^- \\ \mathbf{B}_q^+ \end{pmatrix}. \tag{2.38}$$

Using the scheme to convert the scattering into the transfer matrix, Eqn. (2.28), and the iteration instruction for the transfer matrix in Eqn. (2.37), we can calculate the scattering matrix $\mathbf{S}_{p,q+1}$ via

$$\mathbf{R}_{p,q+1}^{(-)} = \mathbf{R}_{p,q}^{(-)} + \mathbf{T}_{p,q}^{(+)} \mathrm{e}^{\mathrm{i}\mathbf{\Lambda}_{q+1} l_{q+1}} \left(\mathbf{I} - \mathbf{R}_{q+1}^{(-)} \mathrm{e}^{\mathrm{i}\mathbf{\Lambda}_{q+1} l_{q+1}} \mathbf{R}_{p,q}^{(+)} \mathrm{e}^{\mathrm{i}\mathbf{\Lambda}_{q+1} l_{q+1}} \right)^{-1} \mathbf{R}_{q+1}^{(-)} \mathrm{e}^{\mathrm{i}\mathbf{\Lambda}_{q+1} l_{q+1}} \mathbf{T}_{p,q}^{(-)}, \tag{2.39a}$$

$$\mathbf{T}_{p,q+1}^{(+)} = \mathbf{T}_{p,q}^{(+)} \mathrm{e}^{\mathrm{i}\mathbf{\Lambda}_{q+1} l_{q+1}} \left(\mathbf{I} - \mathbf{R}_{q+1}^{(-)} \mathrm{e}^{\mathrm{i}\mathbf{\Lambda}_{q+1} l_{q+1}} \mathbf{R}_{p,q}^{(+)} \mathrm{e}^{\mathrm{i}\mathbf{\Lambda}_{q+1} l_{q+1}} \right)^{-1} \mathbf{T}_{q+1}^{(+)}, \tag{2.39b}$$

$$\mathbf{R}_{p,q+1}^{(+)} = \mathbf{R}_{q+1}^{(+)} + \mathbf{T}_{q+1}^{(-)} \mathrm{e}^{\mathrm{i}\mathbf{\Lambda}_{q+1} l_{q+1}} \left(\mathbf{I} - \mathbf{R}_{p,q}^{(+)} \mathrm{e}^{\mathrm{i}\mathbf{\Lambda}_{q+1} l_{q+1}} \mathbf{R}_{q+1}^{(-)} \mathrm{e}^{\mathrm{i}\mathbf{\Lambda}_{q+1} l_{q+1}} \right)^{-1} \mathbf{R}_{p,q}^{(+)} \mathrm{e}^{\mathrm{i}\mathbf{\Lambda}_{q+1} l_{q+1}} \mathbf{T}_{q+1}^{(+)}, \tag{2.39c}$$

$$\mathbf{T}_{p,q+1}^{(-)} = \mathbf{T}_{q+1}^{(-)} \mathrm{e}^{\mathrm{i}\mathbf{\Lambda}_{q+1} l_{q+1}} \left(\mathbf{I} - \mathbf{R}_{p,q}^{(+)} \mathrm{e}^{\mathrm{i}\mathbf{\Lambda}_{q+1} l_{q+1}} \mathbf{R}_{q+1}^{(-)} \mathrm{e}^{\mathrm{i}\mathbf{\Lambda}_{q+1} l_{q+1}} \right)^{-1} \mathbf{T}_{p,q}^{(-)}, \tag{2.39d}$$

where $\mathbf{I}$ is the two-dimensional identity matrix. Relations similar to those also appear in Chamberlain and Porter 1995, Peter and Meylan 2009, and McPhedran et al. 1999 for scattering of water waves by ripple beds, vast field of bodies and scattering of electromagnetic waves by arrays of cylinders, respectively. For the simulations using the step-approximation method in this work, we use the procedure from above to calculate the respective scattering matrices $\mathbf{S}_{p,q+1}$ rather than merging the transfer matrices only (and converting them to the respective scattering matrices) since the procedure in Eqns. (2.39) to calculate the scattering matrices $\mathbf{S}_{p,q+1}$ is numerically more stable.

As mentioned above, the scattering and transfer matrices describing the wave interaction at all $M+1$ scattering interfaces, $\mathbf{S}_{0,M}$ and $\mathbf{P}_{0,M}$, respectively, can be calculated with this iterative scheme, hence the total reflection and transmission are obtained using $\mathbf{S}_{0,M}$. The iteration for the calculation from left to right starts at the first scattering interface at $x = x_0$ and $\mathbf{S}_{1,1} \equiv \mathbf{S}_1$ (similarly $\mathbf{P}_{1,1} \equiv \mathbf{P}_1$). Although we can retrieve the scattering characteristics of the whole rough interval with this iteration from left-to-right, it does not give us the wave field within the rough interval. To achieve this, we perform the similar iteration procedure from right to left and combine the left-to-right and right-to-left procedures to calculate the wave amplitudes within each sub-interval.

When calculating $\mathbf{P}_{0,M}$ and $\mathbf{S}_{0,M}$ with the right-to-left procedure (which gives the same total reflection and transmission as the left-to-right procedure, of course), we start with $\mathbf{S}_{M,M} \equiv \mathbf{S}_M$ (or $\mathbf{P}_{M,M} \equiv \mathbf{P}_M$, alternatively) and the iterative relation for the transfer matrix in Eqn. (2.37) becomes

$$\mathbf{P}_{p-1,q} = \mathbf{P}_{p,q} \mathbf{X}_p \mathbf{P}_{p-1}. \tag{2.40}$$

This leads to the following entries of the scattering matrix $\mathbf{S}_{p-1,q}$,

$$\mathbf{R}^{(-)}_{p-1,q} = \mathbf{R}^{(-)}_{p,q} + \mathbf{T}^{(+)}_{p,q} \mathrm{e}^{\mathrm{i}\boldsymbol{\Lambda}_p l_p} \left(\mathbf{I} - \mathbf{R}^{(-)}_{p-1} \mathrm{e}^{\mathrm{i}\boldsymbol{\Lambda}_p l_p} \mathbf{R}^{(+)}_{p,q} \mathrm{e}^{\mathrm{i}\boldsymbol{\Lambda}_p l_p} \right)^{-1} \mathbf{R}^{(-)}_{p-1} \mathrm{e}^{\mathrm{i}\boldsymbol{\Lambda}_p l_p} \mathbf{T}^{(-)}_{p,q}, \tag{2.41a}$$

$$\mathbf{T}^{(+)}_{p-1,q} = \mathbf{T}^{(+)}_{p,q} \mathrm{e}^{\mathrm{i}\boldsymbol{\Lambda}_p l_p} \left(\mathbf{I} - \mathbf{R}^{(-)}_{p} \mathrm{e}^{\mathrm{i}\boldsymbol{\Lambda}_p l_p} \mathbf{R}^{(+)}_{p,q} \mathrm{e}^{\mathrm{i}\boldsymbol{\Lambda}_p l_p} \right)^{-1} \mathbf{T}^{(+)}_{p-1}, \tag{2.41b}$$

$$\mathbf{R}^{(+)}_{p-1,q} = \mathbf{R}^{(+)}_{p-1} + \mathbf{T}^{(-)}_{p-1} \mathrm{e}^{\mathrm{i}\boldsymbol{\Lambda}_p l_p} \left(\mathbf{I} - \mathbf{R}^{(+)}_{p,q} \mathrm{e}^{\mathrm{i}\boldsymbol{\Lambda}_p l_p} \mathbf{R}^{(-)}_{p-1} \mathrm{e}^{\mathrm{i}\boldsymbol{\Lambda}_p l_p} \right)^{-1} \mathbf{R}^{(+)}_{p,q} \mathrm{e}^{\mathrm{i}\boldsymbol{\Lambda}_p l_p} \mathbf{T}^{(+)}_{p-1}, \tag{2.41c}$$

$$\mathbf{T}^{(-)}_{p-1,q} = \mathbf{T}^{(-)}_{p-1} \mathrm{e}^{\mathrm{i}\boldsymbol{\Lambda}_p l_p} \left(\mathbf{I} - \mathbf{R}^{(+)}_{p,q} \mathrm{e}^{\mathrm{i}\boldsymbol{\Lambda}_p l_p} \mathbf{R}^{(-)}_{p-1} \mathrm{e}^{\mathrm{i}\boldsymbol{\Lambda}_p l_p} \right)^{-1} \mathbf{T}^{(-)}_{p,q}. \tag{2.41d}$$

When combining the left-to-right and right-to-left procedures to calculate the wave amplitudes in the mth subinterval between x_{m-1} and x_m, we use the transfer matrices $\mathbf{P}_{0,m-1}$ and $\mathbf{P}_{m,M}$, which describe the wave interactions between the scattering interfaces at x_0 and x_{m-1} as well as x_m and x_M, respectively. This gives the following relations between the wave amplitudes in the mth sub-interval and the ambient wave amplitudes,

$$\begin{pmatrix} \mathbf{A}^+_{m-1} \\ \mathbf{B}^+_{m-1} \end{pmatrix} = \mathbf{P}_{0,m-1} \begin{pmatrix} \mathbf{A}^-_0 \\ \mathbf{B}^-_0 \end{pmatrix} \quad \text{and} \quad \begin{pmatrix} \mathbf{A}^+_M \\ \mathbf{B}^+_M \end{pmatrix} = \mathbf{P}_{m,M} \begin{pmatrix} \mathbf{A}^-_m \\ \mathbf{B}^-_m \end{pmatrix}, \tag{2.42}$$

where the wave amplitudes to the right of the scattering interface at x_{m-1} can be expressed through phase change via their equivalent to the left of the scattering interface at x_m analogously to Eqns. (2.32),

$$\mathbf{A}^+_{m-1} = \mathrm{e}^{-\mathrm{i}\boldsymbol{\Lambda}_m l_m} \mathbf{A}^-_m, \tag{2.43a}$$

$$\mathbf{B}^+_{m-1} = \mathrm{e}^{\mathrm{i}\boldsymbol{\Lambda}_m l_m} \mathbf{B}^-_m. \tag{2.43b}$$

This method is illustrated schematically in Fig. 2.4.

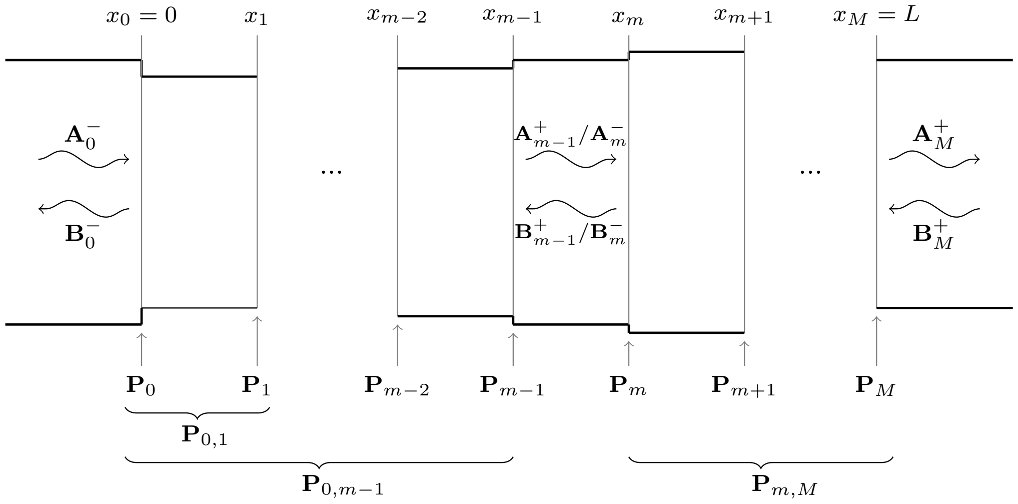

Figure 2.4: Scheme of wave field calculation in mth sub-interval

Solving Eqns. (2.42) for $\mathbf{A}^+_{m-1}$ and $\mathbf{B}^-_m$ with the help of the relations in Eqns. (2.43) finally yields the wave amplitudes

$$\mathbf{A}_{m-1}^{+} = \left(\mathbf{I} - \mathbf{R}_{0,m-1}^{(+)} \mathrm{e}^{\mathrm{i}\boldsymbol{\Lambda}_m l_m} \mathbf{R}_{m,M}^{(-)} \mathrm{e}^{\mathrm{i}\boldsymbol{\Lambda}_m l_m}\right)^{-1} \left(\mathbf{T}_{0,m-1}^{(-)} \mathbf{A}_0^{-} + \mathbf{R}_{0,m-1}^{(+)} \mathrm{e}^{\mathrm{i}\boldsymbol{\Lambda}_m l_m} \mathbf{T}_{m,M}^{(+)} \mathbf{B}_M^{+}\right), \quad (2.44\mathrm{a})$$

$$\mathbf{B}_{m}^{-} = \left(\mathbf{I} - \mathbf{R}_{m,M}^{(-)} \mathrm{e}^{\mathrm{i}\boldsymbol{\Lambda}_m l_m} \mathbf{R}_{0,m-1}^{(+)} \mathrm{e}^{\mathrm{i}\boldsymbol{\Lambda}_m l_m}\right)^{-1} \left(\mathbf{R}_{m,M}^{(-)} \mathrm{e}^{\mathrm{i}\boldsymbol{\Lambda}_m l_m} \mathbf{T}_{0,m-1}^{(-)} \mathbf{A}_0^{-} + \mathbf{T}_{m,M}^{(+)} \mathbf{B}_M^{+}\right). \quad (2.44\mathrm{b})$$

Thus, the wave field in the mth sub-interval is described by the wave amplitudes, which are normalised with respect to both scattering interfaces enclosing the sub-interval. The corresponding wave amplitudes normalised with respect to the same scattering interface can easily be obtained by Eqns. (2.43). With this iterative algorithm it is now possible to calculate the interactions of waves along an elastic beam with continuous (as well as discrete) roughness profiles, in particular the scattering characteristics of the whole rough interval.

2.3 Validation of step approximation

Before we study wave propagation along beams with long random roughness profiles in Sec. 2.5 and the following sections of this chapter, we consider the specific cases in which either the beam mass or the beam rigidity has a deterministic roughness profile. This allows us to compare the solution given by the step approximation, which was introduced in Sec. 2.2, with the solution by an integral equation approach in this section. In both problems, the varying beam mass and beam rigidity, respectively, has a single hump-form in the interval $(0,L)$, where L is not as large as in the random profile cases, and is constant in the ambient semi-infinite intervals, whereas the other quantity is constant in the whole domain. In these semi-infinite intervals, the wave field can be expressed as

$$u(x) = \mathrm{e}^{\mathrm{i}k_0 x} + R^{(0)}\,\mathrm{e}^{-\mathrm{i}k_0 x} + R^{(1)}\,\mathrm{e}^{k_0 x}, \qquad x \in (-\infty,0), \quad (2.45\mathrm{a})$$

$$u(x) = T^{(0)}\,\mathrm{e}^{\mathrm{i}k_0(x-L)} + T^{(1)}\,\mathrm{e}^{-k_0(x-L)}, \qquad x \in (L,\infty), \quad (2.45\mathrm{b})$$

where k_0 is the wavenumber corresponding to the constant beam mass and rigidity in the ambient semi-infinite intervals and $R^{(0)} \equiv b_0^{(0)}$, $R^{(1)} \equiv b_0^{(1)}$ and $T^{(0)} \equiv a_{M+1}^{(0)}$, $T^{(1)} \equiv a_{M+1}^{(1)}$ are the reflection and transmission coefficients corresponding to travelling (0) and evanescent (1) wave modes.

To validate the step approximation, we use a collocation method to solve the integral equation numerically, which arises from the deterministic single-hump problem. For this, the domain $(0,L)$ is discretised into a finite number of collocation points and the solution is calculated from a finite-dimensional space, whereby the solution has to satisfy the deterministic beam equation at the collocation points, see Ascher and Petzold 1998. Amore (2010) applied a collocation method to solve the Helmholtz equation for a one dimensional string with variable density and showed that it provides accurate results. Alternatively, semi-analytical methods such as a Galerkin approach to approximate the solution of the homogeneous beam equation or the equivalent integro-differential formulation with orthogonal polynomials, e.g. Chebyshev polynomials, in terms of u only (similar to e.g.

Townsend 2014) could be used. In this case, care has to be taken in the choice of test and trial functions owing to the presence of the higher-order derivatives.

2.3.1 Deterministic mass variation

For the first problem in this comparison investigation, we consider the case in which the beam rigidity, b, is constant and the beam mass has the single-hump form

$$g(x) = g_0\bigl(1 + \mu(L/2)^{-8}x^4(x-L)^4\bigr), \quad x \in (0,L), \tag{2.46}$$

where μ is a prescribed amplitude and the beam mass takes the constant value $g(x) \equiv g_0$ in the surrounding semi-infinite intervals. Hence, the beam mass does not have discontinuities and the ambient wavenumber k_0 in Eqns. (2.45) corresponds to g_0, i.e. $k_0 = (\alpha g_0/b)^{1/4}$ here. The wavelength of the ambient waves is then $\lambda = \frac{2\pi}{k_0}$. Until specified at the end of this chapter, the mean beam mass and rigidity (and g_0 and b_0, respectively, in this and the next section) are, as generalisation, set to unity for the time being.

Integral equation for varying mass

To obtain comparison results for the step-approximation method in the case of deterministic variation of beam mass, we introduce an integral equation solution based on a collocation method. In order to avoid inconveniences originating from the higher-order derivatives, we use a mixed method by introducing the bending moment as an auxiliary unknown and look for the vector-valued function

$$\tilde{\mathbf{u}}(x) = \begin{pmatrix} u(x) \\ b\partial_x^2 u(x) \end{pmatrix}. \tag{2.47}$$

To rewrite the beam Eqn. (2.9) for the present problem of deterministic single-hump mass variation with solution $\tilde{\mathbf{u}}$, we define

$$\mathbf{M}(x) = \begin{pmatrix} 0 & 1/b \\ \alpha g & 0 \end{pmatrix} \quad \text{and} \quad \mathbf{M}_0 = \begin{pmatrix} 0 & 1/b \\ \alpha g_0 & 0 \end{pmatrix}. \tag{2.48}$$

This leads to the governing equation

$$\partial_x^2 \tilde{\mathbf{u}} - \mathbf{M}\tilde{\mathbf{u}} = 0 \tag{2.49}$$

for the unknown $\tilde{\mathbf{u}}$. Using an associated matrix-valued Green's function,

$$\mathbf{G}(x;\check{x}) = \begin{pmatrix} \bar{G}(x;\check{x}) & \hat{G}(x;\check{x}) \\ \bar{H}(x;\check{x}) & \hat{H}(x;\check{x}) \end{pmatrix}, \tag{2.50}$$

which satisfies Eqn. (2.49) with impulse at $x = \check{x}$,

$$\partial_x^2 \mathbf{G}(x;\check{x}) - \mathbf{G}(x;\check{x})\mathbf{M}_0 = \delta(x-\check{x})\mathbf{I} \tag{2.51}$$

(as well as the usual radiation conditions), where $\mathbf{I}$ is the two-dimensional identity matrix, Eqn. (2.49) can be converted to the integral equation

$$\begin{aligned}\tilde{\mathbf{u}}(x) = \tilde{\mathbf{u}}_{\mathrm{inc}}(x) &+ \langle\langle \partial_x \mathbf{G}(x;\,\cdot\,)\tilde{\mathbf{u}}\rangle\rangle_{x=0} - \langle\langle \partial_x \mathbf{G}(x;\,\cdot\,)\tilde{\mathbf{u}}\rangle\rangle_{x=L} - \langle\langle \mathbf{G}(x;\,\cdot\,)\partial_x\tilde{\mathbf{u}}\rangle\rangle_{x=0} \\ &+ \langle\langle \mathbf{G}(x;\,\cdot\,)\partial_x\tilde{\mathbf{u}}\rangle\rangle_{x=L} + \int_0^L \mathbf{G}(x;\check{x})\,(\mathbf{M}(\check{x}) - \mathbf{M}_0)\,\tilde{\mathbf{u}}(\check{x})\,\mathrm{d}\check{x},\end{aligned} \tag{2.52}$$

where $\tilde{\mathbf{u}}_{\mathrm{inc}}(x)$ is the incident wave and $\langle\langle\,\cdot\,\rangle\rangle_x$ denotes the jump of the included quantity at the point x again. The components of $\mathbf{G}$ can be found from the standard Green's function for the homogeneous beam equation (Eqn. (2.A.23)), which is derived in Appendix 2.A, and k replaced by k_0, noting that

$$\partial_x^4 \hat{G}(x;\check{x}) - k_0^4 \hat{G}(x;\check{x}) = \frac{1}{b}\delta(x-\check{x}), \tag{2.53a}$$

$$\partial_x^2 \hat{G}(x;\check{x}) = \frac{1}{b}\bar{G}(x;\check{x}), \tag{2.53b}$$

and

$$\partial_x^4 \bar{H}(x;\check{x}) - k_0^4 \bar{H}(x;\check{x}) = \alpha g_0 \delta(x-\check{x}), \tag{2.53c}$$

$$\partial_x^2 \bar{H}(x;\check{x}) = \alpha g_0 \hat{H}(x;\check{x}) \tag{2.53d}$$

follows from Eqn. (2.51).

For the numerical approximation of the solution of Eqn. (2.52), we discretise the interval $[0,L]$ by $0 = x_x < x_1 < \ldots < x_{N-1} < x_N = L$ and use a collocation method, in which we discretise the integral using the compound trapezoidal rule. The jump terms for the function are treated as essential conditions whereas the jump terms involving the derivatives are kept in the equation as natural conditions. For this purpose, the derivatives are approximated by difference quotients. This leads to the following system of $2(N+1)+4$ equations for the $2(N+1)+4$ unknowns $\big(\mathbf{u}(x_0), \ldots \mathbf{u}(x_N), R^{(0)}, R^{(1)}, T^{(0)}, T^{(1)}\big)$,

$$\begin{aligned}\tilde{\mathbf{u}}(x_j) = &\begin{pmatrix} \mathrm{e}^{\mathrm{i}k_0 x_j} \\ b(\mathrm{i}k_0)^2 \mathrm{e}^{\mathrm{i}k_0 x_j}\end{pmatrix} \\ &- \mathbf{G}(x_j;x_0)\left((\tilde{\mathbf{u}}(x_1) - \tilde{\mathbf{u}}(x_0))/h - \left(\begin{pmatrix}\mathrm{i}k_0 \\ (\mathrm{i}k_0)^3\end{pmatrix} + \begin{pmatrix} -\mathrm{i}k_0 & k_0 \\ (-\mathrm{i}k_0)^3 & k_0^3\end{pmatrix}\begin{pmatrix}R^{(0)} \\ R^{(1)}\end{pmatrix}\right)\right) \\ &+ \mathbf{G}(x_j;x_N)\left(\begin{pmatrix}\mathrm{i}k_0 & -k_0 \\ (\mathrm{i}k_0)^3 & (-k_0)^3\end{pmatrix}\begin{pmatrix}T^{(0)} \\ T^{(1)}\end{pmatrix} - (\tilde{\mathbf{u}}(x_N) - \tilde{\mathbf{u}}(x_{N-1}))/h\right) \\ &+ h\Bigg(\frac{1}{2}\mathbf{G}(x_j;x_0)(\mathbf{M}(x_0) - \mathbf{M}_0)\tilde{\mathbf{u}}(x_0) + \frac{1}{2}\mathbf{G}(x_j;x_N)(\mathbf{M}(x_N) - \mathbf{M}_0)\tilde{\mathbf{u}}(x_N) \\ &+ \sum_{n=1}^{N-1} \mathbf{G}(x_j;x_n)(\mathbf{M}(x_n) - \mathbf{M}_0)\mathbf{u}(x_n)\Bigg), \quad j = 0, \ldots, N,\end{aligned} \tag{2.54a}$$

and

$$\tilde{\mathbf{u}}(x_0) = \begin{pmatrix} 1 \\ (\mathrm{i}k_0)^2 \end{pmatrix} + \begin{pmatrix} 1 & 1 \\ (-\mathrm{i}k_0)^2 & k_0^2 \end{pmatrix} \begin{pmatrix} R^{(0)} \\ R^{(1)} \end{pmatrix}, \tag{2.54b}$$

$$\tilde{\mathbf{u}}(x_N) = \begin{pmatrix} 1 & 1 \\ (\mathrm{i}k_0)^2 & (-k_0)^2 \end{pmatrix} \begin{pmatrix} T^{(0)} \\ T^{(1)} \end{pmatrix}, \tag{2.54c}$$

where $h = L/N$ and we have used the continuity of $\mathbf{G}$ at $x = 0, L$. Moreover, we have taken the incident wave to be of unit amplitude, i.e. $\mathrm{e}^{\mathrm{i}k_0 x}$, and the reflection and transmission coefficients $R^{(0)}, R^{(1)}, T^{(0)}$ and $T^{(1)}$ derive from Eqns. (2.45).

Alternatively, all boundary conditions could be enforced as essential boundary conditions. In this case, the terms in brackets behind the Green's function in the second and the third line of (2.54a) are set to zero as separate conditions. In turn, they drop from (2.54a), which is then only to be satisfied for $j = 1, \ldots, N-1$. The benefits of this alternative approach will become clear in the following section showing numerical results for the deterministic mass variation problem.

Numerical results

After we have derived an integral equation approach for the beam in vacuo with continuous, deterministic mass variation in $(0,L)$, we study the results for the respective problem produced by the integral equation approach and the step-approximation method now. Firstly, we compare an individual wave field. Fig. 2.5 shows the wave field, calculated by the step-approximation method and integral equation approach, split into real and imaginary part, for non-dimensional hump length $k_0 L = 4$ and hump amplitude $\mu = 5.0 \times 10^{-1}$. For the step approximation, 100 sub-intervals are used over $x \in (0,L)$, in order to obtain a smooth individual wave field, although much coarser resolutions provide sufficiently accurate results in what follows. (The grid size of 100 sub-intervals over $x \in (0,L)$ is kept, though.) For the integral equation approach, 4000 sub-intervals are used.

We can observe in Fig. 2.5 that the wave fields calculated by both methods exhibit very good agreement. The wave fields clearly deviate from the incident wave field, which is also shown for comparison. This deviation can be detected for real and imaginary part as well as the wave field modulus.

To obtain a more quantitative result about the approximation quality of the step-approximation method, we consider the wave field reflection for different hump lengths. Fig. 2.6 shows the moduli of the (complex-valued) reflection coefficients, $|R^{(0)}|$, calculated by the step-approximation method and integral equation approach, as functions of non-dimensional hump lengths, for amplitudes $\mu = 1.0 \times 10^{-1}$ and 5.0×10^{-1}.

We can see in Fig. 2.6 that the two solution methods produce the same reflection coefficient moduli throughout the range of hump lengths considered, $k_0 L \in (1,10)$. We also observe that the reflection coefficient moduli for $\mu = 1.0 \times 10^{-1}$ and 5.0×10^{-1} share the same qualitative behaviour, attaining maxima at $k_0 L \approx 3.2$ and 3.4, respectively, and zeros at $k_0 L \approx 8.2$ and 8.5, respectively.

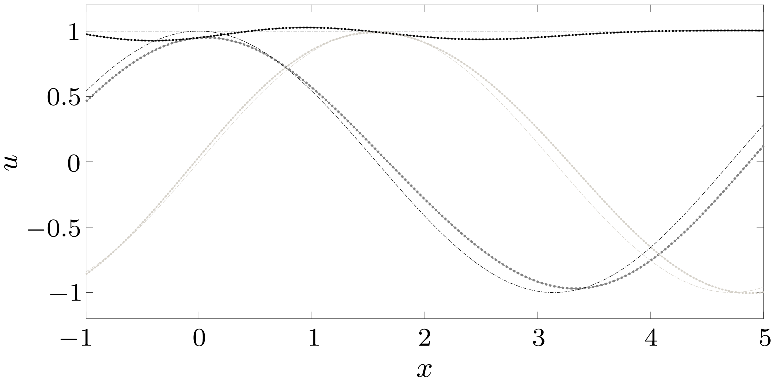

Figure 2.5: Individual wave field for single-hump problem with non-dimensional hump length $k_0L = 4$ and hump amplitude $\mu = 5.0 \times 10^{-1}$, computed by integral equation approach (solid line) and step-approximation method (∘), shown as its modulus (black), and split into real part (dark grey) and imaginary part (light grey). Components of incident wave are shown for comparison (dash-dotted line with same colour scheme).

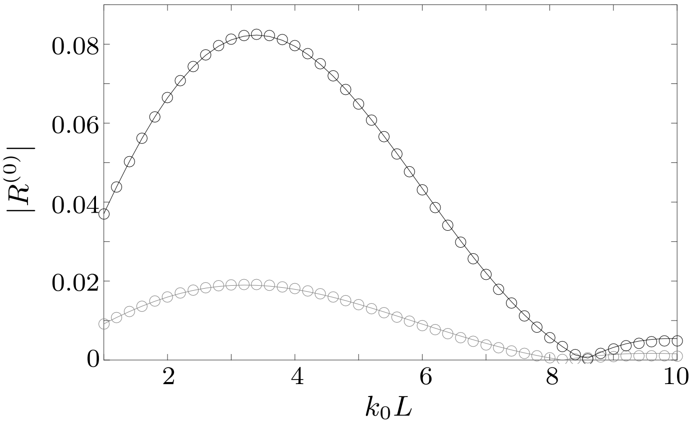

Figure 2.6: Reflection coefficient moduli for single-hump problem as functions of non-dimensional hump length, for hump amplitudes $\mu = 1.0 \times 10^{-1}$ (grey) and $\mu = 5.0 \times 10^{-1}$ (black), computed by integral equation approach (solid line) and step-approximation method (∘)

Next, we investigate the behaviour of the integral equation approach and the step-approximation method throughout a wide range of hump amplitudes. Fig. 2.7 shows the reflection coefficient moduli, calculated by the step-approximation method and integral equation approach, as functions of (non-dimensional) hump amplitudes, for hump lengths $k_0L = 4.0$ (left-hand panel) and $k_0L = 6.0$ (right-hand panel). For comparison, the reflection coefficient moduli obtained by the integral equation approach, where all boundary conditions are enforced as essential boundary conditions, are shown.

We can observe in Fig. 2.7 a linear behaviour of the reflection coefficient moduli as functions

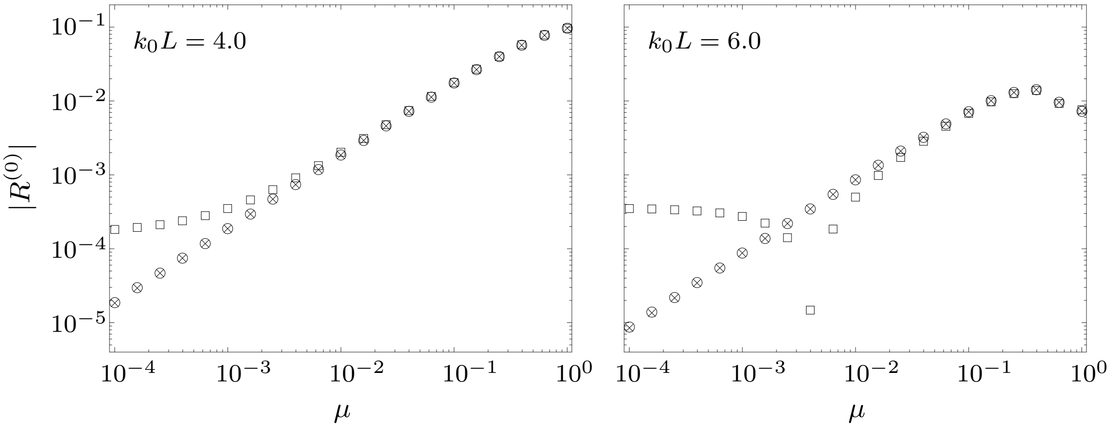

Figure 2.7: Reflection coefficient moduli for single-hump problem as functions of hump amplitudes, for non-dimensional hump lengths $k_0L = 4.0$ (left-hand panel) and $k_0L = 6.0$ (right-hand panel), computed by integral equation approach (□) and step-approximation method (○). Results for integral equation approach with enforced essential boundary conditions (×) are shown for comparison.

of hump amplitudes, μ, for large μ, for both hump lengths, $k_0L = 4.0$ and 6.0. In the case of $k_0L = 4.0$, this proportionality holds for all methods in the hump amplitude regime $\mu \geq 10^{-2}$, where the step-approximation method and both variants of the integral equation approach give the same results. For $\mu \leq 10^{-2}$, the step-approximation method and the integral equation approach with enforced essential boundary conditions still yield the same reflection coefficient moduli (suggesting linearity throughout the whole hump amplitude regime), whereas the standard integral equation approach (including natural boundary conditions) shows a significant upper deviation. For the larger hump length, $k_0L = 6.0$, the step-approximation method and the integral equation approach with enforced essential boundary conditions yield the same values for the reflection coefficient moduli again for all hump amplitudes considered (whereas the standard integral equation approach fails for $\mu \leq 5.0 \times 10^{-2}$). The behaviour is linear as well for $\mu \leq 10^{-1}$ and the reflection coefficient moduli are approximately half of the values of those for $k_0L = 4.0$, which could already be observed in Fig. 2.6. The linear proportionality is lost for $\mu > 10^{-1}$ and the reflection coefficient moduli even decrease for the two largest hump amplitudes, $\mu > 5.0 \times 10^{-1}$. Nevertheless, the step-approximation method and the integral equation approach with enforced essential boundary conditions still show a very good agreement in this large hump amplitude regime.

To investigate the discrepancy between the standard integral equation approach and the integral equation approach with enforced essential boundary conditions, hence also the step-approximation method, we study the convergence behaviour of both variants of the integral equation approach. Fig. 2.8 shows the reflection coefficient moduli as functions of the grid size N, which is used in the calculation of the integral equation via Eqns. (2.54), for both variants of the integral equation approach, for hump lengths $k_0L = 4.0$ and 6.0, and various hump amplitudes. For comparison, Fig. 2.8 also shows the results obtained by the step-approximation method, for which we still use 100 sub-intervals in $(0,L)$.

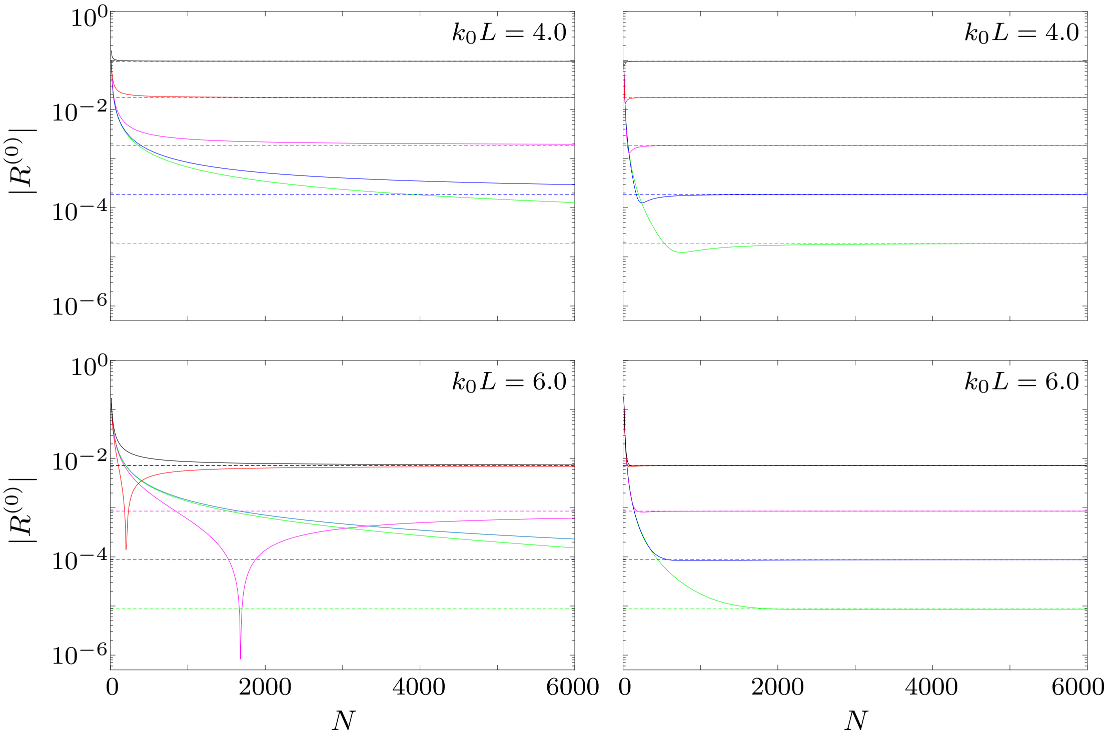

Figure 2.8: Reflection coefficient moduli for single-hump problem as functions of grid size, for non-dimensional hump lengths $k_0L = 4.0$ (top panels) and $k_0L = 6.0$ (bottom panels), computed by standard integral equation approach (left-hand panels) and integral equation approach with enforced essential boundary conditions (right-hand panels), for hump amplitudes $\mu = 1.0 \times 10^{-4}$ (solid, green), 1.0×10^{-3} (solid, blue), 1.0×10^{-2} (solid, magenta), 1.0×10^{-1} (solid, red) and 1.0×10^{0} (solid, black). Results for step-approximation method (dashed line) are shown for comparison (with same color scheme).

We can see in Fig. 2.8 a different convergence behaviour of the two variants of the integral equation approach. For the smaller hump length in consideration, $k_0L = 4.0$, the standard integral equation approach converges quickly to the values calculated by the step-approximation method for the two largest hump amplitudes considered. For $\mu = 10^0$, it takes about 400 evaluation points, for $\mu = 10^{-1}$ about 600 to get converged results. For $k_0L = 6.0$ and the largest hump amplitude, $\mu = 10^0$, converged results are only visible for more than 4000 evaluation points. The case $\mu = 10^{-1}$ shows an interesting behaviour since the calculated reflection coefficient moduli are considerably underestimated for N smaller than 100, even though for the smallest N ($N = 10$) the value is larger than calculated by the step approximation. (Note that the exact reflection coefficient moduli for $\mu = 10^0$ and 10^{-1} are nearly the same.) This convergence behaviour gets even more obvious for $\mu = 10^{-2}$, for which the standard integral equation approach gives larger values than the step approximation for $N \leq 200$, before the values drop to underestimate the reference value by a factor of approximately 10^3 for $N \approx 1700$ and start converging from below for larger N, but convergence cannot be observed for $N \leq 6000$. For the two smallest hump amplitudes, $\mu = 10^{-3}$ and 10^{-4}, this overshooting convergence behaviour does not exist anymore (at least not in the interval $N \leq 6000$) for the larger hump length in consideration, $k_0L = 6.0$. However, for both hump lengths the convergence of the standard integral equation approach is so slow that the reference values are not attained in the interval $N \leq 6000$ for $\mu = 10^{-3}$ and 10^{-4}.

In comparison to the standard integral equation approach, the integral equation approach with enforced essential boundary conditions shows a significantly faster convergence behaviour. For the two largest hump amplitudes, $\mu = 10^0$ and 10^{-1}, this variant needs less than 200 evaluation points to yield converged results for both hump lengths. It is interesting to observe that for this variant, the smaller hump length, $k_0L = 4.0$, leads to the non-monotone convergence behaviour as well and the reference values are attained from below after overestimating them for very small N, whereas for $k_0L = 6.0$, it converges consistently from above for all hump amplitudes. Despite the different convergence behaviour, the integral equation approach with enforced essential boundary conditions provides converged results for both hump lengths for approximately similar N, but for the smallest hump amplitude, $\mu = 10^{-4}$, for which this method needs a grid size of approximately 3000 for $k_0L = 4.0$, but only 2000 for $k_0L = 6.0$ (and the standard integral equation approach yields values still significantly too large for $N = 6000$). Altogether, for the integral equation approach with enforced essential boundary conditions, the reference values are attained for drastically smaller grid sizes N than for the standard integral equation approach.

Concentrating on the values calculated by the integral equation approach with enforced essential boundary conditions and the step-approximation method in Fig. 2.7, for which this variant of the integral equation approach yields already converged results (we use $N = 4000$), we can deduce that the reflection coefficient scales linearly with the hump amplitudes for $\mu \leq 2.0 \times 10^{-1}$, for the hump lengths considered. We also learnt that the standard integral equation approach requires a very large system to capture the reflection of the incident wave for very small hump amplitudes or large hump lengths accurately. Hence, if high accuracy in the reflection and transmission coefficients is required and the problem is such that these are small in value, it may be advisable to enforce all boundary conditions as essential boundary conditions. The results for the beam with deterministic varying beam mass obtained by the integral equation approach with enforced essential boundary conditions for sufficiently large N showed a very good agreement with the values obtained by the step-approximation method. As a consequence of this, the accurate integral equation approach validates the step-approximation method for the present problem and justifies the use of it for more complex problems.

2.3.2 Deterministic rigidity variation

After the successful validation of the step-approximation method in the previous section, we focus on wave propagation along a beam with varying rigidity now. The variation of the beam rigidity in $(0,L)$ shall be characterised deterministically. For this, we choose the beam rigidity to be of the same single-hump form as the beam mass in the previous section,

$$b(x) = b_0\big(1 + \mu(L/2)^{-8}x^4(x-L)^4\big), \quad x \in (0,L), \tag{2.55}$$

where μ is the hump amplitude again. The beam rigidity is constant $b(x) \equiv b_0$ in the surrounding semi-infinite intervals, which ensures continuity of the beam rigidity, and the beam mass, g, is constant. This leads to the ambient wavenumber $k_0 = (\alpha g/b_0)^{1/4}$ here.

Dealing with the varying rigidity problem in this deterministic setting is of interest particularly because of the higher-order derivative of the beam rigidity, which appears in the beam Eqn. (2.9). In the discretisation of the step approximation, the beam rigidity and its first derivative are part of the continuity condition on the shear stress, Eqn. (2.15b), which has to be fulfilled at each scattering interface x_m, $m = 0, 1, \dots, M$, i.e.

$$\begin{aligned}\partial_x b^{(-)}(x_m)\partial_x^2 u_m(x_m) + b^{(-)}(x_m)\partial_x^3 u_m(x_m) &= \\ \partial_x b^{(+)}(x_m)\partial_x^2 u_{m+1}(x_m) &+ b^{(+)}(x_m)\partial_x^3 u_{m+1}(x_m),\end{aligned} \tag{2.56}$$

where the superscripts $(-)$ and $(+)$ denote the evaluation to the left of the scattering interface $x = x_m$ and to the right, respectively. In the build-up of the step-approximation method in Sec. 2.2, we evaluated the roughness profile, which is the rigidity profile here, at the mid-point of each sub-interval and the wavenumber k_m corresponds to this value in the mth sub-interval. To be consistent with this approach, it seems natural to use

$$b^{(-)}(x_m) = b_m \quad \text{and} \quad b^{(+)}(x_m) = b_{m+1}. \tag{2.57}$$

Note that this discretisation is also used in the continuity condition on the bending moment, Eqn. (2.15a). This leads to the question, how to deal with the derivatives of the beam rigidity, $\partial_x b^{(\pm)}(x_m)$. To answer this question, we adjust the integral equation approach for the beam mass variation in Sec. 2.3.1 to the present problem. For reasons of computational efficiency, we use the integral equation approach with enforced essential boundary conditions here and specify the associated system.

The initial formulation of the problem is analogical to the previous one, for which the constant beam rigidity b is replaced now by the beam rigidity profile $b(x)$ in the vector-valued function $\tilde{\mathbf{u}}$ in Eqn. (2.47). This replacement and replacing $g(x)$ as well as the ambient beam mass, g_0, by the constant mass g in the matrix definition in Eqn. (2.48) and the system for Green's function in Eqns. (2.53) has to be done for this purpose. Note that k_0 is the ambient wavenumber corresponding to the present problem, Eqn. (2.55). As mentioned above, we enforce all boundary conditions as essential boundary conditions. Hence, the boundary terms involving $R^{(0)}, R^{(1)}, T^{(0)}$ and $T^{(1)}$ in Eqns. (2.54) are set to zero as separate conditions. Since these imply that Eqns. (2.54) holds for $j = 0, N$, we have the following system of $2(N-1)+8$ equations for the $2(N+1)+4$ unknowns

$\big(\mathbf{u}(x_0), \dots \mathbf{u}(x_N), R^{(0)}, R^{(1)}, T^{(0)}, T^{(1)}\big)$,

$$\begin{aligned}\tilde{\mathbf{u}}(x_j) &= \begin{pmatrix} \mathrm{e}^{\mathrm{i}k_0 x_j} \\ b(\mathrm{i}k_0)^2 \mathrm{e}^{\mathrm{i}k_0 x_j} \end{pmatrix} \\ &\quad + h\bigg(\frac{1}{2}\mathbf{G}(x_j; x_0)(\mathbf{M}(x_0) - \mathbf{M}_0)\tilde{\mathbf{u}}(x_0) + \frac{1}{2}\mathbf{G}(x_j; x_N)(\mathbf{M}(x_N) - \mathbf{M}_0)\tilde{\mathbf{u}}(x_N) \\ &\quad + \sum_{n=1}^{N-1} \mathbf{G}(x_j; x_n)(\mathbf{M}(x_n) - \mathbf{M}_0)\mathbf{u}(x_n)\bigg), \quad j = 1, \dots, N-1, \end{aligned} \tag{2.58a}$$

$$\tilde{\mathbf{u}}(x_0) = \begin{pmatrix} 1 \\ (\mathrm{i}k_0)^2 \end{pmatrix} + \begin{pmatrix} 1 & 1 \\ (-\mathrm{i}k_0)^2 & k_0^2 \end{pmatrix} \begin{pmatrix} R^{(0)} \\ R^{(1)} \end{pmatrix}, \tag{2.58b}$$

$$\tilde{\mathbf{u}}(x_1) = \tilde{\mathbf{u}}(x_0) + h\left(\begin{pmatrix} \mathrm{i}k_0 \\ (\mathrm{i}k_0)^3 \end{pmatrix} + \begin{pmatrix} -\mathrm{i}k_0 & k_0 \\ (-\mathrm{i}k_0)^3 & k_0^3 \end{pmatrix} \begin{pmatrix} R^{(0)} \\ R^{(1)} \end{pmatrix}\right), \tag{2.58c}$$

$$\tilde{\mathbf{u}}(x_N) = \tilde{\mathbf{u}}(x_{N-1}) + h\begin{pmatrix} \mathrm{i}k_0 & -k_0 \\ (\mathrm{i}k_0)^3 & (-k_0)^3 \end{pmatrix} \begin{pmatrix} T^{(0)} \\ T^{(1)} \end{pmatrix}, \tag{2.58d}$$

$$\tilde{\mathbf{u}}(x_N) = \begin{pmatrix} 1 & 1 \\ (\mathrm{i}k_0)^2 & (-k_0)^2 \end{pmatrix} \begin{pmatrix} T^{(0)} \\ T^{(1)} \end{pmatrix}. \tag{2.58e}$$

In analogy to Eqns. (2.54), we have an incident wave of unit amplitude and with wavenumber k_0, i.e. $\mathrm{e}^{\mathrm{i}k_0 x}$, and $h = L/N$ in Eqns. (2.58). Solving this system gives for large N gives an sufficiently accurate solution to the underlying integral equation. The integral equation approach is required to give information about the role of the rigidity slope, appearing in the continuity of shear stress, Eqn. (2.56), in the step-approximation method for varying rigidity. It was already mentioned that it seems to be natural to evaluate the beam rigidity at the mid-point of each sub-interval, which is consistent with the calculation of the wavenumber. One reasonable choice in the shear stress continuity condition would be to neglect the rigidity slope, since the rigidity is chosen to be constant in each sub-interval and the derivative vanishes accordingly. We denote this discretisation scheme as variant I, i.e.

I) the underlying rigidity profile is evaluated at the mid-point of each sub-interval and the rigidity derivative vanishes,

$$\partial_x b^{(-)}(x_m) = 0 \quad \text{and} \quad \partial_x b^{(+)}(x_m) = 0. \tag{2.59}$$

Two alternative ways of calculating the rigidity slope (when evaluating the beam rigidity at the mid-point of each sub-interval) are:

II) the slope of the underlying rigidity profile is evaluated at the mid-point as well and set as the respective value of the derivative of the beam rigidity in the respective interval, i.e.

$$\partial_x b^{(-)}(x_m) = \partial_x b\Big(\frac{x_{m-1} + x_m}{2}\Big) \quad \text{and} \quad \partial_x b^{(+)}(x_m) = \partial_x b\Big(\frac{x_m + x_{m+1}}{2}\Big), \tag{2.60}$$

III) the rigidity slope at the scattering interface $x = x_m$ is calculated as the difference quotient of the point-wise evaluated rigidities in the adjacent sub-intervals, b_m and b_{m+1}, i.e.

$$\partial_x b^{(-)}(x_m) = 2\frac{b_{m+1} - b_m}{l_m + l_{m+1}} = \partial_x b^{(+)}(x_m), \tag{2.61}$$

where l_m denotes the distance between adjacent scattering interfaces, introduced in Eqn. (2.33).

Two additional discretisation schemes involve a linear spline interpolation of the rigidity profile with the location of the scattering interfaces as interpolation points, i.e. $x = x_m$, $m = 0, 1, \dots, M$, and evaluation of the splines at the mid-points of each sub-interval to obtain the discretised beam rigidity, hence Eqn. (2.57) becomes

$$b^{(-)}(x_m) = \frac{b(x_{m-1}) + b(x_m)}{2} =: \tilde{b}_m \tag{2.62a}$$

$$b^{(+)}(x_m) = \frac{b(x_m) + b(x_{m+1})}{2} =: \tilde{b}_{m+1}. \tag{2.62b}$$

Using the analogue schemes of calculating the rigidity slope as in variants II and III gives us the variants 4 and 5 (for linear spline interpolation of the rigidity profile):

IV) the slope of the underlying rigidity profile is evaluated at the mid-point and set as the respective value of the derivative of the beam rigidity in the respective interval, hence this is the same rigidity slope discretisation scheme as in variant II with Eqn. (2.60), i.e.

$$\partial_x b^{(-)}(x_m) = \partial_x b\Big(\frac{x_{m-1} + x_m}{2}\Big) \quad \text{and} \quad \partial_x b^{(+)}(x_m) = \partial_x b\Big(\frac{x_m + x_{m+1}}{2}\Big),$$

V) the rigidity slope in each sub-interval is the slope of the interpolating spline in the respective sub-interval, which gives the scheme

$$\partial_x b^{(-)}(x_m) = \frac{b(x_m) - b(x_{m-1})}{l_m} \quad \text{and} \quad \partial_x b^{(+)}(x_m) = \frac{b(x_{m+1}) - b(x_m)}{l_{m+1}}. \tag{2.63}$$

These five discretisation schemes for the varying rigidity problem are shown schematically in Appendix 2.B.

Now, we want to compare the step-approximation methods based on the five different discretisation schemes of the beam rigidity with the integral equation approach for the beam problem with deterministic single-hump rigidity profile. For this purpose, we use the integral equation approach with enforced essential boundary conditions (for reasons of computational efficiency, as mentioned above) and refer to this approach as the non-standard integral equation approach for the remainder of this section. This investigation is of great importance for the rest of our study, since it influences the choice of the discretisation scheme in the step-approximation method, which is used from now on. Due to the desired accuracy, we choose a very high resolution for the non-standard integral equation approach, $N = 6000$.

To get a first comparison between these different methods, we study the reflection at a beam with a single hump for a wide range of hump amplitudes. Fig. 2.9 shows the reflection coefficient moduli, $|R^{(0)}|$, calculated by the non-standard integral equation approach and step-approximation methods based on discretisation schemes I-V, as functions of (non-dimensional) hump amplitudes, for the hump length $k_0L = 4.0$.

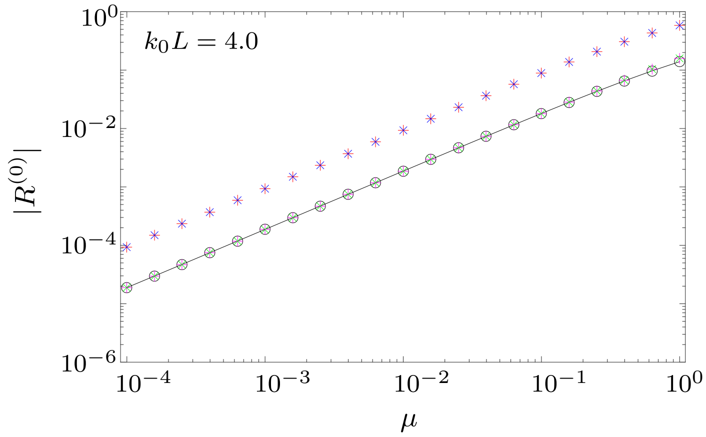

Figure 2.9: Reflection coefficient moduli for single-hump problem as functions of hump amplitudes, for non-dimensional hump lengths $k_0L = 4.0$, computed by non-standard integral equation approach (solid line) and step-approximation method with discretisation variant I (○), II (+), III (+), IV (×), V (×)

We can observe in Fig. 2.9 that the results obtained by the step-approximation method with discretisation variants I, III and V exhibit a very similar behaviour for the whole domain of hump amplitudes. These results also show a very good agreement with the reflection coefficient moduli calculated by the non-standard integral equation approach, although slight upper deviation of the results for discretisation variants III and V is detectable for the largest hump amplitude. In contrast to those results, the step approximation with discretisation variants II and IV overestimates the reflection coefficient moduli by nearly an order of magnitude throughout the whole domain of hump amplitudes considered. Hence, evaluating the slope of the beam rigidity point-wise in each sub-interval in the step approximation seems to be inadequate and the variants II and IV are not considered anymore in the following.

To get further insight into the behaviour of the step approximation with discretisation variants I, III, V and their performance in comparison to the non-standard integral equation approach, we extend the investigation of the reflection as function of hump amplitudes for $k_0L = 4.0$ in Fig. 2.9 to smaller and larger hump lengths. Fig. 2.9 shows the reflection coefficient moduli calculated by the non-standard integral equation approach and step-approximation methods based on discretisation schemes I, III and V, as functions of hump amplitudes, for hump length $k_0L = 2.0$ (left-hand panel) and $k_0L = 7.0$ (right-hand panel).

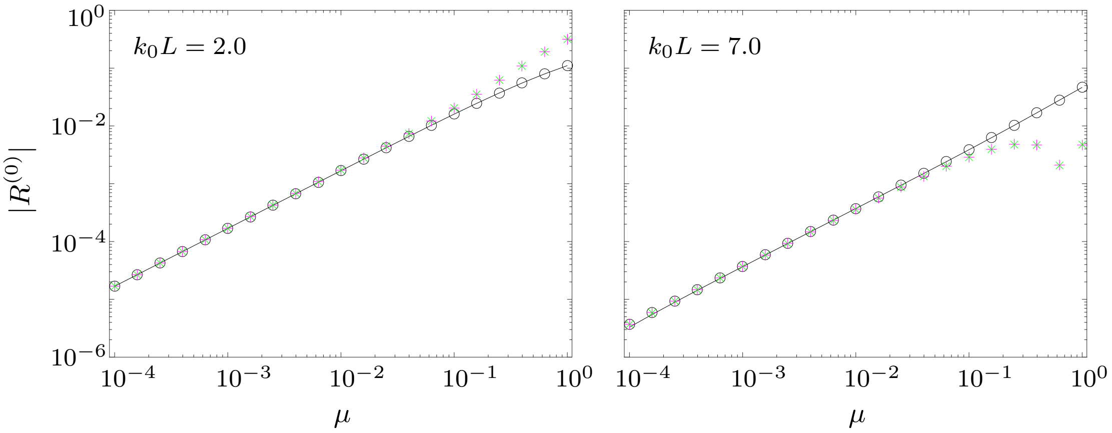

Figure 2.10: Reflection coefficient moduli for single-hump problem as functions of hump amplitudes, for non-dimensional hump lengths $k_0L = 2.0$ (left-hand panel) and $k_0L = 7.0$ (right-hand panel), computed by non-standard integral equation approach (solid line) and step-approximation method with discretisation variants I (○), III (+) and V (×)

We can observe in Fig. 2.10 further aspects of the discretation variants I, III and V. These three discretation schemes yield the same reflection coefficient moduli in the small hump-amplitude regime $\mu \leq 5.0 \times 10^{-2}$ and the results start to deviate for larger hump amplitudes. For the smaller hump amplitude, $k_0L = 2.0$, the discretation variants III and V produce larger reflection than variant I (and the integral equation approach), while for the larger hump amplitude, $k_0L = 7.0$, they give smaller reflection coefficients than variant I (and the integral equation approach, again). The upper deviation for $k_0L = 2.0$ is caused by the additional scattering introduced by the rigidity slope evaluations (via difference quotient and spline slope, respectively) in the rapidly changing rigidity profile, whereas a certain smoothing effect arises for discretisation variants III and V for large hump lengths with only gentle rigidity variations between adjacent sub-intervals. Note that the discretisation variants II and IV (results not shown here) yield reflection coefficients, which overestimate the results by the non-standard integral equation approach by nearly an order of magnitude in both cases, $k_0L = 2.0$ and 7.0, here too, due to the artificial incorporation of scattering by the point-wise evaluation of the rigidity slope. Most important, the discretation variant I shows very good agreement with the non-standard integral equation approach throughout the whole domain of hump amplitudes, $\mu \in (10^{-4},1)$, for the two hump lengths considered, $k_0L = 2.0$ and 7.0. This agreement could already be observed for $k_0L = 4.0$ in Fig. 2.9. We can deduce that neglecting the rigidity slope appearing in the shear stress continuity (Eqns. (2.15b) and (2.56) in detail), which is consistent with our approach of using piece-wise constant rigidity in each sub-interval in the step-approximation method, is the correct discretisation. From now on, the beam rigidity will be be discretised using variant I, Eqn. (2.59), without further note throughout the rest of the work.

We could observe a linear scaling of the reflection coefficient moduli with the hump amplitudes, μ, for not-too-large μ in the case of varying mass in Sec. 2.3.1. For the present problem of rigidity variation, this linear behaviour of the reflection coefficient moduli holds for the cases of L considered, $k_0L = 2.0$, 4.0 and 7.0, throughout the whole hump amplitude regime. To get a more detailed view into the reflection at the single hump in the rigidity profile for various hump lengths and the performance of the step-approximation method in comparison with the integral equation approach, we consider the reflection at humps of length $k_0L \in (1,10)$ now. Fig. 2.11 shows the reflection coefficient moduli, calculated by the step-approximation method and the non-standard integral equation approach, as functions of non-dimensional hump lengths, for amplitudes $\mu = 10^{-1}$ and 5.0×10^{-1} (for which the insufficiency of the alternative discretisation variants became most evident, though).

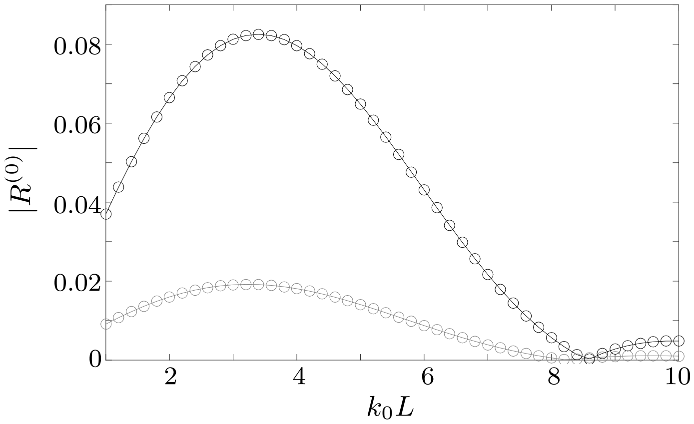

Figure 2.11: Reflection coefficient moduli for single-hump problem as functions of non-dimensional hump length, for hump amplitudes $\mu = 10^{-1}$ (grey) and 5.0×10^{-1} (black), computed by non-standard integral equation approach (solid line) and step-approximation method (○)

Fig. 2.11 confirms for the entire range of hump lengths considered, $k_0L \in (1,10)$, that the step-approximation method produces the same results as the integral equation approach for the large hump amplitudes $\mu = 10^{-1}$ and 5.0×10^{-1}. We can also see that the reflection coefficients feature the same qualitative and quantitative behaviour as those for the varying mass problem. This is consistent with the reflection characteristics we could observe in dependence of the hump amplitude, since they were of the same magnitude in both cases we dealt with for the varying mass and rigidity problem, $k_0L = 2.0$ and 4.0. Hence, the deterministic single hump in the beam mass and rigidity seem to lead to the same total reflection of incident waves in most cases.

Finally, we investigate the wave field for the deterministic hump variation in the beam rigidity, for the same hump length and amplitude as in the mass variation case (Fig. 2.5). Fig. 2.12 shows the wave field, calculated by the step-approximation method and integral equation approach, split into real and imaginary part, for non-dimensional hump length $k_0L = 4$ and hump amplitude $\mu = 5.0 \times 10^{-1}$.

We can observe in Fig. 2.12 that the wave field shows exactly the same deviation from the incident wave field, which is also shown for comparison, as in the varying mass case,

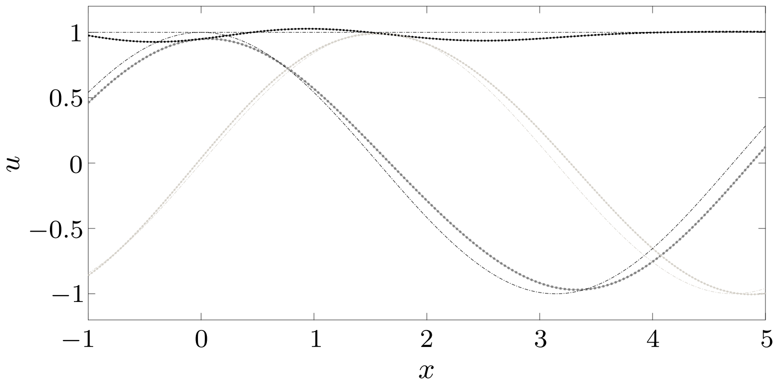

Figure 2.12: Individual wave field for single-hump problem with non-dimensional hump length $k_0L = 4$ and hump amplitude $\mu = 5.0 \times 10^{-1}$, computed by non-standard integral equation approach (solid line) and step-approximation method (∘), shown as its modulus (black), and split into real part (dark grey) and imaginary part (light grey). Components of incident wave are shown for comparison (dash-dotted line with same colour scheme).

i.e. both the real and imaginary part of the wave field as well as the wave field modulus are the same as in the previous problem. In addition, it should not go unmentioned that the step-approximation method exhibits very good agreement with the integral equation approach again. Altogether, this (qualitative) agreement of wave fields together with the (quantitative) agreement of reflection characteristics obtained by the step-approximation method and the integral equation approach for both varying mass and varying rigidity problem make us confident that the step-approximation method is a good and accurate solution method for wave propagation along beams with more general and complex roughness profiles.

2.3.3 Convergence of step-approximation method

This validation section will be concluded with a numerical convergence study of the step-approximation method. For this, we use the single-hump problem formulation and analyse the behaviour of the step-approximation method in comparison to the solution given by the non-standard integral equation approach, again with $N = 6000$. Fig. 2.13 shows the reflection coefficient moduli, $|R^{(0)}|$, calculated by the step-approximation method as functions of the number of sub-intervals, M, used to discretise the hump interval (0,4), which we refer to as the resolution of the step approximation, for the hump amplitudes $\mu = 10^{-1}$ (top panels) and 5.0×10^{-1} (bottom panels), for both varying mass (left-hand panels) and varying rigidity (right-hand panels). The results obtained by the integral equation approach are shown for comparison.

We can observe in Fig. 2.13 that the step-approximation method solution converges quickly towards the accurate integral equation approach solution. For the smaller hump amplitude, $\mu = 10^{-1}$, the step-approximation method already gives acceptable results for both the varying mass and varying rigidity problem for only one sub-interval, $M = 1$, in the hump domain. For $M = 2$ in both problems, the reflection coefficient modulus exhibits

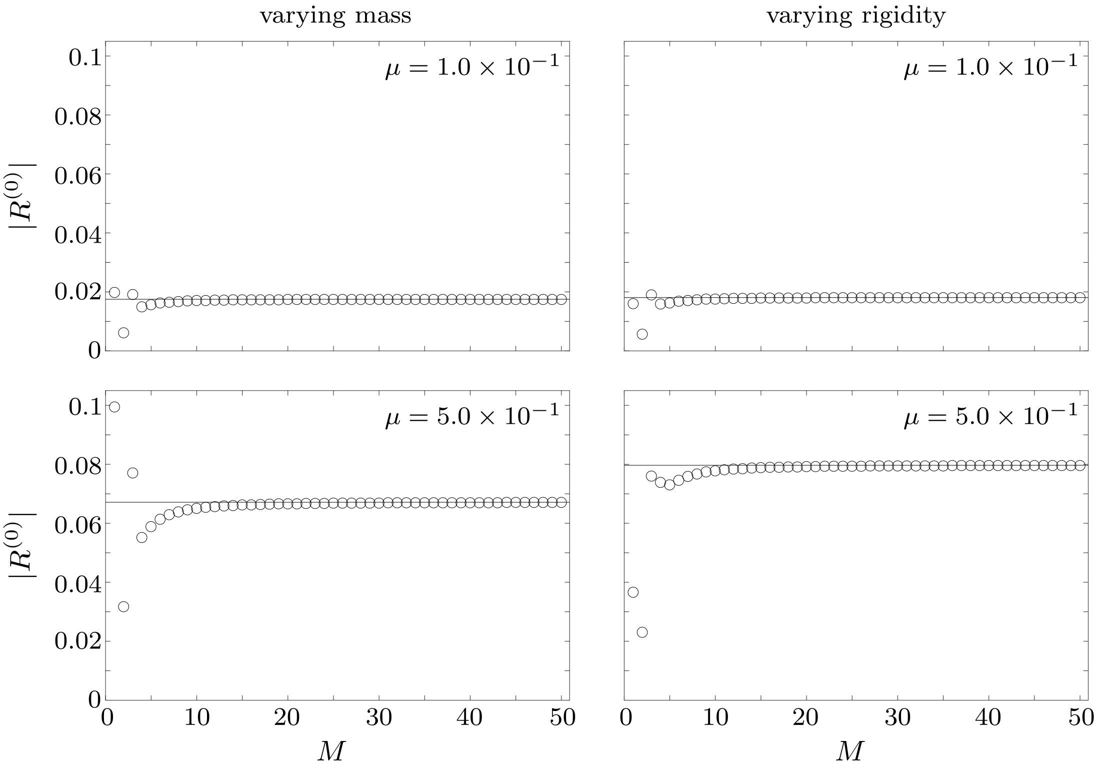

Figure 2.13: Resolution convergence of step-approximation method for single-hump problem with non-dimensional hump length $k_0L = 4.0$ and hump amplitudes $\mu = 1.0 \times 10^{-1}$ (top panels) and $\mu = 5.0 \times 10^{-1}$ (bottom panels) for varying mass (left-hand panels) and varying rigidity problem (right-hand panels). Results obtained by integral equation approach are shown for comparison (solid line).

significantly larger deviation from the integral equation approach solution. This is due to the evaluation of the varying quantity at the mid-point of each sub-interval which leads in the case of two sub-intervals and the symmetric hump-problem to neglect of the hump maximum and vanishing scattering at the interface of the two sub-intervals. Consequently, the reflection is very small for this case. For $M = 3$, we can see a slight overprediction of the reflection coefficient modulus for the smaller hump amplitude and convergence of the reflection coefficient moduli for $M \geq 4$ towards the solution obtained by the integral equation approach. For $M \geq 9$, no deviations of the results are observable anymore and $|R^{(0)}|$ remains constant and in agreement with the integral equation approach result throughout the larger resolution domain.

In the cases of the larger hump amplitude, $\mu = 5.0 \times 10^{-1}$, the deviations in the very small resolution regime are also observable and larger in their extent, but the reflection coefficient moduli start to convergence for $M \geq 4$ and $M \geq 5$ for the varying mass and the varying rigidity problem, respectively. To obtain results from the step-approximation method, which nearly agree with the ones by the integral equation approach, a higher resolution than for the smaller hump amplitude is needed, i.e. $M \geq 15$. It is interesting that we reached the hump amplitude regime, for which the reflection coefficient modulus, $|R^{(0)}|$, is not scaled with the hump amplitude anymore for the varying mass problem, hence the mass variations lead to less scattering than the varying rigidity problem. However, the step-approximation method and the integral equation approach still give coinciding results for sufficiently large resolution.

To study the convergence of the step-approximation method more quantitatively, we use the definition of convergence rates for sequences, see e.g. Isaacson and Keller 1994, and apply it to the present problem. For this, we denote the reflection coefficient modulus obtained for M sub-intervals with $|R_M^{(0)}|$. We say that the step-approximation method converges linearly if $|R_M^{(0)}|$, $M = 1, 2, \ldots$, converges to the value $|R^{(0)}|$ and if there exists a real number $\lambda > 0$ such that

$$\lim_{M\to\infty} \frac{\left||R_{M+1}^{(0)}| - |R^{(0)}|\right|}{\left||R_M^{(0)}| - |R^{(0)}|\right|^{\alpha}} = \lambda \tag{2.64}$$

for $\alpha = 1$. In general, α is the convergence rate of the sequence.

Defining the error of the step-approximation method for M sub-intervals as $e_M = |R_M^{(0)}| - |R^{(0)}|$, Eqn. (2.64) yields for $M \to \infty$

$$|e_{M+1}| \approx \lambda |e_M|^{\alpha} \quad \text{and} \quad |e_M| \approx \lambda |e_{M-1}|^{\alpha}, \tag{2.65}$$

and we can write

$$\frac{e_{M+1}}{e_M} \approx \frac{\lambda |e_M|^{\alpha}}{\lambda |e_{M-1}|^{\alpha}} = \left|\frac{e_M}{e_{M-1}}\right|^{\alpha}. \tag{2.66}$$

Eqn. (2.65) then gives the convergence rate for large M as

$$\alpha \approx \frac{|e_{M+1}|/|e_M|}{|e_M|/|e_{M-1}|}. \tag{2.67}$$

Since we cannot compute $|R^{(0)}|$ exactly, we do not know the ratios of consecutive errors in Eqn. (2.67). Neglecting higher-order terms in analogy to Senning 2017, we can approximate the ratios in Eqn. (2.67) for large M as the ratios of the differences of consecutive $|R_M^{(0)}|$, i.e.

$$\frac{e_{M+1}}{e_M} = \frac{\left|R_{M+1}^{(0)}\right| - |R^{(0)}|}{\left|R_M^{(0)}\right| - |R^{(0)}|} \approx \frac{\left|R_{M+1}^{(0)}\right| - \left|R_M^{(0)}\right|}{\left|R_M^{(0)}\right| - \left|R_{M-1}^{(0)}\right|}. \tag{2.68}$$

This approximation can be used in Eqn. (2.67), which provides us with the approximation of the convergence rate,

$$\alpha \approx \frac{\log\left||R_{M+1}^{(0)}| - |R_M^{(0)}|\right|}{\log\left|\left|R_M^{(0)}\right| - |R_{M-1}^{(0)}|\right|}. \tag{2.69}$$

We can observe the approximated convergence rate via Eqn. (2.69) in the left-hand panel of Fig. 2.14 for the hump length $k_0L = 4.0$ and the large hump amplitude $\mu = 5.0 \times 10^{-1}$, for the varying rigidity problem. The approximated convergence rate clearly tends to 1 for sufficiently large M ($M \geq 20$), which suggests linear convergence of the step approximation.

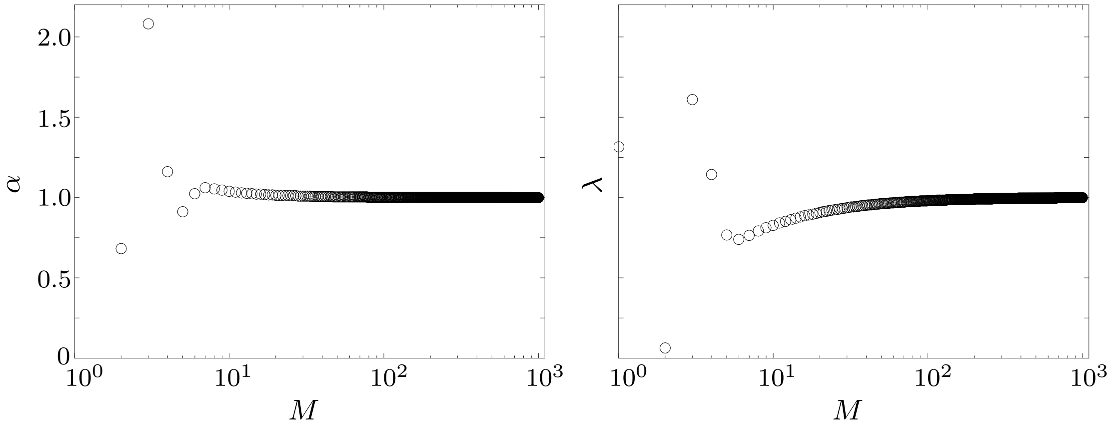

Figure 2.14: Left-hand panel: Approximation of convergence rate for single-hump problem with non-dimensional hump length $k_0L = 4.0$ and hump amplitude $\mu = 5.0 \times 10^{-1}$ for varying rigidity problem. Right-hand panel: Validation of linear convergence of step approximation for the same setting as in left-hand panel

The suggested linear convergence rate is now validated by the convergence definition (2.64). Fig. 2.13 and the results in the previous section suggest that the integral equation approach gives a very accurate approximation for the reflection coefficients modulus. Hence, the value $|R^{(0)}|$ shall be given by the integral equation approach now. The right-hand panel of Fig. 2.14 shows λ from the convergence rate definition (2.64), where the convergence rate α is in accordance to above set equal to one. We can see that λ tends towards a constant value, $\lambda \to 1$, for high resolution of the step approximation discretisation, and reaches 1 for $M \geq 100$. Hence, the reflection coefficient modulus fulfills the definition of linear convergence and we can conclude that the step-approximation method exhibits linear convergence.

2.4 Rough profile generation

The main goal of Chs. 2 and 3 is to understand and describe the attenuation of waves propagating along rough beams in vacuo as well as attenuation of water waves by large ice floes floating on water. As mentioned before, rough surfaces can have significant effects on wave propagation. To study these effects for the beam problems, we incorporate roughness into the beam properties. For this, we may consider problems of beams with varying thickness. Since thickness variations directly influence both the beam mass and the beam rigidity, we firstly focus on variations of each of these quantities only and investigate their effect. In each of these respective problems, the varying quantity shall fluctuate continuously about its mean, where the fluctuation shall be described by a random process. We choose a random processes with Gaussian autocorrelation for this purpose, which is widely used to model rough surfaces, see Tsang et al. 2000. The popularity of this class of random processes is together with other features based on the matter of fact that they are described with their mean and covariance function only. This will prove to be beneficial for the semi-analytical methods to describe wave attenuation over long distances.

When setting up roughness profiles for the beam problems, we want to generate an ensemble of profiles, which share on average the same roughness characteristics. These roughness characteristics are the roughness amplitude and the characteristic length, which describes the correlation between nearby points of the profile (on average). The roughness amplitude, ϵ, can be modified by scaling the random process and can be taken into account later when specifying the roughness profile of either the beam mass or rigidity or both (via the beam thickness). Hence, we want to generate realisations of a random process $\psi(x)$, which have the same (specific) characteristic length, i.e. the relationship between the ensemble of realisations is expressed via the autocorrelation condition

$$\langle \psi(x)\, \psi(x+\xi) \rangle = \rho(|\xi|), \tag{2.70}$$

where $\langle \cdot \rangle$ denotes the ensemble average of the included quantity with respect to realisations and ρ is the autocorrelation function describing the average correlation of two points with distance ξ in-between, x and $x+\xi$. Here, we assume stationarity of the random process ψ, i.e. the distribution function, which specifies the random process, is invariant with respect to shifts in x and only the distance ξ between the two points determines the correlation magnitude, and the random process has mean zero, which ensures that the varying quantity fluctuates about its mean.

To generate individual realisations of roughness profiles, we consider a (target) random process $\psi_0(x)$, which shall have mean zero and a not-yet specified mean-square spectral density function $S_0(r)$, describing the strength of variations as a function of frequency and giving the standard deviation, σ, of the process $\psi_0(x)$ in the mean-square,

$$\sigma = \left[\int_{-\infty}^{\infty} S_0(r)\, \mathrm{d}r \right]^{1/2}. \tag{2.71}$$

The important work towards the formulation we will use later was done by Goto and Toki (1969), who introduced a stationary random process of the form

$$\tilde{\psi} = \frac{1}{\sqrt{N}} \sum_{n=1}^{N} \cos\left(\tilde{r}_n x + \varphi_n\right), \tag{2.72}$$

where the frequencies $\tilde{r}_n$, $n = 1, \dots, N$, are independent random variables identically distributed with probability density function f and the phases φ_n, $n = 1, \dots, N$, are independently selected from a uniform distribution over the interval $(0,2\pi]$.

On the basis of the work by Goto and Toki (1969), Shinozuka (1971) presented the following series to simulate the target random process ψ_0,

$$\psi(x) = \sigma\sqrt{\frac{2}{N}}\sum_{n=1}^{N}\cos\left(r_n x + \varphi_n\right), \tag{2.73}$$

where the frequencies r_n, $n = 1, \ldots, N$, are independently chosen from the probability density function f retrieved from normalising $S_0(r)$ by the process' variance, σ^2, i.e.

$$f(r) = \frac{S_0(r)}{\sigma^2}. \tag{2.74}$$

The extension of the series (2.72) by $\sigma\sqrt{2}$, which leads to the series (2.73), ensures that the the simulated random process has standard deviation σ. Shinozuka and Kobori (1972) used this random process e.g. for modelling the road-surface roughness of a bridge in bridge fatigue life estimations. Based on the studies by Shinozuka (1971), it is shown in Appendix A using the Wiener–Khinchin theorem, an important tool in the stochastic series analysis, that the random process in Eqn. (2.73) has mean zero and (on average) the same autocorrelation and mean-square spectral density function as the target random process ψ_0. The Wiener–Khinchin theorem and the central-limit theorem are also applied to show that the random process is mean-ergodic and ergodic in the mean-square spectral density, hence ergodic in the autocorrelation, i.e. the mean as well as the autocorrelation yield the same results regardless whether the ensemble average or the spatial average is taken, and the ensemble quantities can be deduced from one single, random sample of the process ψ over a sufficiently long interval.

A variety of different random processes could be used to describe roughness profiles of beams both in vacuo and floating on water. Since we are mainly interested in waves travelling through the rough regime, as well as their relations to the associated multiple-scale approaches, we focus on one class of random process here. Since roughness profile variations look closely Gaussian distributed in many rough surface problems, see e.g. Thomas 1999, and Gaussian autocorrelated random processes are (mathematically conveniently) described with their mean and covariance function only, their use is feasible in our problems. The target autocorrelation function, ρ_0, which describes the autocorrelation of the target random process ψ_0, shall be given by a squared exponential (Gaussian) autocorrelation function, i.e.

$$\rho_0(|\xi|) = \mathrm{e}^{-\xi^2/l_{\mathrm{G}}^2}, \tag{2.75}$$

where l_{G} denotes the characteristic length, which is referred to as the correlation length from here on.

To simulate this target random process ψ_0 with the analysed series ψ in Eqn. (2.73), the probability density function f for the frequencies r has to be specified. Because of the relation in Eqn. (2.74), it is sufficient to find the corresponding mean-square spectral density function S_0. Based on the Wiener–Khinchin theorem (see Appendix A for details), S_0 can be determined, and to simulate the target random process satisfying the Gaussian autocorrelation condition (Eqn. (2.75)) in the limit $N \to \infty$ with the series

$$\psi(x) = \sqrt{\frac{2}{N}} \sum_{n=1}^{N} \cos\left(r_n x + \varphi_n\right), \tag{2.76}$$

the frequencies r_n, $n = 1, \ldots, N$, are random variables independently chosen from a Gaussian distribution with zero mean and standard deviation equal to $\sqrt{2}/l_{\mathrm{G}}$, and the phases φ_n, $n = 1, \ldots, N$ are independently selected from a uniform distribution over the interval $(0, 2\pi]$. It is shown numerically in Appendix A that the random process ψ indeed has vanishing ensemble average and spatial mean, and it fulfils the ensemble and spatial autocorrelation condition ρ_0.

We can observe in the statistical analysis in Appendix A that using the computational efficient choice $N = 400$ terms in Eqn. (2.76) to generate the random process ψ is sufficient to meet the Gaussian autocorrelation condition satisfactorily, i.e. the generated random process is autocorrelated squared exponentially accurately enough for our purposes in this work. Hence, we set $N = 400$ for the generation of the random process throughout the rest of this work.

We consider wave propagation along infinitely long beams, which exhibit roughness over a long, finite interval $x \in (0, L)$. If not specified otherwise, the roughness shall extend over an interval of length $\bar{k}L = 400 \times \bar{k}l_{\mathrm{G}}$ for the following results. Since the (continuous) roughness profile shall fluctuate about the mean of the respective varying quantity (beam mass, rigidity or thickness) and the beam profile is assumed to be continuous at the boundaries of the finite interval $(0, L)$, we use a numerical boundary step control, which ensures the continuity at $x = 0, L$. Those boundary continuity conditions between the rough and semi-infinite intervals are ensured numerically by only considering profile realisations with sufficiently small steps at the respective interfaces. It was approved that the boundary step control does not influence the statistical properties of the random process ψ, hence the ensemble and spatial autocorrelation condition ρ_0 remain fulfilled.

2.5 Effective wave field via random sampling

When studying wave propagation through rough media, the effective wave field is often the quantity of interest. The effective wave field is the mean wave field with respect to an ensemble of individual realisations. Numerical calculations of the wave field for each individual realisation of the roughness profile are based on the step-approximation method, which is outlined in Sec. 2.2. To obtain the effective wave field for roughness profiles with the same average characteristics, i.e. roughness amplitude and correlation length, (individual) wave fields are calculated for a large ensemble of randomly generated realisations of roughness profiles, in which profiles share the same amplitude, ϵ, and correlation length, l_{G}. The relationship between an ensemble of roughness profiles is expressed via the Gaussian autocorrelation condition in Eqn. (2.75).

Typically, wave energy decays exponentially in these problems of waves interacting with rough media. In particular, this also applies for wave propagation along rough beams and water waves propagating along rough, floating beams. Hence, the absolute value of the (complex-valued) individual wave fields, $|u|$, and effective wave field, $|\langle u\rangle|$, are expected to decay exponentially over the rough interval. We can measure the exponential decay, which is denoted as the attenuation coefficient, Q, using a least-squares minimisation routine. The effective attenuation coefficient, which describes the exponential decay of the effective wave field, is therefore defined via

$$|\langle u\rangle| \propto \mathrm{e}^{-Q_{\mathrm{eff}}x}, \qquad x \in (0,L). \tag{2.77a}$$

To compare the attenuation behaviour of effective wave fields with respective individual wave fields, we want to measure the exponential decay of the individual wave fields as well. In order to get reliable and representative quantitative results for individual wave fields, we retrieve the attenuation coefficients for each individual wave field in the ensemble of generated roughness profiles and use the average of these attenuation coefficients as the characteristic individual attenuation coefficients, Q_{ind}. In detail, the attenuation coefficient for each roughness profile in the ensemble is accordingly to above obtained via

$$|u_i| \propto \mathrm{e}^{-Q_i x}, \qquad x \in (0,L), \tag{2.77b}$$

and the individual attenuation coefficient is obtained after that by averaging Q_i, i.e.

$$Q_{\mathrm{ind}} = \langle Q_i\rangle. \tag{2.77c}$$

After introducing the effective wave field and the formal definitions, how to describe the exponential decay of the wave fields above, the question remains how large the ensemble of roughness realisations/individual wave fields has to be chosen to obtain representative effective wave fields. To answer this question, we consider beams with mass variations in $(0,L)$, which are described by the Gaussian autocorrelated random process in Eqn. (2.76). This problem will be analysed extensively in Sec. 2.6.

Fig. 2.15 shows box-and-whisker plots of the effective attenuation coefficients, as functions of ensemble size (number of profile realisations used in random sampling process), for the varying mass problem with a specified, reasonable large roughness amplitude and non-dimensional correlation lengths $\bar{k}l_{\mathrm{G}} = 0.9$, 2.5 and 4.1, where $\bar{k}$ is the mean wavenumber, which corresponds to the mean mass. For each ensemble size and non-dimensional correlation length, the effective attenuation coefficients are calculated 40 times to have a sufficiently large sample size for the statistical analysis. The boxes indicate the intervals containing the central 50% of the sampled data (25% to 75% quantiles), and the horizontal lines within them denote the median values (50% quantiles). The whiskers indicate the remaining data lying in the range of 1.5 times the height of the central box next to the quantiles. Points outside this range are considered to be outliers and are shown as bullets. The results are obtained using the random-sampling method based on the step approximation, which we refer to in the following for the sake of simplicity as the random-sampling method only. Since the results serve for qualitative illustration only, the values of the effective attenuation coefficients on the linearly scaled ordinate axis are not specified.

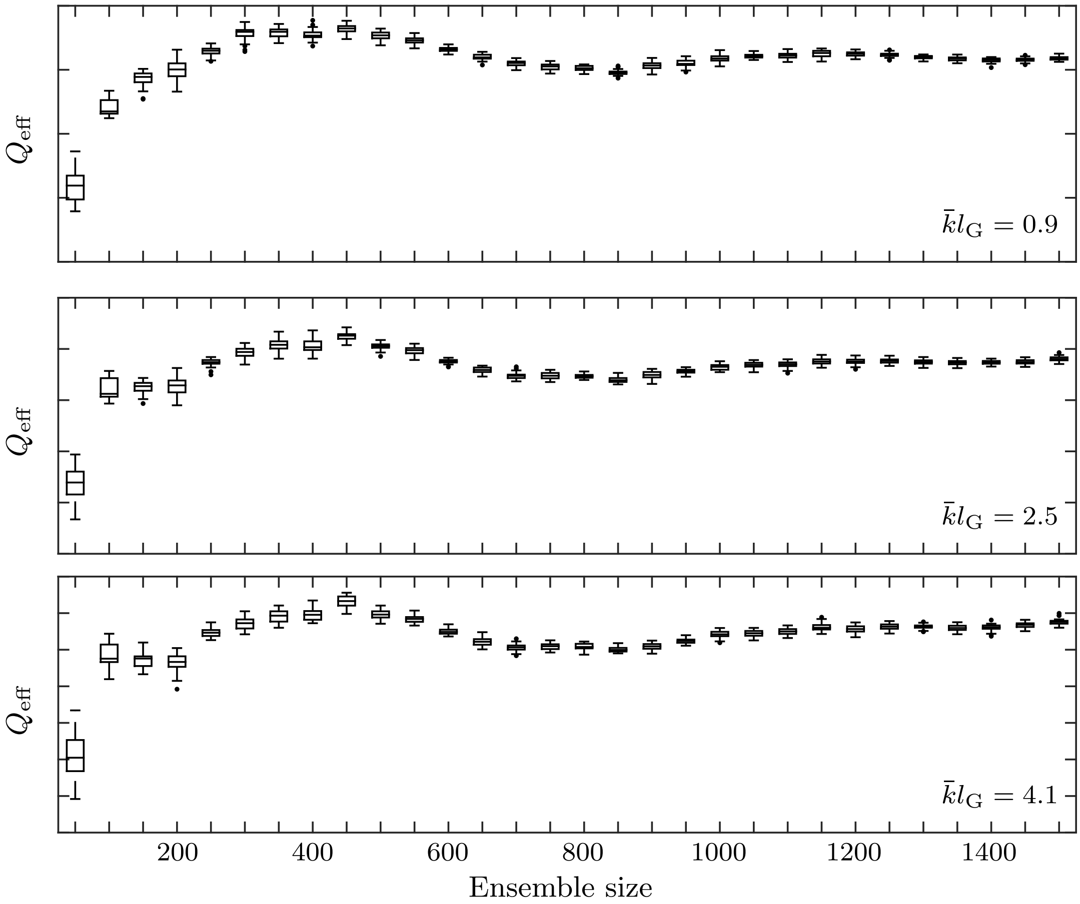

Figure 2.15: Box-and-whisker plots of attenuation coefficients as functions of ensemble size (multiples of 50 up to 1500) for varying mass problem, for non-dimensional correlation lengths $\bar{k}l_{\mathrm{G}} = 0.9$ (top), $\bar{k}l_{\mathrm{G}} = 2.5$ (middle) and $\bar{k}l_{\mathrm{G}} = 4.1$ (bottom)

We can see in Fig. 2.15 that small ensemble sizes lead to an underprediction of the attenuation of the respective effective wave field for all non-dimensional correlation lengths shown. It takes an ensemble size of approximately 1000 to achieve convergence with respect to the attenuation coefficients. Enlarging the ensemble size beyond 1000 provides greater accuracy, which is indicated by the quantiles moving closer together. In following sections, the ensemble used to calculate the effective wave fields consist of 1500 randomly generated roughness profile realisations, which also ensures converged results for the individual attenuation coefficients.

For the step approximation in the random-sampling method, the roughness interval has to be divided into sub-intervals in order to approximate the roughness profile by piece-wise constant functions and calculate the wave fields afterwards. To obtain the numerical results in Fig. 2.15, each correlation length (embodying already a natural division of the rough interval) was divided into four sub-intervals. Fig. 2.16 shows the effective attenuation coefficients as functions of correlations lengths for the cases of dividing each correlation length into four as well as 16 sub-intervals in the step approximation, for an intermediate roughness amplitude ($\epsilon = 1.0 \times 10^{-2}$, left-hand panel) and large roughness amplitude ($\epsilon = 1.0 \times 10^{-1}$, right-hand panel). Again, the values of the effective attenuation coefficients on the linearly scaled ordinate axis are not specified.

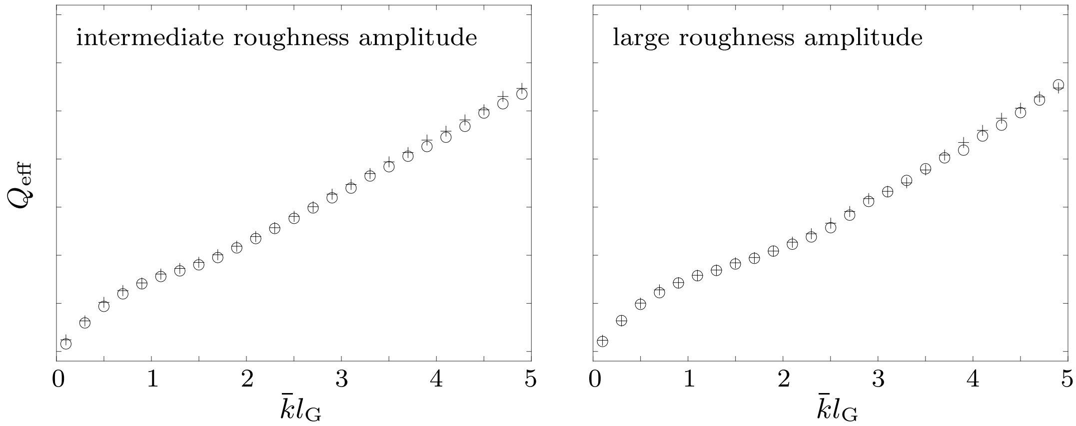

Figure 2.16: Effective attenuation coefficients as functions of correlation length for resolution of four (○) and 16 sub-intervals (+) per correlation length in the step approximation, for intermediate (left-hand panel) and large roughness amplitude (right-hand panel)

We can see in Fig. 2.16 that the resolution of four sub-intervals per correlation length gives the same effective attenuation coefficients as the resolution of 16 sub-intervals per correlation length in the step approximation for both intermediate and large roughness amplitudes. This is consistent with the resolution convergence we could observe for the deterministic hump problem in Fig. 2.13 since the appearing humps in the autocorrelated random process extend over multiple correlation lengths. As a matter of course, we can expect agreement between effective attenuation coefficients calculated with four sub-intervals per correlation length and those calculated with 16 sub-intervals per correlation length also for smaller roughness amplitudes. For computational efficiency, the discretisation resolution of four sub-interval per correlation length will be used for the random-sampling method in the following sections, if not specified otherwise. The quantitative and qualitative behaviour of the effective wave fields and attenuation coefficients are not discussed here and we refer for this to the next sections.

2.6 Rough beam with varying mass

In the following, we consider the problems of a beam with a varying mass $g(x)$ (this section), a beam with varying rigidity $b(x)$ (Sec. 2.7) and a beam with varying thickness leading to variations in both its mass and rigidity (Sec. 2.8). In this section, we focus on the first problem of wave propagation of waves along a beam with varying mass, only. Hence, the linear thin-beam equation (2.9) becomes

$$b\partial_x^4 u(x) - \alpha g(x) u(x) = 0, \qquad x \in (-\infty,\infty) \tag{2.78}$$

for the varying mass problem, for which the beam rigidity is chosen to be constant. The mass variations are caused by density variations and the mass $g(x)$ shall fluctuate about the mean $\bar{g}$. The varying mass is defined as

$$g(x) = \bar{g}(1 + \epsilon\gamma(x)). \tag{2.79}$$

The fluctuations are modelled via the Gaussian autocorrelated random process introduced in Sec. 2.4, i.e. $\gamma \equiv \psi \in \mathcal{O}(1)$. Hence, the fluctuations, $\epsilon\gamma(x)$, have a known characteristic length, the correlation length l_{G}, and root-mean-square amplitude, ϵ, which is referred to as the (non-dimensional) roughness amplitude. Fig. 2.17 shows the roughness characteristics, l_{G} and ϵ, schematically for the varying roughness profile and corresponding step approximation from Fig. 2.2.

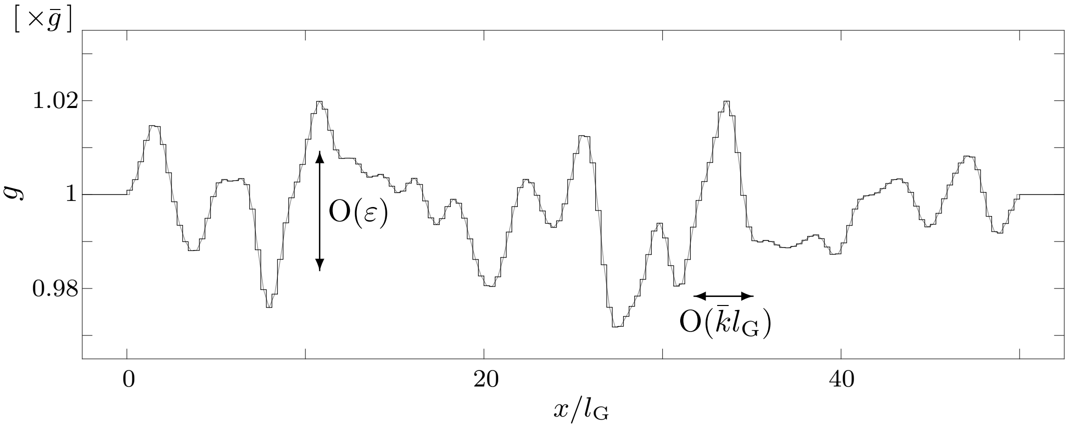

Figure 2.17: Example realisation of continuous roughness profile (grey curve) and corresponding step approximation with four sub-intervals per correlation length (black) for varying mass problem, for roughness amplitude $\epsilon = 1.0 \times 10^{-2}$ and non-dimensional correlation length $\bar{k}l_{\mathrm{G}} = 2.5$.

To establish consistency with the multiple-scale method in Sec. 2.6.2, the assumption $\epsilon \ll 1$ is made, although this is not required in general, up to the point at which the variations are large enough to produce intervals of negative mass ($\epsilon \approx 0.3$) with non-negligible likelihood. We note that the varying mass problem can be expressed as

$$\partial_x^4 u(x) - k^4(x)\, u(x) = 0, \qquad x \in (-\infty,\infty), \tag{2.80}$$

where the wavenumber $k(x) = (\alpha g(x)/b)^{\frac{1}{4}}$.

Individual realisations of the random process, $\gamma(x)$, are generated using Eqn. (2.76), which yields ergodicity in the mean and autocorrelation, as we have seen in Sec. 2.4. Hence,

γ satisfies the Gaussian autocorrelation condition

$$\langle \gamma(x)\,\gamma(x-\xi)\rangle = \mathbf{E}[\gamma(x)\,\gamma(x-\xi)] = \mathrm{e}^{-\xi^2/l_{\mathrm{G}}^2} \tag{2.81}$$

for a sufficiently large number of terms in the generation of the random process. To study the characteristic behaviour of individual and effective waves travelling along a beam with varying mass, wave fields are calculated with the random-sampling method for a large ensemble of randomly generated realisations of roughness profiles, in which profiles share the same amplitude, ϵ, and correlation length, l_{G}, which gives robust results for the (averaged) individual wave propagation and we directly can obtain the effective wave fields.

2.6.1 Preliminary wave field analysis

Before we derive and validate the multiple-scale method and study the wave attenuation quantitatively in the following sections, we compare the effective wave field to the individual wave fields that form the ensemble, first. Fig. 2.18 shows the moduli of example individual wave fields and corresponding effective wave fields, for roughness amplitude $\epsilon = 5.0 \times 10^{-2}$ and non-dimensional correlation lengths $\bar{k}l_{\mathrm{G}} = 0.9$ (left-hand panel) and 4.1 (right-hand panel).

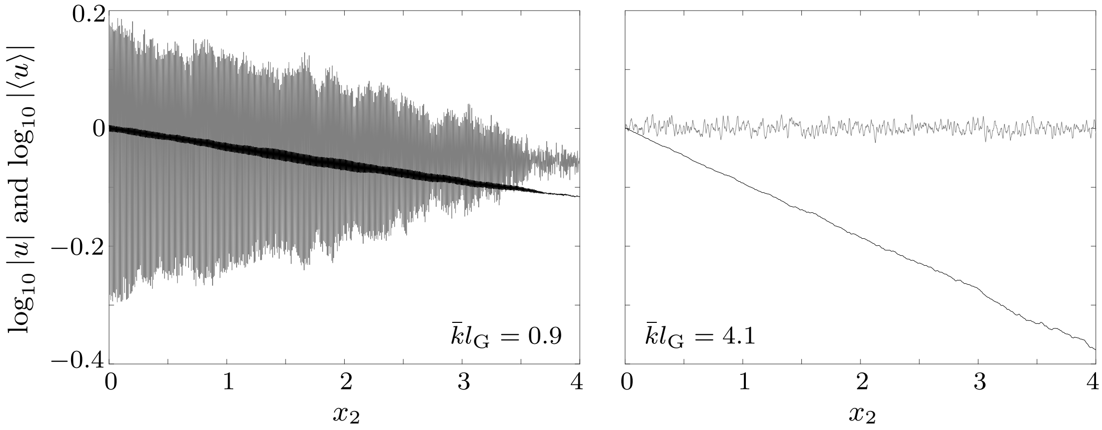

Figure 2.18: Example individual wave fields (grey curves) and effective wave fields (black) for varying mass problem, for roughness amplitude $\epsilon = 5.0 \times 10^{-2}$ and non-dimensional correlation lengths $\bar{k}l_{\mathrm{G}} = 0.9$ (left-hand panel) and $\bar{k}l_{\mathrm{G}} = 4.1$ (right-hand panel)

The smaller correlation length, $\bar{k}l_{\mathrm{G}} = 0.9$, is chosen to produce the strong attenuation of the individual wave fields. Despite this, they attenuate weakly and less than their corresponding effective wave fields. The larger correlation length, $\bar{k}l_{\mathrm{G}} = 4.1$, is chosen to produce strong attenuation of the effective wave fields. In this regime, the fluctuations in the beam are too mild to attenuate the individual wave fields and their moduli randomly fluctuate around unity. It is the de-correlation of the individual wave fields that causes attenuation of the effective wave field. These observations are consistent with those made by Wu (1982) and Bennetts et al. (2015), who studied amplitude attenuation of seismic waves and water waves propagating over a rough seabed in intermediate water depth, respectively.

2.6.2 Multiple-scale method

Since the computational expense for the random-sampling method is very high to obtain the attenuation behaviour of effective wave fields, we now derive a semi-analytical method to obtain an equation for the envelope of the (effective) wave field. We use a two-scale approximation similar to that of Mei and Hancock (2003), Mei et al. (2005) and Bennetts et al. (2015), who considered the problem of water waves travelling over a rough sea bed. For this approach, we consider the rough interval to be unbounded, and let the correlation length, l_{G}, represent a local scale and $L_{\mathrm{ob}} = l_{\mathrm{G}}/\epsilon^2$ an observation scale, for which $\epsilon \ll 1$ is required, i.e. the roughness amplitude ϵ is used to relate the local scale, represented by the correlation length, and the observation scale, over which attenuation is observed. The coordinates x and $x_2 = \epsilon^2 x$ are used to define locations on the local and observation scales, respectively. Since the attenuation coefficients do not depend on an intermediate scale, the coordinate $x_1 = \epsilon x$ is neglected. We adopt a multiple-scale expansion for the wave field, u, to map the wave field into the new coordinate system, i.e.

$$u(x) = u_0(x,x_2) + \epsilon u_1(x,x_2) + \epsilon^2 u_2(x,x_2) + \mathcal{O}\left(\epsilon^3\right). \tag{2.82}$$

By application of the chain rule, the expansion

$$\partial_x u = \sum_j \epsilon^j \left(\partial_x u_j + \epsilon^2 \partial_{x_2} u_j\right) \tag{2.83}$$

for the derivative is obtained. The equations to be satisfied by the u_j are derived by substituting the multiple-scale expansion (2.82) into the governing equation for a beam with varying mass, Eqn. (2.78) and separating the terms with respect to orders of ϵ.

Order ϵ^0

The order ϵ^0 terms provide the governing equation for the leading-order wave field, u_0, to be

$$(\partial_x^4 - \bar{k}^4)u_0(x,x_2) = 0, \qquad x \in (-\infty,\infty), \tag{2.84}$$

where the wavenumber is given by $\bar{k} = (\alpha\bar{g}/b)^{\frac{1}{4}}$, i.e. Eqn. (2.84) is equivalent to that of a uniform beam, Eqn. (2.A.1), with constant mass $\bar{g}$. The solution of Eqn. (2.84) consists of two wave components, a modulated rightward-travelling wave (depicts incident wave travelling along the rough beam) and a random leftward-travelling wave (depicts reflected wave). Bennetts et al. (2015) showed in the setting of water waves travelling over a rough sea-bed in intermediate depth that only a right-travelling wave has to be considered at leading order. We take up their analysis and apply it to the present problem to justify this approach in our setting.

Figs. 2.19 and 2.20 give evidence for this procedure in our setting of wave propagation along a rough beam, too. Fig. 2.19 shows the left- and right-travelling components of the effective wave fields, $|\langle u_-\rangle|$ and $|\langle u_+\rangle|$, respectively, with $\langle u_-\rangle + \langle u_+\rangle = \langle u\rangle$ (as we will see shortly, the method only captures the effective wave field), for the roughness amplitudes

$\epsilon = 5.0 \times 10^{-2}$ (left-hand panel) and 1.0×10^{-1} (right-hand panel), for non-dimensional correlation lengths $\bar{k}l_\mathrm{G} = 0.9$, 2.5 and 4.1. The results are obtained by the random-sampling method and the length of the roughness interval here is $L = 800$. The amplitudes of the incident (right-travelling) waves are chosen to be unity at $x = 0$.

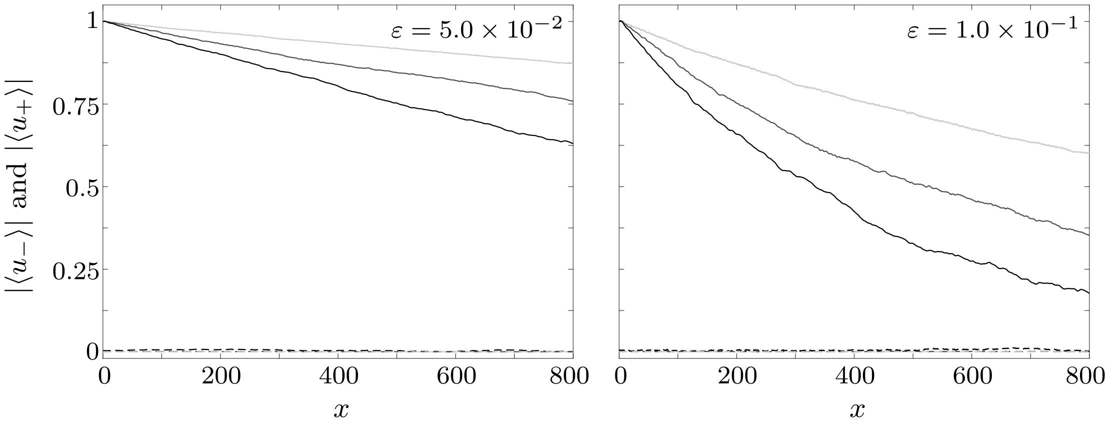

Figure 2.19: Effective wave field, split into rightward- and leftward-travelling components (solid and dashed line, respectively), for non-dimensional correlation lengths $\bar{k}l_\mathrm{G} = 0.9$ (light grey), $\bar{k}l_\mathrm{G} = 2.5$ (dark grey) and $\bar{k}l_\mathrm{G} = 4.1$ (black), for roughness amplitudes $\epsilon = 5.0 \times 10^{-2}$ (left-hand panel) and $\epsilon = 1.0 \times 10^{-1}$ (right-hand panel)

We can observe in Fig. 2.19 that for $\epsilon = 5.0 \times 10^{-2}$ and all three correlation lengths considered, the left-travelling effective wave component is close to zero over the whole rough interval. For the larger roughness amplitude, $\epsilon = 1.0 \times 10^{-1}$, the attenuation of the right-travelling wave is significantly larger, but the left-travelling wave component remains smaller than the right-travelling wave component by more than an order of magnitude over the whole rough interval and is hence insignificant. To validate the assumption of neglecting the left-travelling effective wave component in the multiple-scale method, Fig. 2.20 shows the ratio of the (spatial averaged) leftward- to rightward travelling effective wave components as functions of non-dimensional correlation length, for roughness amplitudes $\epsilon = 10^{-4}$, 10^{-3}, 10^{-2}, 10^{-1} and 2×10^{-1}. The ratio is calculated via

$$U_{-/+} = \frac{U_-}{U_+} \qquad \text{with} \qquad U_\pm = \frac{1}{L}\int_0^L |\langle u_\pm\rangle| \, \mathrm{d}x, \tag{2.85}$$

where $u_\pm$ denotes the right- and left-going wave components, respectively. The interval length, L, in the random-sampling method is set to be 400 times the corresponding correlation length, i.e. $\bar{k}L = 400 \times \bar{k}l_\mathrm{G}$, in the following (if not specified otherwise), which provides a sufficiently large roughness interval to allow comparisons with the multiple-scale method (which is based on the assumption of an infinite roughness interval in our formulation).

We can see in Fig. 2.20 that $\epsilon = 10^{-4}$ and 10^{-3} give very similar scaled ratios and the maximum value of $U_{-/+}$ is approximately 0.2ϵ in the small (non-dimensional) correlation length regime around $\bar{k}l_\mathrm{G} \approx 1$. For very small and larger correlation lengths the scaled ratio

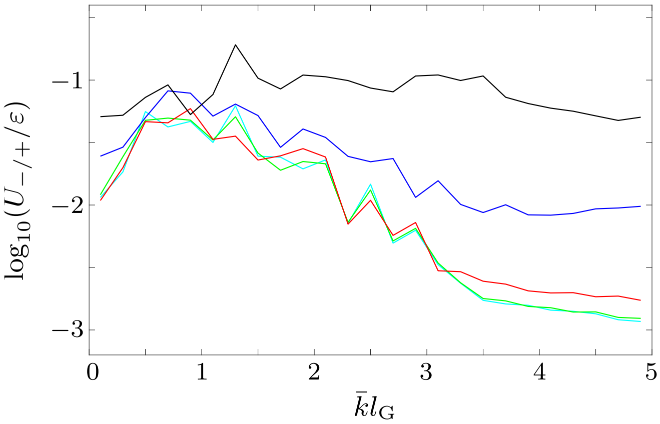

Figure 2.20: Ratio of leftward- to rightward travelling components of effective wave field as functions of non-dimensional correlation length, for roughness amplitudes $\epsilon = 10^{-4}$ (cyan), $\epsilon = 10^{-3}$ (green), $\epsilon = 10^{-2}$ (red), $\epsilon = 10^{-1}$ (blue) and $\epsilon = 2 \times 10^{-1}$ (black)

decreases. Although the scaled ratio curve for $\epsilon = 10^{-2}$ tends towards a larger value in the larger correlation length regime, it still provides evidence that $U_{-/+}$ scales with ϵ for small roughness amplitudes. The scaling of $U_{-/+}$ with ϵ does not hold for $\epsilon = 10^{-1}$ and 2×10^{-1} anymore, which produce much larger values for the ratio of left- to right-travelling effective wave components throughout the whole correlation length regime. For $\epsilon = 2 \times 10^{-1}$, the left-travelling effective wave component clearly cannot be neglected anymore. This might indicate that the limit of validity of the multiple-scale method (with the assumption of a right-travelling wave at leading order only) is already reached.

Under the assumption of $\epsilon \ll 1$, Fig. 2.20 supports the approach to consider only a modulated right-travelling wave at leading order along the (infinite) rough interval, which is chosen to be consistent with the right incident wave for the finite rough interval problem, and the wave field can be expressed as

$$u_0(x,x_2) = A(x_2)\,\mathrm{e}^{\mathrm{i}\bar{k}x}, \tag{2.86}$$

where the (complex-valued) amplitude A is now the principal unknown of the problem, and is sought from the higher-order terms.

As the mean wavenumber is fixed with respect to the ensemble, the leading-order effective wave field is

$$\langle u_0(x,x_2)\rangle = \langle A(x_2)\rangle\,\mathrm{e}^{\mathrm{i}\bar{k}x}, \tag{2.87}$$

with modulus $|\langle u_0(x,x_2)\rangle| = |\langle A(x_2)\rangle|$. It follows that

$$\langle A(x_2)\rangle = A_0\,\mathrm{e}^{\mathrm{i}\Delta k x}\,\mathrm{e}^{-Qx}, \tag{2.88}$$

where A_0 is a constant, and Δk and Q are unknown.

Order ϵ^1

Collecting the terms at order ϵ gives

$$(\partial_x^4 - \bar{k}^4)u_1(x,x_2) = \bar{k}^4\gamma(x)u_0(x,x_2), \quad x \in (-\infty,\infty), \tag{2.89}$$

which is a governing equation for the first-order wave field, u_1, forced by the product of the leading-order wave field, u_0, and the random fluctuation, γ. The solution for a given γ is expressed as

$$u_1(x,x_2) = \bar{k}^4 \int_{-\infty}^{\infty} G(|x-\check{x}|)\gamma(\check{x})u_0(\check{x},x_2)\,\mathrm{d}\check{x}, \tag{2.90}$$

where G is the standard Green's function for the homogeneous beam equation with an impulse at the source point, Eqn. (2.A.23), and k replaced by $\bar{k}$.

Order ϵ^2

The order ϵ^2 terms give the governing equation for u_2 to be

$$(\partial_x^4 - \bar{k}^4)u_2 = -4\partial_x^3\partial_{x_2}u_0 + \bar{k}^4\gamma(x)u_1, \quad x \in (-\infty,\infty). \tag{2.91}$$

For the solution, we have to take the ensemble average of Eqn. (2.91), which yields

$$(\partial_x^4 - \bar{k}^4)\langle u_2\rangle = -4\langle\partial_x^3\partial_{x_2}u_0\rangle + \bar{k}^4\langle\gamma(x)u_1\rangle. \tag{2.92}$$

At this point, it becomes clear that due to averaging, we will obtain $\langle A\rangle$, hence the multiple-scale method approximates the effective wave field. To solve for $\langle u_2\rangle$, we employ the ansatz $\langle u_2\rangle = \mathrm{e}^{\mathrm{i}kx}F(x_2)$, for some function F, so that the left-hand side of Eqn. (2.92) vanishes. While the first term on the right-hand side of Eqn. (2.92) simplifies to

$$-4\langle\partial_x^3\partial_{x_2}u_0\rangle = 4\mathrm{i}\bar{k}^3\partial_{x_2}\langle A\rangle\mathrm{e}^{\mathrm{i}kx}, \tag{2.93}$$

the third term on the right-hand side of Eqn. (2.92) can be written of the form

$$\begin{aligned}\bar{k}^4\langle\gamma(x)u_1\rangle &= \bar{k}^8\Big\langle\gamma(x)\int_{-\infty}^{\infty} G(|x-\check{x}|)\gamma(\check{x})u_0(\check{x},x_2)\,\mathrm{d}\check{x}\Big\rangle \\ &= \bar{k}^8\int_{-\infty}^{\infty} G(|x-\check{x}|)\big\langle\gamma(x)\gamma(\check{x})u_0(\check{x},x_2)\big\rangle\,\mathrm{d}\check{x}.\end{aligned} \tag{2.94}$$

Now, we can confirm our approach that only the effective component appears in the leading-order solution u_0. To show that the random components do not contribute to the term $\langle\gamma(x)\gamma(\check{x})u_0(\check{x},x_2)\rangle$ in Eqn. (2.94), we approximate the leading order solution u_0 with the wave field u obtained by the random-sampling method. Fig. 2.21 shows the results for

$$\rho_u(|\xi|) = \langle\gamma(x)\gamma(\check{x})u(\check{x})\rangle = \langle\gamma(\check{x}+\xi)\gamma(\check{x})u(\check{x})\rangle \tag{2.95}$$

as well as for the terms corresponding to the random component of the wave travelling rightward and the (random) wave travelling leftward,

$$\rho_{u_+}(|\xi|) = \langle \gamma(\check{x}+\xi)\gamma(\check{x})(u_+(\check{x}) - \langle u(\check{x})\rangle)\rangle, \tag{2.96a}$$

$$\rho_{u_-}(|\xi|) = \langle \gamma(\check{x}+\xi)\gamma(\check{x})u_-(\check{x})\rangle, \tag{2.96b}$$

as functions of $|\xi|$, where $\xi = x - \check{x}$, for non-dimensional correlation length $\bar{k}l_\mathrm{G} = 2.5$ and roughness amplitudes $\epsilon = 1.0 \times 10^{-2}$ (left-hand panel) and 1.0×10^{-1} (right-hand panel).

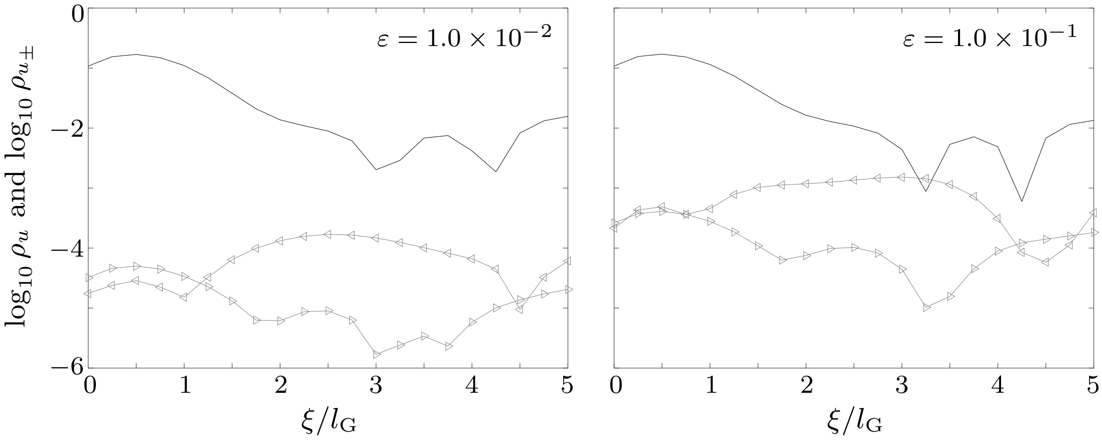

Figure 2.21: Correlation between wave field and mass variation for non-dimensional correlation length $\bar{k}l_\mathrm{G} = 2.5$, for roughness amplitudes $\epsilon = 1.0 \times 10^{-2}$ (left-hand panel) and $\epsilon = 1.0 \times 10^{-1}$ (right-hand panel) (ρ_u,–; ρ_{u_+}, ▷; ρ_{u_-}, ◁)

We can clearly observe in Fig. 2.21 that for the intermediate non-dimensional correlation length $\bar{k}l_\mathrm{G} = 2.5$, neither the random component $u_+(\check{x}) - \langle u(\check{x})\rangle$ nor $u_-(\check{x})$ are correlated to the roughness profile of the beam at leading order. To show that the random components of the wave field are uncorrelated to the roughness profile for the whole range of non-dimensional correlation lengths we will consider in Sec. 2.6.3, $\bar{k}l_\mathrm{G} = 0.1, \dots, 4.9$, we use the approximations of the mean magnitude of the terms $\rho_{u_\pm}$ over the roughness interval,

$$J_\pm = \frac{1}{L}\int_0^L |\rho_{u_\pm}|\,\mathrm{d}\xi, \tag{2.97}$$

as functions of non-dimensional correlation length, which is shown in Fig. 2.22 for roughness amplitudes $\epsilon = 1.0 \times 10^{-2}$ (left-hand panel) and $\epsilon = 1.0 \times 10^{-1}$ (right-hand panel). For comparison, Fig. 2.22 also shows the mean magnitude of the term ρ_u over only one correlation length as well as the whole domain $(0,L)$,

$$J_{l_\mathrm{G}} = \frac{1}{l_\mathrm{G}}\int_0^{l_\mathrm{G}} |\rho_u|\,\mathrm{d}\xi \quad \text{and} \quad J_L = \frac{1}{L}\int_0^L |\rho_u|\,\mathrm{d}\xi. \tag{2.98}$$

We can deduce from Fig. 2.22 that the random components of the beam deflection are uncorrelated to the roughness profile and consequently random components in the leading-

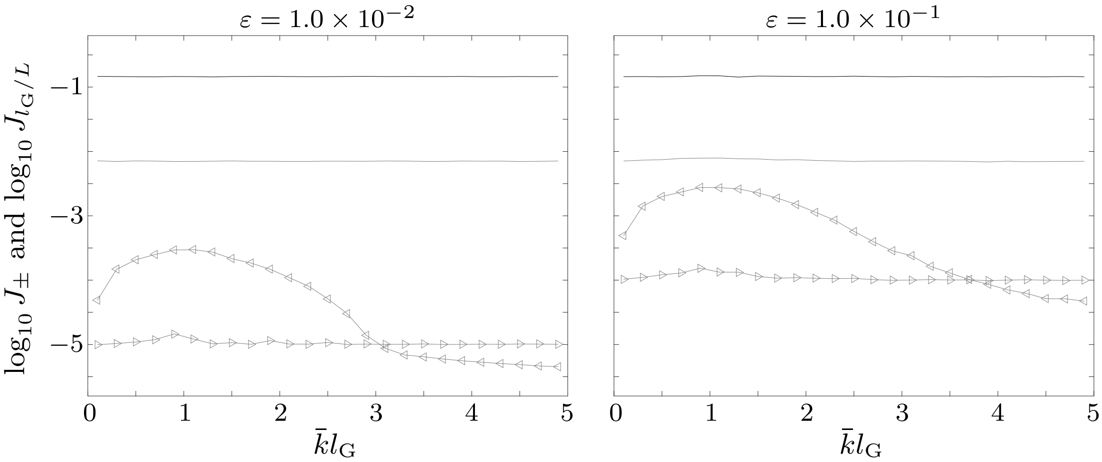

Figure 2.22: Mean correlations of roughness profile with wave field, J_{l_G} (black solid) and J_L (grey solid), and random components of wave field, J_+ (▷) and J_- (◁), as functions of non-dimensional correlation length, for roughness amplitudes $\epsilon = 1.0 \times 10^{-2}$ (left-hand panel) and $\epsilon = 1.0 \times 10^{-1}$ (right-hand panel)

order term u_0 are uncorrelated to the roughness profile, too. Since the correlation of the wave field $u(\check{x})$ with the roughness profile is negligible therefore, we can write

$$\langle \gamma(x)\gamma(\check{x})u_0(\check{x})\rangle = \langle \gamma(\check{x}+\xi)\gamma(\check{x})\rangle\langle u_0(\check{x})\rangle. \tag{2.99}$$

This result together with the representation of the autocorrelated random process, $\langle \gamma(\check{x}+\xi)\gamma(\check{x})\rangle = \rho(|\xi|)$, Eqn. (2.94) may be rewritten in the simplified form

$$\bar{k}^4\langle \gamma(x)u_1\rangle = 4\bar{k}^3\langle A(x_2)\mathrm{e}^{\mathrm{i}\bar{k}x}\rangle \underbrace{\frac{\bar{k}^5}{4}\int_{-\infty}^{\infty} G(|\xi|)\mathrm{e}^{\mathrm{i}\bar{k}\xi}\rho(|\xi|)\,\mathrm{d}\xi}_{=:\,\zeta_{\mathrm{vm}}}. \tag{2.100}$$

With these calculations, the governing equation for order ϵ^2, Eqn. (2.91), becomes the following ordinary differential equation,

$$\partial_{x_2}\langle A(x_2)\rangle - \mathrm{i}\langle A(x_2)\rangle\,\zeta_{\mathrm{vm}} = 0, \tag{2.101}$$

for the effective amplitude $\langle A(x_2)\rangle$. The integral appearing in the complex constant ζ_{vm} is calculated numerically using an adaptive quadrature scheme for the results shown in Sec. 2.6.3. Note that due to the autocorrelation condition on the random process no averaging is required in the (as a result of this efficient) numerical calculation of the integral. The solution of the governing ordinary differential Eqn. (2.101) is

$$\langle A(x_2)\rangle = A_0\,\mathrm{e}^{\mathrm{i}\zeta_{\mathrm{vm}}x_2}, \tag{2.102}$$

giving the effective phase change, $(\Delta k)_{\mathrm{eff}}$, and attenuation coefficient, Q_{eff}, due to the rough mass as, respectively,

$$(\mathit{\Delta} k)_{\text{eff}} = \epsilon^2 \text{Re}(\zeta_{\text{vm}}), \tag{2.103a}$$

$$\text{and} \quad Q_{\text{eff}} = \epsilon^2 \text{Im}(\zeta_{\text{vm}}). \tag{2.103b}$$

In particular, this implies that the complex constant ζ_{vm} is the (complex-valued) wavenumber on the observation scale. Moreover, the effective attenuation coefficient and the effective phase change predicted by the multiple-scale approximation are proportional to ϵ^2.

2.6.3 Numerical results

After the motivation and introduction of the multiple-scale method for the beam in vacuo with varying mass, we compare the attenuation coefficients and phase changes predicted by the multiple-scale method with those obtained by the numerical random-sampling method to validate the multiple-scale method for the underlying problem. Firstly, we compare the attenuation for different roughness amplitudes throughout the (non-dimensional) correlation length regime $\bar{k}l_{\text{G}} \in (0.1,4.9)$. Fig. 2.23 shows the scaled attenuation coefficients, predicted by the multiple-scale method and obtained by the random-sampling method, as functions of non-dimensional correlation length, for roughness amplitudes $\epsilon = 1.0 \times 10^{-3}$ (top-left panel), 1.0×10^{-2} (top-right panel), 5.0×10^{-2} (bottom-left panel) and 1.0×10^{-1} (bottom-right panel). The attenuation coefficient are non-dimensionalised with respect to the mean wavenumber, i.e. $Q/\bar{k}$, and scaled by the roughness amplitude squared, ϵ^2, which is used to relate the local and observation scale to each other. For these and the following results obtained with the random-sampling method, the rough interval length $\bar{k}L = 400 \times \bar{k}l_{\text{G}}$ is used, if not specified otherwise.

We can observe in Fig. 2.23 that the agreement between the attenuation coefficients predicted by the multiple-scale method and obtained by the random-sampling is nearly perfect for roughness amplitudes $\epsilon \leq 5.0 \times 10^{-2}$. In this roughness amplitude regime, only small deviations for the smallest correlation length shown are observable, which is caused by numerical difficulties in capturing the very small attenuation coefficients from the effective wave fields in the random-sampling method accurately. The effective attenuation coefficients (describing the attenuation of the effective beam deflection) are close to zero for the smallest non-dimensional correlation length, $\bar{k}l_{\text{G}} = 0.1$, and increase with increasing correlation length. For $\bar{k}l_{\text{G}} \geq 2$, the attenuation coefficients are linear with respect to $\bar{k}l_{\text{G}}$, for $\epsilon \leq 5.0 \times 10^{-2}$. The good agreement between the two methods shows in particular that the attenuation coefficients obtained by the random-sampling method are also proportional to the square of the roughness amplitude, ϵ^2, as predicted by multiple-scale approach. Hence, the scaled attenuation coefficients are independent of the roughness amplitude. The proportionality of the effective attenuation coefficients with the roughness amplitude is lost in the large correlation length regime $\bar{k}l_{\text{G}} \geq 3$ for the largest roughness amplitude under consideration, $\epsilon = 1.0 \times 10^{-1}$, where we can observe slight down deviations of the effective attenuation coefficients from the values predicted by the multiple-scale method. These deviations for the largest roughness amplitude show that the limit of validity of the

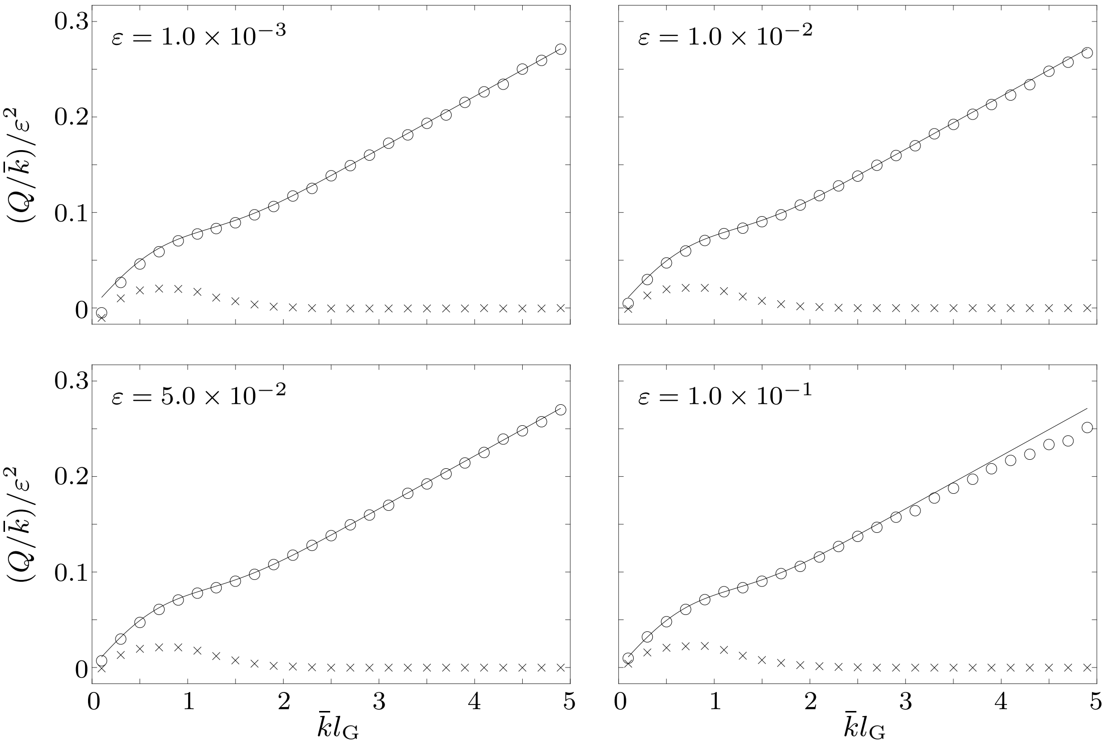

Figure 2.23: Scaled attenuation coefficients of effective wave field for varying mass problem as functions of non-dimensional correlation length, predicted by multiple-scale method (solid line) and random-sampling method (○), for roughness amplitudes $\epsilon = 1.0 \times 10^{-3}$ (top-left panel), $\epsilon = 1.0 \times 10^{-2}$ (top-right panel), $\epsilon = 5.0 \times 10^{-2}$ (bottom-left panel) and $\epsilon = 1.0 \times 10^{-1}$ (bottom-right panel). Corresponding individual attenuation coefficients obtained by random-sampling method (×) are shown for comparison.

multiple-scale approach is reached.

Although this section focuses on the effective wave field and the validation of the multiple-scale method, it is informative to compare the effective with the individual wave fields that form the ensemble – the random-sampling method allows us to do this. Fig. 2.23 also shows the attenuation of the individual wave fields as functions of the correlation length. We can see that the individual attenuation coefficients (describing the attenuation of individual wave fields) are only non-zero for $\bar{k}l_{\mathrm{G}} \in (0.3,2)$. For the smallest correlation length, $\bar{k}l_{\mathrm{G}} = 0.1$, the individual attenuation coefficient is similarly to the effective attenuation coefficient close to zero. From there, the individual attenuation coefficients increase to reach its maximum between $\bar{k}l_{\mathrm{G}} \approx 0.7$ and 0.9. For larger correlation lengths, the individual attenuation coefficients decrease to vanish for correlation lengths $\bar{k}l_{\mathrm{G}} \geq 2$. A hump of similar magnitude in the same correlation length regime is also observable for the effective attenuation coefficients, which show upper deviation from the linear scaling with the correlation length in the same small correlation length regime. The results for the individual attenuation coefficients confirm our finding from Fig. 2.18 that the mass variations are too mild to attenuate the individual wave fields for large correlations lengths, i.e. $\bar{k}l_{\mathrm{G}} \geq 2$ here. We can also deduce that that the mass fluctuations are too rapid for the smallest correlation length, $\bar{k}l_{\mathrm{G}} = 0.1$, to be seen by the waves travelling along the beam in vacuo.

Fig. 2.23 suggested that the (effective) attenuation coefficients scale with the square of the roughness amplitude. This is investigated now. Fig. 2.24 shows the scaled (individual and effective) attenuation coefficients, predicted by the multiple-scale method and obtained by the random-sampling method, as functions of roughness amplitude, for the non-dimensional correlation lengths $\bar{k}l_{\mathrm{G}} = 0.9$ (top-left panel), 1.5 (top-right panel), 2.5 (bottom-left panel) and 4.1 (bottom-right panel).

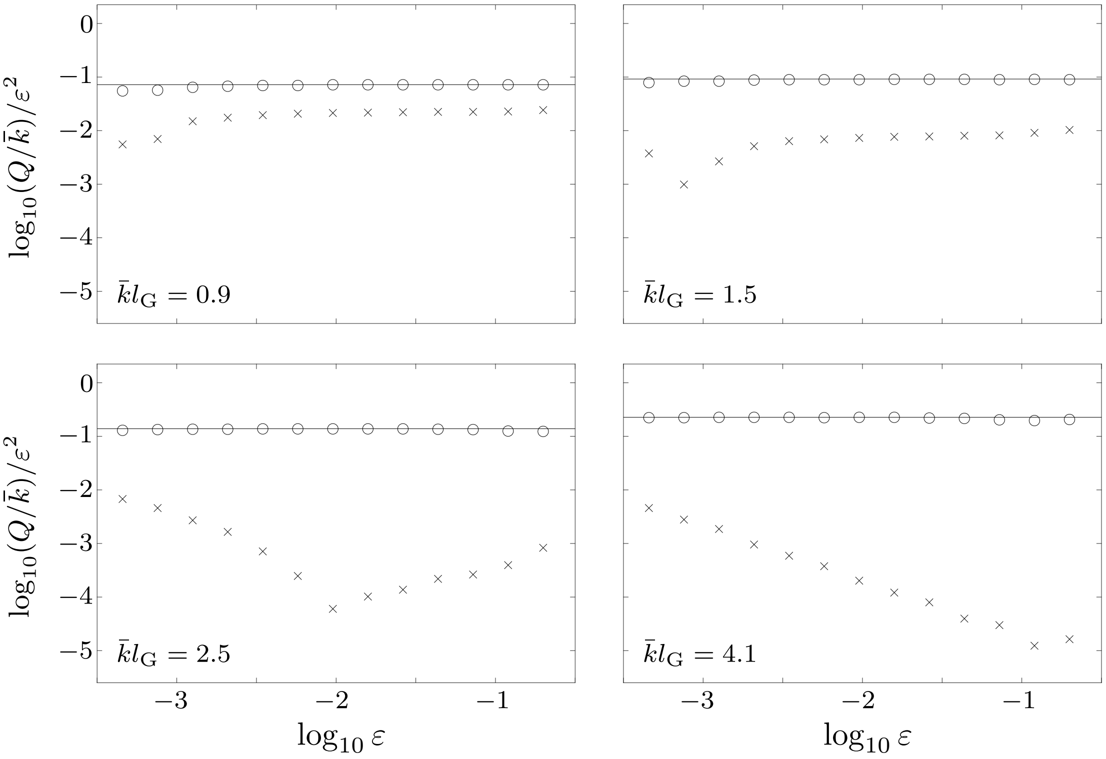

Figure 2.24: Scaled attenuation coefficients for varying mass problem as functions of roughness amplitude, for non-dimensional correlation lengths $\bar{k}l_{\mathrm{G}} = 0.9$ (top-left panel), $\bar{k}l_{\mathrm{G}} = 1.5$ (top-right panel), $\bar{k}l_{\mathrm{G}} = 2.5$ (bottom-left panel) and $\bar{k}l_{\mathrm{G}} = 4.1$ (bottom-right panel), predicted by multiple-scale method (solid line) and for individual (×) and effective (∘) wave fields by random-sampling method

We can see in Fig. 2.24 that, in general, the multiple-scale method and the random-sampling method predict the same effective attenuation coefficients, confirming that the effective attenuation coefficients scale with ϵ^2. Some disagreement is evident for very small values of ϵ and the smaller values of the correlation length, $\bar{k}l_{\mathrm{G}} = 0.9$ and 1.5, which, as above, is attributed to numerical difficulties in capturing very small attenuation coefficients. For $\epsilon \geq 0.1$ and the two larger correlation lengths considered, $\bar{k}l_{\mathrm{G}} = 2.5$ and 4.1, the effective attenuation coefficients obtained by the random-sampling method deviate from those predicted by the multi-scale approximation, becoming slightly smaller than them. This was already observable in Fig. 2.23 for $\epsilon = 1.0 \times 10^{-1}$ for large correlation lengths. This is a genuine feature and indicates the limit of validity of the multi-scale approximation with respect to ϵ.

Fig. 2.24 also shows the individual attenuation coefficients as functions of roughness amplitude. We can observe that the individual attenuation coefficients are not proportional to the roughness amplitude square for all correlation lengths considered. For $\bar{k}l_{\mathrm{G}} = 0.9$ and 1.5, the individual attenuation coefficients are only proportional to ϵ^2 for roughness amplitudes $\epsilon \geq 10^{-3}$ and $\epsilon \geq 10^{-2.5}$, respectively. For $\bar{k}l_{\mathrm{G}} = 2.5$ and 4.1, this does not hold and the scaled individual attenuation coefficients decrease and move further away from the effective attenuation coefficients for $\epsilon \leq 10^{-2}$ and $\epsilon \leq 10^{-1}$, respectively, before they start to increase again. Altogether, the individual attenuation coefficients are much smaller than the effective attenuation coefficients, the discrepancy increases with increasing correlation length and they are not representative for each other.

In addition to the attenuation coefficients, the (real) phase change of the effective wave field, $(\Delta k)_{\mathrm{eff}}$, due to the roughness can be extracted from the ensemble of wave elevations via

$$\langle u \rangle \propto \mathrm{e}^{-Q_{\mathrm{eff}} x}\, \mathrm{e}^{\mathrm{i}(\bar{k}+(\Delta k)_{\mathrm{eff}})x}, \qquad x \in (0,L). \tag{2.104}$$

As we will see shortly (see Fig. 2.26), the phase change of individual wave fields is random, hence we disregard quantitative results for them. Fig. 2.25 shows the phase changes as functions of non-dimensional correlation length, for roughness amplitude $\epsilon = 5.0 \times 10^{-2}$ (left-hand panel) and 1.0×10^{-1} (right-hand panel). Results are given for the multiple-scale method and the random-sampling method using the very long interval length $\bar{k}L = 4\bar{k}/\epsilon^2$ to capture the phase changes accurately.

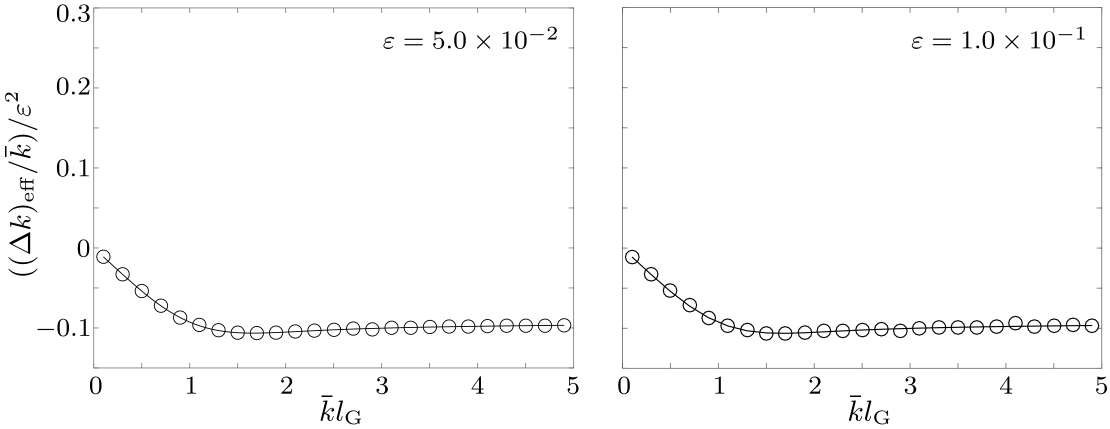

Figure 2.25: Scaled phase changes of the effective wave field for varying mass problem as functions of non-dimensional correlation length, for roughness amplitudes $\epsilon = 5.0 \times 10^{-2}$ (left-hand panel) and $\epsilon = 1.0 \times 10^{-1}$ (right-hand panel), predicted by multiple-scale method (solid line) and random-sampling method (○)

For the chosen parameter values, the two methods produce almost identical predictions of the phase change for both roughness amplitudes, $\epsilon = 5.0 \times 10^{-2}$ and 1.0×10^{-1}. The phase change tends to zero as the correlation length tends to zero (the white noise or homogenisation limit). Thus, when the waves are far longer than fluctuations in mass, they only perceive the mean mass. For finite values of the correlation length, the phase change is negative, meaning that the wavelength of the effective wave field is longer than the wavelength corresponding to the uniform beam. The phase change decreases approximately linearly with increasing correlation length over the interval $\bar{k}l_{\mathrm{G}} \leq 1$, and is approximately constant for $\bar{k}l_{\mathrm{G}} \geq 1.5$ in our correlation length regime. We can also confirm that the proportionality of the phase changes with ϵ^2 holds for the chosen values (which is clear for the multiple-scale method by its derivation).

As a last point in our investigation of the varying mass problem for the beam in vacuo, we will look at phase changes over the whole roughness interval. Fig. 2.26 shows the phase changes for example individual wave fields and corresponding effective wave fields, for roughness amplitude $\epsilon = 5 \times 10^{-2}$ and non-dimensional correlation lengths $\bar{k}l_{\mathrm{G}} = 0.9$ (left-hand panel) and 4.1 (right-hand panel).

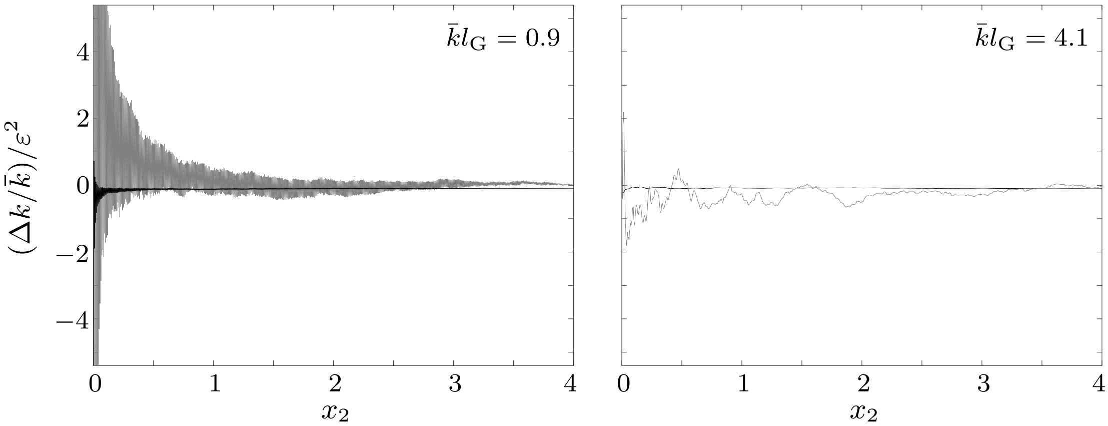

Figure 2.26: Phase changes of example individual wave fields (grey curves) and effective wave fields (black) for varying mass problem, for non-dimensional correlation lengths $\bar{k}l_{\mathrm{G}} = 0.9$ (left-hand panel) and $\bar{k}l_{\mathrm{G}} = 4.1$ (right-hand panel), for roughness amplitude $\epsilon = 5.0 \times 10^{-2}$

We can see in Fig. 2.26 that the phase changes for the effective wave fields tend (after slight noise for small x) to the values predicted by the multiple-scale approximation shown in Fig. 2.25 for the two correlation lengths considered, $\bar{k}l_{\mathrm{G}} = 0.9$ and 4.1. The phase changes of the example individual wave fields show unpredictable behaviour for both correlation length choices, yielding larger values than the phase changes of the effective wave fields. For the smaller correlation length, $\bar{k}l_{\mathrm{G}} = 0.9$, a great variability of the phase change is observable, in particular at the left-end of the rough interval. For the larger correlation length, $\bar{k}l_{\mathrm{G}} = 4.1$, the phase change fluctuates much slower around the phase change of the effective wave field and appears to be essentially random as well.

2.7 Rough beam with varying rigidity

After the investigations of the influence of beam mass variations on the wave attenuation in the previous section, we focus on continuous rigidity variations (which arise due to varying Young's modulus) now and compare their effects with those in the varying mass problem. In the varying rigidity problem, the beam mass g is set to be constant such that the underlying beam Eqn. (2.9) becomes

$$\partial_x^2\big(b(x)\,\partial_x^2 u(x)\big) - \alpha\, g\, u(x) = 0, \qquad x \in (-\infty,\infty). \tag{2.105}$$

In analogy to the varying mass setting, the varying rigidity $b(x)$ shall fluctuate about the mean $\bar{b}$ with roughness amplitude ϵ, i.e.

$$b(x) = \bar{b}(1 + \epsilon\beta(x)), \tag{2.106}$$

where $\beta = \mathcal{O}(1)$ is modelled via the previously introduced Gaussian autocorrelated random process and has the same properties as γ , in particular the correlation length is denoted with l_{G} here, too. ($\epsilon \ll 1$ is assumed for consistency with the multiple-scale method, which is derived for this problem in Sec. 2.7.1, again). Hence, the autocorrelation of β can also be expressed via the Gaussian autocorrelation condition

$$\langle \beta(x)\,\beta(x-\xi)\rangle = \mathbf{E}[\beta(x)\,\beta(x-\xi)] = \mathrm{e}^{-\xi^2/l_{\mathrm{G}}^2}. \tag{2.107}$$

Before we focus on the multiple-scale method for the varying rigidity problem, we compare effective with example individual wave fields for the same average roughness properties as in Fig. 2.18, but for the present problem. Fig. 2.27 shows the moduli of example individual wave fields and corresponding effective wave fields, for roughness amplitude $\epsilon = 5.0 \times 10^{-2}$ and non-dimensional correlation lengths $\bar{k}l_{\mathrm{G}} = 0.9$ (left-hand panel) and 4.1 (right-hand panel), for the varying rigidity problem. The motion is forced by a unit-amplitude incident wave propagating in the positive x-direction again. The random-sampling method is used to calculate the wave fields as well as the numerical results throughout the rest of this chapter. Note that the findings from the convergence study also hold for the varying rigidity problem (results not shown).

We can see in Fig. 2.27 the same quantitative and qualitative behaviour as for the varying mass problem in Fig. 2.18, i.e. only slight attenuation for the small correlation length, $\bar{k}l_{\mathrm{G}} = 0.9$ and a similar discrepancy between attenuation of effective and individual wave fields for the larger correlation length, $\bar{k}l_{\mathrm{G}} = 4.1$, hence the effective and individual wave fields are not representative for each other either.

2.7.1 Multiple-scale method

The multiple-scale method for the varying rigidity problem, which will be presented in the following, is based on the derivation of the multiple-scale method for the varying mass problem, and additional terms are expected due to the presence of derivatives of the beam rigidity. The same local and observation scale are considered as for the varying mass

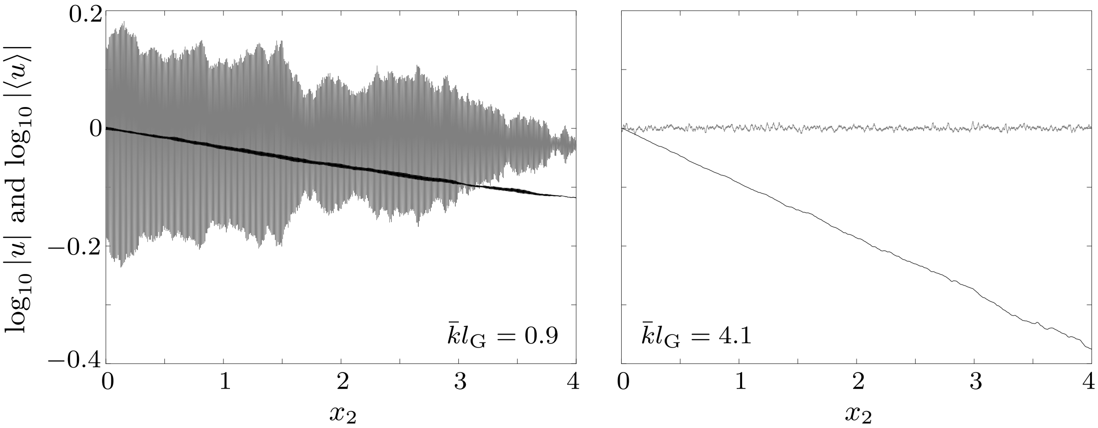

Figure 2.27: Example individual wave fields (grey curves) and effective wave fields (black) for varying rigidity problem, for roughness amplitude $\epsilon = 5.0 \times 10^{-2}$ and non-dimensional correlation lengths $\bar{k}l_{\mathrm{G}} = 0.9$ (left-hand panels) and $\bar{k}l_{\mathrm{G}} = 4.1$ (right-hand panels)

problem (which are connected via ϵ^2 and their coordinates are denoted with x and x_2, respectively) and $\epsilon \ll 1$ has to assumed. We use the same multiple-scale expansion for the wave field, u, as given in Eqn. (2.82) and derive on this basis the governing equations of zeroth, first and second order for the varying rigidity problem.

Order ϵ^0

The governing equation for the leading-order wave field given by the order ϵ^0 terms, u_0, for the varying rigidity problem is identical to Eqn. (2.84),

$$(\partial_x^4 - \bar{k}^4)u_0(x,x_2) = 0, \qquad x \in (-\infty,\infty),$$

where the wavenumber $\bar{k}$ now corresponds to the mean beam rigidity, i.e. $\bar{k} = (\alpha g/\bar{b})^{\frac{1}{4}}$. It can be shown similarly to the varying mass problem that the leading-order solution only consists of a modulated rightward-travelling wave and the intrinsic left-travelling wave can be neglected, i.e. the solution is again expressed in the form (2.86),

$$u_0(x,x_2) = A(x_2)\,\mathrm{e}^{\mathrm{i}\bar{k}x}, \tag{2.108}$$

and the leading-order wave amplitude A, or to be more precise its components (phase change, attenuation coefficient), is now sought from the higher-order terms.

Order ϵ^1

The order ϵ terms give the governing equation for u_1 to be

$$(\partial_x^4 - \bar{k}^4)u_1(x,x_2) = -\partial_x^2\big(\beta(x)\,\partial_x^2 u_0(x,x_2)\big). \tag{2.109}$$

As in the varying mass problem, the Green's function from Eqn. (2.A.23), again with k replaced by $\bar{k}$, is used to obtain the solution, with the first-order wave field in this case expressed as

$$u_1(x,x_2) = -\int_{-\infty}^{\infty} G(|x-\check{x}|)\partial_{\check{x}}^2\big(\beta(\check{x})\,\partial_{\check{x}}^2 u_0(\check{x},x_2)\big)\,\mathrm{d}\check{x}. \tag{2.110}$$

Order ϵ^2

From the order ϵ^2 terms, the governing equation for the second-order wave field is

$$(\partial_x^4 - \bar{k}^4)u_2 = -\partial_x^2\left(\beta(x)\,\partial_x^2 u_1(x,x_2)\right) - 4\partial_x^3\partial_{x_2}u_0(x,x_2), \quad x \in (-\infty,\infty), \tag{2.111}$$

with ensemble average

$$\begin{aligned}(\partial_x^4 - \bar{k}^4)\langle u_2\rangle &= -4\partial_x^3\partial_{x_2}\langle u_0(x,x_2)\rangle - \langle\partial_x^2\left(\beta(x)\,\partial_x^2 u_1(x,x_2)\right)\rangle\\ &= 4\mathrm{i}\bar{k}^3\partial_{x_2}\langle A(x_2)\rangle \mathrm{e}^{\mathrm{i}\bar{k}x} + 4\bar{k}^3\mathrm{e}^{\mathrm{i}\bar{k}x}\langle A(x_2)\rangle\zeta_{\mathrm{vr}},\end{aligned} \tag{2.112}$$

where ζ_{vr} is the complex constant

$$\zeta_{\mathrm{vr}} = -\frac{1}{4\bar{k}^3}\int_{-\infty}^{\infty}\partial_\xi^2\left[\partial_\xi^2 G(|\xi|)(\bar{k}^2\partial_\xi^2\rho(|\xi|) + 2\mathrm{i}\bar{k}^3\partial_\xi\rho(|\xi|) - \bar{k}^4\rho(|\xi|))\right]\mathrm{e}^{\mathrm{i}\bar{k}\xi}\,\mathrm{d}\xi. \tag{2.113}$$

Here, we used that the leading-order beam deflection is uncorrelated to the roughness profile, which can be shown analogously to the varying mass problem. Integrating Eqn. (2.113) by parts twice gives

$$\zeta_{\mathrm{vr}} = \frac{\bar{k}}{4}\int_{-\infty}^{\infty}\partial_\xi^4 G(|\xi|)\rho(|\xi|)\mathrm{e}^{\mathrm{i}\bar{k}\xi}\,\mathrm{d}\xi. \tag{2.114}$$

Using the field equation for the Green's function, Eqn. (2.A.5) with k replaced by $\bar{k}$, we can express ζ_{vr} as

$$\zeta_{\mathrm{vr}} = \frac{\bar{k}^5}{4}\int_{-\infty}^{\infty}G(|\xi|)\rho(|\xi|)\mathrm{e}^{\mathrm{i}\bar{k}\xi}\,\mathrm{d}\xi + \frac{\bar{k}}{4}\underbrace{\int_{-\infty}^{\infty}\delta(\xi)\rho(|\xi|)\mathrm{e}^{\mathrm{i}\bar{k}\xi}\,\mathrm{d}\xi}_{=1}. \tag{2.115}$$

The first term on the right-hand side of Eqn. (2.115) is the complex constant, which appeared in the varying mass problem (Eqn. (2.100)) and characterised the attenuation and the phase change in this problem. Hence, the complex constant in the varying rigidity problem, ζ_{vr}, can be written in term of the complex constant from the varying mass problem,

$$\zeta_{\mathrm{vr}} = \zeta_{\mathrm{vm}} + \frac{\bar{k}}{4}. \tag{2.116}$$

As in the varying mass problem, employing the ansatz $\langle u_2\rangle = \mathrm{e}^{\mathrm{i}\bar{k}x}F(x_2)$ leads us to the ordinary differential equation for the effective amplitude $\langle A(x_2)\rangle$,

$$\partial_{x_2}\langle A(x_2)\rangle - \mathrm{i}\langle A(x_2)\rangle\,\zeta_{\mathrm{vr}} = 0, \tag{2.117}$$

and the solution

$$\langle A(x_2)\rangle = A_0 \mathrm{e}^{\mathrm{i}\zeta_{\mathrm{vr}} x_2}. \tag{2.118}$$

Consequently, the phase change and attenuation coefficient produced by the varying rigidity are, respectively,

$$(\Delta k)_{\mathrm{eff}} = \epsilon^2 \mathrm{Re}(\zeta_{\mathrm{vr}}) = \epsilon^2 \Big(\mathrm{Re}(\zeta_{\mathrm{vm}}) + \frac{\bar{k}}{4}\Big), \tag{2.119a}$$

$$\text{and} \quad Q_{\mathrm{eff}} = \epsilon^2 \mathrm{Im}(\zeta_{\mathrm{vr}}) = \epsilon^2 \mathrm{Im}(\zeta_{\mathrm{vm}}). \tag{2.119b}$$

It is remarkable that the attenuation coefficients for the varying mass and varying rigidity problem are identical, whereas the phase changes for the two problems agree up to addition of the constant $\bar{k}/4$.

2.7.2 Numerical results

Now, we show the numerical results for the attenuation and the phase change for the varying rigidity problem. Again, we use the random-sampling method to validate the multiple-scale method for this problem and to confirm the connection between the varying mass and varying rigidity problem, which is given in Eqns. (2.119). Fig. 2.28 shows the scaled attenuation coefficients, predicted by the multiple-scale method and obtained by the random-sampling method, as functions of non-dimensional correlation length, for roughness amplitudes $\epsilon = 1.0 \times 10^{-3}$ (top-left panel), 1.0×10^{-2} (top-right panel), 5.0×10^{-2} (bottom-left panel) and 1.0×10^{-1} (bottom-right panel).

We can observe in Fig. 2.28 that the varying rigidity yields in our model problem qualitatively and quantitatively the same attenuation coefficients as the varying mass in Sec. 2.6. In particular, the effective attenuation coefficients predicted by the multiple-scale method and obtained by the random-sampling show excellent agreement for roughness amplitudes $\epsilon \leq 5.0 \times 10^{-2}$, and the multiple-scale method slightly overpredicts the attenuation coefficients in the large correlation length regime for the largest roughness amplitude considered, $\epsilon = 1.0 \times 10^{-1}$. Up to this roughness amplitude, the effective attenuation coefficients are proportional to ϵ^2, too, and scale linearly with the correlation length in the correlation length regime, for which no attenuation of the individual wave fields is visible.

We also examine the proportionality of the effective attenuation coefficients with the square of the roughness amplitude for the varying rigidity problem, here. Fig. 2.29 shows the scaled attenuation coefficients, predicted by the multiple-scale method and obtained by the random-sampling method, as functions of roughness amplitude, for the non-dimensional correlation lengths $\bar{k}l_{\mathrm{G}} = 0.9$ (top-left panel), 1.5 (top-right panel), 2.5 (bottom-left panel) and 4.1 (bottom-right panel).

We can observe in Fig. 2.29 that the multiple-scale method and the random-sampling method yield the same effective attenuation coefficients over the whole roughness amplitude regime for correlation lengths $\bar{k}l_{\mathrm{G}} = 0.9$, 1.5 and 2.5. Again, for the largest correlation

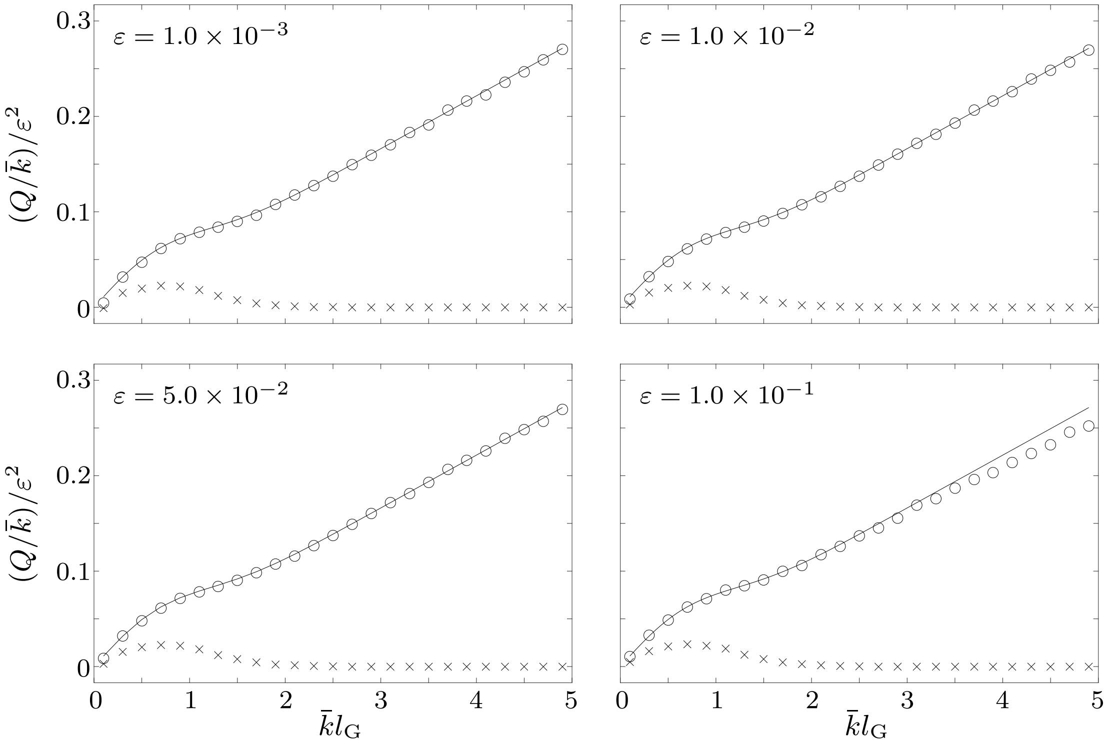

Figure 2.28: Scaled attenuation coefficients of effective wave field for varying rigidity problem as functions of non-dimensional correlation length, predicted by multiple-scale method (solid line) and random-sampling method (○), for roughness amplitudes $\epsilon = 1.0 \times 10^{-3}$ (top-left panel), $\epsilon = 1.0 \times 10^{-2}$ (top-right panel), $\epsilon = 5.0 \times 10^{-2}$ (bottom-left panel) and $\epsilon = 1.0 \times 10^{-1}$ (bottom-right panel). Corresponding individual attenuation coefficients obtained by random-sampling method (×) are shown for comparison.

length under consideration, $\bar{k}l_{\mathrm{G}} = 4.1$, the proportionality of the effective attenuation coefficient with ϵ^2 is lost for $\epsilon \geq 0.1$, for which they show slight lower deviation in comparison with the attenuation coefficients predicted by the multiple-scale method, which is in agreement with the results for the varying mass problem and Fig. 2.28. In particular, the limit of validity of the multi-scale method with respect to ϵ for the varying rigidity problem is the same as for the varying mass problem. The individual attenuation coefficients show a very similar behaviour to their equivalents for the varying mass problem, i.e. they are much smaller than the effective attenuation coefficients. They are only proportional to ϵ^2 for correlation lengths $\bar{k}l_{\mathrm{G}} = 0.9$ and 1.5 in the not-so-small roughness amplitude regime, and for the large correlation length choices, $\bar{k}l_{\mathrm{G}} = 2.5$ and 4.1, they deviate from this proportionality throughout most of the roughness amplitude regime.

With Eqn. (2.104), we obtain the phase change of the effective wave field, $(\Delta k)_{\mathrm{eff}}$, for the varying rigidity problem, too, which we will analyse in the following. Due to the random behaviour of the phase change of individual wave fields, we omit them in our analysis again.

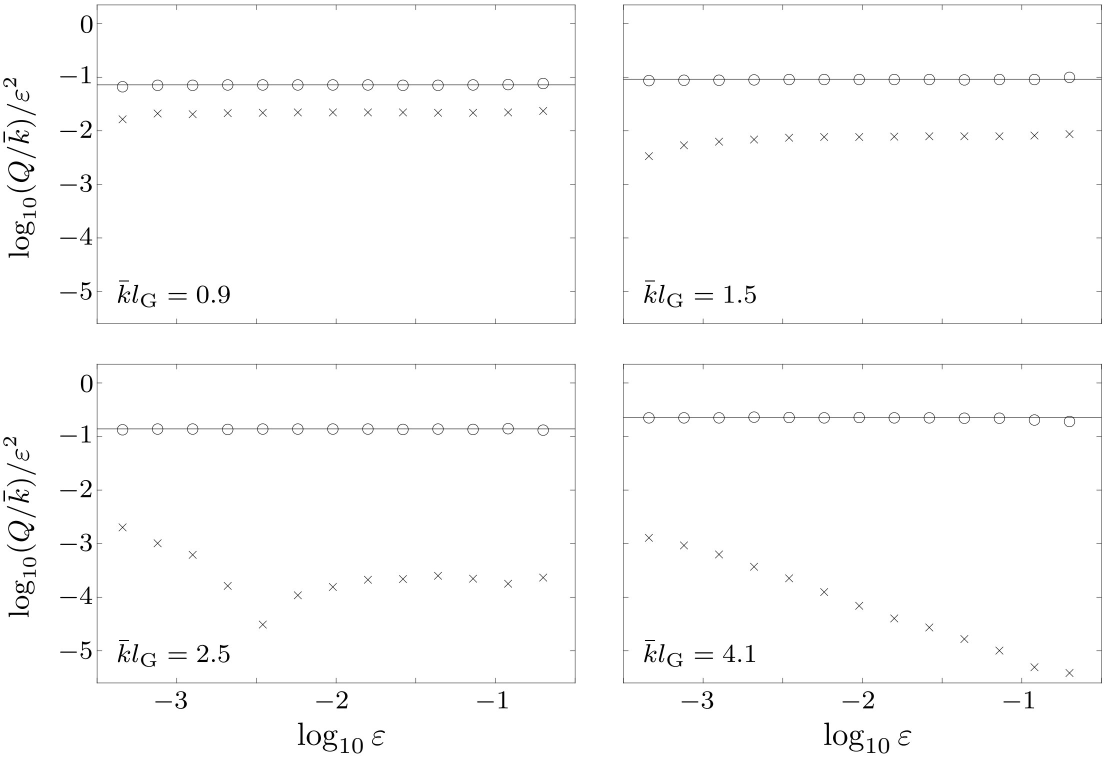

Figure 2.29: Scaled attenuation coefficients for varying rigidity problem as functions of roughness amplitude, for non-dimensional correlation lengths $\bar{k}l_{\mathrm{G}} = 0.9$ (top-left panel), $\bar{k}l_{\mathrm{G}} = 1.5$ (top-right panel), $\bar{k}l_{\mathrm{G}} = 2.5$ (bottom-left panel) and $\bar{k}l_{\mathrm{G}} = 4.1$ (bottom-right panel), predicted by multiple-scale method (solid line) and for individual (×) and effective (○) wave fields by random-sampling method

Fig. 2.30 shows the phase changes as functions of non-dimensional correlation length, for roughness amplitude $\epsilon = 5.0 \times 10^{-2}$ (left-hand panel) and 1.0×10^{-1} (right-hand panel). Again, the interval length is chosen to be $\bar{k}L = 4\bar{k}/\epsilon^2$ in the random-sampling method.

We can observe in Fig. 2.30 that the multiple-scale method and the random-sampling method yield the same phase changes for the roughness amplitude $\epsilon = 5.0 \times 10^{-2}$. For the larger roughness amplitude, $\epsilon = 1.0 \times 10^{-1}$, they still show the same behaviour, but the phase changes obtained by the random-sampling method exhibit small deviations from the values predicted by the multiple-scale method. This noise is attributed to numerical difficulties in capturing the phase changes accurately. The phase changes for the varying rigidity problem have a significantly different feature than those for the varying mass problem. For the correlation length tending to zero, the phase change does not tend to zero, but tends to a constant, finite offset. The offset for the varying rigidity problem is precisely the constant $\bar{k}/4$ from Eqn. (2.119a) and the phase change is positive for the varying rigidity problem, meaning that the effective wavelength is shorter than that of the uniform beam. The phase change decreases approximately linearly (with the same slope as in the varying mass problem) with increasing correlation length over

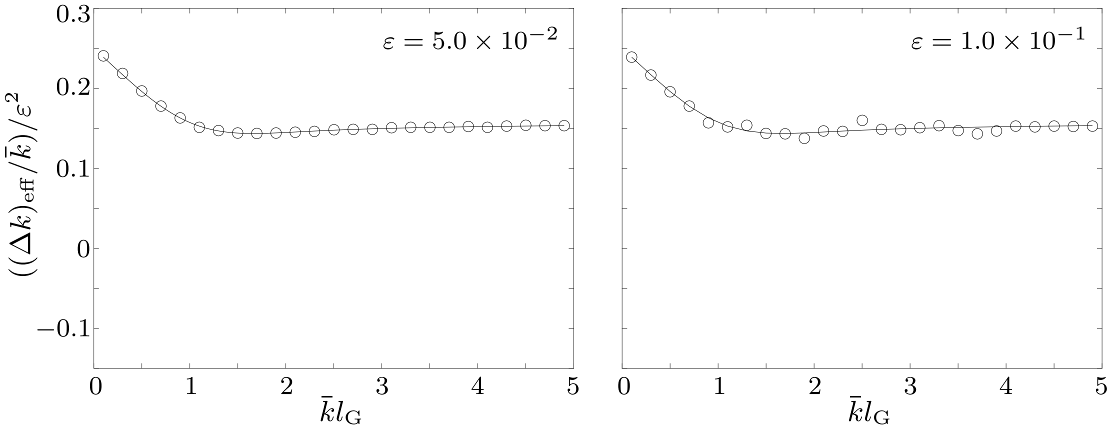

Figure 2.30: Scaled phase changes of effective wave field for varying rigidity problem as functions of non-dimensional correlation length, for roughness amplitudes $\epsilon = 5.0 \times 10^{-2}$ (left-hand panel) and $\epsilon = 1.0 \times 10^{-1}$ (right-hand panel), predicted by multiple-scale method (solid line) and random-sampling method (∘)

the interval $\bar{k}l_{\mathrm{G}} \leq 1$, and is approximately constant for $\bar{k}l_{\mathrm{G}} \geq 1.5$ in our correlation length regime. The fact that the phase change is finite as the correlation length tends to zero is presumably because the derivatives of the rigidity appear in the governing Eqn. (2.9).

The section showing the numerical results for the varying rigidity problem is concluded with qualitative phase changes over the whole roughness interval. Fig. 2.31 shows the phase changes for example individual wave fields and corresponding effective wave fields, for roughness amplitude $\epsilon = 5 \times 10^{-2}$ and non-dimensional correlation lengths $\bar{k}l_{\mathrm{G}} = 0.9$ (left-hand panel) and 4.1 (right-hand panel).

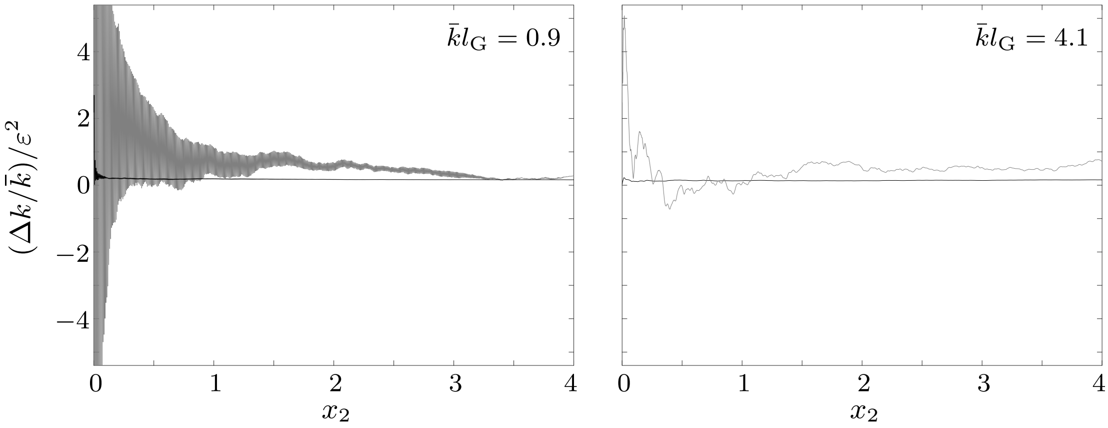

Figure 2.31: Phase changes of example individual wave fields (grey curves) and effective wave fields (black) for varying rigidity problem, for non-dimensional correlation lengths $\bar{k}l_{\mathrm{G}} = 0.9$ (left-hand panel) and $\bar{k}l_{\mathrm{G}} = 4.1$ (right-hand panel), for roughness amplitude $\epsilon = 5.0 \times 10^{-2}$

We can observe in Fig. 2.31 that the phase changes of individual wave fields show similarly to Fig. 2.26 for the varying mass problem a random behaviour for $\bar{k}l_{\mathrm{G}} = 0.9$ and 4.1. In contrast to those, the phase changes of the effective wave fields tend after noisy behaviour for small x to the values predicted by the multiple-scale approximation shown in Fig. 2.30 for both correlation length choices.

2.8 Rough beam with varying thickness

After we learnt the effects of a rough beam with varying mass only and varying rigidity only on wave propagation in the previous sections, both problems are combined now to a more realistic problem appearing due to thickness variations of thin beams. Varying thickness leads to variations of both, the beam mass and beam rigidity, which can be seen in Eqns. (2.7). Variations of the beam thickness, $h(x)$, change the cross-sectional area of the beam, $A(x)$, as well as the moment of inertia of the beam cross section, $I(x)$. (Note that in the varying mass and varying rigidity problems, the variations were assumed to be induced by variations of the beam density and Young's modulus, respectively, which ensured variations of the respective quantity only.) The moment of inertia describes the resistance of a cross section to bending and buckling. It depends on the shape and size of the cross section and is calculated about the bending axis, see e.g. Ghavami 2015. The bending axis in our problem is the centroidal x-axis. The beam width, denoted with w, is centred on the y-axis and is constant along the horizontal x-axis. The axis describing the beam thickness h is denoted with the vertical z-axis, which points upwards, and its mean $\bar{h}$ shall be centred around $z = 0$. Fig. 2.32 shows an illustration of the rectangular beam cross section along the centroidal x-axis.

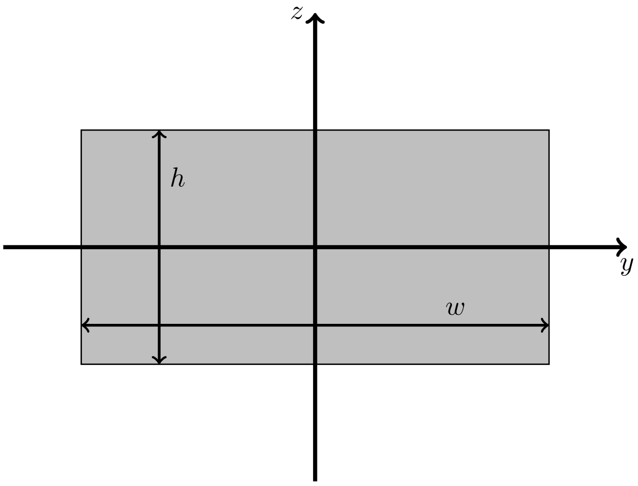

Figure 2.32: Illustration of rectangular beam cross section along centroidal x-axis

The cross-sectional area of the beam, $A(x)$, and the moment of inertia of the beam cross section, $I(x)$, for our problem of a beam with constant width w and varying thickness $h(x)$, both centred around their respective axis, is then given by

$$A(x) = w\,h(x), \tag{2.120a}$$

$$I(x) = \frac{w\,h(x)^3}{12}. \tag{2.120b}$$

The beam thickness, $h(x)$, shall fluctuate about the mean $\bar{h}$ with roughness amplitude ϵ and the variations are modelled via the same Gaussian autocorrelated random process as in the varying mass and varying rigidity problems and we denote the random process here with $\tilde{h}(x)$. This leads us to the representation of the varying beam thickness as

$$h(x) = \bar{h}(1 + \epsilon\tilde{h}(x)), \tag{2.121}$$

where the random process $\tilde{h}(x)$ fulfils the Gaussian autocorrelation condition

$$\langle\tilde{h}(x)\,\tilde{h}(x-\xi)\rangle = \mathbf{E}[\tilde{h}(x)\,\tilde{h}(x-\xi)] = \mathrm{e}^{-\xi^2/l_{\mathrm{G}}^2}\ \big(=\rho(|\xi|)\big). \tag{2.122}$$

The representation of the beam mass and rigidity in Eqns. (2.7) together with Eqns. (2.120) allow us to express the beam mass and rigidity in terms of the varying beam thickness,

$$g(x) = \rho\,w\,h(x) = \rho w\bar{h}(1 + \epsilon\tilde{h}(x)) =: \bar{g}\,(1 + \epsilon\gamma(x)), \tag{2.123a}$$

$$b(x) = E\,\frac{wh(x)^3}{12} = \frac{Ew}{12}\bar{h}^3(1 + 3\epsilon\tilde{h}(x)) + \mathcal{O}(\epsilon^2) =: \bar{b}\,(1 + \epsilon\beta(x)). \tag{2.123b}$$

For the multiple-scale method, we seek the representation of the quantities describing the mass and rigidity variations in terms of $\bar{h}$ and $\tilde{h}$ (up to order ϵ only, for the sake of simplicity), which can directly be derived from Eqns. (2.123):

$$\bar{g} = \rho w\bar{h} \qquad \text{and} \qquad \gamma(x) = \tilde{h}(x), \tag{2.124a}$$

$$\bar{b} = \frac{Ew}{12}\bar{h}^3 \qquad \text{and} \qquad \beta(x) = 3\tilde{h}(x). \tag{2.124b}$$

Although the beam width w appears in the beam mass and rigidity, we do not have to specify it in our calculations, since we assume constant beam width and hence, the width in the governing beam equation cancels away, i.e. the model remains quasi one-dimensional. Since the processes $\gamma(x)$ and $\beta(x)$ are determined from the same underlying (autocorrelated) random process describing the thickness fluctuations, $\tilde{h}(x)$, we know the inherent autocorrelation of the beam mass and rigidity variations, and can identify their cross-correlation:

$$\rho_1(|\xi|) := \langle\gamma(x)\,\gamma(x-\xi)\rangle \ = \ \langle\tilde{h}(x)\,\tilde{h}(x-\xi)\rangle = \rho(|\xi|), \tag{2.125a}$$

$$\rho_2(|\xi|) := \langle\beta(x)\,\beta(x-\xi)\rangle = 9\langle\tilde{h}(x)\,\tilde{h}(x-\xi)\rangle = 9\rho(|\xi|), \tag{2.125b}$$

$$\rho_3(|\xi|) := \langle\gamma(x)\,\beta(x-\xi)\rangle = 3\langle\tilde{h}(x)\,\tilde{h}(x-\xi)\rangle = 3\rho(|\xi|). \tag{2.125c}$$

Note that the cross-correlation is not used explicitly in the random-sampling method, for which the beam mass and rigidity are derived from the beam thickness which is given by realisations of the underlying random process, but the autocorrelation and cross-correlation terms are needed for the multiple-scale method to capture the complex wavenumber. Before we introduce the multiple-scale method in the next section, we look at effective and example individual wave fields for the same average roughness properties as in Figs. 2.18 and 2.27 for the varying mass and rigidity problem, respectively. Fig. 2.33 shows the moduli of example individual wave fields and corresponding effective wave fields, for roughness amplitude $\epsilon = 5.0 \times 10^{-2}$ and non-dimensional correlation lengths $\bar{k}l_{\mathrm{G}} = 0.9$ (left-hand panel) and 4.1 (right-hand panel), for the varying thickness problem with a unit-amplitude incident, right travelling wave, again.

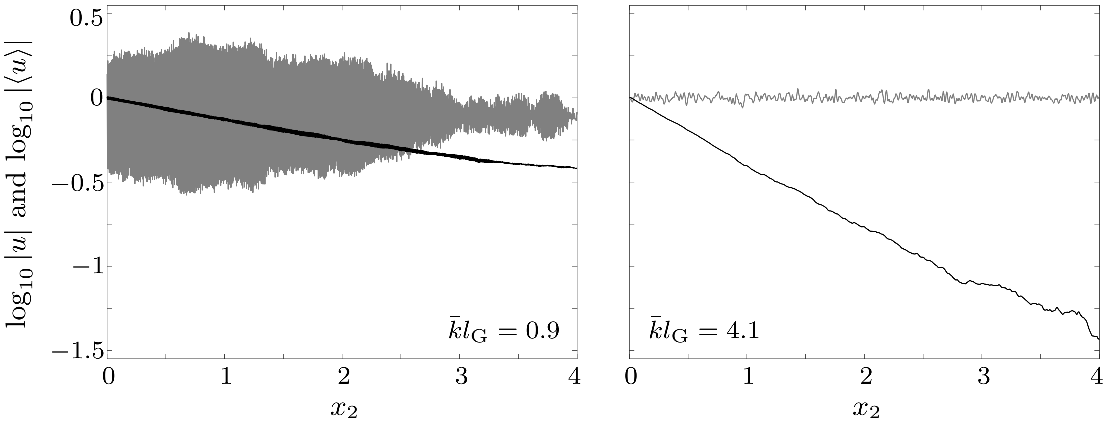

Figure 2.33: Example individual wave fields (grey curves) and effective wave fields (black) for varying thickness problem, for roughness amplitude $\epsilon = 5.0 \times 10^{-2}$ and non-dimensional correlation lengths $\bar{k}l_{\mathrm{G}} = 0.9$ (left-hand panel) and $\bar{k}l_{\mathrm{G}} = 4.1$ (right-hand panel)

We can see in Fig. 2.33 the same qualitative behaviour as for the varying mass and rigidity problems, but it is also observable that the effective wave fields are attenuated significantly more. In particular, this is visible for the larger correlation length, $\bar{k}l_{\mathrm{G}} = 4.1$, where $\log_{10}|\langle u\rangle| \approx -1.45$ at the right end of the rough interval, which suggests that the effective wave field is attenuated approximately four times faster than the effective wave fields in the varying mass and varying rigidity problems ($\log_{10}|\langle u\rangle| \approx -0.37$ at the right end of the rough interval in both cases). Obviously, the increase in attenuation is due to the combination of rough beam mass and rough beam rigidity, as well as the higher order roughness appearing in the beam rigidity.

2.8.1 Multiple-scale method

The multiple-scale method for the varying thickness problem will be presented in the following. Since mass as well as rigidity variation terms appear in this problem, the multiple-scale method is expected to be a combination of the multiple-scale methods for the varying mass and varying rigidity problem. For the sake of completeness, it should not go unmentioned that the same multiple-scale expansion for the wave field, u, as for the previous problems is used on the local and observation scale, l_{G} and L_{ob}, respectively, and $\epsilon \ll 1$ is required. The governing equations up to second order of ϵ are obtained by substituting the multiple-scale expansion (2.82) into the original linear thin-beam Eqn. (2.9).

Order ϵ^0

Since the functions describing the varying mass and varying rigidity are not of order ϵ^0, it is clear that the governing equation for the leading-order wave field given by the order ϵ^0 terms, u_0, for the varying thickness problem is identical to the governing leading-order equation in the varying mass and varying rigidity problems, i.e.

$$(\partial_x^4 - \bar{k}^4)u_0(x,x_2) = 0, \qquad x \in (-\infty,\infty).$$

The wavenumber $\bar{k}$ here corresponds to the mean beam mass and rigidity, i.e. $\bar{k} = (\alpha\bar{g}/\bar{b})^{\frac{1}{4}}$. We could observe in Fig. 2.33 that the attenuation for the present problem is larger than for the varying mass and varying rigidity problems. To validate our approach of neglecting the intrinsic left-travelling wave in this case, we take up the analysis in Sec. 2.6.2, where we showed that the leading-order solution for the varying mass problem only consists of a modulated rightward-travelling wave, and apply it to the varying thickness problem.

The left-hand panel of Fig. 2.34 shows the effective wave fields and the corresponding left- and right-travelling components for roughness amplitude $\epsilon = 5.0 \times 10^{-2}$ and correlation lengths $\bar{k}l_{\mathrm{G}} = 0.9$, 2.5 and 4.1. The right-hand panel of Fig. 2.34 shows the ratio of the (spatial averaged) leftward- to rightward travelling effective wave components as functions of non-dimensional correlation length, for roughness amplitudes $\epsilon = 10^{-4}$, 10^{-3}, 10^{-2}, 10^{-1} and 2×10^{-1}. The ratio of leftward- to rightward travelling effective wave components is defined in Eqn. (2.85).

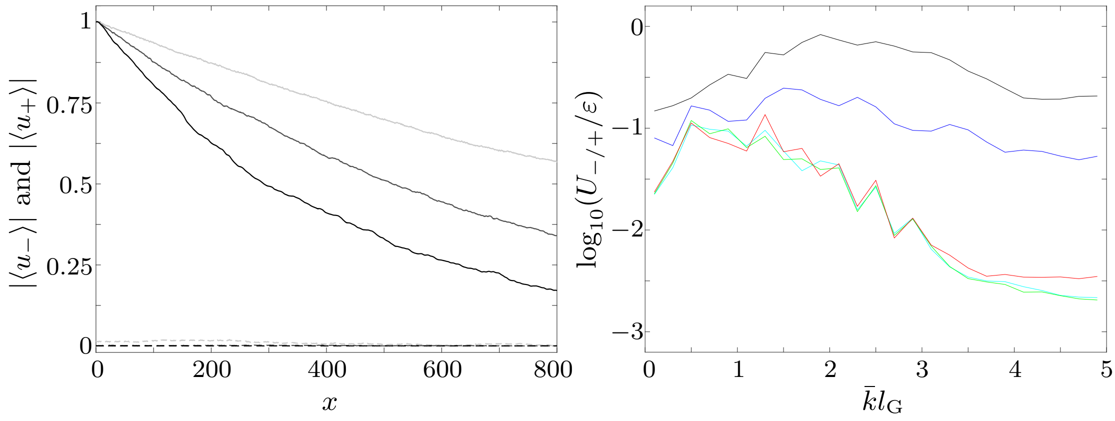

Figure 2.34: Left-hand panel: Effective wave field for roughness amplitude $\epsilon = 5.0 \times 10^{-2}$ and correlation lengths $\bar{k}l_{\mathrm{G}} = 0.9$ (solid line), $\bar{k}l_{\mathrm{G}} = 2.5$ (dashed line) and $\bar{k}l_{\mathrm{G}} = 4.1$ (dotted line), split into rightward- and leftward-travelling components (light and dark grey, respectively). Right-hand panel: Ratio of leftward- to rightward travelling components of effective wave field as functions of non-dimensional correlation length, for roughness amplitudes $\epsilon = 10^{-4}$ (cyan), $\epsilon = 10^{-3}$ (green), $\epsilon = 10^{-2}$ (red), $\epsilon = 10^{-1}$ (blue) and $\epsilon = 2 \times 10^{-1}$ (black).

We can observe in the left-hand panel of Fig. 2.34 that the right-travelling wave component clearly dominates the left-travelling effective wave component over the whole rough interval in all three cases of non-dimensional correlation lengths considered, $\bar{k}l_\mathrm{G} = 0.9$, 2.5 and 4.1, for roughness amplitude $\epsilon = 5.0\times10^{-2}$. The dominance of the right-travelling effective wave components is confirmed in the right-hand panel of Fig. 2.34 for the whole correlation length regime for small roughness amplitudes (which is assumed in the multiple-scale method, though). We can observe that the scaled ratios behave very similarly for $\epsilon \leq 10^{-2}$ and reach their maximum at $l_\mathrm{G} \approx 0.7$, for which the left-travelling effective wave component is still negligible. Again, for $\epsilon \geq 10^{-1}$, the proportionality of $U_{-/+}$ with ϵ does not hold anymore and the left-travelling effective wave component makes a non-negligible contribution to the effective wave field.

With the evidence from Fig. 2.34 and under the assumption of $\epsilon \ll 1$, we can deduce that the random leftward-travelling wave can be neglected at leading order and the leading-order solution only consists of a modulated rightward-travelling wave. Hence, the leading-order solution is again of the form

$$u_0(x,x_2) = A(x_2)\,\mathrm{e}^{\mathrm{i}\bar{k}x}, \tag{2.126}$$

and we seek the mean leading-order wave amplitude, $\langle A(x_2)\rangle$, from the higher-order terms.

Order ϵ^1

When collecting the terms of order ϵ, the inhomogeneous right-hand side of the governing equation for the first-order wave field, u_1, consists of the respective terms of order ϵ appearing for the varying mass (Eqn. (2.89)) and varying rigidity problem (Eqn. (2.109)),

$$(\partial_x^4 - \bar{k}^4)u_1(x,x_2) = \bar{k}^4\gamma(x)u_0(x,x_2) - \partial_x^2\big(\beta(x)\,\partial_x^2 u_0(x,x_2)\big), \quad x \in (-\infty,\infty). \tag{2.127}$$

Using the standard Green's function for the homogeneous beam equation (with k replaced by $\bar{k}$), the solution for the first-order wave field is a linear combination of Eqns. (2.90) and (2.110),

$$u_1(x,x_2) = \int_{-\infty}^{\infty} G(|x-\check{x}|)\left(\bar{k}^4\gamma(\check{x}) - \partial_{\check{x}}^2\big(\beta(\check{x})\,\partial_{\check{x}}^2\big)\right)u_0(\check{x},x_2)\,\mathrm{d}\check{x}. \tag{2.128}$$

Order ϵ^2

In analogy to the first-order governing equation, the right-hand side of the governing equation for the second-order wave field in the present problem, u_2, consists of the respective terms appearing in the formulations of the governing equation for the varying mass (Eqn. (2.91)) and rigidity problems (Eqn. (2.111)) as well. This yields the governing equation for the order ϵ^2 terms,

$$(\partial_x^4 - \bar{k}^4)u_2 = -4\partial_x^3\partial_{x_2}u_0(x,x_2) + \bar{k}^4\gamma(x)u_1 - \partial_x^2\left(\beta(x)\,\partial_x^2 u_1(x,x_2)\right), \quad x \in (-\infty,\infty), \tag{2.129}$$

which can be expressed, taking the ensemble average, as

$$(\partial_x^4 - \bar{k}^4)\langle u_2 \rangle = 4\mathrm{i}\bar{k}^3 \partial_{x_2} \langle A(x_2) \rangle \mathrm{e}^{\mathrm{i}\bar{k}x} + \bar{k}^4 \langle \gamma(x) u_1 \rangle - \langle \partial_x^2 \left(\beta(x)\, \partial_x^2 u_1(x,x_2) \right) \rangle. \tag{2.130}$$

For our solution procedure, we now have to justify that the leading-order solution, u_0, and in particular its random components are uncorrelated to the thickness variations. This has to be done (in analogy to the investigation for the varying mass problem) here, since the varying thickness leads to more attenuation and scattered, hence left-travelling waves. The left-hand panel of Fig. 2.35 shows $\rho_u(|\xi|) = \langle \gamma(\check{x}+\xi)\gamma(\check{x})u(\check{x}) \rangle$, originally defined in Eqn. (2.95), as well as the terms corresponding to the random component of the wave travelling rightward and the (random) wave travelling leftward, defined in Eqns. (2.96b), as functions of $|\xi|$ for non-dimensional correlation length $\bar{k}l_{\mathrm{G}} = 2.5$ and roughness amplitude $\epsilon = 5.0 \times 10^{-2}$. The right-hand panel of Fig. 2.35 shows these quantities averaged over the whole roughness interval (and $J_{l_{\mathrm{G}}}$ averaged over one correlation length, only) as functions of the non-dimensional correlation length, for $\epsilon = 5.0 \times 10^{-2}$. For reference, these averaged functions are defined in Eqns. (2.97) and (2.98).

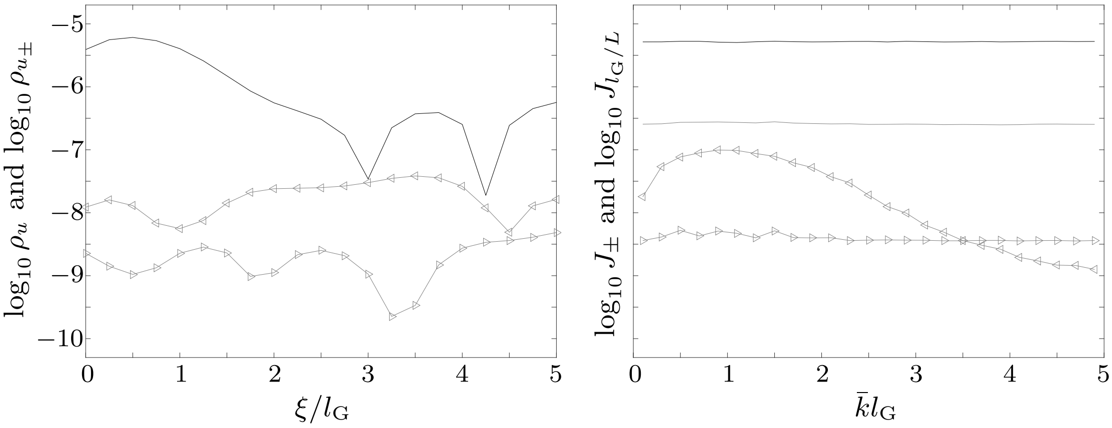

Figure 2.35: Left-hand panel: Correlation between wave field and thickness variation for non-dimensional correlation length $\bar{k}l_{\mathrm{G}} = 2.5$ and roughness amplitude $\epsilon = 5.0 \times 10^{-2}$ (same notation as in Fig. 2.21). Right-hand panel: Mean correlations of roughness profile with wave field, $J_{l_{\mathrm{G}}}$ (black solid) and J_L (grey solid), and random components of wave field, J_+ (▷) and J_- (◁), as functions of non-dimensional correlation length, for roughness amplitude $\epsilon = 5.0 \times 10^{-2}$.

We can observe in Fig. 2.35 that the correlation functions between the wave field and the thickness variations is smaller by 4 orders of magnitude. Clearly, this scaling also holds for the averaged correlation functions. We can deduce that the random components of the wave fields are uncorrelated to the roughness profile, hence the correlation of the wave field with the roughness profile is negligible and we can factor out the wave fields from the ensemble averages as the effective wave field and apply the correlation functions.

Here, the second and third term on the right-hand side of Eqn. (2.130) do not correspond one-to-one to the complex constants ζ_{vm} for the varying mass and ζ_{vr} for the varying rigidity problem because of the mixed terms $\langle\gamma(x)\,\beta(\check{x})\rangle$ appearing due to representation of u_1 in Eqn. (2.128). We can rewrite the second term in the simplified form

$$\bar{k}^4\langle\gamma(x)u_1\rangle = 4\bar{k}^3\mathrm{e}^{\mathrm{i}\bar{k}x}\langle A(x_2)\rangle\zeta_{\mathrm{vm}} + 4\bar{k}^3\mathrm{e}^{\mathrm{i}\bar{k}x}\langle A(x_2)\rangle\underbrace{\frac{\bar{k}^3}{4}\int_{-\infty}^{\infty} G(|\xi|)\partial_x^2\big(\rho_3(|\xi|)\mathrm{e}^{\mathrm{i}\bar{k}\xi}\big)\,\mathrm{d}\xi}_{=:\,\zeta_{\mathrm{mx1}}}, \tag{2.131}$$

where the complex constant ζ_{vm} is defined for the varying mass problem in Eqn. (2.100). The third term on the right-hand side of Eqn. (2.130) can be simplified with the complex constant ζ_{vr} for the varying rigidity problem in Eqn. (2.113),

$$\begin{aligned}-\langle\partial_x^2\left(\beta(x)\,\partial_x^2u_1(x,x_2)\right)\rangle = 4\bar{k}^3\mathrm{e}^{\mathrm{i}\bar{k}x}\langle A(x_2)\rangle\zeta_{\mathrm{vr}}+&\\ + 4\bar{k}^3\mathrm{e}^{\mathrm{i}\bar{k}x}\langle A(x_2)\rangle\underbrace{\left(\frac{-\bar{k}}{4}\right)\int_{-\infty}^{\infty}\partial_x^2\big(\rho_3(|\xi|)\,\partial_x^2G(|\xi|)\big)\mathrm{e}^{\mathrm{i}\bar{k}\xi}\,\mathrm{d}\xi}_{=:\,\zeta_{\mathrm{mx2}}}\,.&\end{aligned} \tag{2.132}$$

For Eqns. (2.131) and (2.132), we implied the de-correlation of the leading-order wave field and the roughness profile, which was shown for the varying mass problem in Figs. 2.21 and 2.22. Note that in the definition ζ_{vm} and ζ_{vr} in Eqns. (2.100) and Eqn. (2.113), respectively, the correlation functions $\rho(|\xi|)$ have to be replaced by the correlation functions describing the mass variations, $\rho_1(|\xi|)$, and the rigidity variations, $\rho_2(|\xi|)$, for the varying thickness problem from Eqns. (2.125). This means in particular, that the factor 9, which takes the cubic dependence of the rigidity variations from the thickness variations into account, has to be included into the original ζ_{vr} from Eqn. (2.113).

With the simplifications from Eqns. (2.131) and (2.132), combining $\zeta_{\mathrm{mx1}} + \zeta_{\mathrm{mx2}} = \zeta_{\mathrm{mx}}$ and employing the ansatz $\langle u_2\rangle = \mathrm{e}^{\mathrm{i}\bar{k}x}F(x_2)$, we can write the averaged second-order governing Eqn. (2.130) as the following ordinary differential equation for the effective amplitude $\langle A(x_2)\rangle$,

$$\partial_{x_2}\langle A(x_2)\rangle = \mathrm{i}\,(\zeta_{\mathrm{vm}} + \zeta_{\mathrm{vr}} + \zeta_{\mathrm{mx}})\,\langle A(x_2)\rangle, \tag{2.133}$$

whose solution is given by

$$\langle A(x_2)\rangle = A_0\,\mathrm{e}^{\mathrm{i}(\zeta_{\mathrm{vm}}+\zeta_{\mathrm{vr}}+\zeta_{\mathrm{mx}})x_2}, \tag{2.134}$$

where we evaluate the integrals appearing in the complex constant ζ_{mx} numerically using an adaptive quadrature scheme in the following results section. The phase change, $(\Delta k)_{\mathrm{eff}}$, and attenuation coefficient, Q_{eff}, produced by the varying thickness are, respectively,

$$(\Delta k)_{\mathrm{eff}} = \epsilon^2\mathrm{Re}(\zeta_{\mathrm{vm}} + \zeta_{\mathrm{vr}} + \zeta_{\mathrm{mx}}), \tag{2.135a}$$

$$\text{and}\quad Q_{\mathrm{eff}} = \epsilon^2\mathrm{Im}(\zeta_{\mathrm{vm}} + \zeta_{\mathrm{vr}} + \zeta_{\mathrm{mx}}). \tag{2.135b}$$

2.8.2 Numerical results

To complete our studies of wave propagation along a beam in vacuo, we analyse the numerical results for the attenuation and the phase change for a beam with continuously varying thickness. This complements the elementary studies in the previous sections of varying mass and varying rigidity only, and gives results for naturally occurring problems. We provide results using the random-sampling method and validate the corresponding multiple-scale method. Again, we start our investigation with the influence of the correlation length on the attenuation. Fig. 2.36 shows the scaled attenuation coefficients, predicted by the multiple-scale method and obtained by the random-sampling method, as functions of non-dimensional correlation length, for roughness amplitudes $\epsilon = 1.0 \times 10^{-3}$ (top-left panel), 1.0×10^{-2} (top-right panel), 5.0×10^{-2} (bottom-left panel) and 1.0×10^{-1} (bottom-right panel).

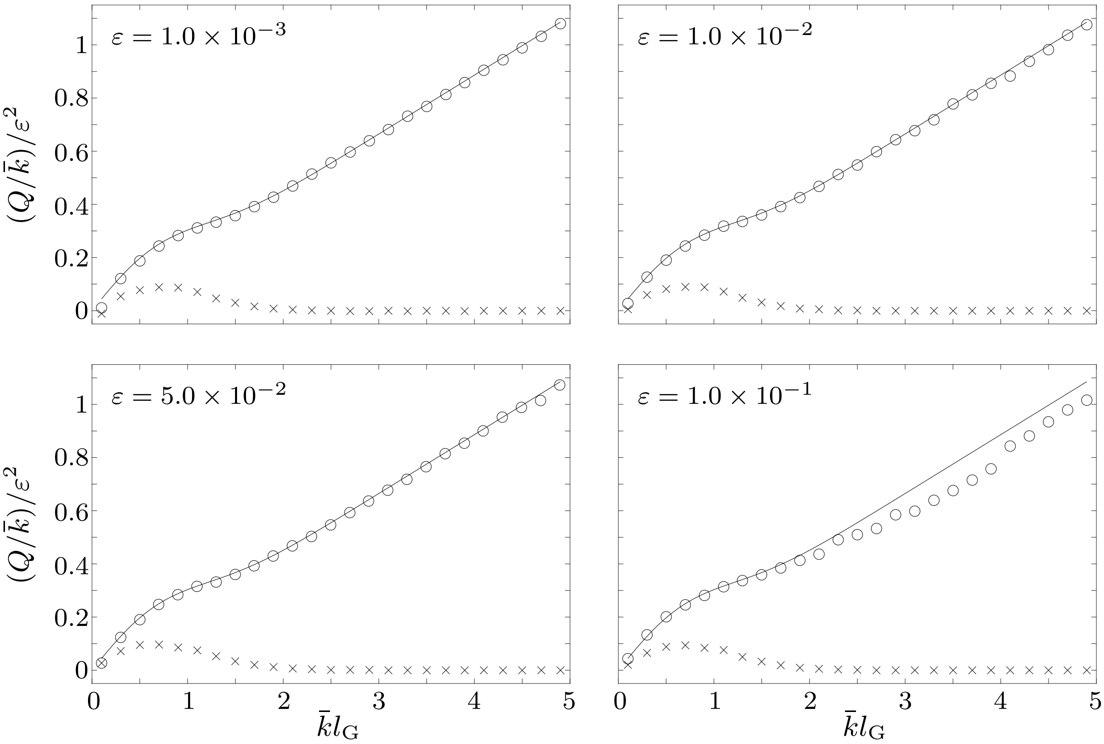

Figure 2.36: Scaled attenuation coefficients of effective wave field for varying thickness problem as functions of non-dimensional correlation length, predicted by multiple-scale method (solid line) and random-sampling method (○), for roughness amplitudes $\epsilon = 1.0 \times 10^{-3}$ (top-left panel), $\epsilon = 1.0 \times 10^{-2}$ (top-right panel), $\epsilon = 5.0 \times 10^{-2}$ (bottom-left panel) and $\epsilon = 1.0 \times 10^{-1}$ (bottom-right panel). Corresponding individual attenuation coefficients obtained by the random-sampling method (×) are shown for comparison.

We can observe in Fig. 2.36 that the varying thickness yields qualitatively the same curve for the effective and individual attenuation coefficients as the varying mass and varying rigidity, i.e. in the roughness amplitude regime $\epsilon \leq 5.0 \times 10^{-2}$, the effective attenuation coefficients are proportional to ϵ^2, and they scale linearly with the correlation length for $\bar{k}l_{\mathrm{G}} \geq 2$. On the contrary, the individual wave fields show only attenuation for $\bar{k}l_{\mathrm{G}} \leq 2$, however, they attenuate significantly slower than the corresponding effective wave fields in this correlation length regime. Although the attenuation coefficients show the same qualitative behaviour as in the varying mass and varying rigidity problems, they differ quantitatively from them and are approximately four times larger than those throughout the whole correlation length regime. This confirms our impression from the effective wave fields in Fig. 2.33 about the increased attenuation, which is due to the simultaneous appearance of both varying mass and rigidity as well as the cubic scaling of the rigidity variations with the thickness variations. We can also see in Fig. 2.36 that the multiple-scale method predicts effective attenuation coefficients, which show a very good agreement with results obtained by the random-sampling, for roughness amplitudes $\epsilon \leq 5.0 \times 10^{-2}$. For $\epsilon = 1.0 \times 10^{-1}$, the overprediction of the attenuation coefficients by the multiple-scale method, which we could already slightly observe for the varying mass and rigidity problem, is magnified and the results already start to deviate for $\bar{k}l_{\mathrm{G}} \geq 2$.

To examine the limit of validity of the multiple-scale method, which is associated with the loss of proportionality of the effective attenuation coefficients with ϵ^2, we study the attenuation coefficients in dependence of the roughness amplitude now. Fig. 2.37 shows the scaled attenuation coefficients, predicted by the multiple-scale method and obtained by the random-sampling method, as functions of roughness amplitude, for the non-dimensional correlation lengths $\bar{k}l_{\mathrm{G}} = 0.9$ (top-left panel), 1.5 (top-right panel), 2.5 (bottom-left panel) and 4.1 (bottom-right panel).

We can observe in Fig. 2.37 that the multiple-scale approximation and the random-sampling method yield the same effective attenuation coefficients for all correlation lengths considered, in the roughness amplitude regime $\epsilon < 0.1$ only. Whereas we obtain very good agreement between both methods for $\bar{k}l_{\mathrm{G}} = 0.9$ over the whole roughness amplitude regime (with only a small deviation for the smallest roughness amplitude due to inaccuracy in capturing this very small attenuation coefficient), the values for the two largest roughness amplitudes in the case $\bar{k}l_{\mathrm{G}} = 1.5$ already suggest that the effective attenuation coefficients become smaller than proportionally to ϵ^2. This effect is novel for this intermediate correlation length and this tendency is confirmed by the results for $\bar{k}l_{\mathrm{G}} = 2.5$, for which we could not observe deviations in the case of varying mass or varying rigidity either. For $\bar{k}l_{\mathrm{G}} = 4.1$, our previous observations are endorsed, i.e. the effective attenuation coefficients start to deviate from the values predicted by the multiple-scale method for $\epsilon \geq 1.0 \times 10^{-1}$, and we note that the deviations turn out to be larger than for the varying mass and varying rigidity. We deduce that this effect occurs due to the increased scattering strength of the varying thickness problem. The individual attenuation coefficients, which are shown for comparison, exhibit the same qualitative behaviour as in the varying mass and varying rigidity problem. Similarly to the effective attenuation coefficients, they are approximately four times larger than their equivalents for mass and rigidity variations, only. Hence, they remain smaller by the same factor than the effective attenuation coefficients and they are only proportional to ϵ^2 for correlation lengths $\bar{k}l_{\mathrm{G}} = 0.9$ and 1.5 in the roughness amplitude regime $\epsilon \geq 10^{-3}$ and $\epsilon \geq 10^{-2.5}$, respectively.

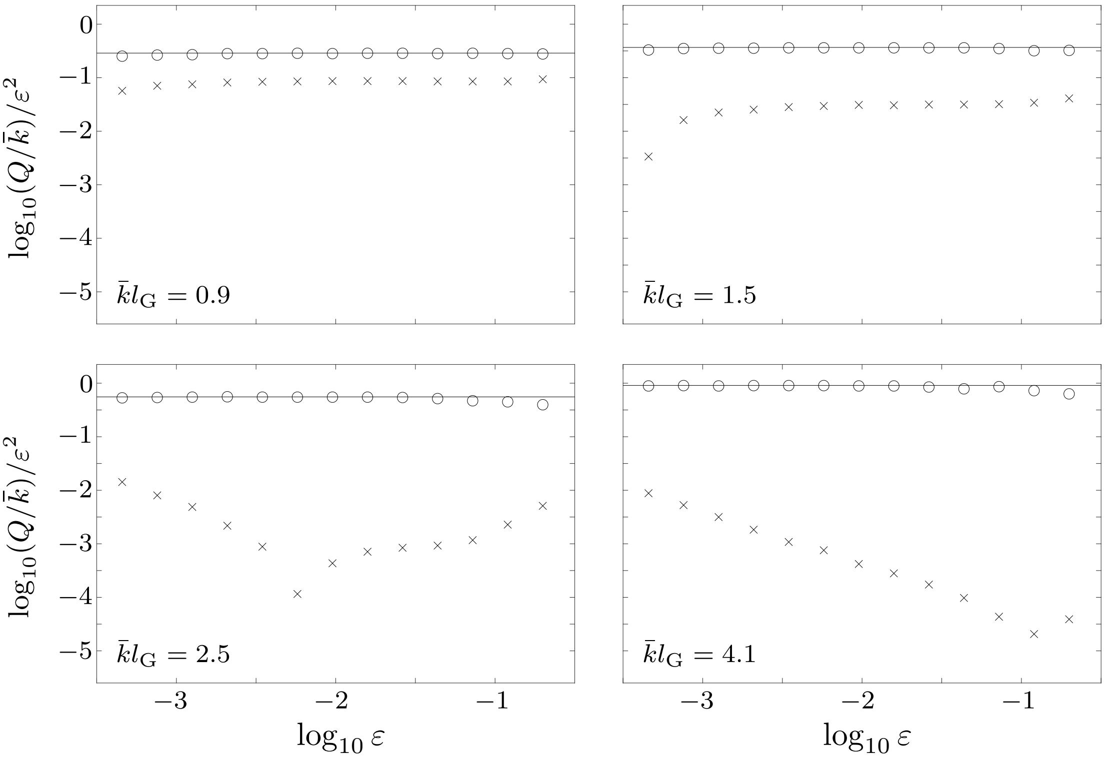

Figure 2.37: Scaled attenuation coefficients for varying thickness problem as functions of roughness amplitude, for non-dimensional correlation lengths $\bar{k}l_{\mathrm{G}} = 0.9$ (top-left panel), $\bar{k}l_{\mathrm{G}} = 1.5$ (top-right panel), $\bar{k}l_{\mathrm{G}} = 2.5$ (bottom-left panel) and $\bar{k}l_{\mathrm{G}} = 4.1$ (bottom-right panel), predicted by multiple-scale method (solid line) and for individual (×) and effective (○) wave fields by random-sampling method

For the numerical results so far, the attenuation coefficients were always non-dimensionalised with the mean wavenumber $\bar{k}$. As a demonstration of the numerical method and its universality with respect to incoming waves with different wavenumbers, we investigate the attenuation for time-harmonic waves of a wide range of angular frequencies now. Note that the wavenumber scales with the root of the angular frequency, ω. Fig. 2.38 shows the scaled attenuation coefficients, predicted by the multiple-scale method and obtained by the random-sampling method, as functions of the angular frequency, for the non-dimensional correlation lengths $\bar{k}l_{\mathrm{G}} = 0.9$ (top-left panel), 1.5 (top-right panel), 2.5 (bottom-left panel) and 4.1 (bottom-right panel), for the roughness amplitude $\epsilon = 5.0 \times 10^{-2}$.

We can observe in Fig. 2.38 that our assumption holds that the attenuation coefficient scales with the root of the angular frequency, hence with the wavenumber. This is valid throughout the whole regime of angular frequencies from 1 to 100000 for all correlation lengths considered, $\bar{k}l_{\mathrm{G}} = 0.9$, 1.5, 2.5 and 4.1, and both the random-sampling method and the multiple-scale method work independently from the frequency regime (and underlying mean beam mass and rigidity), we work in, and the method is not restricted in the frequency domain.

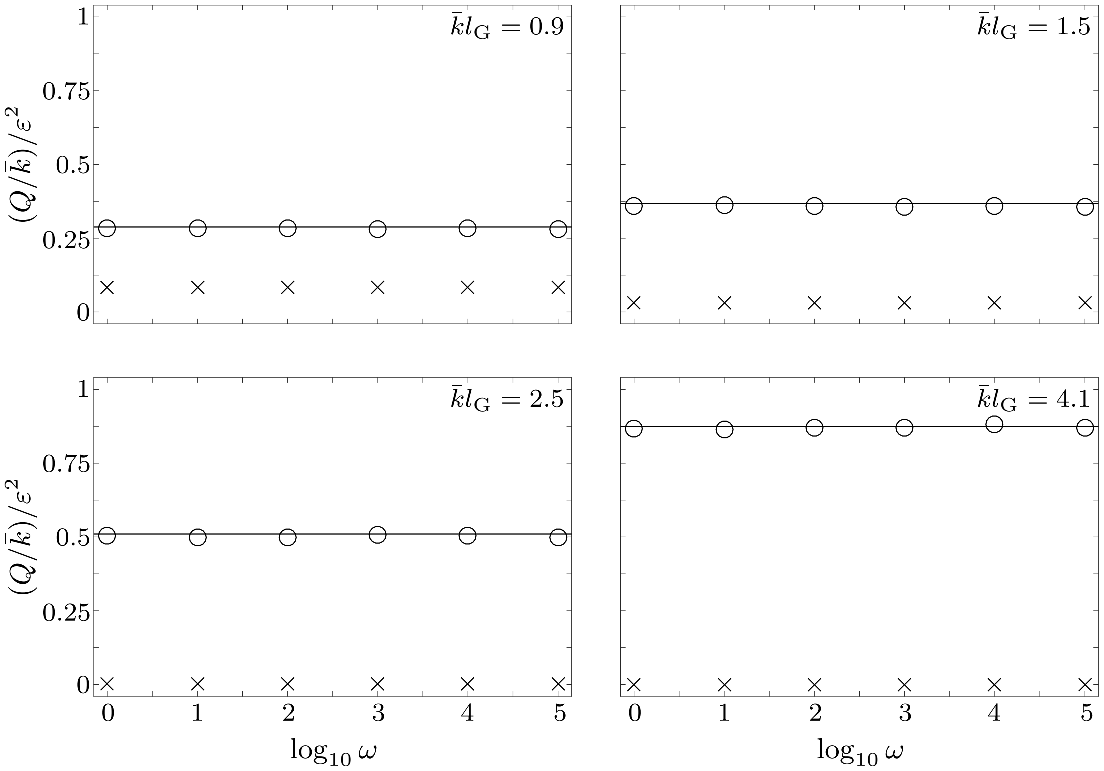

Figure 2.38: Scaled attenuation coefficients for varying thickness problem as functions of angular frequency, for non-dimensional correlation lengths $\bar{k}l_\mathrm{G} = 0.9$ (top-left panel), $\bar{k}l_\mathrm{G} = 1.5$ (top-right panel), $\bar{k}l_\mathrm{G} = 2.5$ (bottom-left panel) and $\bar{k}l_\mathrm{G} = 4.1$ (bottom-right panel), predicted by multiple-scale method (solid line) and for individual (×) and effective (○) wave fields by random-sampling method, for roughness amplitude $\epsilon = 5.0 \times 10^{-2}$

Finally, we investigate the phase changes of the effective wave field for the varying thickness problem, which can be obtained via Eqn. (2.104). Fig. 2.39 shows the phase changes as functions of non-dimensional correlation length, for roughness amplitude $\epsilon = 5.0 \times 10^{-2}$ (left-hand panel) and 1.0×10^{-1} (right-hand panel). The interval length is chosen to be $\bar{k}L = 4\bar{k}/\epsilon^2$ in the random-sampling method again.

We can observe in Fig. 2.39 that the multiple-scale method predicts (similarly to the previous problems) essentially the same phase changes as the random-sampling method for both roughness amplitudes, $\epsilon = 5.0 \times 10^{-2}$ and 1.0×10^{-1}, showing only small deviations in few cases. We notice that the phase changes are qualitatively similar to those we obtained for the varying rigidity problem. The phase changes tend to a constant, finite offset for the correlation length tending to zero. The offset is approximately five times larger than the corresponding offset for the varying rigidity problem for the smallest correlation length considered, $\bar{k}l_\mathrm{G} = 0.1$, i.e. the varying rigidity and the corresponding cross-correlation terms dominate the phase change. From there, the phase change decreases much more

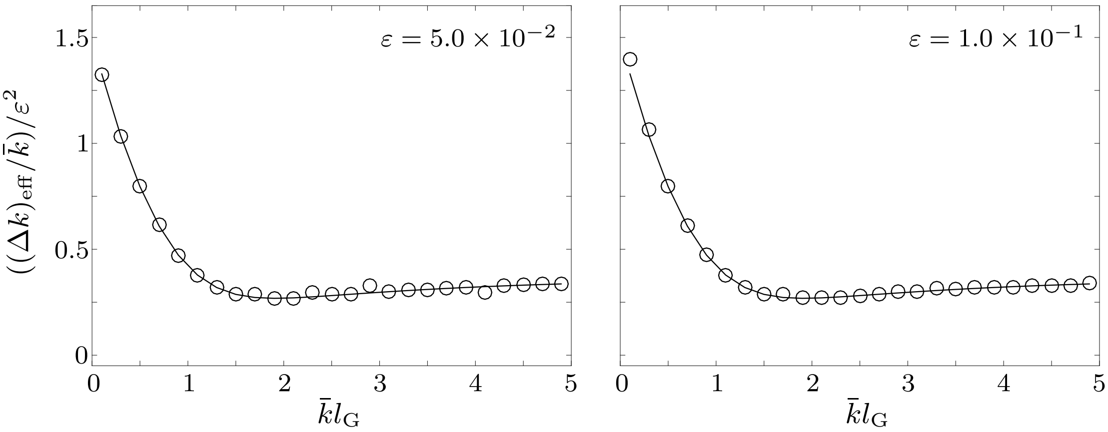

Figure 2.39: Scaled phase changes of effective wave field for varying rigidity problem as functions of non-dimensional correlation length, for roughness amplitudes $\epsilon = 5.0 \times 10^{-2}$ (left-hand panel) and $\epsilon = 1.0 \times 10^{-1}$ (right-hand panel), predicted by multiple-scale method (solid line) and random-sampling method ($\circ$)

rapidly than in the previous cases to reach its minimum around $\bar{k}l_{\text{G}} = 1.7$. The slope of the phase-change decrease is in its absolute magnitude significantly larger than for the varying mass and varying rigidity problem, which can be explained by the same qualitative decreasing behaviour associated to the varying mass and rigidity in this correlation length regime. From the minimum phase change-value on, $\bar{k}l_{\text{G}} \geq 1.7$, the phase change shows a very mild increasing behaviour, which is visible only weakly for the varying mass and varying rigidity problem. Altogether, the phase change is positive for the varying thickness problem throughout the whole correlation length regime, which means that the effective wavelength is shorter than that of the uniform beam.

Finally, we compare qualitative phase changes of individual and effective wave fields in the varying thickness problem. Fig. 2.40 shows the phase changes for example individual wave fields and corresponding effective wave fields, for roughness amplitude $\epsilon = 5 \times 10^{-2}$ and non-dimensional correlation lengths $\bar{k}l_{\text{G}} = 0.9$ (left-hand panel) and 4.1 (right-hand panel).

We can see in Fig. 2.40 that the phase changes of individual wave fields are also random, here for $\bar{k}l_{\text{G}} = 0.9$ and 4.1. Hence, quantitative results for individual phase changes are not informative for the varying thickness problem either. It is completely different for the phase changes of effective wave fields again, which tend after noisy behaviour for small x to the values observed in Fig. 2.39 for both correlation lengths, $\bar{k}l_{\text{G}} = 0.9$ and 4.1.

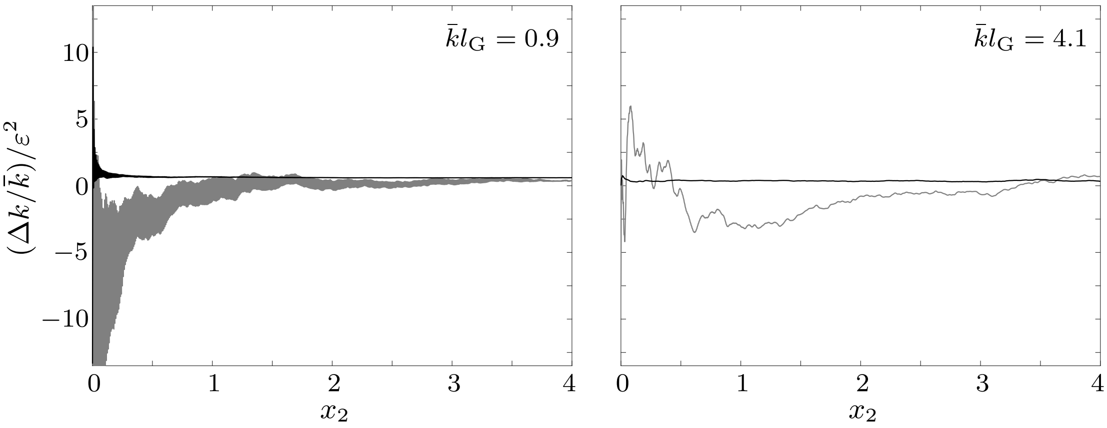

Figure 2.40: Phase changes of example individual wave fields (grey curves) and effective wave fields (black) for varying thickness problem and non-dimensional correlation lengths $\bar{k}l_{\mathrm{G}} = 0.9$ (left-hand panel) and $\bar{k}l_{\mathrm{G}} = 4.1$ (right-hand panel), for roughness amplitude $\epsilon = 5.0 \times 10^{-2}$

2.9 Summary and discussion

After introducing the problem formulation and deriving the governing Euler–Bernoulli beam equation, we extended the numerical method of Bennetts et al. (2015) to waves along a thin-elastic beam, whose roughness can be incorporated by varying thickness as well as beam property variations leading to varying mass and varying rigidity. To validate the step-approximation method, sample problems of thin-elastic beams with a deterministic single hump in its mass and rigidity characteristics, respectively, were considered. With knowledge of the Green's function for a homogeneous beam in vacuo, which is derived in Appendix 2.A, integral equations were formulated to describe the wave propagation along beam with deterministically varying mass and rigidity, respectively. The deterministic integral equations were solved using a numerical collocation method. We have seen that keeping the appearing jump terms involving the derivatives as natural conditions leads to very slow convergence of the method and impractical results for small hump amplitudes. To avoid this deficiency for small hump amplitudes, the natural conditions were enforced as essential boundary conditions, which yields much better convergence of the integral equation method. The integral equation method with enforced essential boundary conditions was used to produce comparing results to the step approximation and it could be observed in the varying mass problem that both methods showed excellent agreement throughout a wide hump-amplitude regime for different hump lengths. For the problem of deterministic rigidity variations, different discretisation schemes for the beam rigidity and its derivatives in the step-approximation method were examined. Comparisons with the integral equation method pointed out the correct discretisation scheme, for which we could subsequently validate the step approximation for varying beam rigidity, and we analysed the convergence of the step approximation with the respective discretisation scheme.

To incorporate roughness in the beam properties and beam thickness over a very long interval, we presented the underlying random process and the generation of rough profile realisations. The chosen random process is Gaussian autocorrelated and widely used to model rough surfaces for isotropic and homogeneous media, producing roughness profiles sharing the same roughness characteristics. Before we focused on wave attenuation along rough thin-elastic beams, we presented the random-sampling method, which is essential to generate effective wave fields, and the technique to measure the attenuation of wave fields. This was followed by an investigation of the convergence of the attenuation coefficients with respect to the size of the ensemble.

We studied effective waves along a rough thin-elastic beam, where the roughness occurs over a long, finite interval, and is in the form of random fluctuations in the beam's mass, rigidity or thickness, with a prescribed amplitude and correlation length. The step-approximation method was used to calculate the beam deflection for a given realisation of the roughness, and the effective wave field was constructed as the mean wave field for an ensemble of randomly generated realisations of the roughness for a given amplitude and correlation length with the random-sampling method. Analytic, multiple-scale approximations for the phase changes and attenuation coefficients were derived, on the assumption that the roughness amplitude is small. Solving the equations of higher orders using the stationarity of the random processes, which describe the variations, lead to the respective evolution equation of the leading-order-wave amplitude, from which the phase changes and attenuation coefficients could be derived, where a complex-valued integral had to be evaluated numerically. The phase changes and attenuation coefficients predicted by the random-sampling method and the multiple-scale approximation were compared over a range of correlation lengths and roughness amplitudes.

We showed that the multiple-scale method and the step-approximation method predict the same phase changes and attenuation coefficients, as long as ϵ is small enough (less than ~ 0.1). Giving analytical expressions, the multiple-scale method allowed more direct insights, e.g. we could read off directly that the effective wavenumbers scaled with the square of the roughness amplitude. It turned out that the effective wavenumbers between the cases of varying beam mass and rigidity only differ by a real constant. This implied in particular that the varying mass and varying rigidity produce identical attenuation coefficients, and identical phase changes up to the addition of a constant. One consequence of the constant difference was that, although the phase change tends to zero in the limit $\bar{k}l_{\mathrm{G}} \to 0$ for varying mass, it tends to a finite constant for varying rigidity. Moreover, the effective wavelength of the rough medium was found to be longer than that of the underlying incident wave forcing in the case of varying mass, but shorter for the case of varying rigidity. Introducing thickness variations leads to significantly larger attenuation than varying mass and varying rigidity only, and the effective wavelength is shorter than the wavelength of the corresponding uniform plate, since the inherent rigidity variations dominate the corresponding mass variations. We also found that the effective wave fields differ from the individual wave fields, particularly in the large-correlation-length regime. It was shown that individual wave fields attenuate at a far slower rate for small-amplitude roughness than the effective wave fields and deduced that it is the de-correlation of the individual wave fields that causes attenuation of the effective wave field.

Appendix

2.A Derivation of Green's function

The Green's function for the Euler–Bernoulli beam Eqn. (2.9) is needed for the validation of the step approximation via an integral equation in Sec. 2.3 and the derivation of the multiple-scale methods in Secs. 2.6–2.8. Green's functions play an important role for solving inhomogeneous problems, such as both inhomogeneous ordinary and inhomogeneous partial differential equations. In our case of an ordinary differential equation, the Green's function is the solution for the problem, where the inhomogeneous right-hand side is a Dirac delta distribution. Thus, with the principle of superposition the Green's function can be used to calculate further solutions, see e.g. Olver 2014. We now seek the solution for the homogeneous Euler–Bernoulli beam (i.e. with constant beam mass, g, and rigidity, b), hence, Eqn. (2.9) can be rewritten as

$$\partial_x^4 u(x) - k^4\, u(x) = 0, \qquad x \in (-\infty,\infty), \tag{2.A.1}$$

where the (constant) wavenumber is given by

$$k = (\alpha g/b)^{1/4}. \tag{2.A.2}$$

The Green's function is then the solution of Eqn. (2.A.1) with the right-hand side replaced by the Dirac delta distribution δ, i.e. the Green's function is the deflection response, which is produced by a point load. The Dirac delta distribution is defined formally as

$$\delta(x) = \begin{cases} \infty, & x = 0, \\ 0, & x \neq 0, \end{cases} \tag{2.A.3}$$

which has to satisfy

$$\int_{-\infty}^{\infty} \delta(x)\,\mathrm{d}x = 1. \tag{2.A.4}$$

Now, we replace the right-hand side of Eqn. (2.A.1), which describes the deflection of a homogeneous beam, by the Dirac delta distribution at $x = \check{x}$, i.e. the inhomogeneity corresponds to a harmonic point force in Eqn. (2.6) for a homogeneous beam. Hence, Eqn. (2.A.1) becomes under this point force

$$\frac{\partial^4 \mathrm{G}(x;\check{x})}{\partial x^4} - k^4 \mathrm{G}(x) = \delta(x - \check{x}). \tag{2.A.5}$$

Green's functions for elastic beams and plates under e.g. impulsive and moving time-harmonic loads are presented in Watanabe 2014. To solve Eqn. (2.A.5), we use the limit absorption principle, which is shown in Filippi 2008. It says that

$$\frac{\partial^4 \mathrm{G}_\epsilon(x;\check{x})}{\partial x^4} - \left[k(1+\mathrm{i}\epsilon)\right]^4 \mathrm{G}_\epsilon(x;\check{x}) = \delta(x-\check{x}) \tag{2.A.6}$$

for small $\epsilon > 0$ has a unique bounded solution G_ϵ with a unique limit G for $\epsilon \to 0$. The limit absorption principle follows from the knowledge that a perfectly elastic solid can be regarded as an idealisation of a weakly absorbing material. It ensures a unique solution for our problem.

We denote the Fourier transform of G_ϵ with

$$\widehat{\mathrm{G}_\epsilon}(\xi;\check{x}) = \int_{-\infty}^{\infty} \mathrm{G}_\epsilon(x;\check{x})\,\mathrm{e}^{-2\pi\mathrm{i}x\xi}\,\mathrm{d}x. \tag{2.A.7}$$

Then, the Fourier transform of the fourth-order derivative of G_ϵ can be integrated by parts four times such that we end up with

$$\begin{aligned}\widehat{\mathrm{G}_\epsilon^{(4)}}(\xi;\check{x}) &= \int_{-\infty}^{\infty} \mathrm{G}_\epsilon^{(4)}\mathrm{e}^{-2\pi\mathrm{i}x\xi}\,\mathrm{d}x = \left[\mathrm{G}_\epsilon^{(3)}\mathrm{e}^{-2\pi\mathrm{i}x\xi}\right]_{x=-\infty}^{\infty} + 2\mathrm{i}\pi\xi\left[\mathrm{G}_\epsilon^{(2)}\mathrm{e}^{-2\pi\mathrm{i}x\xi}\right]_{x=-\infty}^{\infty} \\ &+ (2\mathrm{i}\pi\xi)^2\left[\mathrm{G}_\epsilon^{(1)}\mathrm{e}^{-2\pi\mathrm{i}x\xi}\right]_{x=-\infty}^{\infty} + (2\mathrm{i}\pi\xi)^3\left[\mathrm{G}_\epsilon\mathrm{e}^{-2\pi\mathrm{i}x\xi}\right]_{x=-\infty}^{\infty} + (2\mathrm{i}\pi\xi)^4\int_{-\infty}^{\infty}\mathrm{G}_\epsilon\mathrm{e}^{-2\pi\mathrm{i}x\xi}\,\mathrm{d}x.\end{aligned} \tag{2.A.8}$$

Since G_ϵ and its derivatives up to order three vanish for $|x| \to \infty$ and

$$\int_{-\infty}^{\infty} \delta(x-\check{x})\,\mathrm{e}^{-2\pi\mathrm{i}x\xi}\,\mathrm{d}x = \mathrm{e}^{-2\pi\mathrm{i}\check{x}\xi}, \tag{2.A.9}$$

applying the Fourier transform to Eqn. (2.A.6) gives

$$(2\pi\xi)^4\,\widehat{\mathrm{G}_\epsilon}(\xi;\check{x}) - \left[k(1+\mathrm{i}\epsilon)\right]^4\widehat{\mathrm{G}_\epsilon}(\xi;\check{x}) = \mathrm{e}^{-2\pi\mathrm{i}\check{x}\xi}. \tag{2.A.10}$$

Hence, the Fourier transform of the solution of Eqn. (2.A.6) is

$$\widehat{\mathrm{G}_\epsilon}(\xi;\check{x}) = \frac{\mathrm{e}^{-2\pi\mathrm{i}\check{x}\xi}}{16\pi^4\xi^4 - k^4(1+\mathrm{i}\epsilon)^4}. \tag{2.A.11}$$

To obtain the solution of Eqn. (2.A.6) in the original spatial domain, we have to apply the inverse Fourier transform, i.e.

$$\mathrm{G}_\epsilon(x;\check{x}) = \int_{-\infty}^{\infty}\widehat{\mathrm{G}_\epsilon}(\xi;\check{x})\mathrm{e}^{2\pi\mathrm{i}x\xi}\,\mathrm{d}\xi. \tag{2.A.12}$$

Using the inverse Fourier transform then gives

$$\mathrm{G}_\epsilon(x;\check{x}) = \int_{-\infty}^{\infty} \frac{\mathrm{e}^{2\pi\mathrm{i}(x-\check{x})\xi}}{16\pi^4\xi^4 - k^4(1+\mathrm{i}\epsilon)^4}\,\mathrm{d}\xi. \tag{2.A.13}$$

In order to calculate the integral in Eqn. (2.A.13), we have to deal with the four singularities of the integrand, namely

$$\xi_{1-4} = \begin{cases} \pm\frac{k(1+\mathrm{i}\epsilon)}{2\pi}\,, \\ \pm\mathrm{i}\frac{k(1+\mathrm{i}\epsilon)}{2\pi}\,, \end{cases} \tag{2.A.14}$$

and apply Cauchy's residue theorem, which evaluates integrals over closed curves. For this purpose, we find contours containing each two of the singularities for both cases, $x > \check{x}$ and $x < \check{x}$, respectively ($x = \check{x}$ is the trivial case).

For $x > \check{x}$, the two singularities, $\xi_1 = \frac{k(1+\mathrm{i}\epsilon)}{2\pi}$ and $\xi_3 = \mathrm{i}\frac{k(1+\mathrm{i}\epsilon)}{2\pi}$, lie within the integration contour $\mathcal{C}_+$, which includes the half-circle of radius $R \to \infty$ in the upper complex half-plane, i.e. $\mathrm{Im}(\xi) > 0$, which is closed by the real ξ-axis. The situation is depicted in the left-hand panel of Fig. 2.A.1.

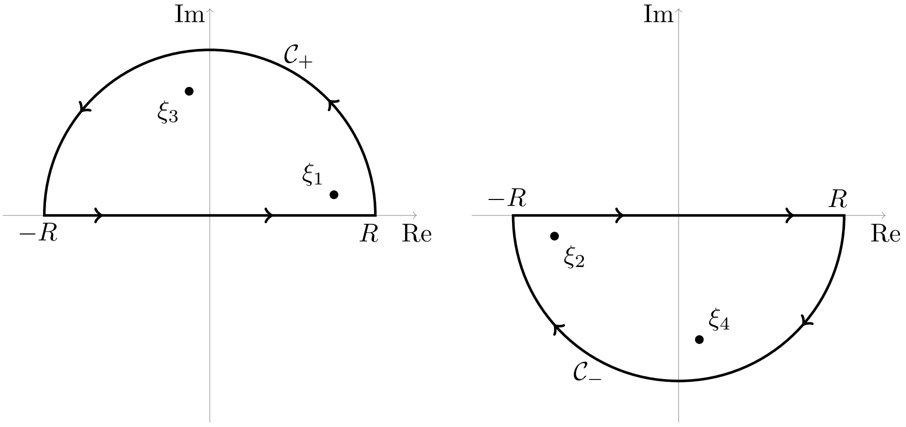

Figure 2.A.1: Left-hand panel: Integration contour $\mathcal{C}_+$ containing ξ_1 and ξ_3. Right-hand panel: Integration contour $\mathcal{C}_-$ containing ξ_2 and ξ_4.

Before we can make use of Cauchy's residue theorem to calculate the contour integral

$$\oint_{\mathcal{C}_+} f(\xi)\,\mathrm{d}\xi := \int_{\mathcal{C}_+} \frac{\mathrm{e}^{2\pi\mathrm{i}(x-\check{x})\xi}}{(2\pi)^4\left(\xi - \frac{k(1+\mathrm{i}\epsilon)}{2\pi}\right)\left(\xi + \frac{k(1+\mathrm{i}\epsilon)}{2\pi}\right)\left(\xi - \mathrm{i}\frac{k(1+\mathrm{i}\epsilon)}{2\pi}\right)\left(\xi + \mathrm{i}\frac{k(1+\mathrm{i}\epsilon)}{2\pi}\right)}\,\mathrm{d}\xi, \tag{2.A.15}$$

$f(\xi)$ is decomposed into its partial fractions, i.e.

$$f(\xi) = \frac{1}{8\pi k^3(1+\mathrm{i}\epsilon)^3}\mathrm{e}^{2\pi\mathrm{i}(x-\check{x})\xi}\left[\frac{1}{\xi - \frac{k(1+\mathrm{i}\epsilon)}{2\pi}} + \frac{-1}{\xi + \frac{k(1+\mathrm{i}\epsilon)}{2\pi}} + \frac{\mathrm{i}}{\xi - \mathrm{i}\frac{k(1+\mathrm{i}\epsilon)}{2\pi}} + \frac{-\mathrm{i}}{\xi + \mathrm{i}\frac{k(1+\mathrm{i}\epsilon)}{2\pi}}\right]. \tag{2.A.16}$$

The residues of $f(\xi)$ for the two singularities ξ_1 and ξ_3 are

$$\begin{aligned}\operatorname{Res}(f,\xi_1) &:= \operatorname{Res}_{\xi=\frac{k(1+\mathrm{i}\epsilon)}{2\pi}} f(\xi) = \frac{1}{8\pi k^3(1+\mathrm{i}\epsilon)^3}\mathrm{e}^{\mathrm{i}k(1+\mathrm{i}\epsilon)(x-\check{x})}\,,\\ \operatorname{Res}(f,\xi_3) &:= \operatorname{Res}_{\xi=\mathrm{i}\frac{k(1+\mathrm{i}\epsilon)}{2\pi}} f(\xi) = \frac{1}{8\pi k^3(1+\mathrm{i}\epsilon)^3}\mathrm{i}\mathrm{e}^{-k(1+\mathrm{i}\epsilon)(x-\check{x})}\,.\end{aligned}$$

Since $\mathcal{C}_+$ is a positively oriented simple closed contour, the winding number in Cauchy's residue theorem is unity, see e.g. Freitag and Busam 2009, and we obtain

$$\oint_{\mathcal{C}_+} f(\xi)\,\mathrm{d}\xi = 2\pi\mathrm{i}\sum_{k=1,3}\operatorname{Res}(f,\xi_k) = \frac{1}{4k^3(1+\mathrm{i}\epsilon)^3}\left[\mathrm{i}\mathrm{e}^{\mathrm{i}k(1+\mathrm{i}\epsilon)(x-\check{x})} - \mathrm{e}^{-k(1+\mathrm{i}\epsilon)(x-\check{x})}\right]\,. \tag{2.A.17}$$

To finally calculate the integral Eqn. (2.A.13) for $x > \check{x}$ over the real ξ-axis, the contour integral is split into the integral over the ξ-axis and the arc segment, i.e.

$$\lim_{R\to\infty}\int_{-R}^{R} f(\xi)\,\mathrm{d}\xi = \oint_{\mathcal{C}_+} f(\xi)\,\mathrm{d}\xi - \int_{\mathrm{arc}} f(\xi)\,\mathrm{d}\xi. \tag{2.A.18}$$

Using the monotony of the integral and the reverse triangle inequality, it can be shown that the arc-integral vanishes,

$$\begin{aligned}\left|\int_{\mathrm{arc}} f(\xi)\,\mathrm{d}\xi\right| &\le \int_{\mathrm{arc}} \frac{1}{|16\pi^4\xi^4 - k^4(1+\mathrm{i}\epsilon)^4|}\,\mathrm{d}\xi\\ &\le \int_{\mathrm{arc}} \frac{1}{16\pi^4|\xi^4| - k^4}\,\mathrm{d}\xi = \lim_{R\to\infty}\frac{\pi R}{16\pi^4 R^2 - k^4} = 0.\end{aligned} \tag{2.A.19}$$

This provides us with the solution of Eqn. (2.A.6) to the right of the point source $\check{x}$:

$$\mathrm{G}_\epsilon(x;\check{x}) = \frac{1}{4k^3(1+\mathrm{i}\epsilon)^3}\left[\mathrm{i}\mathrm{e}^{\mathrm{i}k(1+\mathrm{i}\epsilon)(x-\check{x})} - \mathrm{e}^{-k(1+\mathrm{i}\epsilon)(x-\check{x})}\right],\quad x > \check{x}. \tag{2.A.20}$$

For $x < \check{x}$, the integration contour $\mathcal{C}_-$ consists of the real ξ-axis closed by the half-circle of radius $R \to \infty$ in the lower complex half-plane, i.e. $\mathrm{Im}(\xi) < 0$, as we can see in the right-hand panel of Fig. 2.A.1. Hence, the contour $\mathcal{C}_-$ contains the two singularities $\xi_2 = -\frac{k(1+\mathrm{i}\epsilon)}{2\pi}$ and $\xi_4 = -\mathrm{i}\frac{k(1+\mathrm{i}\epsilon)}{2\pi}$. Calculating the residues of $f(\xi)$ for both singularities ξ_2 and ξ_4 gives

$$\begin{aligned}\operatorname{Res}(f,\xi_2) &:= \operatorname{Res}_{\xi=-\frac{k(1+\mathrm{i}\epsilon)}{2\pi}} f(\xi) = \frac{-1}{8\pi k^3(1+\mathrm{i}\epsilon)^3}\mathrm{e}^{-\mathrm{i}k(1+\mathrm{i}\epsilon)(x-\check{x})},\\ \operatorname{Res}(f,\xi_4) &:= \operatorname{Res}_{\xi=-\mathrm{i}\frac{k(1+\mathrm{i}\epsilon)}{2\pi}} f(\xi) = \frac{-\mathrm{i}}{8\pi k^3(1+\mathrm{i}\epsilon)^3}\mathrm{i}\mathrm{e}^{k(1+\mathrm{i}\epsilon)(x-\check{x})}.\end{aligned}$$

Because $\mathcal{C}_-$ is negatively oriented, the contour integral of f over $\mathcal{C}_-$ is the negative sum of the residues,

$$\oint_{\mathcal{C}_-} f(\xi)\,\mathrm{d}\xi = 2\pi\mathrm{i}\sum_{k=2,4}(-1)\mathrm{Res}(f,\xi_k) = \frac{1}{4k^3(1+\mathrm{i}\epsilon)^3}\left[\mathrm{i}\mathrm{e}^{-\mathrm{i}k(1+\mathrm{i}\epsilon)(x-\check{x})} - \mathrm{e}^{k(1+\mathrm{i}\epsilon)(x-\check{x})}\right]. \tag{2.A.21}$$

To obtain the solution of the integral Eqn. (2.A.13) as well for $x < \check{x}$, the integral over the contour $\mathcal{C}_-$ is also split into the integral over the real ξ-axis and an arc-segment as it is done in Eqn. (2.A.18) with $\mathcal{C}_+$ replaced by $\mathcal{C}_-$ and using the corresponding arc-integral.

With the same arguments as before, it can be shown that the integral along the lower arc-segment vanishes such that the lower contour integral calculated with Cauchy's residue theorem already gives the solution of Eqn. (2.A.6) for $x < \check{x}$,

$$\mathrm{G}_\epsilon(x;\check{x}) = \frac{1}{4k^3(1+\mathrm{i}\epsilon)^3}\left[\mathrm{i}\mathrm{e}^{-\mathrm{i}k(1+\mathrm{i}\epsilon)(x-\check{x})} - \mathrm{e}^{k(1+\mathrm{i}\epsilon)(x-\check{x})}\right], \quad x < \check{x}. \tag{2.A.22}$$

Taking the limits $\epsilon \to 0$ of G_ϵ in both cases, $x > \check{x}$ and $x < \check{x}$, provides us with the unique limit

$$\mathrm{G}(x;\check{x}) = \frac{1}{4k^3}\left[\mathrm{i}\mathrm{e}^{\mathrm{i}k|x-\check{x}|} - \mathrm{e}^{-k|x-\check{x}|}\right], \tag{2.A.23}$$

which is the unique solution of Eqn. (2.A.5). Fig. 2.A.2 shows the Green's function and its derivatives up to order three, which contains the discontinuity at the source point $\check{x} = 0$ in its real part, for the constant wavenumber k scaled to unity.

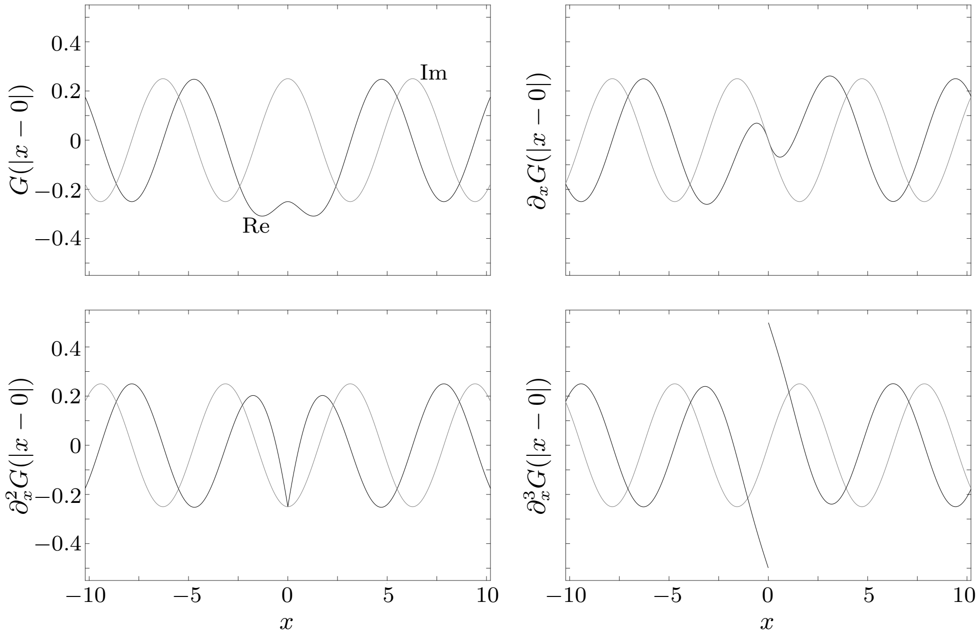

Figure 2.A.2: Green's function (top-left panel), its first (top-right panel), second (bottom-left panel) and third derivative (bottom-right panel) for homogeneous beam equation with point load at source point $\check{x} = 0$, for k scaled to unity

2.B Discretisation schemes for beam rigidity in step approximation

We summarise the different discretisation variants, which we consider to incorporate the beam rigidity and its slope into the continuity conditions to obtain the scattering matrix at each scattering interface, here. In the first discretisation variant (I), the beam rigidity is evaluated at the mid-point of each sub-interval, which is consistent with the calculation of the wavenumber, and set to be constantly this value in the respective sub-interval, and the rigidity slope is neglected because of the piece-wise constant rigidity profile.

Variant I)
- point-wise evaluation of beam rigidity b
- neglecting beam rigidity slope $\partial_x b$

The discretisation variant I is schematically shown in Fig. 2.B.1 for the scattering interface at $x = x_m$. The depicted profile variation is exaggerated for the purpose of better visualisation. It is clear that the grid of sub-intervals is much finer when applying the step approximation.

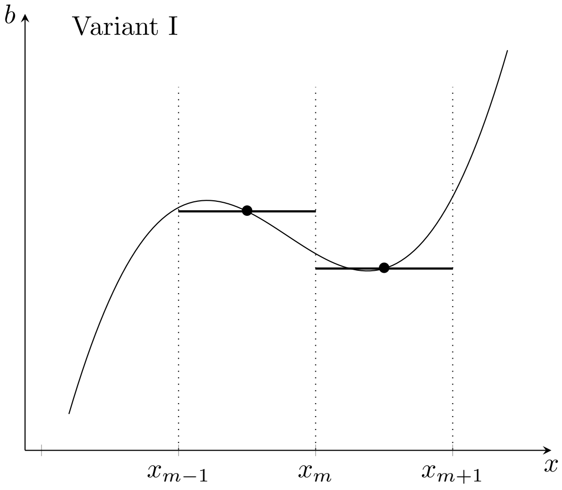

Figure 2.B.1: Scheme of discretisation variant I in step approximation

The discretisation variants II - V involve the evaluation or approximation of the rigidity slope and are outlined briefly in following and shown schematically in Fig. 2.B.2.

Variant II)

- point-wise evaluation of beam rigidity b
- point-wise evaluation of beam rigidity slope $\partial_x b$

Variant III)

- point-wise evaluation of beam rigidity b
- approximation of beam rigidity slope $\partial_x b$ by difference quotient

Variant IV)

- approximation of beam rigidity b by spline interpolation
- point-wise evaluation of beam rigidity slope $\partial_x b$

Variant V)

- approximation of beam rigidity b by spline interpolation
- approximation of beam rigidity slope $\partial_x b$ by spline slope

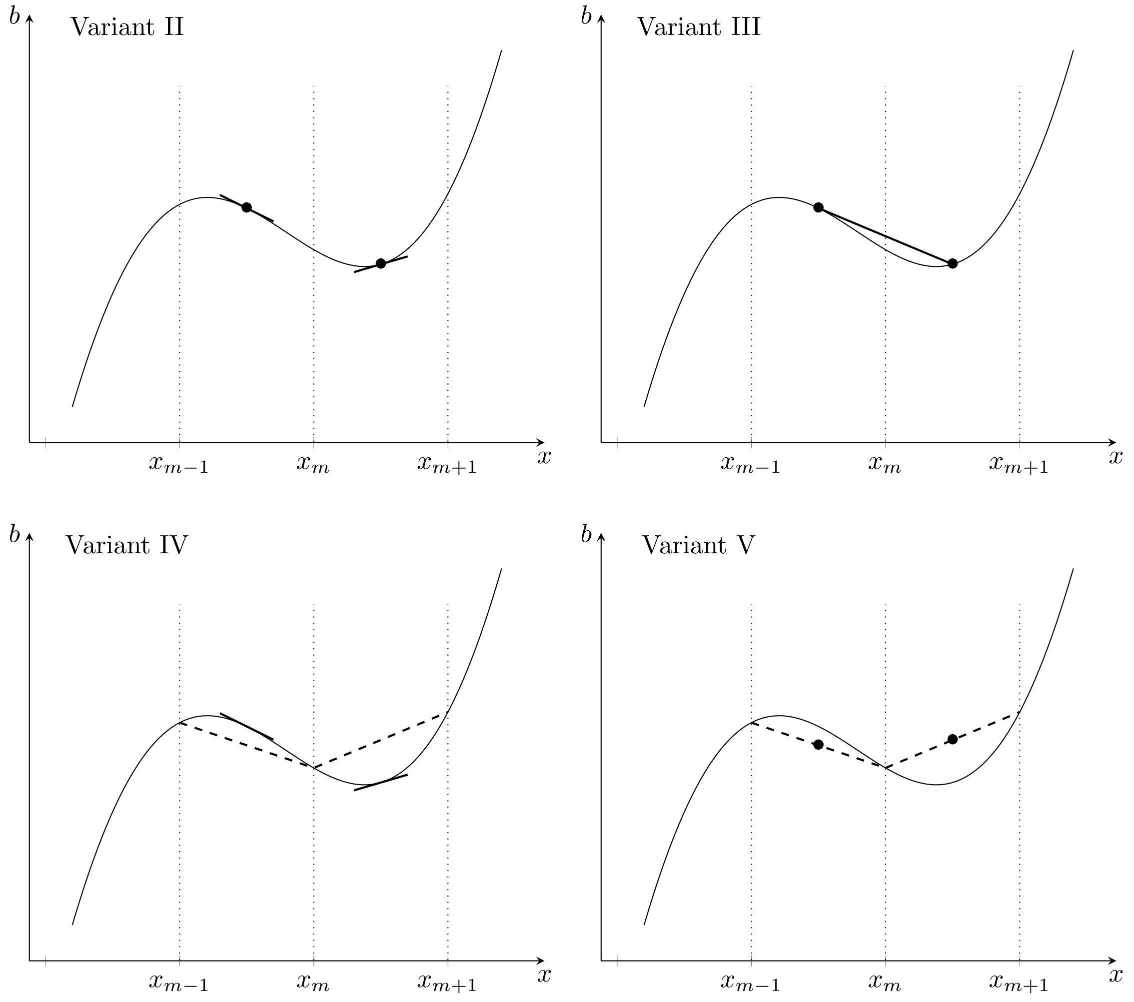

Figure 2.B.2: Scheme of discretisation variants II-V in step approximation (from top-left to bottom-right panel)

CHAPTER 3

Wave attenuation along a rough floating thin-elastic plate

In the previous chapter, we have successfully validated a multiple-scale approach describing the propagation of effective wave fields along rough beams in vacuo. The multiple-scale approach yields a computationally efficient way to obtain the scattering characteristics for long structures with continuous roughness profiles. A field of application of this approach are water waves, which are attenuated by very long, floating rough structures. An important example of this is the attenuation of ocean waves along very long ice floes in the marginal ice zone.

Under the assumption that the water is an incompressible, inviscid fluid and its flow is irrotational, we can use linear water wave theory. Due to the dimensionality of this problem, numerical calculations are hard to perform and computationally very expensive to obtain the attenuation behaviour of water waves along long, rough floating structures, and our goal is to find an efficient approach describing the water wave propagation. Hence, we want to find an analytical (or semi-analytical) solution method, which leads us to a multiple-scale method based on the respective method for the beam in vacuo. Since large ice floes are highly flexible and their thickness is much smaller than their horizontal extent and the wavelengths of the incident waves, we can model them as elastic plates, see e.g. Meylan 2002. In contrast to small ice floes in the marginal ice zone close to the open ocean, which should be modelled as rigid plates, see Masson and LeBlond 1989, and ice floes of the size of the incoming wave, which should be modelled as finite and flexible plates, we focus on ice floes, which are much larger than the wavelengths of the incoming waves, and hence can be modelled as infinite and flexible plates, see Fox and Squire 1994. With their small thickness and provided that the wave length is not too short, it is not limiting to neglect their submergence for this preliminary study, since the additional value of the much more complex models is limited, see e.g. Vaughan and Squire 2008 and Williams and Squire 2008. This is a study on a large scale, complementing the existing models of linear wave scattering by ice floes and the extensive literature for interactions of ocean waves with sea ice on a local scale, which has been studied extensively in the last two decades, see for an overview e.g. Squire 2010.

Before we introduce the multiple-scale method for the present problem, we derive the governing system of equations in Sec. 3.1 and describe the numerical method in Sec. 3.2, which will be used to validate the multiple-scale method. The numerical method is an extension to the step-approximation method from Sec. 2.2. After a preliminary wave field analysis in Sec. 3.3, we derive the multiple-scale method in Sec. 3.4 and finally validate the multiple-scale method with the numerical method in Sec. 3.5.

3.1 Problem formulation

We extend the in-vacuo beam model from Sec. 3.1. An infinitely long thin plate shall be floating on water of finite depth H. Since the plate is assumed to have uniform geometry along the horizontal y-axis and waves are travelling along the (horizontal) x-axis only, we consider a two-dimensional model, where the coordinate x allows us to describe the Euler–Bernoulli plate of negligible submergence, which lies flat on water. The vertical z-axis is orientated upwards and its origin coincides with the position of the plate at rest ($z = 0$). In the following, we briefly derive the system of partial differential equations (PDEs), which describes the propagation of water waves along a rough Euler–Bernoulli plate floating on water of finite and constant depth H, in analogy to Wang 2004.

The equation of continuity for inviscid, incompressible fluids yields non-divergence for the velocity field $\mathbf{u}$, i.e.

$$\nabla \cdot \mathbf{u} = 0, \tag{3.1}$$

and the simplified equation of moment conservation,

$$\frac{\partial \mathbf{u}}{\partial t} + \mathbf{u}\,\nabla \mathbf{u} = -\frac{1}{\rho_w}\nabla p + \mathbf{g}_{\mathrm{acc}}, \tag{3.2}$$

where ρ_w denotes the water density, p the water pressure and $\mathbf{g}_{\mathrm{acc}}$ the gravitational field. The gradient operates on the spatial variables only, i.e. $\nabla = (\partial_x, \partial_z)^{\mathrm{T}}$. Eqns. (3.1) and (3.2) are also known as Navier–Stokes equations for incompressible fluids and form a PDE system for incompressible fluxes with unknowns $\mathbf{u}$ (velocity field) and p (pressure). Under the assumption that the water motion is irrotational, the velocity field can be expressed as the gradient of the velocity potential $\varPhi$,

$$\mathbf{u} = \nabla \varPhi. \tag{3.3}$$

Therefore, the (time-dependent) velocity potential of the water, $\varPhi(x,z,t)$, fulfils the Laplace equation in the water domain,

$$\varDelta \varPhi(x,z,t) = 0, \tag{3.4}$$

where the Laplace operator is $\varDelta = \partial_x^2 + \partial_z^2$. Eqn. (3.4) describes the water motion in the water domain.

At the sea-floor, the vertical component of the flow velocity has to vanish, i.e. the normal derivative of the velocity potential has to be zero, which gives the boundary condition on the sea-floor (for finite water depth),

$$\frac{\partial}{\partial z}\mathit{\Phi}(x, -H, t) = 0. \tag{3.5}$$

To couple the water motion with the elastic plate, which lies on its surface, we derive the dynamic boundary condition describing the interaction between the water domain and the plate in analogy to Billingham and King 2001. Using the identity

$$\mathbf{u} \times (\nabla \times \mathbf{u}) = \nabla\left(\frac{1}{2}\mathbf{u} \cdot \mathbf{u}\right) - \mathbf{u} \cdot \nabla \mathbf{u}, \tag{3.6}$$

where $\cdot$ denotes the inner product, and under the assumption that the flux is irrotational, i.e. $\nabla \times \mathbf{u} = 0$, we can write the consecutive acceleration as

$$\mathbf{u} \cdot \nabla \mathbf{u} = \nabla\left(\frac{1}{2}\nabla\mathit{\Phi} \cdot \nabla\mathit{\Phi}\right). \tag{3.7}$$

The consecutive acceleration is the part of the substantial acceleration,

$$\underbrace{\frac{D\mathbf{u}}{Dt}}_{\substack{\text{substantial}\\ \text{acceleration}}} := \underbrace{\frac{\partial \mathbf{u}}{\partial t}}_{\substack{\text{local}\\ \text{acceleration}}} + \underbrace{\mathbf{u} \cdot \nabla \mathbf{u}}_{\substack{\text{convective}\\ \text{acceleration}}}, \tag{3.8}$$

which arises through location change of the particles, since location change from one location to another one in the flow field modifies the velocity. In Eqn. (3.8), $\frac{D}{Dt}$ is the Stokes derivative, which describes the location change of a particle with time as it flows along its trajectory, see e.g. Batchelor 2000. The local acceleration occurs due to the temporal change of the velocity at a fixed location, see Kümmel 2007. Since the gravitational field acts in negative z-direction, we can express it with the help of the acceleration due to gravity, g_{acc}, as

$$\mathbf{g}_{\text{acc}} = \nabla(-g_{\text{acc}} z) \tag{3.9}$$

and we can rewrite Eqn. (3.9) as

$$\mathbf{g}_{\text{acc}} = -\nabla(g_{\text{acc}}\mathcal{U}), \tag{3.10}$$

where $\mathcal{U}(x,t)$ is the deflection of the water surface in z-direction. These considerations allow us to express Eqn. (3.2) as

$$\frac{\partial}{\partial t}(\nabla\mathit{\Phi}) + \nabla\left(\frac{1}{2}\nabla\mathit{\Phi} \cdot \nabla\mathit{\Phi}\right) = -\frac{1}{\rho_w}\nabla p - \nabla(g_{\text{acc}}\mathcal{U}). \tag{3.11}$$

Under the assumption of a sufficiently smooth velocity potential $\mathit{\Phi}$, we obtain

$$\nabla\left(\frac{\partial\mathit{\Phi}}{\partial t} + \frac{1}{2}\nabla\mathit{\Phi} \cdot \nabla\mathit{\Phi} + \frac{p}{\rho_w} + g_{\text{acc}}\mathcal{U}\right) = \mathbf{0}. \tag{3.12}$$

Since the gradient only depends on the spatial variables, we have

$$\frac{\partial \varPhi}{\partial t} + \frac{1}{2}\nabla \varPhi \cdot \nabla \varPhi + \frac{p}{\rho_w} + g_{\mathrm{acc}}\mathcal{U} = C(t) \tag{3.13}$$

for a non-specified function $C(t)$. Due to the transformation

$$\varPhi \mapsto \varPhi + \int_0^t C(s)\,\mathrm{d}s, \tag{3.14}$$

we can set $C(t) = 0$ without influencing the velocity field. Finally, we obtain the Bernoulli equation,

$$\frac{\partial \varPhi}{\partial t} + \frac{1}{2}\nabla \varPhi \cdot \nabla \varPhi + \frac{p}{\rho_w} + g_{\mathrm{acc}}\mathcal{U} = 0. \tag{3.15}$$

Under the assumption of linear wave motion, the Bernoulli Eqn. (3.15) can be linearised by neglecting the non-linear term $\frac{1}{2}\nabla \varPhi \cdot \nabla \varPhi$,

$$-\rho_w \left(\frac{\partial}{\partial t}\varPhi(x{,}0{,}t) + g_{\mathrm{acc}}\mathcal{U}(x{,}t) \right) = p(x{,}t), \tag{3.16}$$

The linearised Bernoulli Eqn. (3.16) is the dynamic boundary condition between the water surface and the floating plate.

We also have to take into account that each particle, which is located at the water surface at an arbitrary time, never leaves the water surface, see Sarpkaya and Isaacson 1981. This is described with the following equation, see e.g. Billingham and King 2001,

$$\frac{D}{Dt}\left(z - \mathcal{U}(x{,}t)\right) = \frac{\partial}{\partial t}\left(z - \mathcal{U}(x{,}t)\right) + \mathbf{u} \cdot \nabla \left(z - \mathcal{U}(x{,}t)\right) = 0. \tag{3.17}$$

To derive the kinematic boundary condition between the water surface and the floating plate, we rewrite Eqn.(3.17) as

$$\begin{aligned} -\frac{\partial \mathcal{U}}{\partial t} + \mathbf{u} \cdot \nabla (z - \mathcal{U}) &= -\frac{\partial \mathcal{U}}{\partial t} + \nabla \varPhi \cdot (\nabla z - \nabla \mathcal{U}) = \\ &= -\frac{\partial \mathcal{U}}{\partial t} + \begin{pmatrix} \frac{\partial \varPhi}{\partial x} \\ \frac{\partial \varPhi}{\partial z} \end{pmatrix} \cdot \left(\begin{pmatrix} 0 \\ 1 \end{pmatrix} - \begin{pmatrix} \frac{\partial \mathcal{U}}{\partial x} \\ 0 \end{pmatrix} \right) = -\frac{\partial \mathcal{U}}{\partial t} - \frac{\partial \varPhi}{\partial x} \cdot \frac{\partial \mathcal{U}}{\partial x} + \frac{\partial \varPhi}{\partial z} = 0. \end{aligned} \tag{3.18}$$

Hence, the general kinematic boundary condition on the water surface is

$$\frac{\partial \varPhi}{\partial z} = \frac{\partial \mathcal{U}}{\partial t} + \frac{\partial \varPhi}{\partial x} \cdot \frac{\partial \mathcal{U}}{\partial x}. \tag{3.19}$$

Linearising Eqn. (3.19) yields the kinematic boundary condition on the water surface for our linear problem,

$$\frac{\partial \varPhi}{\partial z} = \frac{\partial \mathcal{U}}{\partial t} \qquad \text{on} \quad z = 0. \tag{3.20}$$

As mentioned above, the ice sheet shall be modelled as a thin, elastic plate of negligible submergence with varying material properties (plate mass, plate rigidity) or varying plate thickness along the x-axis. We assume that the plate is floating on top of the water at all times and is in contact with the water surface, hence the water surface and the plate are described with the same deflection $\mathcal{U}(x,t)$. The deflection is described in our setting with the slightly modified dynamic Euler–Bernoulli plate equation for a non-uniform plate,

$$\frac{\partial^2}{\partial x^2}\left(EI(x)\frac{\partial^2\mathcal{U}(x,t)}{\partial x^2}\right)+\rho h(x)\frac{\partial^2\mathcal{U}(x,t)}{\partial t^2}=p(x,t). \tag{3.21}$$

Eqn. (3.21) essentially agrees with the Euler-Bernoulli beam Eqn. (2.6), where the pressure p in Eqn. (3.21) corresponds to the external force f in Eqn. (2.6). However, to take the plate structure into account, the cross-sectional area of the beam, $A(x)$, is replaced by the plate thickness, h, only, and the width also disappears from the moment of inertia of the beam cross section, $I(x)$, which is given in Eqn. (2.120) for the beam in vacuo, but Poisson's ratio is included, see e.g. Landau and Lifshitz 1986. Poisson's ratio, denoted with ν, is a measure of transverse strain due to strain in the loaded direction and is characterised by the ratio of transverse strain to axial strain, see e.g. Boresi and Schmidt 2002. With this, the moment of inertia becomes

$$I(x)=\frac{h(x)^3}{12(1-\nu^2)}. \tag{3.22}$$

Note for the sake of completeness that in Eqn. (3.21) ρ is the mass density of the plate and E Young's modulus, which is a material constant for the linear, elastic deformation of the plate.

The plate Eqn. (3.21) can now be combined with the linearised dynamic boundary condition, Eqn. (3.16), by eliminating the pressure p. We obtain a coupled equation for the elevation of the water surface, covered with the plate,

$$\frac{\partial^2}{\partial x^2}\left(EI(x)\frac{\partial^2\mathcal{U}(x,t)}{\partial x^2}\right)+\rho h(x)\frac{\partial^2\mathcal{U}(x,t)}{\partial t^2}=-\rho_w\left(\frac{\partial\Phi}{\partial t}+g_{\mathrm{acc}}\mathcal{U}\right). \tag{3.23}$$

Note that external forces, such as the atmospheric pressure, are normalised to zero when coupling the Euler–Bernoulli plate equation and the linearised kinematic boundary condition. Taking the temporal derivative of Eqn. (3.23) and using the linearised kinematic boundary condition, Eqn. (3.20), we can write

$$\frac{\partial^2}{\partial x^2}\left(EI(x)\frac{\partial^2}{\partial x^2}\partial_z\Phi\right)+\rho h(x)\frac{\partial^2}{\partial t^2}\partial_z\Phi=-\rho_w\left(\frac{\partial^2\Phi}{\partial t^2}+g_{\mathrm{acc}}\partial_z\Phi\right). \tag{3.24}$$

Collecting the governing equations, Eqn. (3.4) for the velocity potential of the water, Eqn. (3.5) for the no-impedance condition on the sea-bed and the coupled plate Eqn. (3.24), we obtain the following (time-dependent) PDE system for our problem of wave propagation along an elastic plate floating on water:

$$\varDelta\varPhi(x,z,t) = 0, \qquad -H < z < 0, \tag{3.25a}$$

$$\frac{\partial}{\partial z}\varPhi(x,-H,t) = 0, \qquad z = -H, \tag{3.25b}$$

$$\frac{\partial^2}{\partial x^2}\left(EI(x)\frac{\partial^2}{\partial x^2}\partial_z\varPhi\right) + \rho h(x)\frac{\partial^2}{\partial t^2}(\partial_z\varPhi) = -\rho_w\left(\frac{\partial^2\varPhi}{\partial t^2} + g_{\mathrm{acc}}\partial_z\varPhi\right), \qquad z = 0. \tag{3.25c}$$

The linear model allows us again to focus on incoming time-harmonic waves with angular frequency ω. Since the equations of motion are linear in our model, the plate deflection and velocity potential depend on the same single frequency. Hence, we can factor out the time-dependency via $\mathrm{e}^{-\mathrm{i}\omega t}$ and the (complex-valued) spatial parts of the plate deflection, $\hat{u}(x)$, and velocity potential, $\hat{\phi}(x)$, fulfil

$$\mathfrak{U}(x,t) = \operatorname{Re}\left\{\hat{u}(x)\mathrm{e}^{-\mathrm{i}\omega t}\right\}, \tag{3.26a}$$

$$\varPhi(x,t) = \operatorname{Re}\left\{\hat{\phi}(x)\mathrm{e}^{-\mathrm{i}\omega t}\right\}. \tag{3.26b}$$

For consistency with the in-vacuo beam problem in Ch. 2, we take up the notation from Eqn. (2.7) and refer to the mass per unit length, $\rho h(x)$, as the plate mass, denoted with $\hat{g}(x)$, and $EI(x)$ as the plate rigidity, denoted with $\hat{b}(x)$, i.e.

$$\hat{g}(x) := \rho h(x), \tag{3.27a}$$

$$\hat{b}(x) := EI(x). \tag{3.27b}$$

Hence, the time-harmonic velocity potential, $\hat{\phi}$, satisfies the following (time-independent) PDE system for our problem of wave propagation along an elastic plate floating on water:

$$\varDelta\hat{\phi}(x,z) = 0, \qquad -H < z < 0, \tag{3.28a}$$

$$\frac{\partial}{\partial z}\hat{\phi}(x,-H) = 0, \qquad z = -H, \tag{3.28b}$$

$$\left(\frac{\partial^2}{\partial x^2}\left(\hat{b}(x)\frac{\partial^2}{\partial x^2}\right) - \alpha\hat{g}(x) + \rho_w g_{\mathrm{acc}}\right)\partial_z\hat{\phi} = \alpha\rho_w\hat{\phi}, \qquad z = 0, \tag{3.28c}$$

where $\alpha = \omega^2/g_{\mathrm{acc}}$ is the angular frequency squared over the acceleration due to gravity. For the sake of simplicity, we can transform this system in a similar way to Meylan and Squire 1996. We scale the following variables,

$$t \mapsto \sqrt{g_{\mathrm{acc}}}\,t\ ,\ \phi = \frac{\hat{\phi}}{\sqrt{g_{\mathrm{acc}}}}\ ,\ g = \frac{\hat{g}}{\rho_w}\ ,\ b = \frac{\hat{b}}{g_{\mathrm{acc}}\rho_w}, \tag{3.29}$$

and thereby, we obtain the PDE system (3.28) in a simplified form,

$$\Delta\phi(x,z) = 0, \qquad -H < z < 0, \tag{3.30a}$$

$$\frac{\partial}{\partial z}\phi(x,-H) = 0, \qquad z = -H, \tag{3.30b}$$

$$\left(\frac{\partial^2}{\partial x^2}\left(b(x)\frac{\partial^2}{\partial x^2}\right) - \alpha g(x) + 1\right)\partial_z\phi = \alpha\phi, \qquad z = 0, \tag{3.30c}$$

The model of our problem of wave propagation along a elastic plate floating on water is shown schematically in Fig. 3.1.

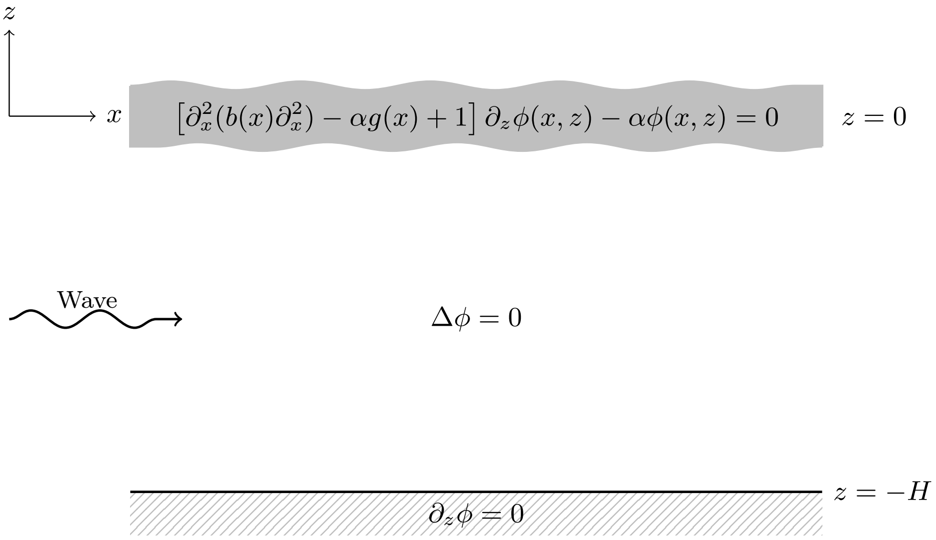

Figure 3.1: Two-dimensional model of water-wave propagation along rough Euler–Bernoulli plate floating on water of finite depth H

Using the representation of the spatial plate deflection and velocity potential, Eqns. (3.26), and the scaling of the (spatial) velocity potential, we can rewrite the linearised kinematic boundary condition, Eqn. (3.20), as

$$\partial_z\phi = -i\sqrt{\alpha}u, \quad z = 0. \tag{3.31}$$

This formulation is given e.g. by Meylan (2002). Note that the (spatial) plate deflection, u, is, unlike the velocity potential, not scaled by $\sqrt{g_{\text{acc}}}$, but the scaling is incorporated into $\omega/\sqrt{g_{\text{acc}}} = \sqrt{\alpha}$. In analogy to the in-vacuo beam setting, the Sommerfeld radiation condition is applied to all problem formulations in this chapter to ensure the well-definedness of the problem.

3.2 Numerical formulation

We want to solve the problem of wave propagation along a thin, elastic plate with continuously varying material properties or thickness profile. Before a multiple-scale method for these problems is presented in Sec. 3.4, we adopt a numerical method, which solves our problems for piecewise constant roughness profile. The numerical method represents a natural extension of the step-approximation method, which was introduced in Sec. 2.2 for the beam in vacuo. However, the numerical method to solve the present problem is much more expedient than the previous step-approximation method due to the additional vertical dimension and the coupling of the water and the floating plate, which results in a higher-order boundary condition. The numerical method was derived by Bennetts (2007) for finite and semi-infinite ice floes of uniform and piecewise uniform geometry. We apply it to our problem of wave propagation along very long floating plates and consider them to be infinite with continuously varying roughness profile over a long, finite interval $x \in (0, L)$. The continuous roughness profile of the plate is discretised similarly to the procedure in the step-approximation method into $M+1$ sub-intervals, with $(-\infty, 0)$ and (L, ∞) the 0th and $(M+1)$th sub-intervals, respectively. Based on the introduction of the step-approximation method, we briefly present the numerical method for the present problem. For details, we refer to Bennetts 2007.

We had derived the continuity conditions for the beam in vacuo, Eqns. (2.15) (continuity of deflection, deflection slope, bending moment and shear stress), which were used to couple the wave fields in adjacent sub-intervals, with the help of the weak formulation of the beam equation. To derive the continuity conditions for the present problem, the functional formulation of the problem was used in Bennetts 2007. The functional formulation was originally presented by Porter and Porter (2004) and a variational principle was applied for this purpose. The boundary terms in this formulation are integrated as jump conditions at internal boundaries of connected plate regions. Application of this ansatz on our two-dimensional problem with plates of negligible submergence yields the two essential conditions at each scattering interface $x = x_m$, $m = 0, 1, \ldots, M$, between adjacent sub-intervals,

$$\langle\langle u(x) \rangle\rangle_{x=x_m} = 0, \tag{3.32a}$$

$$\langle\langle \partial_x u(x) \rangle\rangle_{x=x_m} = 0. \tag{3.32b}$$

These continuity conditions imply continuity of the plate deflection and deflection slope, respectively. We also obtain the following natural conditions:

$$\langle\langle b(x)\partial_x^2 u(x) \rangle\rangle_{x=x_m} = 0, \tag{3.32c}$$

$$\langle\langle \partial_x \big(b(x)\partial_x^2 u(x)\big) \rangle\rangle_{x=x_m} = 0, \tag{3.32d}$$

$$\langle\langle \phi(x,z) \rangle\rangle_{z,x=x_m} = 0, \tag{3.32e}$$

$$\langle\langle \partial_x \phi(x,z) \rangle\rangle_{z,x=x_m} = 0. \tag{3.32f}$$

Additionally to the four already known continuity conditions from Eqns. (2.15) for the beam in vacuo, two more continuity conditions appear, continuity of the velocity potential of the fluid (Eqn. (3.32e)) and continuity of the fluid velocity (Eqn. (3.32f)). While the continuity conditions of deflection, deflection slope, bending moment and shear stress (Eqns. (3.32a)–(3.32d)) act at each scattering interface for $z = 0$, the continuity of the velocity and its potential must be satisfied across the whole scattering interfaces, $x = x_m$, $m = 0, 1, \ldots, M$, and $-H \leq z \leq 0$, which is denoted with $\langle\langle\cdot\rangle\rangle_{z,x=x_m}$. These continuity conditions are used to couple the wave fields in adjacent sub-intervals and provide the basis for the numerical method.

The full-linear solution, $\phi(x,z)$, which solves the the governing PDE system (3.30) for uniform geometry, can be written in the form

$$\phi(x,z) = \sum_{n=-2}^{\infty} \varphi_n(x)\, w_n(x,z), \tag{3.33}$$

where the functions φ_n, $n = -2, -1, \ldots$, are unknown and w_n, $n = -2, -1, \ldots$, are the vertical modes, which describe the depth dependency of the solution, see e.g. Evans and Porter 2003. Since the configuration of our problem is (piece-wise) uniform, the vertical dimension of the problem can be separated from the horizontal coordinate and we can write the full-linear solution as

$$\phi(x,z) = \sum_{n=-2}^{\infty} \varphi_n(x)\, w_n(z). \tag{3.34}$$

The separation of the horizontal and vertical dimension reduces the complexity greatly. The depth dependency via the vertical modes for intermediate water depths can be expressed as

$$w_n(z) = \cosh(k_n(z + H)), \tag{3.35}$$

where k_n, $n = -2, -1, \ldots$, are the roots of the dispersion relation for fluid coupled elastic plates of constant mass g and rigidity b,

$$k \tanh(kH) = \frac{\alpha}{bk^4 + 1 - \alpha g}. \tag{3.36}$$

The dispersion relation (3.36) has an infinite number of solutions, which are shown schematically in Fig. 3.2.

The solutions of the dispersion relation (3.36) have to be calculated numerically:

- The dispersion relation contains two real solutions with different signs, only. We denote the positive, real solution with k_0, which corresponds to the propagating wave mode. It can be found in the interval $(0, \max\{\alpha \coth(\alpha), \frac{\alpha}{H}, (\frac{\alpha g}{b})^{\frac{1}{4}}\})$.
- The dispersion relation also has four complex solutions with non-zero real part, which appear as positives and negatives of their complex conjugates, for most combinations of α, g, b, H. We denote the complex root in the left complex plane and positive imaginary part with k_{-1} and its negative complex conjugate with k_{-2}, i.e. $k_{-2} = -\overline{k}_{-1}$.

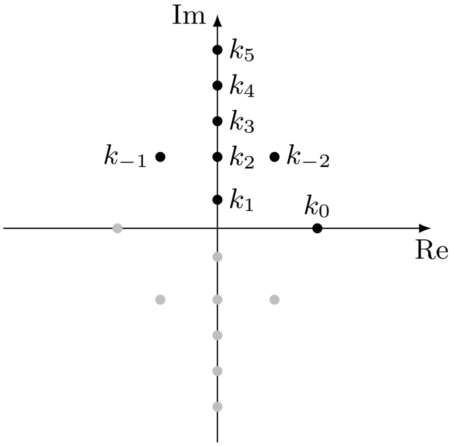

Figure 3.2: Schemata of roots of dispersion relation for elastic plates of constant mass and rigidity

They correspond to damped propagating wave modes, i.e. for waves which attenuate as they propagate, and it can be shown that $\mathrm{Im}(|k_{-n}|) > \mathrm{Re}(|k_{-n}|)$, $n = 1,2$. For details about parameter combinations to produce purely imaginary k_{-n}, $n = 1,2$, and the arising bifurcations, we refer to the analyses by Williams (2006) and Bennetts (2007).

- Moreover, the dispersion relation contains an infinite number of purely imaginary solutions, which appear as conjugate pairs. We denote the purely imaginary solutions with positive imaginary part with k_n, $n = 1, 2, \ldots$, ordered in ascending magnitude, $0 < -\mathrm{i}k_n < -\mathrm{i}k_{n+1}$. These purely imaginary roots correspond to evanescent wave modes and can be found in $\mathrm{i}(n - \frac{1}{2})\pi/H < k_n < \mathrm{i}n\pi/H$, see Fox and Squire 1994. In the case of purely imaginary k_{-n}, $n = 1,2$, these roots lie in the same interval.

It was shown in Bennetts 2007 that the set of modes (one propagating, two damped propagating, infinite number of evanescent modes) has a two-fold linear dependence. In analogy to this study, we eliminate the two complex roots k_{-n}, $n = 1,2$, from the set of vertical modes to avoid numerical difficulties. The unknowns φ_{-n}, $n = 1,2$, corresponding to the removed vertical modes are taken into account by redistributing them among the unknowns corresponding to the remaining vertical modes.

In the numerical method, we restrict the vertical motion to a finite-dimensional subspace, i.e. we only consider a finite number of vertical modes to approximate the full-linear solution,

$$\phi(x,z) \approx \phi_N(x,z) = \sum_{n=0}^{N} \varphi_n(x)\, w_n(z). \tag{3.37}$$

Note that the φ_n, $n = 0, \ldots, N$, in Eqn. (3.37) do not correspond to the respective quantities in Eqn. (3.34) due to the redistribution of the unknowns corresponding to the evanescent wave modes. The described method provides an approximation to the full-linear solution to arbitrary accuracy by including a sufficient number of vertical modes into Eqn. (3.37). However, a relatively small N already gives accurate results, which is vital for our solution procedure over the rough interval $(0,L)$ with a large number of scattering interfaces.

With the help of the variational principle, the governing PDE system (3.30) can be written as

$$\partial_x\left(\mathbf{F}\partial_x\mathbf{\Phi}_N\right)+\mathbf{D}\partial_x\mathbf{\Phi}_N+\mathbf{G}\mathbf{\Phi}_N+\alpha u\mathbf{C}\mathbf{f}=\mathbf{0}, \tag{3.38a}$$

$$\left(\partial_x^2(b\partial_x^2)-\alpha g+1\right)u-\sum_{n=0}^{N}w_n|_{z=0}\,\varphi_n=0, \tag{3.38b}$$

where $\mathbf{0}$ is a $(N+1)$-dimensional vector with zero entries,

$$\begin{aligned}
\mathbf{\Phi}_N&=\begin{pmatrix}\varphi_0 & \dots & \varphi_N\end{pmatrix}^{\mathrm{T}},\\
\mathbf{f}&=\begin{pmatrix}1 & \dots & 1\end{pmatrix}^{\mathrm{T}},\\
\mathbf{C}&=\operatorname{diag}\begin{pmatrix}w_0|_{z=0} & \dots & w_N|_{z=0}\end{pmatrix}=\operatorname{diag}\begin{pmatrix}\cosh(k_0H) & \dots & \cosh(k_NH)\end{pmatrix},\\
\mathbf{D}_{m,n}&=\int_{-H}^{0}\overline{w}_{m-1}(\partial_x,0)w_{n-1}-w_{n-1}(\partial_x,0)\overline{w}_{m-1}\,\mathrm{d}z,\\
\mathbf{F}_{m,n}&=\int_{-H}^{0}\overline{w}_{m-1}w_{n-1}\,\mathrm{d}z,\\
\mathbf{G}_{m,n}&=\int_{-H}^{0}\overline{w}_{m-1}\left(\partial_z^2w_{n-1}\right)\,\mathrm{d}z-\left[\overline{w}_{m-1}\left(\partial_zw_{n-1}\right)\right]_{z=-H}^{0}\\
&\quad+(\partial_x,0)\cdot\int_{-H}^{0}\overline{w}_{m-1}\left((\partial_x,0)w_{n-1}\right)\,\mathrm{d}z\\
&\quad-\int_{-H}^{0}\left((\partial_x,0)\overline{w}_{m-1}\right)\cdot\left((\partial_x,0)w_{n-1}\right)\,\mathrm{d}z,
\end{aligned} \tag{3.39}$$

for $m,n=1,\dots,N+1$, where the overbar denotes the complex conjugate of the quantity, a notation, which is not used after Eqn. (3.41) anymore. With the introduced notation, we can express the continuity conditions (3.32) as

$$\begin{aligned}
\langle\langle\mathbf{\Phi}_N\rangle\rangle&=0, & \langle\langle\mathbf{F}\partial_x\mathbf{\Phi}_N+\mathbf{J}\mathbf{\Phi}_N\rangle\rangle&=0,\\
\langle\langle\overline{\mathbf{F}}^{\mathrm{T}}\mathbf{\Phi}_N\rangle\rangle&=0, & \langle\langle\left(\partial_x\mathbf{\Phi}_N+\mathbf{F}^{-1}\mathbf{J}\mathbf{\Phi}_N\right)\rangle\rangle&=0,\\
\langle\langle b\partial_x^2u\rangle\rangle&=0, & \langle\langle\partial_x(\partial_x^2u)\rangle\rangle&=0,
\end{aligned} \tag{3.40}$$

where $\langle\langle\cdot\rangle\rangle$ again denotes the jump of the included quantity at the scattering interfaces and

$$\mathbf{J}_{m,n}=\int_{-H}^{0}-\overline{w}_{m-1}\partial_xw_{n-1}\,\mathrm{d}z \tag{3.41}$$

for $m,n=1,\dots,N+1$. We can clearly observe an essential feature of the solution procedure in the problem formulation (PDE system (3.38)): The vertical motion of the fluid is approximated by vertical averaging. This approach decouples the vertical from the horizontal motion of the fluid.

Since our discretisation procedure via the step approximation yields piecewise uniform geometry, the PDE system (3.38) becomes a system of ordinary differential equations with constant coefficients for each sub-interval, which is solved in the following analogously to Bennetts et al. 2007 with the eigenvalue method. By introducing the compact notation

$$\mathbf{\Psi}_N = \big(\mathbf{\Phi}_N{}^{\mathrm{T}} \quad u \quad b\partial_x^2 u\big)^{\mathrm{T}}, \tag{3.42}$$

we seek solutions of the form

$$\mathbf{\Psi}_N(x) = \hat{\mathbf{c}}(\lambda)\, \mathrm{e}^{\mathrm{i}\lambda x}. \tag{3.43}$$

The constant λ shall represent the eigenvalues and the constant vector, $\hat{\mathbf{c}}$,

$$\hat{\mathbf{c}}^{\mathrm{T}}(\lambda) = \big(\mathbf{c}^{\mathrm{T}}(\lambda) \quad \gamma^{(1)}(\lambda) \quad \gamma^{(2)}(\lambda)\big) \tag{3.44}$$

the corresponding eigenvectors of the system. Since $\mathbf{D}_{m,n} = 0$ for $m,n = 1, \ldots, N+1$ and $\mathbf{G}$ can be expressed via $\mathbf{F}$,

$$\mathbf{G}_{m,n} = \mathbf{F}_{m,n} k_n^2 - k_n \sinh(k_n H) \cosh(k_m H)$$

for intervals of uniform geometry, the PDE system (3.38) becomes the following eigenvalue problem

$$\Big(\mathbf{F}\left(\mathbf{K}^2 - \lambda^2 \mathbf{I}\right) - \mathbf{C}\,\mathbf{f}\,\mathbf{f}^{\mathrm{T}}\mathbf{K}\mathbf{S}\Big)\,\mathbf{c} + \alpha\gamma^{(1)}\mathbf{C}\mathbf{f} = \mathbf{0}, \tag{3.45a}$$

$$\left(b\lambda^4 - \alpha g + 1\right)\gamma^{(1)} - \mathbf{f}^{\mathrm{T}}\mathbf{C}\mathbf{c} = 0, \tag{3.45b}$$

where $\mathbf{I}$ is the $(N+1)$-dimensional identity matrix and

$$\mathbf{S} = \begin{pmatrix} \sinh(k_0 H) & & \\ & \ddots & \\ & & \sinh(k_N H) \end{pmatrix} \qquad \text{and} \qquad \mathbf{K} = \begin{pmatrix} k_0 & & \\ & \ddots & \\ & & k_N \end{pmatrix}.$$

To find the solution of the PDE system (3.38), we have to find the $2N + 6$ eigenvalues λ and the corresponding eigenvectors $\hat{\mathbf{c}}(\lambda)$ from the eigenvalue problem (3.45). Note that $\gamma^{(2)}$, which does not appear in the eigenvalue problem (3.45), can directly be retrieved from $\gamma^{(1)}$. With some algebraic manipulations, Eqn. (3.45a) provides $2N+2$ pairs of eigenvalues and eigenvectors $(\lambda_n, \hat{\mathbf{c}}(\lambda_n))$ with

$$(\lambda^2, \mathbf{c}) = (\lambda_n^2, \mathbf{I}_{n+1}) = (k_n^2, \mathbf{I}_{n+1}) \tag{3.46}$$

and

$$\gamma^{(1)}(\lambda_n) = \frac{k_n \sinh(k_n H)}{\alpha}$$

for $n = 0, \dots, N+1$. The remaining four eigenvalues are obtained from Eqn. (3.45b),

$$\lambda^2 = \lambda_{-n}^2 = k_{-n}^2 \tag{3.47}$$

for $n = 1{,}2$. The entries $\mathbf{c}$ from the corresponding eigenvectors can be calculated via

$$\mathbf{F}\mathbf{c} + b\,\gamma^{(1)}\left(\mathbf{K}^2 + \lambda^2\mathbf{I}\right)\mathbf{K}\mathbf{S}\mathbf{f} = \mathbf{0} \tag{3.48}$$

and $\gamma^{(1)}$ are set $\gamma^{(1)}(\lambda_{-n}) = 1$ for $n = 1{,}2$. Hence, the $2N+6$ pairs of eigenvalues and eigenvectors of the PDE system (3.38) are now given. The eigenvalues $\lambda_n = k_n$ with corresponding eigenvectors $\mathbf{I}_n$, $n = 0, \dots, N$, characterise the horizontal wave modes in the full-linear solution. The eigenvalue–eigenvector pairs $(\lambda_{-n} = k_{-n}, \mathbf{c}(\lambda_{-i}))$, $n = 1{,}2$, characterise the horizontal wave modes corresponding to the vertical wave modes, which were eliminated from the full-linear solution in Eqn. (3.34) and redistributed among the other vertical wave modes. In the numerical method, these two eigenvalue–eigenvector pairs try to offset the excluded vertical wave modes and as a consequence, they are adjusted, if the number of included vertical modes, $N+1$, is changed. For $N \to \infty$, the eigenvalues λ_{-n}, $n = 1{,}2$, converge to the exact horizontal wave modes corresponding to the eliminated vertical modes.

In each of the intervals with uniform geometry, the numerical method yields the approximated solution

$$\boldsymbol{\Psi}_N(x) = \mathcal{C}\left(\mathrm{e}^{\mathrm{i}\boldsymbol{\Lambda}x}\mathbf{A} + \mathrm{e}^{-\mathrm{i}\boldsymbol{\Lambda}x}\mathbf{B}\right), \tag{3.49}$$

where

$$\begin{aligned}
\boldsymbol{\Lambda} &= \operatorname{diag}\begin{pmatrix}\lambda_0 & \dots & \lambda_N & \lambda_{-1} & \lambda_{-2}\end{pmatrix},\\
\mathrm{e}^{\pm\mathrm{i}\boldsymbol{\Lambda}x} &= \operatorname{diag}\begin{pmatrix}\mathrm{e}^{\pm\mathrm{i}\lambda_0 x} & \dots & \mathrm{e}^{\pm\mathrm{i}\lambda_N x} & \mathrm{e}^{\pm\mathrm{i}\lambda_{-1} x} & \mathrm{e}^{\pm\mathrm{i}\lambda_{-2} x}\end{pmatrix},\\
\mathcal{C} &= \begin{pmatrix}\hat{\mathbf{c}}(\lambda_0) & \dots & \hat{\mathbf{c}}(\lambda_N) & \hat{\mathbf{c}}(\lambda_{-1}) & \hat{\mathbf{c}}(\lambda_{-}2)\end{pmatrix},
\end{aligned}$$

and $\mathbf{A}$ and $\mathbf{B}$ are the $(N+3)$-dimensional vectors containing the amplitudes of the left- and rightward going and evanescent waves, respectively. $\boldsymbol{\Lambda}$ and $\mathcal{C}$ depend on the (constant) plate properties and thickness in the respective interval.

To calculate the wave field and the plate deflection in the whole domain for our problem of a plate with varying material properties or thickness variations in the interval $(0,L)$, which is floating on water of intermediate depth, we extend the iterative algorithm for the beam in vacuo, which was presented in Sec. 2.2. Considering a single scattering interface at $x = 0$ only, we can write the approximations in the left interval, $\boldsymbol{\Psi}_N^{(0)}$, and the right interval, $\boldsymbol{\Psi}_N^{(1)}$, as

$$\boldsymbol{\Psi}_N^{(0)}(x) = \mathcal{C}^{(0)}\left(\mathrm{e}^{\mathrm{i}\boldsymbol{\Lambda}_{(0)}x}\mathbf{A}_0 + \mathrm{e}^{-\mathrm{i}\boldsymbol{\Lambda}_{(0)}x}\mathbf{B}_0\right), \quad x \le 0, \tag{3.50a}$$

$$\boldsymbol{\Psi}_N^{(1)}(x) = \mathcal{C}^{(1)}\left(\mathrm{e}^{\mathrm{i}\boldsymbol{\Lambda}_{(1)}x}\mathbf{A}_1 + \mathrm{e}^{-\mathrm{i}\boldsymbol{\Lambda}_{(1)}x}\mathbf{B}_1\right), \quad x \ge 0. \tag{3.50b}$$

Assuming we know the incoming wave amplitudes $\mathbf{A}_0$ (from the left) and $\mathbf{B}_1$ (from the right), we want to determine the (unknown) outgoing wave amplitudes $\mathbf{B}_0$ and $\mathbf{A}_1$.

In analogy to Sec. 2.2, we can calculate a scattering matrix $\mathbf{S}$ by employing the continuity conditions (3.40). The scattering matrix is now $(2N + 6) \times (2N + 6)$-dimensional and consists of the $(N + 3) \times (N + 3)$-dimensional (complex) matrices describing the full reflection and transmission behaviour for left- and right-going waves, i.e.

$$\mathbf{S} := \begin{pmatrix} \mathbf{R}_- & \mathbf{T}_+ \\ \mathbf{T}_- & \mathbf{R}_+ \end{pmatrix}. \tag{3.51}$$

The square matrices $\mathbf{R}_-$ and $\mathbf{T}_-$ characterise the reflection and transmission of an incident wave from the left, respectively, and $\mathbf{R}_+$ and $\mathbf{T}_+$ the corresponding quantities for an incident wave from the right. The scattering matrix $\mathbf{S}$ allows us to transcribe the amplitudes of the outgoing waves, $\mathbf{B}_0$ (left-going in the left interval) and $\mathbf{A}_1$ (right-going in the right interval), in terms of the amplitudes of the incoming waves, $\mathbf{A}_0$ (right-going in the left interval) and $\mathbf{B}_1$ (left-going in the right interval),

$$\begin{pmatrix} \mathbf{B}_0 \\ \mathbf{A}_1 \end{pmatrix} = \underbrace{\begin{pmatrix} \mathbf{R}_- & \mathbf{T}_+ \\ \mathbf{T}_- & \mathbf{R}_+ \end{pmatrix}}_{=\mathbf{S}} \begin{pmatrix} \mathbf{A}_0 \\ \mathbf{B}_1 \end{pmatrix}. \tag{3.52}$$

Analogously to the solution procedure for the beam in vacuo, we can derive the transfer matrix $\mathbf{P}$ for this problem with the help of the scattering matrix $\mathbf{S}$ and Eqn. (2.27), which allows us to write the waves to the right of the scattering interface in terms of the waves to the left of the scattering interface.

Illustratively speaking, to obtain $\mathbf{B}_0$ and $\mathbf{A}_1$ (with $2N + 6$ unknowns), we apply the four continuity conditions on the floating plate, continuity of plate deflection, continuity of deflection slope, continuity of bending moment and continuity of shear stress, which reduces the degrees of freedom to $2N + 2$. To get the remaining $2N + 2$ unknowns, continuity of the fluid velocity potential and the fluid velocity are applied in a weak sense with the vertical modes as test functions. As mentioned above, two modes are linearly dependent, hence the space of trial functions is $N + 1$ and we have a unique solution for $\mathbf{B}_0$ and $\mathbf{A}_1$.

For the well-definedness of the problem, the Sommerfeld radiation condition has to be satisfied. This is ensured by the solution $\mathbf{\Psi}_N$, which yields in the far-fields

$$\phi_N(x,z) \sim \begin{cases} \left(a_0^{(0)} \mathrm{e}^{\mathrm{i}k_0^{(0)}x} + b_0^{(0)} \mathrm{e}^{-\mathrm{i}k_0^{(0)}x}\right) \cosh(k_0^{(0)}(z+H)), & x \to -\infty, \\ \left(a_1^{(0)} \mathrm{e}^{\mathrm{i}k_0^{(1)}x} + b_1^{(0)} \mathrm{e}^{-\mathrm{i}k_0^{(1)}x}\right) \cosh(k_0^{(1)}(z+H)), & x \to \infty, \end{cases} \tag{3.53}$$

where $k_0^{(0)}$ and $k_0^{(1)}$ are the propagating wave modes in the left and right interval, respectively, and $a_0^{(0)}$ and $b_0^{(0)}$ are the amplitudes of the corresponding right- and left-travelling waves in the left interval and $a_1^{(0)}$ and $b_1^{(0)}$ in the right interval.

To calculate the wave field in the whole domain for a floating plate with continuous roughness variations, which are discretised by the step approximation over $(0,L)$, we use the iterative algorithm, which was presented in Sec. 2.2 for the beam in vacuo. For this, we proceed to the problem involving the $M+1$ scattering interfaces, located at x_m, $m = 0, 1, \ldots, M$. We denote the approximated solutions in the mth and $(m+1)$th intervals, which meet at the $(m+1)$th scattering interface (located at x_m), as $\mathbf{\Psi}_N^{(m)}$ and $\mathbf{\Psi}_N^{(m+1)}$, respectively. By application of the continuity conditions (3.40) at each scattering interface, we obtain the scattering and transfer matrices, $\mathbf{S}_m$ and $\mathbf{P}_m$, $m = 0, 1, \ldots, M$, relating the left- and right-going waves at the $(m+1)$th scattering interface.

With the help of the diagonal matrix $\mathrm{e}^{\mathrm{i}\mathbf{\Lambda}x}$ appearing in Eqn. (3.49), we can express the amplitudes corresponding to the left of the $(m+1)$th scattering interface, $\mathbf{A}_{m+1}^-$ and $\mathbf{B}_{m+1}^-$, in terms of those right of the mth scattering interface, $\mathbf{A}_m^+$ and $\mathbf{B}_m^+$, via

$$\mathbf{A}_{m+1}^- = \mathrm{e}^{\mathrm{i}\mathbf{\Lambda}_{m+1} l_{m+1}} \mathbf{A}_m^+, \tag{3.54a}$$

$$\mathbf{B}_{m+1}^- = \mathrm{e}^{-\mathrm{i}\mathbf{\Lambda}_{m+1} l_{m+1}} \mathbf{B}_m^+ \tag{3.54b}$$

for $m = 0, 1, \ldots, M$, where l_{m+1} in the diagonal phase-change matrices $\mathrm{e}^{\pm\mathrm{i}\mathbf{\Lambda}_{m+1} l_{m+1}}$ is the distance between adjacent scattering interfaces, $l_m = x_m - x_{m-1}$. Hence, we can use the same iterative procedure described in Sec. 2.2 to merge scattering matrices (numerical more stable than merging transfer matrices), relate the wave fields in the pth and qth sub-interval $(0 \leq p < q \leq M)$ with $\mathbf{S}_{p,q}$, apply the iteration from left-to-right as well as from right-to-left with the result that we finally obtain the wave amplitudes and thus the wave field in each of the sub-intervals by Eqns. (2.44). Altogether, the iterative algorithm also allows us to calculate the wave propagation along a floating plate with continuous roughness profile over the whole domain $(-\infty,\infty)$.

3.3 Preliminary attenuation analysis

Before we introduce the multiple-scale method for the floating plate problem in Sec. 3.4, we calculate individual and effective wave fields first and compare them. To obtain wave fields for individual roughness realisations of the plate thickness or properties (plate mass, plate rigidity), we use the step-approximation method to approximate the continuous roughness profile with piece-wise constant functions. The uniform plate geometry on these sub-intervals allows us to use the numerical method to calculate the fluid potential and the plate deflection, which is indirectly approximated by the fluid potential, over the whole domain. Note that the plate shall extend to infinity in both horizontal directions on the x-axis again and be uniform in the y-direction. For the numerical method based on the step approximation, the plate roughness shall extend over the long, finite interval $(0,L)$. To obtain the effective wave field, we use the random sampling from Ch. 2, i.e. the effective wave field is calculated as the mean wave field with respect to a large ensemble of randomly generated realisations, which share the same average roughness characteristics (roughness amplitude, ϵ, and correlation length, l_{G}). We use the same Gaussian autocorrelated random processes as in Ch. 2 to describe the plate roughness. The roughness profiles are generated with Eqn. (2.76), which ensures that an ensemble of roughness profiles fulfils the Gaussian autocorrelation condition (Eqn. (2.75)). For the results provided by the numerical method in this chapter, the step approximation divides each correlation length in the rough interval $(0,L)$ into four sub-intervals, which is an accurate resolution for this problem. The beam deflections, u, which can be obtained via Eqn. (3.31) as

$$u = \mathrm{i}\phi/\sqrt{\alpha}, \quad -\infty < x < \infty,\, z = 0, \tag{3.55}$$

are calculated for large ensembles containing 1500 samples (ensemble size analogously to the in-vacuo beam problem) of randomly generated plate realisations. For the sake of simplicity, we denote the numerical method based on step approximation and random sampling as random-sampling method only.

Fig. 3.3 shows the moduli of example individual plate deflections over $(0,L)$ and corresponding effective plate deflections, for roughness amplitude $\epsilon = 5.0 \times 10^{-2}$ and non-dimensional correlation lengths $\bar{k}l_{\mathrm{G}} = 0.9$ (left-hand panel) and 4.1 (right-hand panel) for the varying thickness problem. For computations, the number of modes in the numerical method has to be truncated. It is shown by Bennetts (2007) that a small number of modes provides accurate results in the numerical method. We choose $N = 1$, for which it is ensured numerically to yield accurate results in our problem formulation. The amplitude of the monochromatic incident (right-travelling) wave is chosen now and in the following to give unit plate deflection at $x = 0$, and the plate's thickness shall be $h = 1.0\,\mathrm{m}$. The Young's modulus is chosen to be $E = 6.4\,\mathrm{GPa} = 6.4 \times 10^9\,\mathrm{N/m^2}$ and we set Poisson's ratio as $\nu = 0.3$, which are generic values for sea ice, see Timco and Weeks 2010. According to Lüthi 2012, the water density is $\rho_w = 999.84\,\mathrm{kg/m^3}$ (for 0°C) and the density of the ice $\rho = 917\,\mathrm{kg/m^3}$. The acceleration due to gravity is set $g_{\mathrm{acc}} = 9.81\,\mathrm{m/s^2}$. However, the physical properties of sea-ice in the marginal ice zone is more complex, but for the purpose of this theoretical study, we work with these common quantities for the remainder of this chapter.

We can observe in Fig. 3.3 that for the smaller correlation length, $\bar{k}l_{\mathrm{G}} = 0.9$, the example individual wave field attenuates. However, the individual wave field attenuates weakly only and significantly less than the corresponding effective wave field. For the larger correlation length, $\bar{k}l_{\mathrm{G}} = 4.1$, strong attenuation of the effective wave field can be noticed and we can deduce that this is caused by the same effects as for the beam in vacuo. In the following, the attenuation coefficients describing the exponential decay of individual and effective wave fields are extracted via the same least-squares minimisation routine as for the in-vacuo beam problem and Eqns. (2.77b) and (2.77a), respectively.

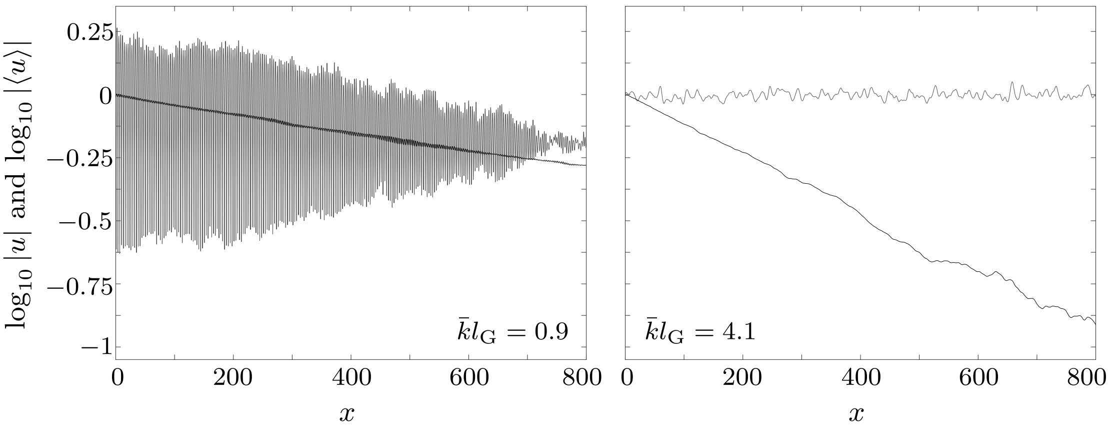

Figure 3.3: Example individual plate deflections (grey curves) and effective plate deflections (black) for varying thickness problem, for roughness amplitude $\epsilon = 5.0 \times 10^{-2}$ and non-dimensional correlation lengths $\bar{k}l_G = 0.9$ (left-hand panel) and $\bar{k}l_G = 4.1$ (right-hand panel)

3.4 Multiple-scale method

We present a semi-analytical approach to describe the attenuation of the effective wave fields with low computational expense now. Following the approach for the in-vacuo beam problem, we develop a multiple-scale method for the problem of a floating plate with continuous roughness variations, which are modelled again by the the Gaussian autocorrelated random process. We noticed for the in-vacuo beam setting that the varying thickness problem contains the varying mass and varying rigidity problem. Hence, we determine the multiple-scale method for the problem of a floating plate with continuous thickness variations. This allows us to derive the multiple-scale methods for the varying mass and varying rigidity problems, respectively, without difficulty. The multiple-scale method is based on the work of Bennetts and Peter (2012), who conducted a preliminary investigation of wave attenuation in the ice-covered ocean due to ice roughness, and was published by Rupprecht (2013), who took up this preliminary investigation and described the approach in the following form.

As mentioned above, we derive the multiple-scale method for the floating plate with Gaussian autocorrelated thickness variations. The varying thickness leads to variations in both the plate mass and rigidity, and the velocity potential of the water is described for this problem via the PDE system (3.30). Once the solution is obtained, the plate deflection can be retrieved via Eqn. (3.55). Due to this relation, the attenuation of the wave fields ϕ for $z = 0$ corresponds to the attenuation of the plate deflections u. Analogously to the beam in vacuo with thickness variations (Sec. 2.8), the varying plate thickness, $h(x)$, for the present problem shall be characterised by Eqn. (2.121),

$$h(x) = \bar{h}(1 + \epsilon\tilde{h}(x)),$$

i.e. the plate thickness, $h(x)$, shall fluctuate about the mean $\bar{h}$ with roughness amplitude ϵ and the variations are described via the random process $\tilde{h}(x)$, which fulfils the Gaussian autocorrelation condition (2.122) with correlation length l_G.

Combining Eqns. (3.22), (3.27) and (3.29), we obtain the characterisation of the plate mass, $g(x)$, and plate rigidity, $b(x)$, as

$$g(x) = \frac{\rho h(x)}{\rho_w}, \tag{3.56a}$$

$$b(x) = \frac{E h(x)^3}{12 g_\mathrm{acc} \rho_w (1-\nu^2)}. \tag{3.56b}$$

Motivated by the accurate results of the multiple-scale method for the beam in vacuo, we express the plate mass and rigidity in terms of $\bar{h}$ and $\tilde{h}$ up to order ϵ only,

$$g(x) = \frac{\rho \bar{h}}{\rho_w}(1 + \epsilon \tilde{h}(x)) =: \bar{g}\,(1 + \epsilon\gamma(x)), \tag{3.57a}$$

$$b(x) = \frac{E \bar{h}^3}{12 g_\mathrm{acc} \rho_w (1-\nu^2)}(1 + 3\epsilon \tilde{h}(x)) + \mathcal{O}(\epsilon^2) =: \bar{b}\,(1 + \epsilon\beta(x)), \tag{3.57b}$$

where $\bar{g}, \gamma(x)$ are the mean plate mass and the mass variations, respectively, and $\bar{b}, \beta(x)$ are the mean plate rigidity and the rigidity variations, respectively. Eqns. (3.57) lead to the representation of these quantities,

$$\bar{g} = \frac{\rho \bar{h}}{\rho_w} \qquad \text{and} \qquad \gamma(x) = \tilde{h}(x), \tag{3.58a}$$

$$\bar{b} = \frac{E \bar{h}^3}{12 g_\mathrm{acc} \rho_w (1-\nu^2)} \qquad \text{and} \qquad \beta(x) = 3\tilde{h}(x). \tag{3.58b}$$

We adopt the multiple-scale approach from Ch. 2 to approximate the velocity potential ϕ, considering two scales: the local scale l_G (coordinate denoted by x), which is represented by the correlation length, and the observation scale L_ob (coordinate denoted by x_2), over which attenuation is observed. It is assumed that the scales are related by $L_\mathrm{ob} = l_\mathrm{G}/\epsilon^2$ for small $\epsilon \ll 1$. Applying a multiple-scale expansion of the complex, time-harmonic velocity potential $\phi(x,z)$ to map the wave field into the new coordinate system gives

$$\phi(x,z) = \phi_0(x,x_2,z) + \epsilon\phi_1(x,x_2,z) + \epsilon^2\phi_2(x,x_2,z) + \mathcal{O}\left(\epsilon^3\right), \tag{3.59}$$

where $x_2 = \epsilon^2 x$. While derivatives with respect to z remain the same, derivatives with respect to x become (similarly to Eqn. (2.83)) by application of the chain rule

$$\partial_x \phi(x,z) = \sum_j \epsilon^j \left(\partial_x \phi_j(x,x_2,z) + \epsilon^2 \partial_{x_2}\phi_j(x,x_2,z)\right). \tag{3.60}$$

Employing the multiple-scale expansion (3.59) on the underlying PDE system (3.30) yields the following equations. For the fluid domain, we have

$$\varDelta\phi = \varDelta\phi_0 + \epsilon\varDelta\phi_1 + \epsilon^2\left(\varDelta\phi_2 + 2\partial_x\partial_{x_2}\phi_0\right) + \mathcal{O}(\epsilon^3) \overset{!}{=} 0. \tag{3.61a}$$

Since differentiation with respect to z remains unchanged, the boundary condition at the sea-floor is trivially given by

$$\partial_z\phi = \partial_z\phi_0 + \epsilon\partial_z\phi_1 + \epsilon^2\partial_z\phi_2 + \mathcal{O}(\epsilon^3) \overset{!}{=} 0. \tag{3.61b}$$

Writing the plate Eqn. (3.30c), using the differential operator $\tilde{\mathcal{L}}$, as

$$\tilde{\mathcal{L}}\phi := \left[\frac{\partial^2}{\partial x^2}\left(b(x)\frac{\partial^2}{\partial x^2}\right) - \alpha g(x) + 1\right]\partial_z\phi - \alpha\phi = 0$$

and plugging in the expanded potential from Eqn. (3.59), we obtain

$$\begin{aligned}\tilde{\mathcal{L}}\phi = \mathcal{L}\phi_0 + \epsilon&\left[\mathcal{L}\phi_1 + \left(\frac{\partial^2}{\partial x^2}\left(\bar{b}\beta\frac{\partial^2}{\partial x^2}\right) - \alpha\bar{g}\gamma\right)\partial_z\phi_0\right] + \\ &+ \epsilon^2\left[\mathcal{L}\phi_2 + \left(\frac{\partial^2}{\partial x^2}\left(\bar{b}\beta\frac{\partial^2}{\partial x^2}\right) - \alpha\bar{g}\gamma\right)\partial_z\phi_1 + \left(4\bar{b}\frac{\partial^4}{\partial x^3\,\partial x_2}\right)\partial_z\phi_0\right] + \mathcal{O}(\epsilon^3) \overset{!}{=} 0,\end{aligned} \tag{3.61c}$$

where the differential operator $\mathcal{L}$ characterises the plate equation for constant plate mass and rigidity,

$$\mathcal{L}\phi_i := \left[\bar{b}\frac{\partial^4}{\partial x^4} - \alpha\bar{g} + 1\right]\partial_z\phi_i - \alpha\phi_i, \quad i = 0{,}1{,}2.$$

Separating Eqns. (3.61) with respect to orders of ϵ provides systems of order $\mathcal{O}(\epsilon^0)$, $\mathcal{O}(\epsilon)$, $\mathcal{O}(\epsilon^2)$.

Order ϵ^0

Extracting the terms of zeroth order from the PDE system (3.61), we obtain the system for the leading-order wave field, ϕ_0, which is identical to the PDE system (3.30) for constant plate mass and rigidity,

$$\varDelta\phi_0 = 0, \qquad z \in (-H{,}0), \tag{3.62a}$$

$$\partial_z\phi_0 = 0, \qquad z = -H, \tag{3.62b}$$

$$\mathcal{L}\phi_0 = \left[\bar{b}\frac{\partial^4}{\partial x^4} - \alpha\bar{g} + 1\right]\partial_z\phi_0 - \alpha\phi_0 = 0, \qquad z = 0. \tag{3.62c}$$

Since the solution of Eqns. (3.62) consists of a modulated right-travelling and a reflected left-travelling wave, we compare these two wave components in Fig. 3.4 using the random-sampling method for the finite roughness interval length $L = 800$. Fig. 3.4 shows the left- and right-travelling components of the effective plate deflections, $|\langle u_-\rangle|$ and $|\langle u_+\rangle|$, respectively, for roughness amplitude $\epsilon = 5.0 \times 10^{-2}$, for non-dimensional correlation lengths $\bar{k}l_{\mathrm{G}} = 0.9$, 2.5 and 4.1.

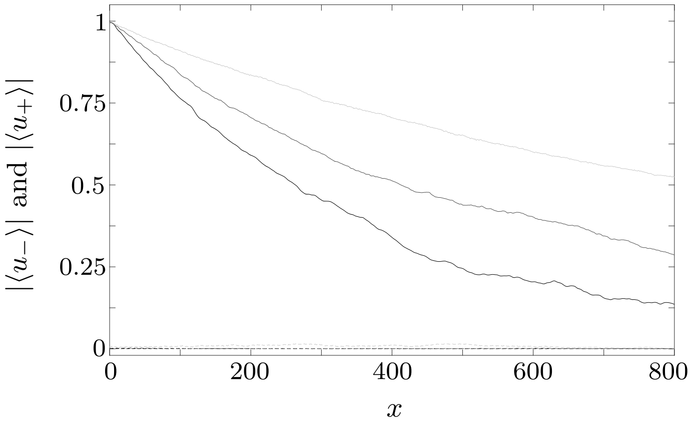

Figure 3.4: Effective plate deflections, split into rightward- and leftward-travelling components (solid and dashed line, respectively), for correlation lengths $\bar{k}l_{\mathrm{G}} = 0.9$ (light grey), $\bar{k}l_{\mathrm{G}} = 2.5$ (dark grey) and $\bar{k}l_{\mathrm{G}} = 4.1$ (black), for roughness amplitudes $\epsilon = 5.0 \times 10^{-2}$ (left-hand panel) and $\epsilon = 1.0 \times 10^{-1}$ (right-hand panel)

We can see in Fig. 3.4 that for all three correlation lengths considered, $\bar{k}l_{\mathrm{G}} = 0.9$, 2.5 and 4.1, the left-travelling effective wave component for the floating plate problem is only slightly larger than zero. To show that this holds for a wide range of roughness amplitudes over the whole correlation length regime, we consider the ratio of the (spatial averaged) leftward- to rightward travelling effective wave components as a function of non-dimensional correlation length, for roughness amplitudes $\epsilon = 10^{-4}$, 10^{-3}, 10^{-2}, 10^{-1} and 2×10^{-1} in Fig. 3.5, where the ratio is calculated via Eqn. (2.85) for the right- and left-going wave components of the plate deflection, $u_{\pm}$. The interval length, L, in the random-sampling method is set to be 400 times the corresponding correlation length, i.e. $L = 400 \times l_{\mathrm{G}}$, which provides a sufficiently large roughness interval to allow comparisons with the multiple-scale method.

We can see in Fig. 3.5 that $\epsilon = 10^{-4}$, 10^{-3} and 10^{-2} give very similar scaled ratios and the maximum value of $U_{-/+}$ is slightly larger than 0.1ϵ in the small (non-dimensional) correlation length regime around $\bar{k}l_{\mathrm{G}} \approx 1$. For very small and larger correlation lengths, the scaled ratios decrease similarly, so evidence is provided that $U_{-/+}$ scales with ϵ for small roughness amplitudes. For the two largest roughness amplitudes, $\epsilon = 10^{-1}$ and 2×10^{-1}, this scaling does not hold anymore and the left-travelling effective wave components rise in comparison to the right-travelling effective wave component. Hence, they may not be neglected anymore, which indicates the limit of validity of the multiple-scale method here too.

As we have confirmed in Figs. 3.4 and 3.5, the left-travelling wave is negligible for $\epsilon < 0.1$ and only the modulated right-travelling wave has to be considered at leading order. This

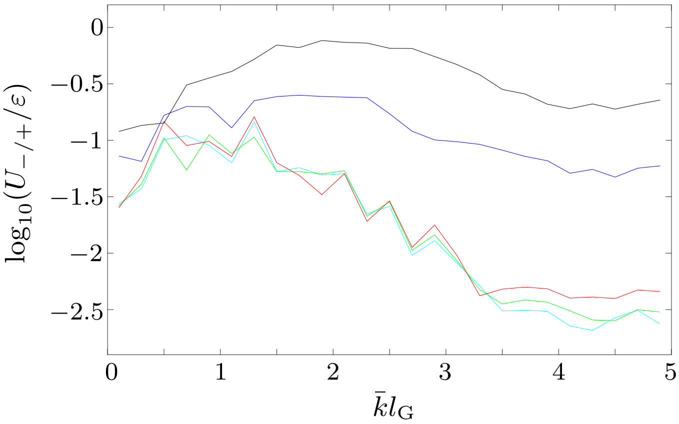

Figure 3.5: Ratio of leftward- to rightward travelling components of effective plate deflection as a function of non-dimensional correlation length, for roughness amplitudes $\epsilon = 10^{-4}$ (cyan), $\epsilon = 10^{-3}$ (green), $\epsilon = 10^{-2}$ (red), $\epsilon = 10^{-1}$ (blue) and $\epsilon = 2 \times 10^{-1}$ (black)

leads to the leading-order solution

$$\phi_0(x,x_2,z) = A(x_2)\cosh(\bar{k}(z+H))\mathrm{e}^{\mathrm{i}\bar{k}x}, \tag{3.63}$$

where the wavenumber $\bar{k}$ is the real positive solution satisfying the dispersion relation for elastic plates of constant mass $\bar{g}$ and rigidity $\bar{b}$, which correspond to the mean plate thickness, $\bar{h}$,

$$\bar{k}\tanh(\bar{k}H) = \frac{\alpha}{\bar{b}\bar{k}^4 - \alpha\bar{g} + 1}, \tag{3.64}$$

i.e. the wavenumber $\bar{k}$ is the travelling wave mode k_0, and $\cosh(\bar{k}(z+H))$ is the vertical mode w_0. The (complex-valued) wave amplitude of leading order, $A = A(x_2)$, is undetermined and sought from the higher-order systems, providing the attenuation coefficient Q_{eff} via

$$|\langle A(x_2)\rangle| = A_0\,\mathrm{e}^{-Q_{\mathrm{eff}}x}, \tag{3.65}$$

where A_0 is a constant.

Order ϵ^1

The terms of order $\mathcal{O}(\epsilon)$ lead to following governing system for the first-order wave field, ϕ_1,

$$\varDelta\phi_1 = 0, \qquad z \in (-H,0), \tag{3.66a}$$

$$\frac{\partial}{\partial z}\phi_1 = 0, \qquad z = -H, \tag{3.66b}$$

$$\mathcal{L}\phi_1 = -\left(\frac{\partial^2}{\partial x^2}\left(\bar{b}\beta\frac{\partial^2}{\partial x^2}\right) - \alpha\bar{g}\gamma\right)\frac{\partial}{\partial z}\phi_0, \qquad z = 0. \tag{3.66c}$$

The inhomogeneous PDE system (3.66) is solved for given δ (given γ and β, respectively) with the help of the Green's function, which shall satisfy the following system with a singularity at the source point $\check{x}$ for $z = 0$,

$$\Delta G(x,\check{x},z) = 0, \qquad z \in (-H,0), \tag{3.67a}$$

$$\frac{\partial}{\partial z} G(x,\check{x}) = 0, \qquad z = -H, \tag{3.67b}$$

$$\mathcal{L} G(x,\check{x}) = \delta(x - \check{x}), \qquad z = 0. \tag{3.67c}$$

The solution can be found in Porter and Evans 2006, which is based on the work of Chung (2002),

$$G(x,\check{x},z) = G(|x - \check{x}|,z) = -\sum_{n=-2}^{\infty} \frac{\sin(\bar{k}_n H)\cos(\bar{k}_n(z+H))}{2\alpha C(\bar{k}_n)} \mathrm{e}^{-\bar{k}_n |x-\check{x}|}, \tag{3.68}$$

where

$$C(\bar{k}_n) = \frac{1}{2}\left(H - \frac{\left(5\bar{b}\bar{k}_n^4 - \alpha\bar{g} + 1\right)\sin^2(\bar{k}_n H)}{\alpha}\right). \tag{3.69}$$

The wave modes $\bar{k}_n$, $n = -2, -1, \ldots$, appearing in Eqn. (3.68) are the solutions of the dispersion relation (3.64) multiplied by $-\mathrm{i}$, and ordered such that $\bar{k}_{-2}$ and $\bar{k}_{-1}$ denote the complex solutions with positive real part corresponding to the damped travelling waves, $\bar{k}_0$ is the purely imaginary, negative wave mode corresponding to the travelling wave and $\bar{k}_n$ for $n > 0$ are the positive, real solutions corresponding to the evanescent waves. Fig. 3.6 shows the Green's function and its first derivative.

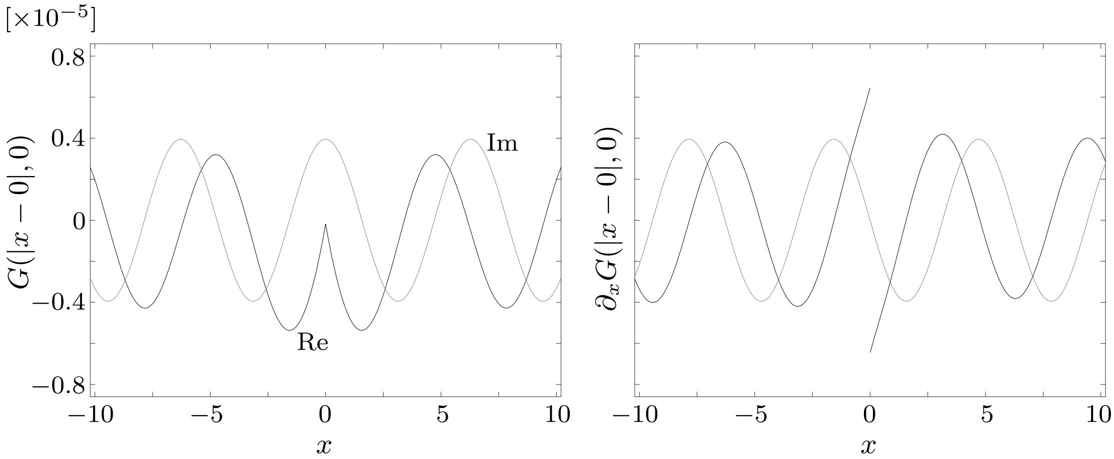

Figure 3.6: Green's function (left-hand panel) and first derivative (right-hand panel) for homogeneous floating plate with impulse at the source point $\check{x} = 0$, for $z = 0$

The approach with Green's function leads to the solution of the PDE system (3.66) for given γ and β,

$$\phi_1(x,x_2,z) = \int_{-\infty}^{\infty} - \left[\left(\frac{\partial^2}{\partial \check{x}^2} \left(\bar{b}\beta \frac{\partial^2}{\partial \check{x}^2} \right) - \alpha \bar{g} \gamma \right) \partial_z \phi_0 \right] G(|x-\check{x}|, z=0) \, \mathrm{d}\check{x}. \tag{3.70}$$

Using the leading-order solution ϕ_0 from Eqn. (3.63), ϕ_1 can be written as

$$\phi_1(x,x_2,z) = -A(x_2) \, (\partial_z w_0) \int_{-\infty}^{\infty} \left[\left(\frac{\partial^2}{\partial \check{x}^2} \left(\bar{b}\beta \frac{\partial^2}{\partial \check{x}^2} \right) - \alpha \bar{g} \gamma \right) \mathrm{e}^{\mathrm{i}\bar{k}\check{x}} \right] G(|x-\check{x}|, 0) \, \mathrm{d}\check{x}. \tag{3.71}$$

Order ϵ^2

The order ϵ^2 terms yield the governing PDE system for ϕ_2 to be

$$\Delta \phi_2 = -2 \frac{\partial}{\partial x_2} \frac{\partial}{\partial x} \phi_0, \qquad z \in (-H,0), \tag{3.72a}$$

$$\partial_z \phi_2 = 0, \qquad z = -H, \tag{3.72b}$$

$$\mathcal{L} \phi_2 = - \left(\frac{\partial^2}{\partial x^2} \left(\bar{b}\beta \frac{\partial^2}{\partial x^2} \right) - \alpha \bar{g} \gamma \right) \partial_z \phi_1 - \left(4\bar{b} \frac{\partial^4}{\partial x^3 \, \partial x_2} \right) \partial_z \phi_0, \qquad z = 0. \tag{3.72c}$$

We apply the same solution procedure as for in-vacuo beam problem, i.e. we take the ensemble average of Eqns. (3.72) to find the averaged solution $\langle \phi_2 \rangle$, which we factorise as $\langle \phi_2 \rangle = \mathrm{e}^{\mathrm{i}\bar{k}x} F(x_2, z)$, for some function F. Taking the ensemble average and using the mean leading-order solution $\langle \phi_0(x,x_2,z) \rangle = \langle A(x_2) \rangle f(z) \mathrm{e}^{\mathrm{i}\bar{k}x}$, Eqn. (3.72a) becomes

$$- \bar{k}^2 \mathrm{e}^{\mathrm{i}\bar{k}x} F(x_2, z) + \mathrm{e}^{\mathrm{i}\bar{k}x} \partial_z^2 F(x_2, z) = -2\mathrm{i}\bar{k} w_0(z) \partial_{x_2} \langle A(x_2) \rangle \mathrm{e}^{\mathrm{i}\bar{k}x}. \tag{3.73}$$

This approach simplifies the impermeability condition at the sea-floor, Eqn. (3.72b), to

$$\partial_z F = 0. \tag{3.74}$$

Whereas the left-hand side of Eqn. (3.72c) can be written as

$$\mathcal{L} \langle \phi_2 \rangle = \left[\left(\bar{b}\bar{k}^4 - \alpha \bar{g} + 1 \right) \partial_z F - \alpha F \right] \mathrm{e}^{\mathrm{i}\bar{k}x}, \tag{3.75}$$

we give the respective expressions of the first and second term in the right-hand side of Eqn. (3.72c) separately. Using the leading-order solution ϕ_0 and $\partial_z^2 w_0(z) = \bar{k}^2 w_0(z)$, the second term becomes

$$\langle -4\bar{b} \partial_x^3 \partial_{x_2} \partial_z \phi_0 \rangle = 4\mathrm{i}\bar{b}\bar{k}^4 \sinh(\bar{k}H) \, \partial_{x_2} \langle A(x_2) \rangle \, \mathrm{e}^{\mathrm{i}\bar{k}x}. \tag{3.76}$$

For the first term of the right-hand side of Eqn. (3.72c) we get with the help of the solution ϕ_1 from Eqn. (3.71)

$$
\begin{aligned}
&-\left(\partial_x^2\left(\bar{b}\beta\partial_x^2\right)-\alpha\bar{g}\gamma\right)\partial_z\phi_1 = \\
&\quad= \langle A\rangle\left\langle\left(\partial_x^2\left(\bar{b}\beta\partial_x^2\right)-\alpha\bar{g}\gamma\right)\frac{\partial}{\partial z}\left[(\partial_z w_0)\int_{-\infty}^{\infty}\left[\left(\partial_{\check{x}}^2\left(\bar{b}\beta\partial_{\check{x}}^2\right)-\alpha\bar{g}\gamma\right)\mathrm{e}^{\mathrm{i}\bar{k}\check{x}}\right]G(|x-\check{x}|,0)\,\mathrm{d}\check{x}\right]\right\rangle \\
&\quad= \bar{k}^2 w_0(0)\langle A\rangle\left\langle\left(\partial_x^2\left(\bar{b}\beta\partial_x^2\right)-\alpha\bar{g}\gamma\right)\int_{-\infty}^{\infty}\left[\left(\partial_{\check{x}}^2\left(\bar{b}\beta\partial_{\check{x}}^2\right)-\alpha\bar{g}\gamma\right)\mathrm{e}^{\mathrm{i}\bar{k}\check{x}}\right]G(|x-\check{x}|,0)\,\mathrm{d}\check{x}\right\rangle
\end{aligned}
\tag{3.77}
$$

Here, we assumed that the random components of the leading-order velocity potential ϕ_0 are uncorrelated to the plate mass and rigidity variations, which is shown in the following similarly to analysis of the wave field for the in-vacuo beam problem in Ch. 2. Fig. 3.7 shows the mean correlations of the thickness variations with the plate deflection for the whole range of non-dimensional correlation lengths we will consider in Sec. 3.5, $\bar{k}l_\mathrm{G} = 0.1, \dots, 4.9$. The mean correlation functions are defined in Eqns. (2.97) and (2.98).

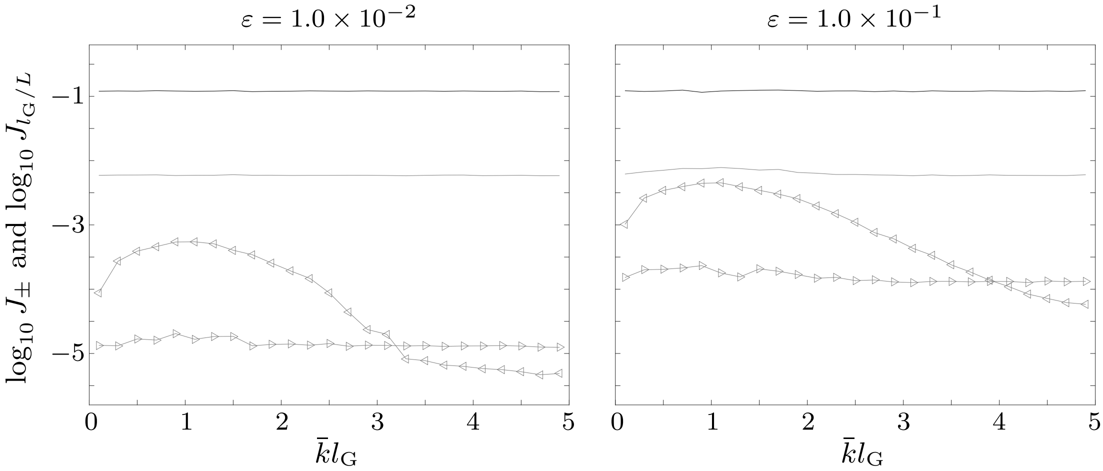

Figure 3.7: Mean correlations of roughness profile with plate deflection, J_{l_G} (black solid) and J_L (grey solid), and random components of wave field, J_+ (▷) and J_- (◁), as functions of non-dimensional correlation length, for roughness amplitudes $\epsilon = 1.0 \times 10^{-2}$ (left-hand panel) and $\epsilon = 1.0 \times 10^{-1}$ (right-hand panel)

We can observe in Fig. 3.7 that the random components of the plate deflection are uncorrelated to the roughness profile. Hence, the assumption holds that the random components in the leading-order velocity potential ϕ_0 are uncorrelated to the plate mass and rigidity variations, and Eqn. (3.77) is valid. Expanding the fourth-order differential

$$
\partial_x^2(\bar{b}\beta\partial_x^2) = (\partial_x^2\bar{b}\beta)\partial_x^2 + 2(\partial_x\bar{b}\beta)\partial_x^3 + \bar{b}\beta\partial_x^4,
$$

we can rewrite Eqn. (3.77) as

$$\bar{k}^2 \cosh(\bar{k}H)\langle A\rangle \mathrm{e}^{\mathrm{i}\bar{k}x} \Bigg\langle \left(\partial_x^2 \left(\bar{b}\beta\partial_x^2\right) - \alpha\bar{g}\gamma\right) \int_{-\infty}^{\infty} \left(\bar{k}^4\bar{b}\beta - 2\mathrm{i}\bar{k}^3\partial_{\check{x}}\bar{b}\beta - \bar{k}^2\partial_{\check{x}}^2\bar{b}\beta - \alpha\bar{g}\gamma\right) \cdot \\ \cdot\, \mathrm{e}^{\mathrm{i}\bar{k}(\check{x}-x)} G(|x-\check{x}|,0)\,\mathrm{d}\check{x} \Bigg\rangle =: \bar{k}^2 \cosh(\bar{k}H)\langle A\rangle \mathrm{e}^{\mathrm{i}\bar{k}x}\,\zeta. \quad (3.78)$$

The complex constant ζ is calculated numerically using an adaptive quadrature scheme. The autocorrelation of the mass variations and rigidity variations are denoted with ρ_1 and ρ_2, respectively, and the cross-correlation of both quantities is denoted with ρ_3, i.e.

$$\rho_1(|\xi|) = \rho_1(|x-\check{x}|) := \langle\gamma(x)\,\gamma(\check{x})\rangle, \quad (3.79a)$$
$$\rho_2(|\xi|) = \rho_2(|x-\check{x}|) := \langle\beta(x)\,\beta(\check{x})\rangle, \quad (3.79b)$$
$$\rho_3(|\xi|) = \rho_3(|x-\check{x}|) := \langle\gamma(x)\,\beta(\check{x})\rangle. \quad (3.79c)$$

The complex constant ζ can then be written as

$$\begin{aligned}\zeta = \int_{-\infty}^{\infty} \Big[&\left(\bar{k}^4\bar{b}^2\rho_2(|\xi|) - 2\mathrm{i}\bar{k}^3\bar{b}^2(\partial_\xi\rho_2(|\xi|)) - \bar{k}^2\bar{b}^2(\partial_\xi^2\rho_2(|\xi|)) - \alpha\bar{g}\bar{b}\rho_3(|\xi|)\right) \mathrm{e}^{\mathrm{i}\bar{k}\xi}\,\partial_\xi^4 G(|\xi|,0) \\ &+ 2\left(\bar{k}^4\bar{b}^2(\partial_\xi\rho_2(|\xi|)) - 2\mathrm{i}\bar{k}^3\bar{b}^2(\partial_\xi^2\rho_2(|\xi|)) - \bar{k}^2\bar{b}^2(\partial_\xi^3\rho_2(|\xi|)) - \alpha\bar{g}\bar{b}(\partial_\xi\rho_3(|\xi|))\right)\mathrm{e}^{\mathrm{i}\bar{k}\xi}\,\partial_\xi^3 G(|\xi|,0) \\ &+ \left(\bar{k}^4\bar{b}^2(\partial_\xi^2\rho_2(|\xi|)) - 2\mathrm{i}\bar{k}^3\bar{b}^2(\partial_\xi^3\rho_2(|\xi|)) - \bar{k}^2\bar{b}^2(\partial_\xi^4\rho_2(|\xi|)) - \alpha\bar{g}\bar{b}(\partial_\xi^2\rho_3(|\xi|))\right) \mathrm{e}^{\mathrm{i}\bar{k}\xi}\,\partial_\xi^2 G(|\xi|,0) \\ &+ \alpha\left(\alpha\bar{g}^2\rho_1((|\xi|) - \bar{k}^4\bar{g}\bar{b}\rho_3(|\xi|) + 2\mathrm{i}\bar{k}^3\bar{g}\bar{b}(\partial_\xi\rho_3(|\xi|)) + \bar{k}^2\bar{g}\bar{b}(\partial_\xi^2\rho_3(|\xi|))\right) \mathrm{e}^{\mathrm{i}\bar{k}\xi}\, G(|\xi|,0)\Big]\,\mathrm{d}\xi. \quad (3.80)\end{aligned}$$

With the above expressions for the ensemble average of the PDE system (3.72) of order $\mathcal{O}(\epsilon^2)$, we can derive the following PDE system, which has to be satisfied by F:

$$\partial_z^2 F - \bar{k}^2 F = -2\mathrm{i}\bar{k}w_0\partial_{x_2}\langle A(x_2)\rangle, \qquad z \in (-H,0), \quad (3.81a)$$
$$\partial_z F = 0, \qquad z = -H, \quad (3.81b)$$
$$\begin{aligned}\left(\bar{b}\bar{k}^4 - \alpha\bar{g} + 1\right)\partial_z F - \alpha F &= \cosh(\bar{k}H)\bar{k}^2\zeta\langle A(x_2)\rangle \\ &\quad + 4\mathrm{i}\bar{k}^4\bar{b}\partial_{x_2}\langle A(x_2)\rangle \sinh(\bar{k}H), \qquad z = 0. \quad (3.81c)\end{aligned}$$

Our goal now is to derive an equation for the ensemble average of the leading order wave amplitude $\langle A(x_2)\rangle$, which accordingly determines the leading order velocity potential ϕ_0 and thereof the multiple-scale approximation of the effective plate deflection. Application of the second Green's identity, which corresponds to integration by parts twice in 1D, leads to

$$\begin{aligned}\int_{-H}^{0} F\partial_z^2 w_0 - w_0\partial_z^2 F\,\mathrm{d}z &= \int_{-H}^{0} \bar{k}^2 w_0 F - w_0\left(\bar{k}^2 F - 2\mathrm{i}\bar{k}w_0\frac{\partial}{\partial x_2}\langle A\rangle\right)\mathrm{d}z \\ &= F\partial_z w_0 - w_0\partial_z F\big|_{z=-H}^{0} \\ &= F(x_2,0)\bar{k}\sinh(\bar{k}H) - \partial_z F(x_2,0)\cosh(\bar{k}H). \quad (3.82)\end{aligned}$$

Multiplication of Eqn. (3.81a) with w_0 and integration over the interval $(-H,0)$ afterwards gives

$$\int_{-H}^{0} w_0 \partial_z^2 F - \underbrace{\bar{k}^2 w_0}_{=\partial_z^2 w_0} F \,\mathrm{d}z = \int_{-H}^{0} -2\mathrm{i}\bar{k} w_0^2 \partial_{x_2} A \,\mathrm{d}z. \tag{3.83}$$

The left-hand side of Eqn. (3.83) corresponds to the left-hand side of Eqn. (3.82) (multiplied with the factor -1) such that the following equivalence holds,

$$2\mathrm{i}\bar{k}\left(\partial_{x_2}\langle A\rangle\right)\int_{-H}^{0} w_0^2 \,\mathrm{d}z = \bar{k}F(x_2,0)\sinh(\bar{k}H) - \partial_z F(x_2,0)\cosh(\bar{k}H). \tag{3.84}$$

Deploying the dispersion relation (3.64) on Eqn. (3.81c) yields

$$\partial_z F(x_2,0) - F(x_2,0)\underbrace{\frac{\alpha}{\bar{b}\bar{k}^4 - \alpha\bar{g} + 1}}_{\bar{k}\tanh(\bar{k}H)} = \frac{\cosh(\bar{k}H)\bar{k}^2\zeta\langle A(x_2)\rangle + 4\mathrm{i}\bar{k}^4\bar{b}\partial_{x_2}\langle A\rangle\sinh(\bar{k}H)}{\bar{b}\bar{k}^4 - \alpha\bar{g} + 1}. \tag{3.85}$$

By scaling Eqn. (3.84) with $\cosh(\bar{k}H)$ and equating with Eqn. (3.85), we obtain

$$2\mathrm{i}\bar{k}\partial_{x_2}\langle A\rangle\frac{1}{\cosh^2(\bar{k}H)}\underbrace{\int_{-H}^{0}\cosh^2(\bar{k}(z+H))\,\mathrm{d}z}_{\frac{1}{2\bar{k}}\left(\cosh(\bar{k}H)\sinh(\bar{k}H)+\bar{k}H\right)} = -\frac{\bar{k}^2\zeta\langle A\rangle + 4\mathrm{i}\bar{k}^4\bar{b}\partial_{x_2}\langle A\rangle\tanh(\bar{k}H)}{\bar{b}\bar{k}^4 - \alpha\bar{g} + 1}. \tag{3.86}$$

Using the dispersion relation for the right-hand side of Eqn. (3.86) (multiplied with α) and using the addition theorem

$$\sinh(2\bar{k}H) = 2\sinh(\bar{k}H)\cosh(\bar{k}H), \tag{3.87}$$

which can be found in Bronstein et al. 2012, gives

$$\begin{aligned}\mathrm{i}\,\partial_{x_2}\langle A(x_2)\rangle\frac{\alpha}{\sinh(2\bar{k}H)}\left(\sinh(2\bar{k}H) + 2\bar{k}H\right) = \\ -\bar{k}\left[\langle A(x_2)\rangle\bar{k}^2\zeta + 4\mathrm{i}\bar{k}^4\bar{b}\partial_{x_2}\langle A(x_2)\rangle\tanh(\bar{k}H)\right].\end{aligned} \tag{3.88}$$

Rewriting Eqn. (3.88) gives the following ordinary differential equation for the leading-order (effective) wave amplitude $\langle A(x_2)\rangle$,

$$\left[4\bar{k}^5\bar{b}\tanh(\bar{k}H) + \alpha\left(1 + \frac{2\bar{k}H}{\sinh(2\bar{k}H)}\right)\right]\partial_{x_2}\langle A(x_2)\rangle = \mathrm{i}\bar{k}^3\zeta\langle A(x_2)\rangle. \tag{3.89}$$

The solution of this simple, linear ordinary differential equation is then obtained via separation of variables,

$$\langle A(x_2)\rangle = A_0 \exp\left(\mathrm{i}\frac{\bar{k}^3\zeta}{4\bar{b}\bar{k}^5\tanh(\bar{k}H)+\alpha\left(1+\frac{2\bar{k}H}{\sinh(2\bar{k}H)}\right)}x_2\right). \tag{3.90}$$

Therefore, we can describe the evolution of the leading-order wave amplitude of the effective wave field with the help of the complex constant ζ and the wavenumber $\bar{k}$, which corresponds to the travelling wave mode for a plate with mean mass $\bar{g}$ and mean rigidity $\bar{b}$ (obtained via dispersion relation for elastic plates with constant rigidity and mass, Eqn. (3.64)). The attenuation coefficient, Q_{eff}, for the floating plate problem is

$$Q_{\text{eff}} = \epsilon^2 \mathrm{Im}\left[\frac{\bar{k}^3\zeta}{4\bar{b}\bar{k}^5\tanh(\bar{k}H)+\alpha\left(1+\frac{2\bar{k}H}{\sinh(2\bar{k}H)}\right)}\right]. \tag{3.91}$$

Note that the correlation functions $\rho_j(|\xi|)$, $j = 1,2,3$, in the calculation of the complex constant ζ in Eqn. (3.80) are not specified yet. This is done in the following yielding the varying mass and varying rigidity problem in addition to the varying thickness problem.

Floating rough plate with varying thickness

Here, we assume that the plate density and Young's modulus are uniform along the plate and the plate mass and rigidity only depend on its thickness, $h(x)$. The multiple-scale method for the floating plate problem was derived for autocorrelated thickness variations leading to varying mass and varying rigidity, hence all the terms are included to describe the varying thickness problem. The random processes $\gamma(x)$ and $\beta(x)$ describing the mass and rigidity variations, respectively, are determined from the rough thickness profile via Eqns. (3.58). This gives the autocorrelation of the plate mass variations, $\gamma(x)$, and rigidity variations, $\beta(x)$, and their cross-correlation for Eqn. (3.79),

$$\rho_1(|\xi|) = \langle\gamma(x)\,\gamma(x-\xi)\rangle = \rho(|\xi|), \tag{3.92a}$$

$$\rho_2(|\xi|) = \langle\beta(x)\,\beta(x-\xi)\rangle = 9\rho(|\xi|), \tag{3.92b}$$

$$\rho_3(|\xi|) = \langle\gamma(x)\,\beta(x-\xi)\rangle = 3\rho(|\xi|), \tag{3.92c}$$

where ρ denotes the Gaussian autocorrelation condition of the thickness variations.

Floating rough plate with varying mass and varying rigidity

For each of the varying mass and varying rigidity problem, the respective quantity is assumed to fluctuate about its mean, where the variations are described with the same random process as in the varying thickness problem, and the respective other quantity is chosen to be constant. Similar to the beam in vacuo, the varying mass is assumed to be caused by plate density variations, and the varying rigidity is assumed to be caused by variations in Young's modulus. It is clear that the cross-correlation function ρ_3 has to vanish for both the varying mass and varying rigidity problem, since only one of these quantities is allowed to vary, whereas the other is held constant. Since the random process describing the mass and rigidity variations, respectively, is the same as in the varying thickness case with Gaussian autocorrelation function ρ, we can express the correlation functions ρ_j, $j = 1,2,3$, for both problems as

$$\text{varying mass:} \begin{cases} \rho_1(|\xi|) = \rho(|\xi|), \\ \rho_2(|\xi|) = 0, \\ \rho_3(|\xi|) = 0, \end{cases} \qquad \text{varying rigidity:} \begin{cases} \rho_1(|\xi|) = 0, \\ \rho_2(|\xi|) = \rho(|\xi|), \\ \rho_3(|\xi|) = 0. \end{cases} \tag{3.93}$$

This means in particular, that for the same roughness amplitude ϵ the rigidity variations are significantly larger in the varying thickness problem than in the varying rigidity problem. We could already observe this determining influence of the varying rigidity for the beam in vacuo, where thickness variations lead to larger attenuation of the wave fields than varying mass or rigidity, only.

3.5 Numerical results

To conclude this chapter about the problem of wave attenuation along a large plate floating on water, we validate the multiple-scale method over a large range of correlation lengths and restrict ourselves to small roughness amplitudes again. Besides showing results for the problem of plates with continuously varying thickness, we will also show results for plates with (continuously) varying mass and rigidity. To validate the multiple-scale method, we apply the random-sampling method for an ensemble of 1500 randomly generated realisations of roughness profiles, in which profiles share the same amplitude, ϵ, and correlation length, l_{G}. For the interval length in the numerical method, L, we choose 400 times the corresponding correlation length, which already provided accurate results for the previous investigations and is sufficiently large to allow comparisons with the multiple-scale method (for which it is assumed that the plate extends to infinity). For the comparison of the attenuation coefficients obtained by the random-sampling method with those predicted by the multiple-scale method, 40 terms are used in the calculation of Green's function in Eqn. (3.68), which is sufficiently large to capture the evanescent waves accurately. Fig. 3.8 shows the attenuation coefficients, which are non-dimensionalised with $\bar{k}$ and scaled by the roughness amplitude squared, predicted by the multiple-scale method and obtained by the random-sampling method, as functions of non-dimensional correlation length, for roughness amplitudes $\epsilon = 1.0 \times 10^{-3}$ (top-left panel), 1.0×10^{-2} (top-right panel), 5.0×10^{-2} (bottom-left panel) and 1.0×10^{-1} (bottom-right panel).

We can observe in Fig. 3.8 that the plate with varying thickness floating on water yields qualitatively the same curve for the effective and individual attenuation coefficients as the in-vacuo beam problem. The effective attenuation coefficients are proportional to ϵ^2, and they scale linearly with the correlation length for $\bar{k} l_{\mathrm{G}} \geq 2$. Although the numerical method is more intricate than for the previous problem and computationally expensive (with the computing time a multiple thereof), the results for the numerical method and the multiple-scale method show very good agreement, in particular in the roughness amplitude regime

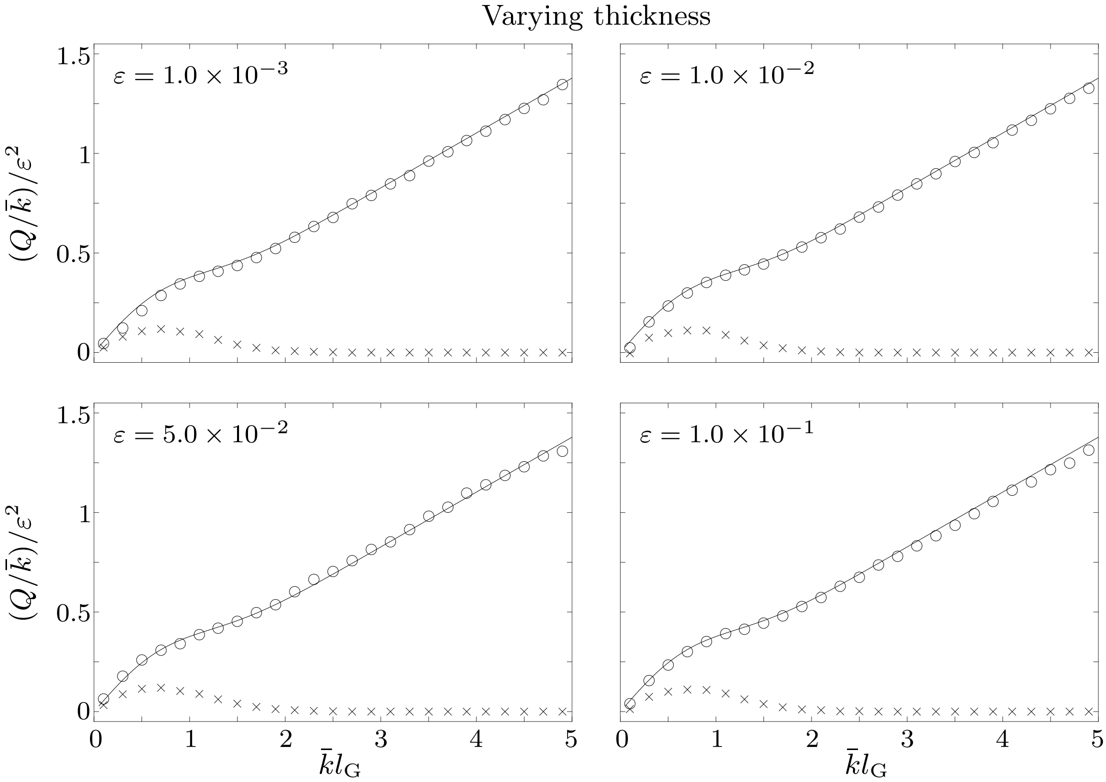

Figure 3.8: Scaled attenuation coefficients of effective wave field for varying thickness problem as functions of non-dimensional correlation length, predicted by multiple-scale method (solid line) and random-sampling method (○), for roughness amplitudes $\epsilon = 1.0 \times 10^{-3}$ (top-left panel), $\epsilon = 1.0 \times 10^{-2}$ (top-right panel), $\epsilon = 5.0 \times 10^{-2}$ (bottom-left panel) and $\epsilon = 1.0 \times 10^{-1}$ (bottom-right panel). Corresponding individual attenuation coefficients obtained by the random-sampling method (×) are shown for comparison.

$\epsilon \leq 5.0 \times 10^{-2}$. For $\epsilon = 1.0 \times 10^{-1}$, the attenuation coefficients from the multiple-scale method slightly overpredict the effective attenuation coefficients obtained by the numerical method in the large correlation length regime. This indicates that for this problem, too, the multiple-scale method loses its validity around $\epsilon = 1.0 \times 10^{-1}$. The problem formulation does not change the behaviour of the individual wave fields, which, in contrast to the effective wave fields, attenuate only for the small correlation length regime $\bar{k}l_G \leq 2$, and the attenuation coefficients in this regime are significantly smaller than for the corresponding effective wave fields.

To get an insight into the effects of plate mass variations and plate rigidity variations for the floating plate problem, we study the respective attenuation coefficients. Fig. 3.9 shows the scaled attenuation coefficients, predicted by the multiple-scale method and obtained by the random-sampling method, as functions of non-dimensional correlation length, for the varying mass problem (top panels) and varying rigidity problem (bottom panels) and for roughness amplitudes $\epsilon = 5.0 \times 10^{-3}$ (left-hand panels) and $\epsilon = 5.0 \times 10^{-2}$ (left-hand panels).

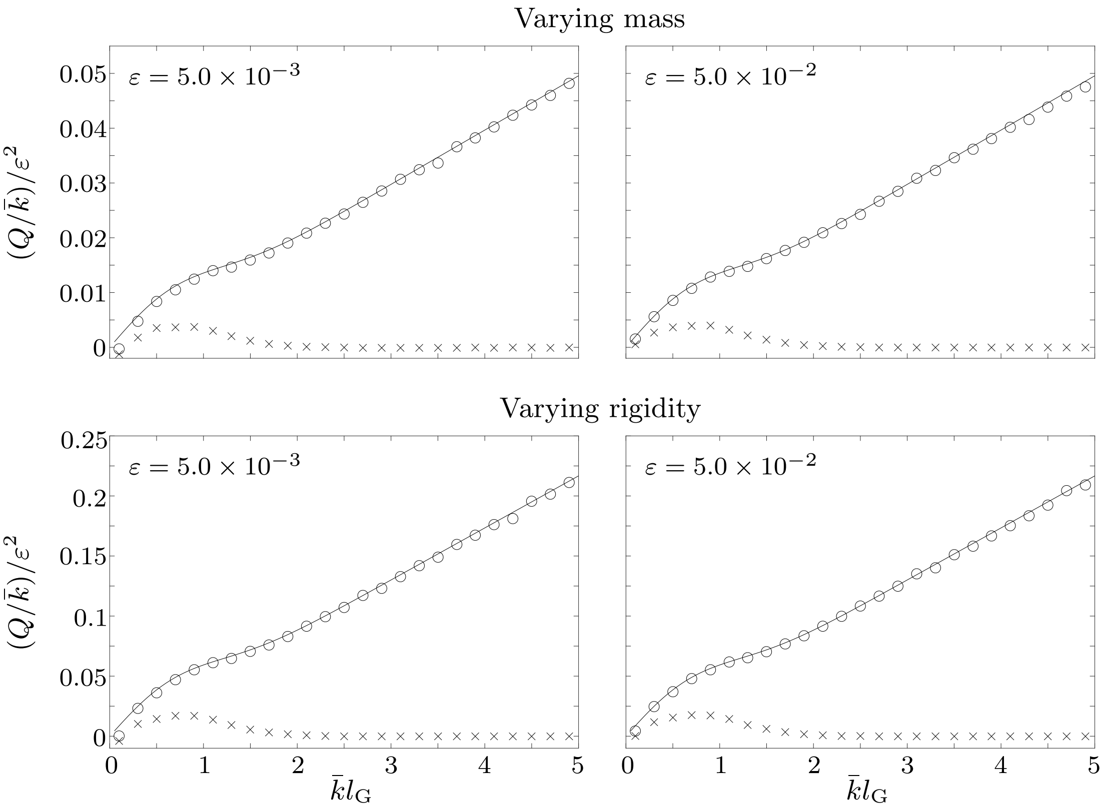

Figure 3.9: Scaled attenuation coefficients of effective wave field for varying mass (top panels) and varying rigidity problem (bottom panels) as functions of non-dimensional correlation length, predicted by multiple-scale method (solid line) and random-sampling method (∘), for roughness amplitudes $\epsilon = 5.0 \times 10^{-3}$ (left-hand panels) and $\epsilon = 5.0 \times 10^{-2}$ (right-hand panels). Corresponding individual attenuation coefficients obtained by the random-sampling method (×) are shown for comparison.

Most important, we can observe a very good agreement between the multiple-scale method and the numerical method for both the varying mass and varying rigidity problem for the whole correlation length regime considered, and both roughness amplitudes, which are small enough that the assumption of small ϵ in the multiple-scale method holds. Both problems yield the same qualitative curves for the effective and individual attenuation coefficients as the varying thickness problem. However, the effective attenuation coefficients are not the same for the varying mass and the varying rigidity problem. This is due to the non-dimensionalised problem formulation with the plate rigidity b taking much larger values that the plate mass g. As a result, variations in the plate rigidity lead to more variations in an absolute sense than plate mass variations for the same (non-dimensional) roughness amplitude, and hence, varying rigidity leads to more than four times larger attenuation than varying mass. Added together, the attenuation coefficients for the respective problems are still much smaller than for the varying thickness problem. This discrepancy is caused by the derivation of the mass and rigidity variations from the varying thickness, leading to a cubic scaling of the rigidity variations with the thickness variations and resulting scaled autocorrelation functions, see Eqns. (3.92).

3.6 Summary and discussion

We extended the study of wave propagation along beams in vacuo to plates floating on water. The water was modelled as an incompressible, inviscid fluid with irrotational flow, which are reasonable assumptions in the marginal ice zone, where the amplitudes of the incoming ocean waves are small compared to the wavelengths, hence we can apply linear water wave theory. Our focus lay on very large ice floes, which can be found close to the continuous ice. Due to their small thickness (compared to their large horizontal extent) and high flexibility, these very large ice floes can be be modelled as semi-infinite elastic plates. Since we want to neglect the boundary interactions for the sake of simplicity in this preliminary study, we assume the plates to be infinite. Our goal was to describe the effects of continuous thickness variations analytically, since the thickness variations are essential for attenuating the waves travelling along the ice floes and computations on this large scale are very expensive. Working with infinite plates allowed us to apply a multiple-scale method based on the one, which was successfully validated in the previous chapter for beams in vacuo. We restricted ourselves to thickness variations, which are uniform along the y-axis, and waves travelling straight along the x-axis, which made the model two-dimensional. However, due to this simplification, no information about the direction of scattered waves can be retrieved from this model, see e.g. Meylan 2002. The problem characteristics allowed us to model the floating plate with the Euler–Bernoulli theory, which proved to yield good results for the in-vacuo beam problem.

Under the above assumptions, the velocity potential of the water could be described by Laplace's equation. Furthermore, we assumed the sea-floor in intermediate depth to be impermeable. Using the linearised version of Bernoulli's plate equation and the linearised kinematic surface condition at the interface between beam and water, we obtained the PDE system for the spatial velocity potential (for time-harmonic waves) and the plate deflection could be retrieved. To validate the multiple-scale method, a numerical method was introduced, for which the continuous roughness profile had to be approximated by piece-wise constant functions. Whereas the solution for the in-vacuo beam problem only consists of one travelling and one evanescent wave mode in both directions and each subinterval, the full-linear solution of the the velocity potential here contains one travelling, two damped-travelling and an infinite number of evanescent wave modes in both directions and each subinterval. For numerical computations, the full-linear solution in each sub-interval had to be approximated with a finite number of wave modes and an iterative algorithm similar to the one in the previous chapter was used to obtain the solution by applying continuity conditions at each scattering interface of adjacent sub-intervals.

The numerical method allowed us to confirm the assumptions made in the derivation of the multiple-scale method, which is more elaborate than the multiple-scale method for the in-vacuo beam problem and the corresponding Green's function presented by Porter and Evans (2006) is used to find the higher-order solutions. It is clear from the derivation of the multiple-scale method that it captures the attenuation of the effective wave fields only and therefore, conclusions about wave attenuation by sea ice cannot directly be drawn from this semi-analytical method. The continuous variations were modelled via the Gaussian autocorrelation process described in Ch. 2 and the multiple-scale method was derived for thickness variations. By setting the autocorrelation functions for the mass and rigidity variations, which are derived from the underlying process describing the varying thickness, zero, respectively, the multiple-scale methods for varying mass and varying rigidity could then directly be obtained. Finally, the attenuation coefficients predicted by the multiple-scale method and the numerical method were compared over a range of correlation lengths for small roughness amplitudes, which the multiple-scale method inherently assumes. The two methods showed a very good agreement, which validates the multiple-scale method and allows to calculate the attenuation of effective wave fields in a very efficient way.

CHAPTER 4

Wave attenuation along inhomogeneous strings: From continuous to discrete scatterers

The attenuation of effective wave fields in the problems of a beam in vacuo and a floating plate in Chs. 2 and 3 is predominantly a statistical effect caused by wave cancellation in the averaging process of an ensemble of different realisations. Hence, the effective wave field is not representative for individual realisations in these cases and, in particular, powerful analytic theories approximating the effective wave fields are not applicable to describe attenuation of individual wave fields. This discrepancy does not necessarily exist for discrete scatterers though, which was demonstrated e.g. in Bennetts and Peter 2013, where individual and effective wave fields showed the same attenuation behaviour in their problem setting of waves propagating through rows of discrete scatterers. To get a deeper understanding of these fundamental differences, we focus on wave propagation along one-dimensional strings and the relation between continuous and discrete scattering problems. Focusing on the string setting has the advantage not to have to deal with higher-order conditions and results from this fairly simple setting might be extended to more complex problems. In the case of large deflections, very thin plates can be considered as membranes, see Timoshenko and Woinowsky-Krieger 1959, hence very thin beams can for the sake of simplicity be considered (in the setting of non-linear theory) as strings.

Studying vibrations in strings and membranes has a long history, see e.g. Morse 1948, who gave an overview over applications of strings and membranes with varying density. Analysis of reflection and transmission behaviour can be found in Morin 2016 for non-uniform strings and Dall'Agnol 2011 for a two-string problem with two different mass densities. In contrast to homogeneous string problems, exact solutions cannot be found in general for inhomogeneous string problems. It needs additional assumptions, such as assumptions on density distributions, to obtain exact solutions, e.g. Wang and Wang (2013) studied homogeneous as well as inhomogeneous strings, deriving exact solutions for non-homogeneous strings with a power law density distribution and an exponential density distribution. Further examples for density distributions, which give closed-form exact solutions, are given in Horgan and Chan 1999. An approach using functional-analysis techniques was used by Limaco et al. (2008) to give estimates for the attenuation of energy for non-homogeneous elastic strings. To study wave propagation along an inhomogeneous string with varying densities of no particular distribution, for which no closed-form solutions can be obtained, numerical methods have to be adopted. A Chebyshev expansion method was used for solving integral equations describing oscillating inhomogeneous strings by Rawitscher and Liss (2011). Amore (2010, 2011) adopted a perturbation theory and collocation method for an inhomogeneous string with fixed ends. Work on vibrations of a non-homogeneous string under non-linear time-periodic forcing can be found in Baldi and Berti 2008.

Problems with disordered discrete scatterers received significant attention in the second half of the last century. The main reason for this is the work of Anderson (1958), who proposed localisation of electrons in disordered systems for sufficiently large randomness. This phenomenon can be observed e.g. for quantum, electromagnetic or acoustic waves. Research about electrons in crystal lattices dates from the fundamental work of de L. Kronig and Penney (1931), who described one-dimensional propagation of pressure fields through resonant point scatterers and observed pass- and stopband behaviour of electrons. The pass- and stopband behaviour is also a well known feature of classical (i.e. acoustic and electromagnetic) waves in periodic media, see e.g. Figotin and Kuchment 1995a,b for acoustic and 2D-periodic dielectric structures. It was observed in Figotin and Klein 1996 that Anderson localisation happens in those passbands in vicinity of the transition edge to the stopband. They also showed that similarities exist between localisation of quantum-mechanical electrons and localisation of classical waves, but it is more challenging to localise classical waves. A broad investigation of Anderson localisation can be found in Sheng 2006 and Richoux et al. 2007, who give a good overview of localisation in different contexts.

Localisation occurs in beaded strings as shown by Ottarsson and Pierre (1997), who studied effects of disorder on both bead mass and bead spacing for the beaded-string problem. They showed that bead-mass disorder produces only enhanced backscattering, whereas spacing disorder produces both enhanced scattering and localisation, where the localisation factor depends on disorder coupling and strength. Bead-mass disorder also leads to a conflict between disorder-induced localisation and periodicity-induced constructive interferences in passbands. The localisation behaviour for spacing disorder could also be observed experimentally by He and Maynard (1986). The one-dimensional model described by the Helmholtz equation for point scatterers represents not only vibrations in beaded strings, but also propagation of waves through an acoustic duct with Helmholtz resonators, see e.g. Richoux and Pagneux 2002, which is also an important application of guided waves with one propagating mode in the low frequency regime, see Richoux et al. 2015. A good introduction into vibration analysis of a finite number of masses on a taut string is given by Gladwell (2005). Besides the already mentioned experimental literature about this problem, agreement between theory and measurements for vibrations in beaded strings with nearly periodic structure is shown by Hodges and Woodhouse (1983). In addition, agreement between theoretical and experimental results for the cases with one and two concentrated masses on a homogeneous string fixed at both ends is shown by Gómez et al. (2007).

The perturbed periodic problem has been studied extensively over the last decades and analytical theories have been adopted to describe the effective wave field, i.a. a quasi-crystalline assumption considering perturbations from an underlying periodic setting (see Parnell and Abrahams 2008) and the coherent potential approximation based on closure assumptions (see Maurel et al. 2010). Maurel et al. (2010) also compared those approaches with direct calculations presented in Maurel 2010. A Monte Carlo method for vibrations in beaded strings was shown in Romack and Weaver 1990, who studied effective waves in one-dimensional random media composed of uncorrelated point scatterers with exponentially distributed scatterer spacings. Maurel and Martin (2013) showed that localised modes appear not only in infinite disordered media, but also in disordered media of finite size (using perturbation theory), and additionally studied compositional disorder. Perturbation theory was also used by Martin (2014) to study finite beaded strings with perturbations of the masses from their periodic structure by a small distance.

The two problems of strings with continuous and discrete inhomogeneities have been studied only separately to the knowledge of the author. To get an understanding why localisation does not happen in the problems of waves travelling along beams in vacuo and plates floating on water in Chs. 2 and 3, where the (continuous) beam and plate roughness are modelled via a Gaussian process, we will firstly introduce the continuous problem of wave propagation along a string with a (continuous) Gaussian correlated roughness profile in Sec. 4.1. The numerical method to calculate the wave fields for the continuous problem is based on the step-approximation method, which was introduced in Sec. 2.2. Each roughness realisation of the profile is approximated by discrete steps, which allows to use an efficient iterative scheme to calculate individual and effective wave fields. The iterative scheme also serves as the basis for the computations for the discrete beaded-string problem, for which evidently localisation will be observed for positional disorder of the scatterers. This problem setting is introduced in Sec. 4.2. For both problem settings, the attenuation behaviour of individual and effective wave fields will be investigated distinctly. The attenuation analysis for the beaded-string problem is conducted in dependence of positional disorder of the beads on the string for a broad regime of scattering strengths and we compare the results with the theoretical Berry–Klein limit. The Berry–Klein limit, which is derived by Berry and Klein (1997), is the attenuation coefficient determined originally for a stack of transparent plates and calculated on the assumption that all phases are included in wave interactions between adjacent plates. Bennetts and Peter (2013) showed that this limit is reached for waves travelling through a perturbed periodic array of point scatterers for large disorder from the underlying periodic setting.

To establish a connection between the continuous and discrete problem in Sec. 4.3, a numerical method is adopted to cluster a very long roughness realisation into single humps and their statistical properties (i.e. reflection coefficient moduli and arguments) are examined. The mean reflection coefficient modulus is then transferred to the discrete problem and assigned as the scattering strength. Furthermore, the distribution of phase angles obtained for the continuous problem is fitted with a non-parametric distribution and then used as the distribution of positional disorder in the discrete problem, before comparing the attenuation of the continuous and the adjusted discrete problem. A summary and discussion of the results of the chapter are given in Sec. 4.4.

4.1 String with continuously varying density

4.1.1 Problem formulation

We consider an infinitely long, one-dimensional string and denote the horizontal coordinate with x. The spatial part $u(x)$ of the time-harmonic string deflection $\mathrm{Re}\{u(x)\mathrm{e}^{-\mathrm{i}\omega t}\}$ satisfies the (spatial) Helmholtz equation

$$\partial_x^2 u(x) + k^2 u(x) = 0, \qquad x \in (-\infty,\infty), \tag{4.1}$$

where ω is the angular frequency and k the wavenumber. The one-dimensional Helmholtz equation can be derived from the wave equation with one spatial dimension,

$$\left(\frac{\partial^2}{\partial x^2} - \frac{1}{c^2}\frac{\partial^2}{\partial t^2}\right)\mathcal{U}(x,t) = 0, \tag{4.2}$$

where c is depends on the string density and $\mathcal{U}$ is the (time-dependent) string deflection. Assuming that $\mathcal{U}$ is separable into a factor only depending on x and one only on t (which is e.g. possible for a time-harmonic string deflection with angular frequency ω), the Helmholtz equation results from using separation of variables and substituting $k = \omega/c$.

In the following, we consider a string with a varying density profile. These variations in the string density lead to a varying wavenumber $k(x)$, such that the varying wavenumber fluctuates about the mean wavenumber $\bar{k}$ and is defined as $k(x) = \bar{k}(1 + \epsilon\kappa(x))$, with $\kappa = \mathcal{O}(1)$. In analogy to the continuous roughness profiles in the previous chapters, the fluctuations, $\epsilon\kappa(x)$, have a known characteristic length, l_{G}, and (non-dimensional) roughness amplitude, ϵ, and are prescribed by the Gaussian autocorrelated random process given in Sec. 2.4. The ergodicity of the random process $\kappa(x)$ ensures the spatial and ensemble Gaussian autocorrelation conditions,

$$\mathbf{E}[\kappa(x)\kappa(x-\xi)] = \langle \kappa(x)\,\kappa(x-\xi)\rangle = \rho(|\xi|), \tag{4.3}$$

where $\mathbf{E}[\cdot]$ denotes the spatial average and $\langle\cdot\rangle$ the ensemble average of the included quantity, respectively. Note that the frequencies and phases in the generation of the random process via Eqn. (2.76) are not random variables, but sample values in the case of the spatial Gaussian autocorrelation condition dealing with individual process realisations over long intervals.

For numerical computations, let the string roughness similarly to the previous problems extend over the long, finite interval $x \in (0,L)$ and be constant in the surrounding intervals $(-\infty, 0)$ and (L,∞). The roughness profile is approximated by a piece-wise constant function on $M \gg 1$ sub-intervals, with $(-\infty, 0)$ and (L,∞) the 0-th and $(M + 1)$-th sub-intervals, respectively. We continue to use the discretisation method introduced in Sec. 2.2, for which each correlation length is divided into four sub-intervals to obtain the numerical results involving the step approximation in this chapter. For the numerical results, an interval length, L, of 400 times the correlation length is chosen to be sufficiently large to capture attenuation coefficients accurately.

We hold on our scheme to denote the value of the wavenumber in the m-th sub-interval as k_m, and set it to be equal to the value of the corresponding continuous wavenumber profile at the mid-point. In the m-th sub-interval, the wave field can be expressed as

$$u_m(x) = a_m \, \mathrm{e}^{\mathrm{i}k_m x} + b_m \, \mathrm{e}^{-\mathrm{i}k_m x}. \tag{4.4}$$

The wave amplitudes a_m and b_m correspond to right- and left-travelling waves, respectively, and no damped-travelling or evanescent waves appear here. Setting $a_0 = 1$ and $b_{M+1} = 0$ ensures the motion forcing by a unit-amplitude incident wave propagating in the positive x-direction from $x \to -\infty$.

To couple wave fields in adjacent sub-intervals in this second-order problem, only two continuity conditions are needed: continuity of deflection (u) and deflection slope ($\partial_x u$). Those are applied in the same fashion as described in Sec. 2.2 (see Eqns. (2.15)) and the iterative algorithm calculating the amplitudes a_m ($m = 1, \ldots, M+1$) and b_m ($m = 0, \ldots, M$) for a given roughness realisation is based on the familiar step-approximation method.

4.1.2 Numerical results

Since we do not focus on analytical approaches and the investigation of their validity in this chapter anymore, we can suspend the restriction on the upper bound of the roughness amplitude, which automatically ensured that the beam mass, beam rigidity and beam thickness, respectively, did not become negative in the previous problems. To avoid unphysical negative wavenumbers here, which might appear for roughness amplitudes larger than about $\epsilon \approx 0.2$, a numerical scheme is used, which sets the wavenumbers smaller than 10^{-2} to this value in the respective sub-intervals. The numerical cut-off scheme leads to a relaxation of the autocorrelation conditions in Eqn. (4.3) for large roughness amplitudes.

Fig. 4.1 shows individual and effective attenuation coefficients, calculated by the random-sampling method, scaled by ϵ^2 as functions of non-dimensional correlation length, for the roughness amplitudes $\epsilon = 1.0 \times 10^{-3}$ (top-left panel), 1.0×10^{-2} (top-right panel), 1.0×10^{-1} (bottom-left panel) and 5.0×10^{-1} (bottom-right panel). To obtain the attenuation coefficients in Fig. 4.1, we use an ensemble size of 1500 in analogy to our studies in the previous chapters. A semi-analytical solution using a multiple-scale approach for wave propagation along a string with continuously varying string density is shown for comparison. The derivation can be found in Appendix 4.A. The attenuation coefficients describing the exponential decay of individual and effective wave fields are calculated via the previously used least-squares minimisation routine and Eqns. (2.77).

We can see in Fig. 4.1 that the attenuation coefficients of individual wave fields are close to zero for the smallest non-dimensional correlation length considered, $\bar{k}l_{\mathrm{G}} = 0.1$, and for correlation lengths greater than two. Similarly to the results in Chs. 2 and 3, the fluctuations for $\bar{k}l_{\mathrm{G}} = 0.1$ are too rapid to affect the wave propagation and, for the larger correlation length regime, the roughness is too mild to attenuate the waves. In between those two regimes, the attenuation coefficients increase significantly with a maximum attenuation

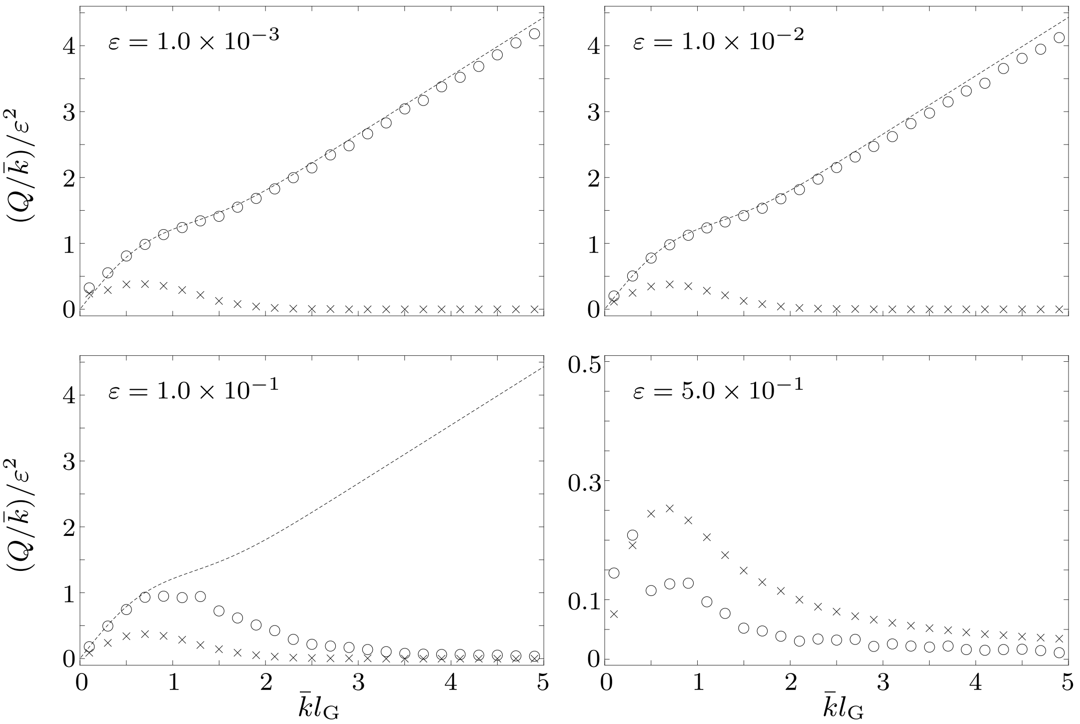

Figure 4.1: Individual (×) and effective (∘) attenuation coefficients for continuous non-homogeneous string problem as functions of correlation length, for roughness amplitudes $\epsilon = 1.0 \times 10^{-3}$ (top-left panel), $\epsilon = 1.0 \times 10^{-2}$ (top-right panel), $\epsilon = 1.0 \times 10^{-1}$ (bottom-left panel) and $\epsilon = 5.0 \times 10^{-1}$ (bottom-right panel). Attenuation coefficients predicted by multiple-scale method (dashed line) are shown for comparison.

coefficient $Q_{\mathrm{ind}} \approx 0.4\epsilon^2$ for $\bar{k}l_{\mathrm{G}} = 0.7$ for the smaller roughness amplitudes $\epsilon = 1.0 \times 10^{-3}$ and 1.0×10^{-2}. For the largest roughness amplitude considered, $\epsilon = 5.0 \times 10^{-1}$, the attenuation coefficient maximum decreases to $Q_{\mathrm{ind}} \approx 0.27\epsilon^2$ (again for $\bar{k}l_{\mathrm{G}} = 0.7$).

In comparison to this, the effective attenuation coefficients show significantly different properties, both qualitatively and quantitatively. While the effective attenuation coefficient is also close to zero for the non-dimensional correlation length $\bar{k}l_{\mathrm{G}} = 0.1$, it increases with increasing correlation length and for $\bar{k}l_{\mathrm{G}} \geq 2$, the attenuation coefficients are linear with respect to $\bar{k}l_{\mathrm{G}}$ for the smaller roughness amplitudes. This different attenuation behaviour of individual and effective wave fields is due to wave cancellation again, which arises for the de-coherent individual wave fields. For the two larger roughness amplitudes considered, $\epsilon = 1.0 \times 10^{-1}$ and 5.0×10^{-1}, this behaviour is notably different. For $\epsilon = 1.0 \times 10^{-1}$, the effective attenuation coefficients are of the same magnitude as for the smaller roughness amplitude cases for $\bar{k}l_{\mathrm{G}} \leq 0.7$. Instead of exhibiting larger attenuation for increasing correlation lengths then, the effective attenuation coefficients decrease similarly to the individual attenuation coefficients, but are still larger. For $\bar{k}l_{\mathrm{G}} \geq 3.5$, the effective attenuation coefficients are close to zero. For the largest roughness amplitude case, $\epsilon = 5.0 \times 10^{-1}$, the effective attenuation coefficients also show a hump in the small correlation length regime, but the values are even smaller than their individual counterparts.

Furthermore, the attenuation coefficients predicted by the multiple-scale method show a good agreement with the effective attenuation coefficients obtained by the random-sampling method for the two smaller roughness amplitude cases up to the large correlation length regime, where small lower deviations are especially observable for $\epsilon = 1.0 \times 10^{-2}$. Since the attenuation coefficients predicted by the multiple-scale method are perfectly scaled with ϵ^2, the agreement between them and the effective attenuation coefficients is lost and they clearly overpredict the latter for large roughness amplitudes. While for the largest roughness amplitudes, $\epsilon = 5.0 \times 10^{-1}$, the limit of validity for the multiple-scale method is clearly exceeded, the attenuation coefficients predicted by the multiple-scale method still agree with the effective attenuation coefficients in the small correlation length regime $\bar{k}l_{\mathrm{G}} \leq 0.7$ for $\epsilon = 1.0 \times 10^{-1}$.

For the largest roughness amplitude, $\epsilon = 5.0 \times 10^{-1}$, the effective attenuation coefficients are smaller than the corresponding individual attenuation coefficients for $\bar{k}l_{\mathrm{G}} \geq 0.5$, which is due to the averaging process to calculate the effective wave field. Under the assumption of exponential decay of the wave fields with comparable attenuation and the triangle inequality, $|\langle u(x) \rangle| \leq \langle |u(x)| \rangle$ must hold and we can deduce that the average of individual attenuation coefficients represent a lower limit of the effective attenuation coefficients. However, for roughness amplitudes larger than $\epsilon \approx 0.2$, individual wave fields exist which attenuate much slower than the vast majority of the other wave fields. These wave fields dominate when averaging all individual wave fields in the random-sampling method to calculate the effective wave field and distort the results. This can be clearly observed when calculating the attenuation coefficient of the averaged wave field modulus, i.e. $\langle |u(x)| \rangle$, which gives significantly smaller results than the average of attenuation coefficients calculated for each individual wave field. To overcome the sensitivity to outliers for large roughness amplitudes in the averaging process, only wave fields with individual attenuation coefficients lying between the 25% and 75% quantiles of all individual attenuation coefficients are taken into account for the averaging process to obtain the effective wave field. To ensure that effective wave fields are calculated using an ensemble size of 1500 randomly generated roughness profile realisations, for which the effective attenuation coefficients are converged with respect to the ensemble size as shown for the in-vacuo beam problem in Fig. 2.15, an ensemble size of 3000 roughness profile realisations is used before applying the quantile approach to obtain the effective attenuation coefficient. We will refer to this approach as the quantile approach in the following. It should be noted that due to the strong scattering in the large roughness amplitude regime, individual wave field realisations might exist, which do not necessarily attenuate clearly exponentially such that the least-squares approach to extract the attenuation coefficients might not be adequate anymore. These individual wave field realisations are inherently disregarded by the quantile approach. (Note that the individual attenuation coefficients are calculated for the ensemble with respect to the quantiles as well.)

Fig. 4.2 shows the same quantities as in Fig. 4.1, i.e. individual and effective attenuation coefficients, calculated by the random-sampling method, together with attenuation coefficients predicted by the multiple-scale method, but now the quantile approach is used.

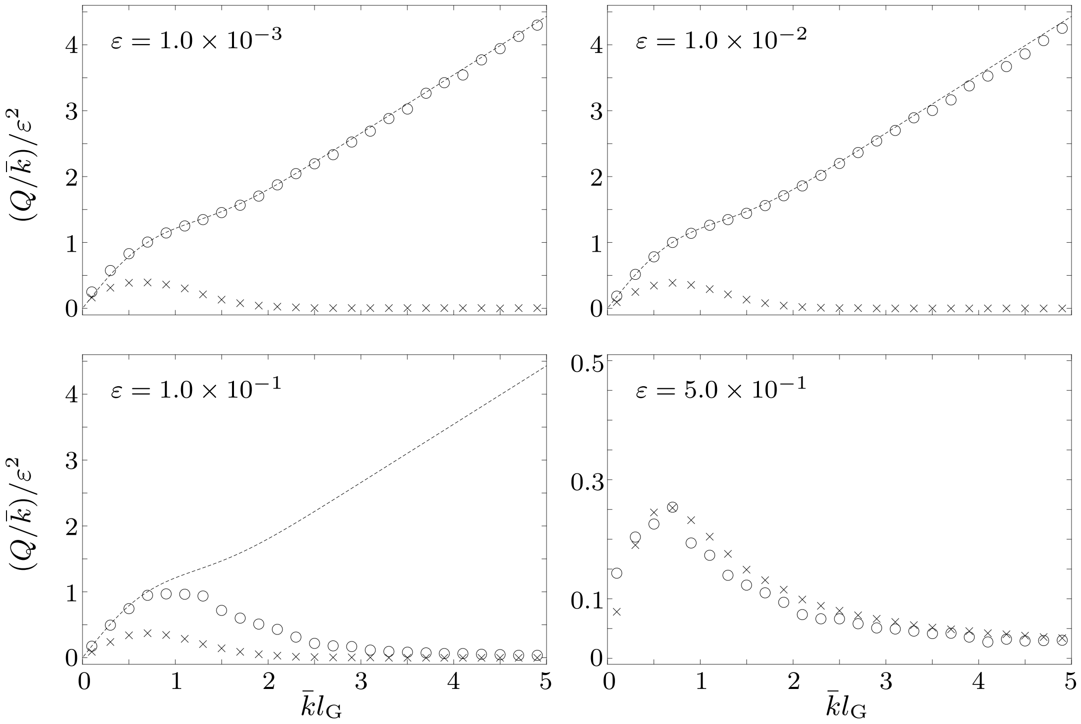

Figure 4.2: Individual (×) and effective (∘) attenuation coefficients with quantile approach for continuous non-homogeneous string problem as functions of correlation length, for roughness amplitudes $\epsilon = 1.0 \times 10^{-3}$ (top-left panel), $\epsilon = 1.0 \times 10^{-2}$ (top-right panel), $\epsilon = 1.0 \times 10^{-1}$ (bottom-left panel) and $\epsilon = 5.0 \times 10^{-1}$ (bottom-right panel). Attenuation coefficients predicted by multiple-scale method (dashed line) are shown for comparison.

By comparisons with the results shown in Fig. 4.1, we can see in Fig. 4.2 that the quantile approach has only marginal effects on the effective attenuation coefficients for $\epsilon = 1.0 \times 10^{-3}$, 1.0×10^{-2} and 1.0×10^{-1}, for which slightly larger attenuation coefficients are obtained in the large correlation length regime (only visible in the two small roughness amplitude cases due to the scaling). As a result, the effective attenuation coefficients obtained by the random-sampling method move closer to the attenuation coefficients predicted with the multiple-scale method. For the largest roughness amplitude in consideration, $\epsilon = 5.0 \times 10^{-1}$, we can observe that the effective attenuation coefficients nearly coincide with the individual attenuation coefficients using the quantile approach for $\bar{k}l_{\mathrm{G}} \geq 0.5$, i.e. the effective attenuation coefficients are of the same magnitude as the individual attenuation coefficients and share the same qualitative features with both attenuation coefficients attaining their maxima at $\bar{k}l_{\mathrm{G}} = 0.7$. Furthermore, we can see that the individual attenuation coefficients give the same values using the quantile approach as in Fig. 4.1, for which all attenuation coefficients in the ensemble of size 1500 realisations were used, throughout the whole correlation length regime. Also, wave field outliers do not affect the individual attenuation coefficients since the obtained attenuation coefficients of individual wave fields in the averaging process are all of the same order. This does not hold for averaging the wave fields to obtain the effective wave field without the quantile approach for large roughness amplitudes.

The behaviour of individual and effective attenuation coefficients over a regime of roughness amplitudes is investigated now. With the numerical scheme of cutting off unphysical values in rough-profile realisations, it is now possible to study regimes of large roughness amplitudes. To capture effective attenuation coefficients for large roughness amplitudes accurately, it is necessary to use the quantile approach to calculate effective wave fields as explained above. Hence and for matters of consistency, the effective attenuation coefficients are calculated using the quantile approach throughout the whole roughness amplitude regime.

Fig. 4.3 depicts the scaled attenuation coefficients as functions of roughness amplitude, for the non-dimensional correlation lengths $\bar{k}l_{\mathrm{G}} = 0.7$ (top-left panel), 1.5 (top-right panel), 2.5 (bottom-left panel) and 4.1 (bottom-right panel). The results predicted by the multiple-scale method are shown for comparison.

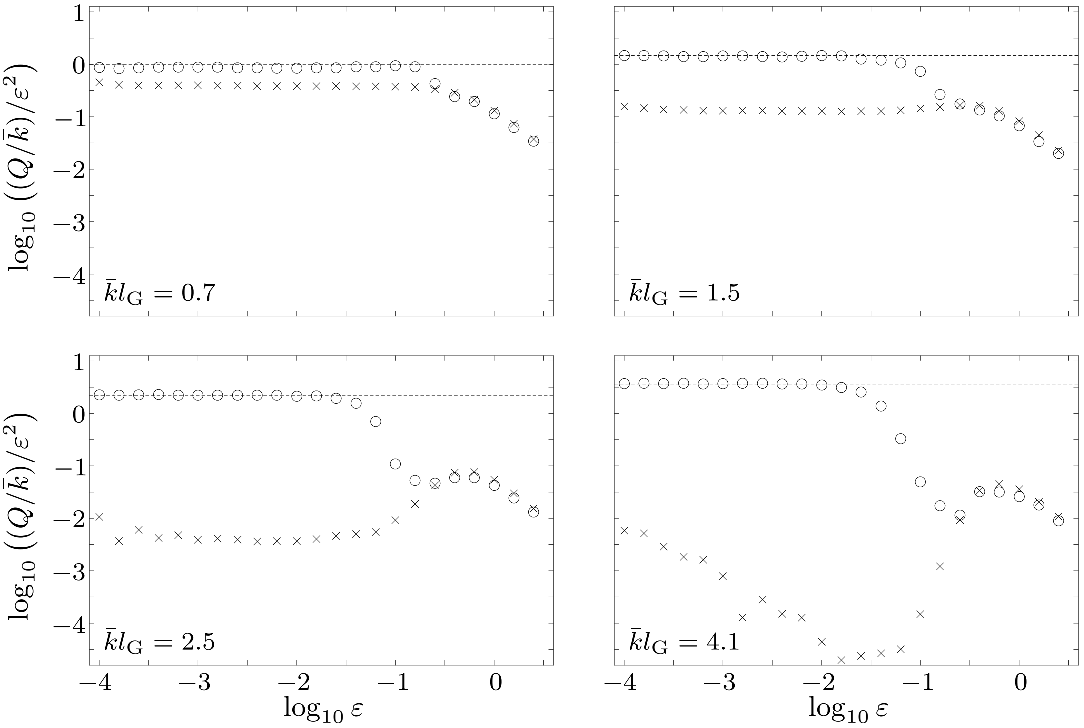

Figure 4.3: Individual (×) and effective (∘) attenuation coefficients for continuous non-homogeneous string problem as functions of roughness amplitude, for non-dimensional correlation length $\bar{k}l_{\mathrm{G}} = 0.7$ (top-left panel), $\bar{k}l_{\mathrm{G}} = 1.5$ (top-right panel), $\bar{k}l_{\mathrm{G}} = 2.5$ (bottom-left panel) and $\bar{k}l_{\mathrm{G}} = 4.1$ (bottom-right panel). Attenuation coefficients predicted by multiple-scale method (dashed line) are shown for comparison.

The top-left panel of Fig. 4.3 shows for the non-dimensional correlation length $\bar{k}l_{\mathrm{G}} = 0.7$, which produces maximum attenuation of individual wave fields, that the individual and effective attenuation coefficients are proportional to the roughness amplitude squared for roughness amplitudes less than $10^{-0.8}$. The effective attenuation coefficients are significantly greater than the individual attenuation coefficients in this regime. The proportionality of the attenuation coefficients disappears for larger roughness amplitudes and both attenuation coefficients increase with increasing roughness amplitudes slower than the roughness amplitude squared. It is most remarkable that the effective attenuation coefficients are very close to the individual attenuation coefficients in this regime. This qualitative behaviour is confirmed for the non-dimensional correlation length $\bar{k}l_{\mathrm{G}} = 1.5$, but the proportionality to the roughness amplitude squared is lost for $\epsilon > 10^{-1.2}$.

The bottom panels of Fig. 4.3 show the behaviour of the attenuation coefficients as functions of the roughness amplitude for the cases $\bar{k}l_{\mathrm{G}} = 2.5$ and 4.1. The discrepancy between the effective and individual attenuation coefficients is larger for the small roughness amplitude regime in these cases due to the smoother roughness profile leading to less attenuation and a fortified wave cancellation effect (for the effective wave field). For $\bar{k}l_{\mathrm{G}} = 2.5$, the proportionality of both the effective and individual attenuation coefficients is already lost for $\epsilon > 10^{-1.4}$, and for the largest correlation length, $\bar{k}l_{\mathrm{G}} = 4.1$, the proportionality of the effective attenuation coefficients is lost slightly earlier and the individual attenuation coefficients do not exhibit this proportionality in the small roughness amplitude regime, which is due to numerical difficulties in capturing these very small attenuation coefficients.

The attenuation coefficients predicted by the multiple-scale method show a very good agreement with the effective attenuation coefficients for small roughness amplitudes in all cases considered. We can see that with increasing correlation length the limit of validity of the multiple-scale method is reached earlier. It is also remarkable that the scaled attenuation coefficients do not only decrease for large roughness amplitudes for the two large correlation lengths considered, $\bar{k}l_{\mathrm{G}} = 2.5$ and 4.1, but the effective attenuation coefficients show a small increasing hump in these cases and the (scaled) individual attenuation coefficients start to increase for the not-so-small roughness amplitude $\epsilon \approx 10^{-1}$ to meet the effective attenuation coefficients for $\epsilon \approx 10^{-0.5}$ and decrease together with them in the large roughness amplitude regime. Again, for the considered regime $\epsilon > 10^{-0.6}$, the individual and effective attenuation coefficients are representative of each other.

Fig. 4.4 shows example individual wave fields and corresponding effective wave fields, for non-dimensional correlation length $\bar{k}l_{\mathrm{G}} = 0.7$ and roughness amplitudes $\epsilon = 5.0 \times 10^{-2}$ (left-hand panel), 1.0×10^{-1} (middle panel) and 2.0×10^{-1} (right-hand panel).

We can observe in Fig. 4.4 the qualitative transitional behaviour of individual and effective wave fields from small to large roughness amplitudes. For the smallest roughness amplitude, $\epsilon = 5.0 \times 10^{-2}$, the discrepancy between individual and effective wave fields is obvious and the individual wave field attenuates only weakly and less than its corresponding effective wave field. For $\epsilon = 1.0 \times 10^{-1}$, the attenuation is significantly larger for both individual and effective wave fields, but the attenuation of the effective wave field still dominates the attenuation of the individual wave field. This changes for $\epsilon = 2.0 \times 10^{-1}$, for which both

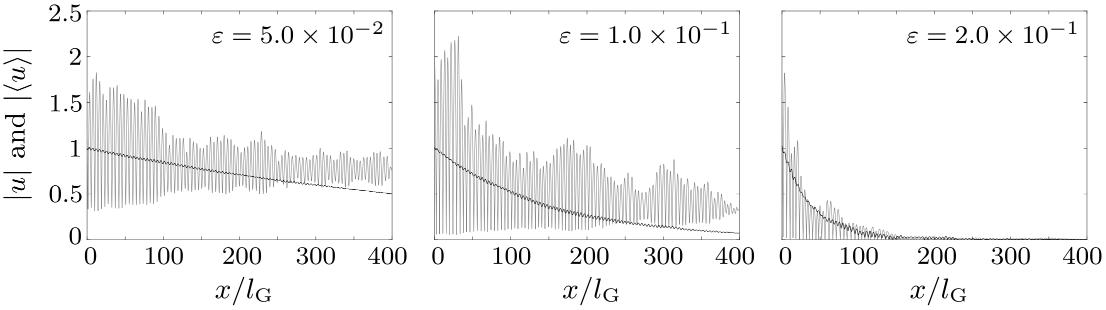

Figure 4.4: Example individual wave fields (grey curves) and effective wave fields (black) for continuous non-homogeneous string problem for roughness amplitudes $\epsilon = 5.0 \times 10^{-2}$ (left-hand panel), $\epsilon = 1.0 \times 10^{-1}$ (middle panel) and $\epsilon = 2.0 \times 10^{-1}$ (right-hand panel), for correlation length $\bar{k}l_{\mathrm{G}} = 0.7$

wave fields attenuate at a comparable rate and the wave fields vanish almost completely after half of the rough interval.

The agreement of individual and effective attenuation coefficients for large continuous scattering enhances the understanding of the results not only for the in-vacuo beam and floating beam problems in Chs. 2 and 3, but also for previous works on attenuation with continuous scatterers only dealing with small roughness amplitude regimes, for which the individual and effective wave fields are not representative for each other. This changes observably in our problem for large roughness amplitudes. Before connecting this problem of wave attenuation along a string with varying density with the discrete problem of wave attenuation along a beaded string in Sec. 4.3, we focus in the following section on the one-dimensional beaded-string problem with a perturbed periodic arrangement of point scatterers, i.e. the roughness is incorporated via positional disorder of the discrete point scatterers.

4.2 Beaded string

4.2.1 Problem formulation

We model time-harmonic wave propagation along a beaded string with N scatterers of the same scattering strength η, positioned at $x = x_n$, $n = 1, \ldots, N$, which is described by the following Helmholtz equation for point scatterers,

$$\partial_x^2 u(x) + k^2 u(x) = 2\mathrm{i}k\eta \sum_{n=1}^{N} \delta(x - x_n) u(x), \tag{4.5}$$

where δ is the Dirac delta distribution. In contrast to Eqn. (4.1) the wavenumber k is constant here and the scattering properties are incorporated via the inhomogeneous right-hand side. This equation is obtained for the case that the string, which is described by the one-dimensional wave equation, Eqn. (4.2), is loaded with point masses $-2\mathrm{i}\eta/(\omega c)$.

For a string with a single bead at the position $x = x_n$, the wave equation becomes

$$\frac{\partial^2}{\partial x^2}\mathcal{U}(x,t) = \left(\frac{1}{c^2} - \frac{2\mathrm{i}\eta}{\omega c}\delta(x - x_n)\right)\frac{\partial^2}{\partial t^2}\mathcal{U}(x,t). \tag{4.6}$$

To describe wave propagation along N masses positioned at x_n, $n = 1, \dots, N$, Eqn. (4.6) has to be extended to

$$\frac{\partial^2}{\partial x^2}\mathcal{U}(x,t) = \left(\frac{1}{c^2} - \frac{2\mathrm{i}\eta}{\omega c}\sum_{n=1}^{N}\delta(x - x_n)\right)\frac{\partial^2}{\partial t^2}\mathcal{U}(x,t). \tag{4.7}$$

The underlying equation for the beaded-string problem, Eqn. (4.5), is obtained for time-harmonic waves with angular frequency ω and substituting $k = \omega/c$.

The position of the scatterers, x_n, is perturbed around the distance between adjacent scatterers in periodic position, d. (Note that $x_n = (n-1)d$ would be the position of the n-th scatterer in the periodic case.) The positional disorder is introduced with random variables $\nu_n, n = 1, \dots, N$, which describe the positional offset of the n-th scatterer from the underlying periodic case, i.e. $x_n = (n-1+\nu_n)d$. The random variable ν_n is randomly chosen from a prescribed distribution such that the n-th scatterer does not leave its imaginary cell $x_{n+1} \in ((n-1/2)d, (n+1/2)d)$. It follows that for all realisations of disorder each of these imaginary cells contains a single scatterer, hence the scatterers stay in ordered position with ascending index. Restricting the positional disorder in this way ensures that all scatterers are distributed around their mean, i.e. periodic, positions. Loosening this restriction and allowing all scatterers to be located randomly in the whole space would lead to Poisson distributed distances between nearest scatterers, which can be observed in Maurel and Pagneux 2008. Note that the choice $\nu_n = 0$ for all $n = 1, \dots, N$, gives the periodic problem. Fig. 4.5 schematically shows the configuration of discrete scatterers for the beaded-string problem.

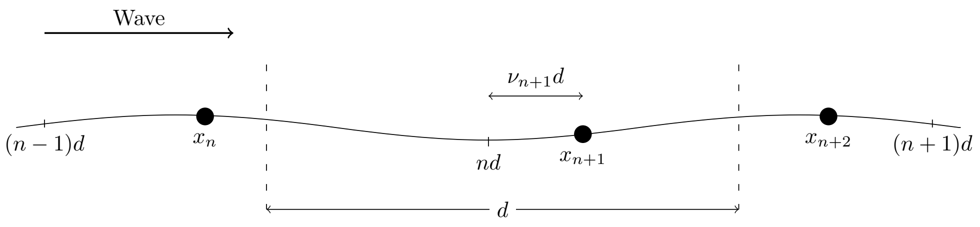

Figure 4.5: Configuration of discrete scatterers located at x_n, x_{n+1} and x_{n+2} in beaded-string problem

The wave field between each scatterer can be written as

$$u(x) = a_n \mathrm{e}^{\mathrm{i}k(x-x_n)} + b_n \mathrm{e}^{-\mathrm{i}k(x-x_n)}, \quad x_{n-1} \le x \le x_n, \tag{4.8}$$

where a_n and b_n are the wave amplitudes corresponding to the right- and left-travelling wave, respectively, between the $(n-1)$-th and n-th scatterer. Again, the motion is forced by a unit-amplitude incident wave propagating in the positive x-direction from $x \to -\infty$, which is set via $a_0 = 1$ and $b_{N+1} = 0$. The wave fields in the interval left and right to the n-th scatterer are coupled via a continuity of deflection and a continuity of force condition,

$$\langle\langle u \rangle\rangle_{x_n} = 0, \tag{4.9a}$$

$$\langle\langle \partial_x u \rangle\rangle_{x_n} = 2\mathrm{i}k\eta u(x_n), \tag{4.9b}$$

where $\langle\langle \cdot \rangle\rangle_{x_n}$ denotes the jump of the included quantity at $x = x_n$. The force continuity condition arises from the equivalence of the slope difference across the bead and the force exerted on the bead positioned at $x = x_n$ for time-harmonic waves (see Barnwell 2014), i.e. Newton's law gives for the underlying time-dependent problem

$$\langle\langle \partial_x \mathfrak{U}(x,t) \rangle\rangle_{x_n} = -\frac{2\mathrm{i}\eta}{\omega c} \frac{\partial^2 \mathfrak{U}(x,t)}{\partial t^2}\bigg|_{x=x_n}. \tag{4.10}$$

This force balance corresponds to the jump condition for a single point mass at the origin, which is obtained by integrating Eqn. (4.6) over $x \in (-\epsilon,\epsilon)$ for $\epsilon \to 0$ and using that the integral of the Dirac delta distribution over this vanishingly region is unity.

To calculate the wave field $u(x)$ for N scatterers, a discrete iterative scheme corresponding to the numerical method in Sec. 4.1 is used and the scattering matrices at the interfaces of adjacent intervals are obtained by the continuity conditions (4.9). This approach can be transferred to the direct numerical scheme used by Maurel et al. (2010).

4.2.2 Validation of numerical approximation

The direct numerical scheme in Maurel et al. 2010 is based on a recurrence relation for the amplitudes of left-travelling waves in each interval between scatterers. This approach is presented in Appendix 4.B. The left-hand panels in Fig. 4.6 show the individual wave fields calculated by the direct numerical scheme and the discrete iterative scheme for the parameter combinations used in Maurel et al. 2010, i.e. (a) $kd = 14.2\pi$ and $\eta = 0.67/(2\mathrm{i})$, (b) $kd = 14.2\pi$ and $\eta = 3/(2\mathrm{i})$, (c) $kd = 2\pi/5.1$ and $\eta = 1.45/(2\mathrm{i})$. The right-hand panels depict the error of the wave field moduli between both methods at each scatterer.

We can see in Fig. 4.6 that the direct numerical scheme (used in Maurel et al. 2010) and the discrete iterative scheme (which will be used in the following) yield individual wave fields, which are very close to each other. This is confirmed by the wave field moduli differences at each scatterer, which indicate that both methods produce results and agree nearly up to machine precision. This agreement is expected since both methods can be converted into one another. The one-dimensional string problem allows to simplify the more elaborate method using the full iterative scheme in this easy manner and results in the computationally more efficient direct numerical scheme.

To study the pass- and stopband behaviour of the beaded-string problem, we investigate the eigenvalues of the transfer matrix at each scatterer (see Fig. 4.8). We consider

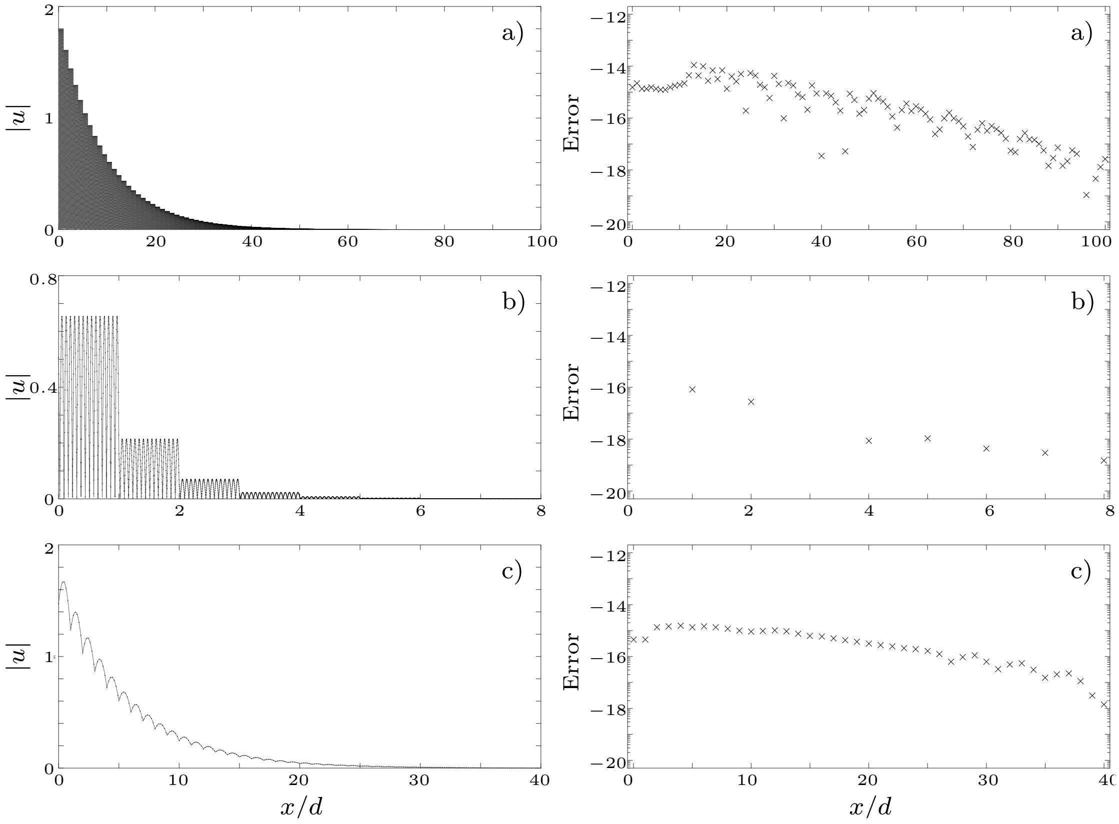

Figure 4.6: Left-hand panels: Wave field moduli obtained by direct numerical scheme (grey line) and discrete iterative scheme (black dotted line) for (a) $kd = 14.2\pi$ and $\eta = 0.67/(2\mathrm{i})$, (b) $kd = 14.2\pi$ and $\eta = 3/(2\mathrm{i})$, (c) $kd = 2\pi/5.1$ and $\eta = 1.45/(2\mathrm{i})$ (parameters from Maurel et al. 2010). Right-hand panels: Absolute error of wave fields obtained by those two methods for same parameters as in left-hand panels.

a single point scatterer, which is located at the origin, and write the wave fields left and right of the scatterer, u_- and u_+, respectively, with the help of the cell's reflection and transmission coefficients, $R^{(\pm)}$ and $T^{(\pm)}$. The superscript $-$ corresponds to the reflection and transmission properties for waves incident on the scatterer from the left and the superscript $+$ for waves from the right. Considering a wave incident from the left, the wave field can be written as

$$u(x) = \begin{cases} \mathrm{e}^{\mathrm{i}kx} + R^{(-)}\mathrm{e}^{-\mathrm{i}kx}, & x < 0, \\ T^{(-)}\mathrm{e}^{\mathrm{i}kx}, & x > 0. \end{cases} \tag{4.11}$$

For a wave incident from the right, we have

$$u(x) = \begin{cases} T^{(+)}\mathrm{e}^{-\mathrm{i}kx}, & x < 0, \\ \mathrm{e}^{-\mathrm{i}kx} + R^{(+)}\mathrm{e}^{\mathrm{i}kx}, & x > 0. \end{cases} \tag{4.12}$$

Using the wave field representation from Eqn. (4.8), the relationship between amplitudes in the adjacent intervals at the scatterer x_n can be written via a scattering matrix $\mathbf{S}$ as

$$\begin{pmatrix} b_n \\ a_{n+1} \end{pmatrix} = \underbrace{\begin{pmatrix} R^{(-)} & T^{(+)} \\ T^{(-)} & R^{(+)} \end{pmatrix}}_{=:\mathbf{S}} \begin{pmatrix} a_n \\ b_{n+1} \end{pmatrix}. \tag{4.13}$$

The point scatterers are assumed to be energy conserving, which yields

$$T^{(-)} = T^{(+)} \equiv T, \tag{4.14a}$$
$$1 - |T|^2 = |R^{\pm}|^2 \equiv |R|^2, \tag{4.14b}$$
$$(R^{(-)})^* T + R^{(+)} T^* = 0, \tag{4.14c}$$

where the complex conjugation is denoted by the asterisk, see Martin et al. 2015. The entries of the scattering matrix $\mathbf{S}$ are then given by

$$R^{(-)} = \frac{\eta}{\eta - 1}, \tag{4.15a}$$
$$R^{(+)} = \frac{\eta\, \mathrm{e}^{-2\mathrm{i}k(x_n - x_{n+1})}}{\eta - 1}, \tag{4.15b}$$
$$T^{(-)} = \frac{\mathrm{e}^{-\mathrm{i}k(x_n - x_{n+1})}}{\eta - 1} = T^{(+)}. \tag{4.15c}$$

For a point scatterer with scattering strength η located at the origin, the following representation of reflection and transmission coefficients can be obtained,

$$R(\eta) = \frac{\eta}{1 - \eta}, \tag{4.16a}$$
$$T(\eta) = \frac{1}{1 - \eta} = 1 + R(\eta). \tag{4.16b}$$

Now, we show in analogy to Maurel et al. 2010 that the scattering strength η has to be purely imaginary to obtain energy-conserving solutions for the scattering problems. It follows from Eqn. (4.14b) that

$$|R|^2 + |1 + R|^2 = 1 \quad \Longrightarrow \quad |R|^2 + \mathrm{Re}(R) = 0. \tag{4.17}$$

The solution to Eqn. (4.17) is shown in Fig. 4.7.

Thus, the solution has to be of the form

$$R = \mathrm{i}\mathrm{e}^{\mathrm{i}\varphi} \sin(\varphi) \tag{4.18}$$

for some real φ. With this, the scattering strength can be written as

$$\eta = \frac{R}{1 + R} = \mathrm{i} \tan(\varphi), \tag{4.19}$$

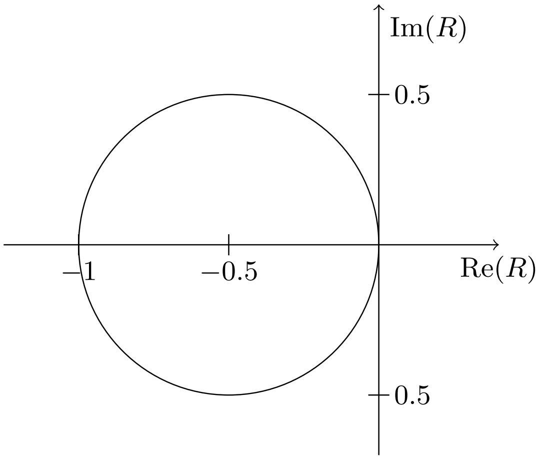

Figure 4.7: Reflection coefficient in energy-conserving setting

which implies that the scattering strength η has to be purely imaginary in our energy-conserving setting. Note that the reflection and transmission coefficients are complex and involve a phase shift. The phase shift is caused by the slope discontinuity at the point scatterers to provide the force balance, see Barnwell 2014.

We analyse the eigenvalues of the transfer matrix in order to study the pass- and stopband behaviour. The transfer matrix, which is associated to the scattering matrix $\mathbf{S}$ in analogy to the previous problem formulations (Secs. 2.2 and 3.2), describing

$$\begin{pmatrix} a_{n+1} \\ b_{n+1} \end{pmatrix} = \mathbf{P} \begin{pmatrix} a_n \\ b_n \end{pmatrix}, \tag{4.20}$$

is defined by

$$\mathbf{P} = \begin{pmatrix} T^{(+)} - R^{(+)}R^{(-)}/T^{(-)} & R^{(+)}/T^{(-)} \\ -R^{(-)}/T^{(-)} & 1/T^{(-)} \end{pmatrix}. \tag{4.21}$$

The top panels in Fig. 4.8 show the the eigenvalues of the transfer matrix, λ, for $\mathrm{i}\eta = 0.2$ (top-left panel) and additionally for $\mathrm{i}\eta = 0.4$ (top-right panel) over the interval $kd \in (0{,}11\pi)$. The bottom panel shows the moduli of the eigenvalues of the transfer matrix, which lie within the unit circle, as functions of kd/π for the scattering strengths $\mathrm{i}\eta = 0.2$ 0.4, 0.6, . . . , 2.0.

We can observe in the top panels that the eigenvalues pass along the unit circle and form conjugate pairs. As soon as the eigenvalues get close to the real axis, they leave the unit circle and appear as (real) reciprocal pairs. For $\mathrm{i}\eta = 0.2$, the eigenvalues with the larger modulus of the reciprocal pairs depart up to approximately ± 0.54 from the unit circle for $kd/\pi \approx 1/8 + 2l$ and $kd/\pi \approx 9/8 + 2l$, with $l \in \mathbb{N}$. The top-right panel shows additionally the eigenvalues for $\mathrm{i}\eta = 0.4$, for which we can observe that the eigenvalues with the larger modulus depart up to approximately ± 1.1 from the unit circle for $kd/\pi \approx 0.2 + 2l$ and

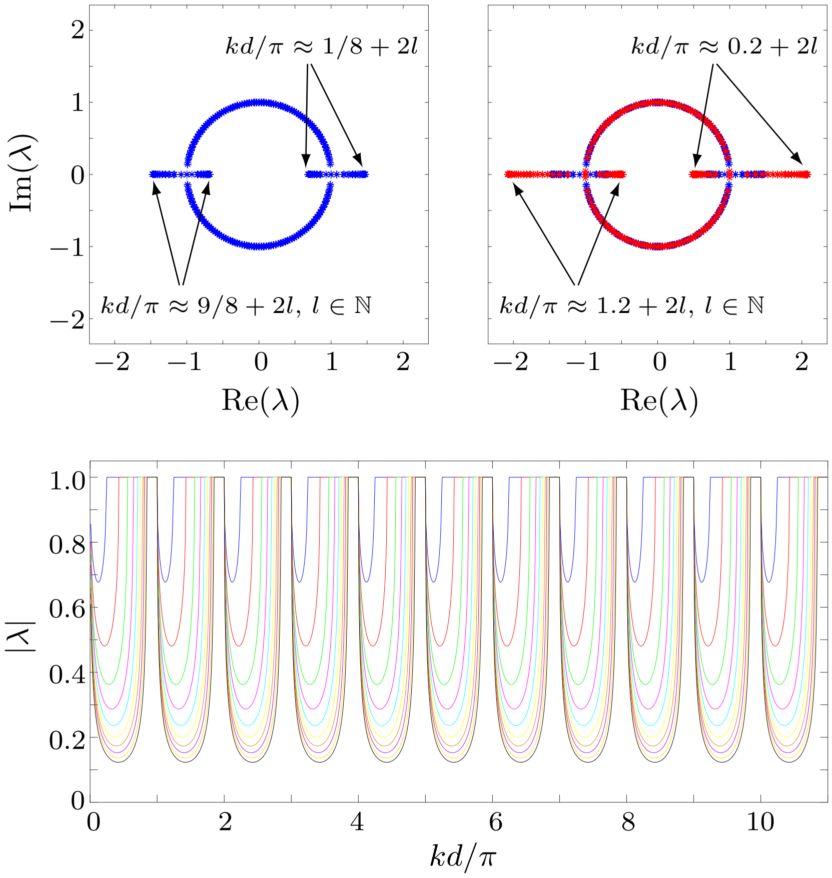

Figure 4.8: Top panels: Eigenvalues of transfer matrix in interval $kd \in (0,11\pi)$ for $\mathrm{i}\eta = 0.2$ (blue, top-left panel) and $\mathrm{i}\eta = 0.4$ (red, top-right panel). Bottom panel: Eigenvalue moduli of transfer matrix as functions of distance between adjacent scatterers for $\mathrm{i}\eta = 0.2$ (blue), $\mathrm{i}\eta = 0.4$ (red), $\mathrm{i}\eta = 0.6$ (green), $\mathrm{i}\eta = 0.8$ (magenta), $\mathrm{i}\eta = 1.0$ (cyan), $\mathrm{i}\eta = 1.2$ (yellow), $\mathrm{i}\eta = 1.4$ (brown), $\mathrm{i}\eta = 1.6$ (violet), $\mathrm{i}\eta = 1.8$ (orange) and $\mathrm{i}\eta = 2.0$ (black).

$kd/\pi \approx 1.2 + 2l$ with $l \in \mathbb{N}$. It could be shown analytically that the scattering strength and the maximum departure of the eigenvalues with the larger modulus from the unit circle are directly proportional.

We can observe in the bottom panel of Fig. 4.8 that the shown eigenvalue moduli are unity for non-dimensional spacings between scatterers around multiples of π, i.e. at the Bragg resonances $kd = p\pi$, p integer, see e.g. Le Bas and Conoir 2005 and Aristégui and Angel 2002. The shown eigenvalues are simply the inverses of the eigenvalues with the larger modulus, hence the eigenvalues are equal to unity in the passbands and less than unity in the stopbands. While the intervals indicating the passband state get smaller for increasing scattering strength, the eigenvalue moduli diminish in the stopbands for increasing scattering strength, revealing stronger total reflection and attenuating wave fields. For a fixed scattering strength, the eigenvalues in the stopbands are of the same magnitude suggesting that the maximum attenuation in each stopband is equal in this undamped system, which was already suggested by the top panels, since the eigenvalues depart equally far from unity in each circulation.

To study the influence of the scattering strength and the positional disorder on the attenuation of wave fields, the distance between scatterers in the underlying periodic structure is chosen to be in a passband throughout the rest of this chapter. This implies that the wavenumber of the Floquet mode has to be imaginary, see e.g. John 1991. The wavenumber of the Floquet mode, $\tilde{Q}$, is given by the dispersion relation

$$\cos(\tilde{Q}d) = \cos(kd) + \mathrm{i}\eta \sin(kd). \tag{4.22a}$$

The dispersion relation in Eqn. (4.22a) simplifies to

$$\cos(\tilde{Q}d)\cos(\varphi) = \cos(kd + \varphi). \tag{4.22b}$$

in our energy-conserving setting.

Fig. 4.9 shows the imaginary parts of the wavenumbers of the Floquet modes as functions of the non-dimensional spacing between periodic scatterers for purely imaginary, negative scattering strengths (top-left panel) and the corresponding attenuation coefficients calculated by the discrete iterative scheme (bottom-left panel). The right-hand panels show the respective quantities for purely imaginary, positive scattering strengths. To investigate the exponential attenuation of individual wave fields, we extract the attenuation coefficients for single realisations via Eqn. (2.77b) and average the obtained individual attenuation coefficients for a large ensemble size.

We can see in Fig. 4.9 that the imaginary part of the wavenumber of the Floquet mode, which describes the attenuation of the wave field, vanishes in the case of negative scattering strengths at the Bragg resonances, i.e. for non-dimensional spacings between scatterers around multiples of π. Between these passbands, the attenuation coefficients get larger with increasing scattering strength moduli and the curves broaden indicating larger stopbands. This pass- and stopband behaviour was already visible in Fig. 4.8, where the eigenvalues of the transfer matrix were analysed. Furthermore, the maximum attenuation in each stopband is equal which confirms the finding in Fig. 4.8.

Choosing scattering strengths with positive imaginary part (top-right panel) gives a segmentation into pass- and stopbands shifted towards larger spacings by $\pi/4$ and the wavenumbers of the Floquet mode are of the same magnitude as for scattering strengths with negative imaginary part. Furthermore, the attenuation coefficients calculated by the discrete iterative scheme (shown in bottom panels of Fig. 4.9) agree with the analytical results from the dispersion relation Eqn. (4.22) in both cases of scattering strengths with negative and positive scattering strengths. Note that we will use purely imaginary, negative scattering strengths throughout the rest of this chapter, which is motivated in Sec. 4.3.

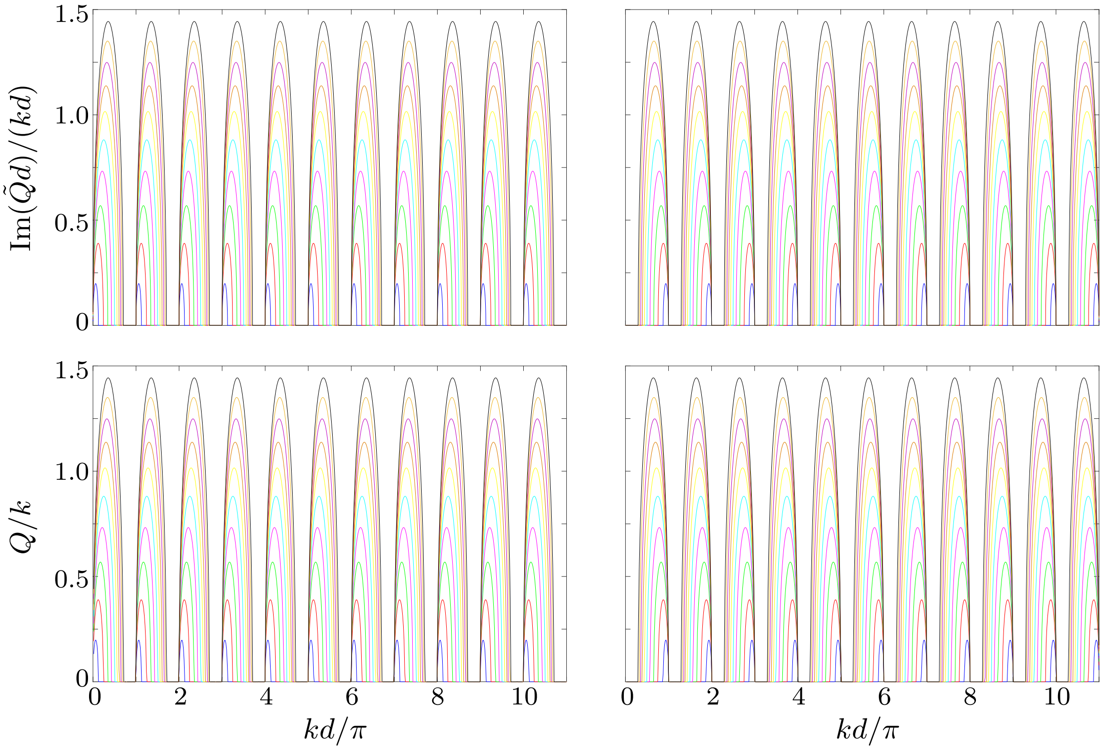

Figure 4.9: Top panels: Wavenumbers (imaginary part) of Floquet mode as functions of non-dimensional spacing between scatterers for scattering strengths with negative imaginary part (top-left panel) and positive imaginary part (top-right panel), $\pm \mathrm{i}\eta = 0.2\ 0.4, \ldots, 2.0$ (same colour scheme as in Fig. 4.8). Bottom panels: Corresponding attenuation coefficients calculated by discrete iterative scheme as functions of non-dimensional spacing between scatterers for scattering strengths with negative imaginary part (bottom-left panel) and positive imaginary part (top-right panel), $\pm \mathrm{i}\eta = 0.2\ 0.4, \ldots, 2.0$ (same colour scheme as in Fig. 4.8).

For the remainder of this chapter, the underlying periodic structure shall consist of scatterers with spacings chosen numerically to be at the centre of the global passband, i.e. the resulting range of spacings ensures passbands for all different scattering strengths in consideration. Choosing the midpoint of the global passband is necessary to obtain robust results for all considered scattering strengths. It was shown by Godin et al. (2007) that wave propagation in a one-dimensional periodic medium becomes highly sensitive to small deviations from the periodic structure near the band edges, which we avoid with the choice above.

4.2.3 Numerical results

Before we analyse the influence of the scatterers' distance, the positional disorder and the scattering strength on the attenuation of both individual and effective wave fields quantitatively in this section, we look at example wave fields for individual beaded-string realisations. For the numerical simulations of the beaded-string problem, we use $N = 200$ in the following, which provides a similar number of scatterers as number of humps appearing in the roughness profiles for the continuous problem configuration with roughness profile lengths of 400 correlation lengths.

Fig 4.10 shows example individual wave field moduli calculated by the discrete iterative scheme for values of positional disorder $k\nu = 0.01$, 0.05 and 0.10, for the non-dimensional distance between scatterers chosen to be at the global passband around 8π and scattering strength $\mathrm{i}\eta = 0.14$. The values of positional disorder are chosen to produce different attenuation behaviours.

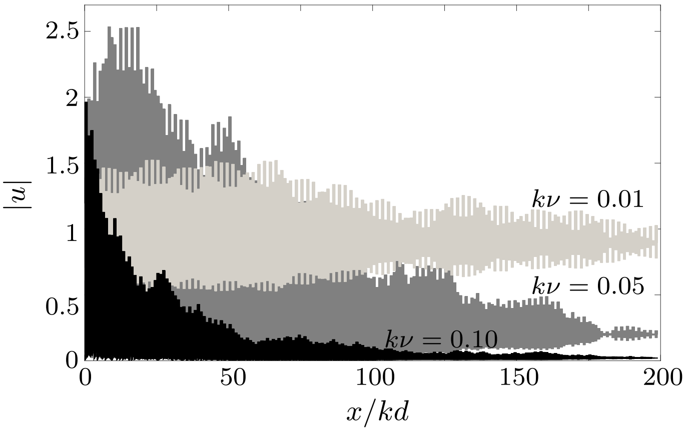

Figure 4.10: Example individual wave fields for beaded-string problem for values of positional disorder $k\nu = 0.01$ (light grey), $k\nu = 0.05$ (dark grey) and $k\nu = 0.10$ (black), for scattering strength $\mathrm{i}\eta = 0.14$

We can observe in Fig. 4.10 that the example individual wave field for the smallest positional disorder value, $k\nu = 0.01$, shows only a slightly attenuating behaviour, whereas the wave field modulus for $k\nu = 0.05$ drops significantly over the interval of 200 beads on a string. For the largest value of positional disorder here, $k\nu = 0.10$, strong attenuation can be noticed and most of the wave energy is attenuated after only half of the beaded string interval. Furthermore, we can see that the deflection close to the left end of the beaded string is largest for the intermediate value of positional disorder, $k\nu = 0.05$, for which the scattering is strong enough to produce significant reflection (in contrast to the case of $k\nu = 0.01$), but not too strong to lead to large attenuation (as for $k\nu = 0.10$).

It was shown e.g. in Hodges and Woodhouse 1983 for a stretched string with masses attached to it that exponential attenuation is induced by positional disorder when the underlying periodic setting is in a passband. Choosing kd as discussed above ensures the passband state and positional disorder is introduced via uniformly distributed random variables $\nu_n \in \mathcal{U}(-\nu/2,\nu/2)$, where $\nu \in [0,1)$, for the following results.

The attenuation coefficients calculated with the discrete iterative scheme are compared with the analytical Berry–Klein limit derived by Berry and Klein (1997). Here, the Berry–Klein limit is given by $-\ln|T(\eta)|$, where $T(\eta)$ is the transmission coefficient for a single scatterer of scattering strength η. With the representation of the transmission coefficient from Eqn. (4.16b), we can write the Berry–Klein limit as

$$\varGamma_{\mathrm{BK}} = -\ln|T(\eta)| = -\ln|1 + R(\eta)| = -\ln\left|\frac{1}{1-\eta}\right|. \tag{4.23}$$

All phases to be included in wave interactions between two adjacent scatterers requires $\nu kd \geq \pi$, to which we will refer as the positional-disorder threshold.

Fig. 4.11 shows the Berry–Klein limit as a function of the scattering strength η. Furthermore, the individual attenuation coefficients calculated by the discrete iterative scheme are depicted as functions of the scattering strength for values of positional disorder $k\nu = 0.01$, 0.05 and 1.00, for the non-dimensional distance between scatterers chosen to be at the global passband around 8π.

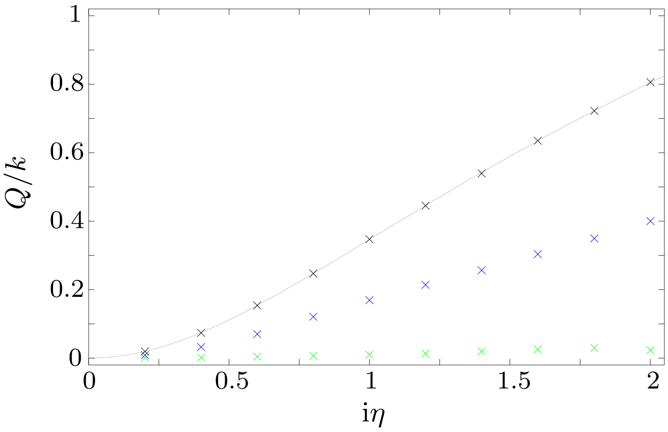

Figure 4.11: Berry–Klein limit as function of scattering strength (dotted line). Attenuation coefficients for beaded-string problem as functions of scattering strength for $k\nu = 0.01(\times)$, $k\nu = 0.05(\times)$ and $k\nu = 1.0(\times)$, for $kd \approx 8\pi$, are shown for comparison.

We can observe in Fig. 4.11 that the Berry–Klein limit is close to zero for very small scattering strengths and increases with increasing scattering strength. This can also be directly derived from its definition, since the transmission at a single scatterer naturally decreases for increasing scattering strength. The individual attenuation coefficients for each value of positional disorder also exhibit an increasing behaviour with increasing scattering strength. Whereas the attenuation coefficients for the smallest value of positional disorder, $k\nu = 0.01$, are very small throughout the whole scattering strength regime, the attenuation coefficients for $k\nu = 0.05$ already reach values half of those suggested by the Berry–Klein limit, e.g. for $\mathrm{i}\eta = 2.0$, the attenuation coefficient for $k\nu = 0.05$ is 0.4, the Berry–Klein limit gives 0.8. This holds for all scattering strengths in the regime considered, $\mathrm{i}\eta \in [0,2]$. Since for the largest value of positional disorder, $k\nu = 1.0$, the positional-disorder threshold is obviously exceeded, all phases are included in the wave interaction between adjacent scatterers and the attenuation coefficients should meet the Berry–Klein limit. This certainly holds for all scattering strengths and the attenuation coefficients agree with the predicted limit. The behaviour of the attenuation coefficients for the values of positional disorder considered suggest that they are proportional to the Berry–Klein limit. For large $|\eta|$ (remember that η is purely imaginary to ensure that energy is conserved), the Berry–Klein limit behaves asymptotically like

$$\mathit{\Gamma}_{\mathrm{BK}} = -\ln\left|\frac{1}{1-\eta}\right| \overset{|\eta|\gg 1}{\approx} \ln|\eta|\,. \tag{4.24}$$

We can deduce from Eqn. (4.24) that the nearly linear scaling of the Berry–Klein limit with the scattering strength in Fig. 4.11 for $\mathrm{i}\eta > 0.8$ is elusive and it actually increases logarithmically for large $|\eta|$. The possible proportionality of the attenuation coefficients and the Berry–Klein limit (indicated in Fig. 4.11) is investigated together with the influence of the distance between scatterers on the attenuation in Fig. 4.13. Before we get to this analysis, the Berry–Klein limit is explained in more detail now.

Fig. 4.12 shows the probability density function of the uniform distribution, from which all random variables ν_n, $n = 1,\dots,N$, are chosen, in dependence of the value of positional disorder (left-hand panel). The right-hand panel of Fig. 4.12 depicts all phases which are included in wave interactions between adjacents scatterers if their positions are (as used above) perturbed around their periodic positions with uniformly distributed random variables $\nu_n \in \mathfrak{U}(-\nu/2,\nu/2)$, where $\nu \in [0,1)$.

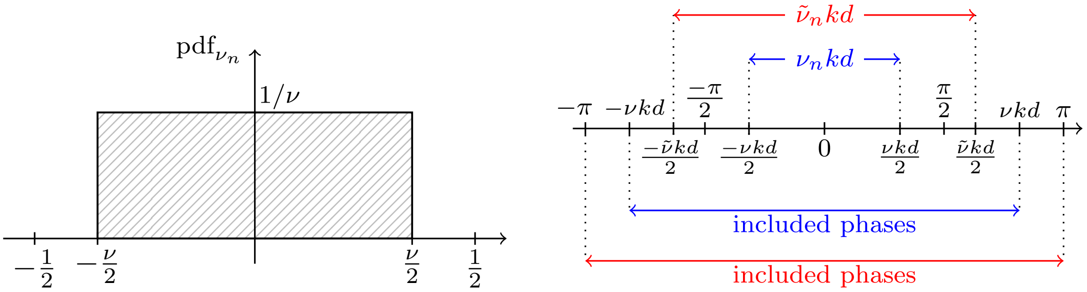

Figure 4.12: Left-hand panel: Uniform probability density function of random variables ν_n. Right-hand panel: Included phases in wave interactions between positionally disordered adjacent scatterers for positional disorder below positional-disorder threshold (blue) and exceeding positional-disorder threshold (red).

The concept of the positional disorder threshold for the Berry–Klein limit is visualised in the right-hand panel of Fig. 4.12. If the positional-disorder threshold is not attained yet, i.e. $\nu kd < \pi$ and hence $-\pi/2 < \nu_n kd < \pi/2$ for the nth scatterer, a single scatterer can change the phase of an incoming wave by $-\nu kd/2$ up to $\nu kd/2$. This means in particular that between two positionally disordered adjacent scatterers the included phases in wave interactions stretch from $-\nu kd$ and νkd. If the positional-disorder threshold is reached though, i.e. $\nu kd = \pi$, a single scatterer can change the phase of an incoming wave by $-\pi/2$ up to $\pi/2$. For this value of positional disorder, two adjacent scatterers are then able to change the phase of an incoming wave by $-\pi$ to π. However, if the positional-disorder threshold is exceeded, i.e. $\nu kd > \pi$, the two adjacent scatterers cannot change the phase of an incoming wave more than by $-\pi$ to π (which might already be reached for the positional-disorder threshold case), since all phases are already included in wave interactions between adjacent scatterers. This is the fundamental idea of the Berry–Klein limit predicting maximum attenuation if all phases are included. Fig. 4.11 already showed that exceeding the positional disorder threshold (as it is the case for the choice $\nu = 1.0$ in the setting of Fig. 4.11) does not lead to a deviation from the Berry–Klein limit.

To study the relation between the attenuation coefficients for different values of positional disorder and the Berry–Klein limit, we look at the attenuation coefficients scaled with the Berry–Klein limit. Furthermore, to get insight into the influence of the distance between scatterers in the underlying periodic structure on the attenuation of the perturbed problem, we consider the cases of perturbing the scatterers in different passbands. Fig. 4.13 shows the individual attenuation coefficients calculated by the discrete iterative scheme as functions of scattering strength for values of positional disorder $k\nu = 0.01$, 0.05, 0.10 and 1.00, for the non-dimensional distance between scatterers in the passbands around $kd \approx 2\pi$ (top-left panel), $kd \approx 4\pi$ (top-right panel), $kd \approx 8\pi$ (bottom-left panel) and $kd \approx 12\pi$ (bottom-right panel). As mentioned, the attenuation coefficients shown are scaled by the Berry–Klein limit which is also shown (scaled to unity).

We can observe in Fig. 4.13 that the attenuation coefficients for the beaded-string problem show proportionality to the Berry–Klein limit and only small deviations due to numerical difficulties in capturing very small attenuation coefficients can be detected. For the largest value of positional disorder, $k\nu = 1.00$, the attenuation coefficients again coincide with the values predicted by the Berry–Klein limit, for all non-dimensional distances between scatterers, $kd \approx 2\pi$, 4π, 8π and 12π. The same level of (relative) positional disorder leads to larger attenuation for the larger non-dimensional distances between scatterers. While in fact the scaled attenuation coefficients for $k\nu = 0.10$ are between 0.10 and 0.15 for $kd \approx 2\pi$ with slightly increasing tendency with increasing $\mathrm{i}\eta$, they increase to around 0.5 for $kd \approx 4\pi$ and 0.9 for $kd \approx 8\pi$, before the maximum attenuation is already close to be reached for $kd \approx 12\pi$. This behaviour also holds for the other values of positional disorder and follows directly from the fact that the positional disorder threshold, $\nu kd = \pi$, for which all phases are included in the wave interactions of adjacent scatterers, is attained sooner for large kd. The slightly increasing behaviour of the attenuation coefficients for small $k\nu$ and small $\mathrm{i}\eta$ cannot be observed for large positional disorder and larger scattering strengths (leading to more attenuation) anymore, and we can deduce that this is due to numerical difficulties for extracting the attenuation coefficients if they are very small. It is confirmed that exceeding the positional disorder threshold still leads to the Berry–Klein limit since all phase changes remain in the wave interactions (although the distribution of phase changes changes). For the remainder of this chapter, the spacing between scatterers in the underlying structure is chosen to be at the centre of the global passband around $kd \approx 8\pi$.

Next, we want to compare the attenuation coefficients of the effective wave fields with the individual attenuation coefficients. The effective attenuation coefficients are extracted from

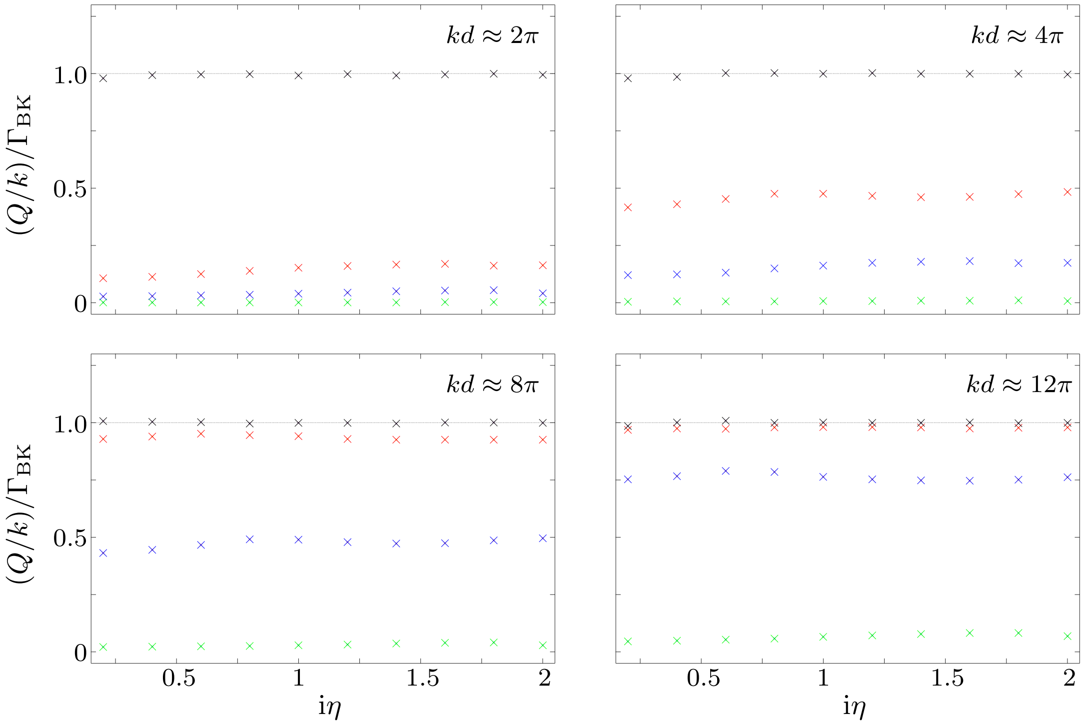

Figure 4.13: Scaled individual attenuation coefficients (×) for beaded-string problem as functions of scattering strength for values of disorder $k\nu = 0.01$ (green), $k\nu = 0.05$ (blue), $k\nu = 0.10$ (red) and $k\nu = 1.00$ (black) for different distances between scatterers in the underlying periodic problem, $kd \approx 2\pi$ (top-left panel), $kd \approx 4\pi$ (top-right panel), $kd \approx 8\pi$ (bottom-left panel) and $kd \approx 12\pi$ (bottom-right panel). Scaled Berry–Klein limit (dotted line) is shown for comparison.

the effective wave fields via Eqn. (2.77a). Since the effective wave field is similarly to the continuous problem sensitive to outliers, we again use an ensemble size of 3000 individual beaded-string realisations and average the calculated wave fields with respect to the 25% and 75% attenuation coefficients quantiles afterwards to obtain the effective wave field.

Fig. 4.14 enhances the bottom-left panel of Fig. 4.13 by the effective attenuation coefficients and shows the scaled individual and effective attenuation coefficients as functions of scattering strength for values of positional disorder $k\nu = 0.01$, 0.05, 0.10 and 1.00.

We can observe important features of the attenuation coefficients for the beaded-string problem in Fig. 4.14. The effective attenuation coefficients also increase with increasing level of disorder and agree with the individual attenuation coefficients for the large scattering strengths considered. While the individual attenuation coefficients are proportional to the Berry–Klein limit for the whole scattering strength regime considered, the effective attenuation coefficients are proportional to the Berry–Klein limit in the large scattering strength regime only. They show a qualitative different behaviour compared to the individual attenuation coefficients in the smaller scattering strength regime, which

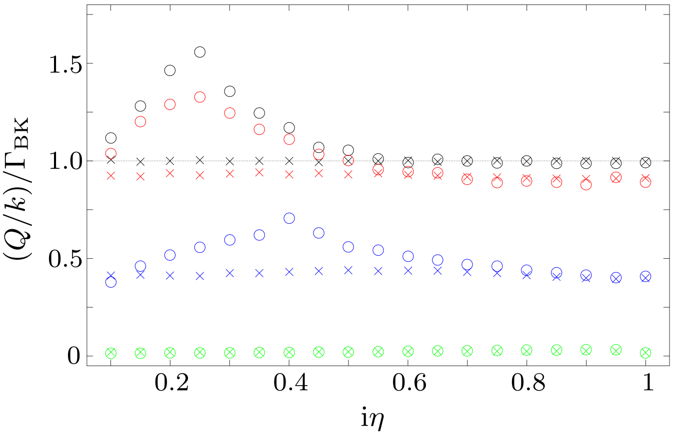

Figure 4.14: Scaled individual (×) and effective (∘) attenuation coefficients for beaded-string problem as functions of scattering strength for values of disorder $k\nu = 0.01$ (green), $k\nu = 0.05$ (blue), $k\nu = 0.10$ (red) and $k\nu = 1.00$ (black), for non-dimensional distance between scatterers $kd = 8\pi$. Scaled Berry–Klein limit (dotted line) is shown for comparison.

complements e.g. the observations of Bennetts and Peter (2013), who studied perturbed periodic arrays of point scatterers and found similar attenuation coefficients of individual and effective wave fields in this setting. The effective attenuation coefficients exceed the individual attenuation coefficients for scattering strengths i$\eta < 0.45$ for the largest value of positional disorder, $k\nu = 1.0$. In the small scattering strength regime, the effective attenuation coefficients increase for increasing scattering strength until i$\eta \approx 0.2$, where they reach their maximum, and decrease afterwards until hitting the Berry–Klein limit. For smaller positional disorder, the limit from where on the effective attenuation coefficients are proportional to the Berry–Klein limit is shifted to the right.

The agreement of individual and effective attenuation coefficients for large iη deepens our understanding of the attenuation coefficients' behaviour for the continuous problem in Sec. 4.1. It confirms the finding that significantly different individual and effective wave field attenuation due to wave cancellation only appears up to certain strengths of scatterers. For large scattering strengths, the individual and effective wave fields are representative for each other.

To complete the analysis of the beaded-string problem, we study the impact of positional disorder now. Fig. 4.15 shows individual and effective attenuation coefficients scaled with the Berry–Klein limit as functions of scaled positional disorder for scattering strengths i$\eta = 0.2$ (top-left panel), 0.6 (top-right panel), 1.2 (bottom-left panel) and 2.0 (bottom-right panel). The positional disorder is scaled such that the same value of ν leads to the same absolute positional disorder, independent of the choice of kd. Here, the positional disorder threshold is positioned at the origin, i.e. $\nu kd = \pi \iff \log_{10}(\nu kd/\pi) = 0$. The results can be compared with the coherent potential approximation (CPA) derived by Maurel et al. (2010), which yields the effective wavenumber. To avoid cluttered figures and distraction from the essential findings in Fig. 4.15, the effective attenuation coefficients obtained without using the quantile approach and predicted by the CPA are shown for i$\eta = 2.0$ only. The derivation for the CPA is outlined in Appendix 4.C.

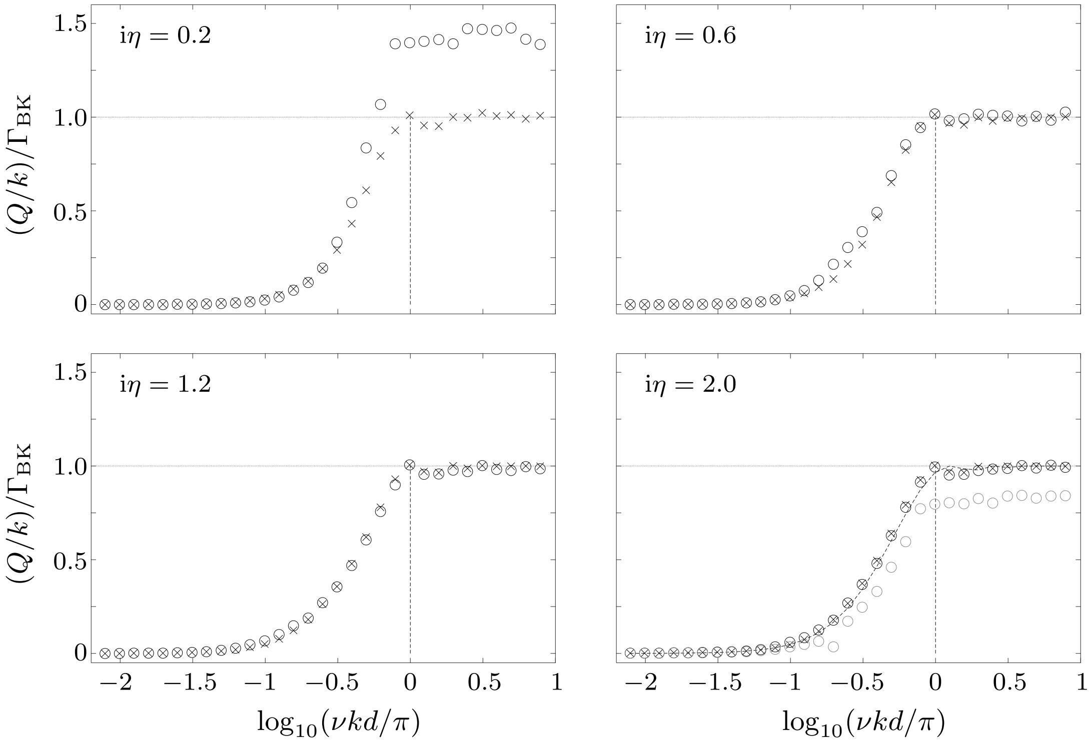

Figure 4.15: Scaled individual (×) and effective (∘) attenuation coefficients for beaded-string problem as functions of scaled positional disorder for scattering strength i$\eta = 0.2$ (top-left panel), i$\eta = 0.6$ (top-right panel), i$\eta = 1.2$ (bottom-left panel) and i$\eta = 2.0$ (bottom-right panel). Berry–Klein limit and its positional disorder threshold is shown as horizontal and vertical dotted line, respectively. Results with CPA (dashed line) and effective attenuation coefficients without quantile approach (∘) are shown for comparison for i$\eta = 2.0$ (bottom-right panel).

We can observe in Fig. 4.15 that the attenuation coefficients are negligible for small values of positional disorder. Hence, small deviations do not affect the passband state significantly. For values of $\log_{10}(\nu kd/\pi)$ slightly smaller than -1, the attenuation coefficients start increasing until the attenuation coefficients reach the Berry–Klein limit for the positional disorder threshold. As soon as the limit is attained, the attenuation coefficients level off and remain there even for larger positional disorder, which confirms the finding in Fig. 4.13 quantitatively that exceeding the positional disorder threshold does not lead to deviations from the maximum value predicted by the Berry–Klein limit. The individual and effective attenuation coefficients agree throughout the whole positional disorder regime for the three larger scattering strengths, i$\eta = 0.6$, 1.2 and 2.0. For i$\eta = 0.2$, the effective attenuation coefficients are visibly larger than the individual attenuation coefficients in the regime $\log_{10}(\nu kd/\pi) \geq -0.3$. This is due to the wave cancellation, which could already be observed in Fig. 4.14 in the small scattering strength regime.

For comparison, the effective attenuation coefficients without using the quantile approach are depicted for the largest scattering strength, $\mathrm{i}\eta = 2.0$. Although these attenuation coefficients are very small for small positional disorder and increase with increasing positional disorder as well, they show great deviations from the individual attenuation coefficients in the large positional disorder regime. They are significantly shifted down by about 20% from the Berry–Klein limit and effective attenuation coefficients calculated with the quantile approach. The attenuation coefficients predicted by the CPA behave similarly to the individual and effective attenuation coefficients with the quantile approach, i.e. they are also negligible for small values of positional disorder and start increasing for values of $\log_{10}(\nu kd/\pi)$ greater than -1 until the attenuation coefficients reach the Berry–Klein limit for the positional disorder threshold, where they level off and remain there for larger positional disorder. So, the attenuation coefficients predicted by the CPA agree with the numerical results obtained with the quantile approach.

Before we establish a connection between the attenuation behaviour of the continuous and the beaded-string problem in Sec. 4.3, we conclusively study the impact of the scattering strength and the level of positional disorder on the attenuation coefficient of individual and effective wave fields in a detailed illustration. Fig. 4.16 shows heatmaps of the individual and effective attenuation coefficients (left-hand panel and right-hand panel, respectively) in dependence of the scattering strength and the scaled positional disorder.

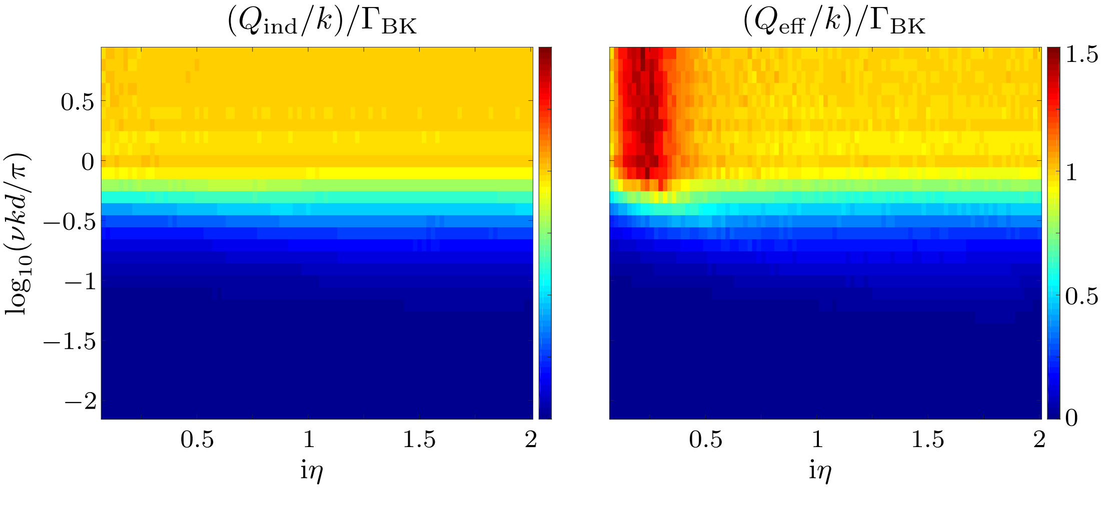

Figure 4.16: Heatmap of scaled individual (left-hand panel) and effective (right-hand panel) attenuation coefficients for beaded-string problem as functions of scattering strength and scaled positional disorder

We can observe in Fig. 4.16 that the individual attenuation coefficients (left-hand panel) are proportional to the Berry–Klein limit throughout the whole scattering strength regime considered. Increasing the positional disorder leads to larger attenuation coefficients of the individual wave fields. The magnitude of the increase in the scaled attenuation coefficients depends on the positional disorder only and is the same for all scattering strengths. We can also see that the transition zone for the positional disorder from small to large attenuation is narrow and located between $\log_{10}(\nu kd/\pi) \in (-0.4, -0.2)$. The right-hand panel, which depicts the effective attenuation coefficients, shows that the individual and the effective attenuation coefficients agree for all considered combinations of ν for $\mathrm{i}\eta \geq 0.5$. In the scattering strength regime $\mathrm{i}\eta < 0.5$, the effective attenuation coefficients exceed their individual equivalents due to wave cancellation, which can be observed for sufficiently large positional disorder.

To complement the insights for the scaled individual and effective attenuation coefficients, Fig. 4.17 shows the heatmap of the non-scaled individual and effective attenuation coefficients (left-hand panel and right-hand panel, respectively) in dependence of the scattering strength and the scaled positional disorder. The quantile approach is used again for these simulations.

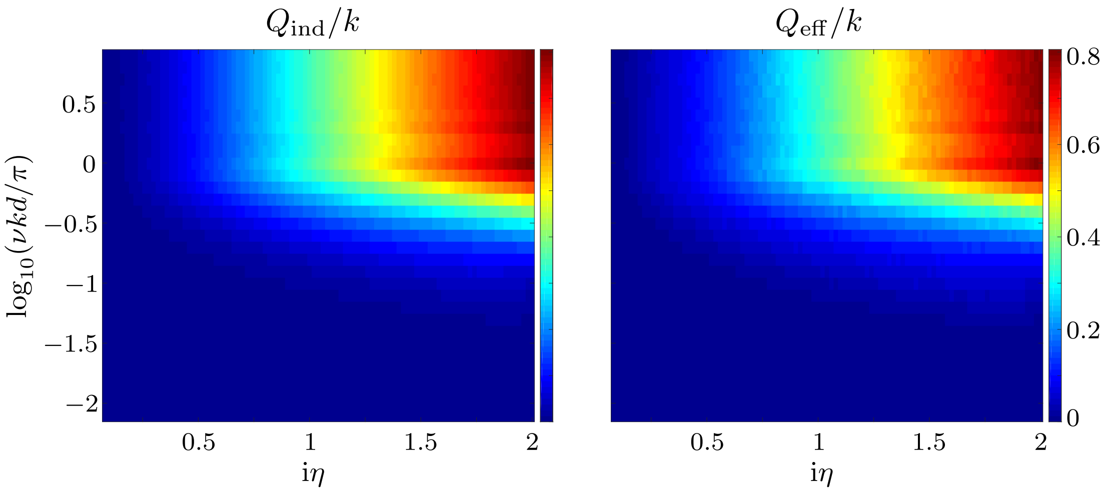

Figure 4.17: Heatmap of individual (left-hand panel) and effective (right-hand panel) attenuation coefficients for beaded-string problem as functions of scattering strength and scaled positional disorder

Fig. 4.17 confirms that increasing scattering strength as well as increasing positional disorder lead to larger attenuation for the whole considered regime of disorder and scattering strengths for both individual and effective wave fields. As firstly observed in Fig. 4.11, both a large scattering strength and positional disorder are necessary to produce large attenuation.

In Secs. 4.1 and 4.2, we could observe agreement of individual and effective attenuation coefficients in the beaded-string problem and especially found large roughness regimes for the continuous problems providing agreement of individual and effective attenuation coefficients, too. This behaviour might indicate similarity of both problems. We move on from investigating individual and effective attenuation coefficients for the respective problems and put our focus on individual wave fields only in the next section, in which we map the continuous problem into the beaded-string problem.

4.3 Connection between continuous and discrete problem

We establish a connection between the attenuation behaviour of the (continuous) non-homogeneous string and the (discrete) beaded-string problem in the following. To achieve this, we convert the continuous roughness profile into discrete scatterers. As it will be shown schematically in Sec. 4.3.1, we cluster the roughness profile into humps, denote the (complex) total reflection coefficient of the i-th hump with R_i and use the mean reflection coefficient modulus of these clustered humps, $\mathbf{E}[|R_i|]$, to calculate the equivalent scattering strength modulus of the discrete point scatterers as

$$|\eta| = \frac{\mathbf{E}[|R_i|]}{1 + \mathbf{E}[|R_i|]}, \tag{4.25a}$$

which directly follows from the relation for single scatterers in Eqn. (4.16a). Since our problem formulation shall be energy-conserving, the scattering strength has to be purely imaginary and we choose the corresponding scattering strength with negative imaginary part, which can be shown is closer to the reflection coefficient arguments of the clustered humps (see Fig. 4.25 for further details).

Fig. 4.18 shows the individual attenuation coefficients scaled by the Berry–Klein limit for the discrete problem as functions of scaled non-dimensional positional disorder for $\mathrm{i}\eta = 0.14$ (top panels) and $\mathrm{i}\eta = 0.26$ (bottom panels). The individual attenuation coefficient for the continuous problem is shown for comparison. The roughness amplitude in the continuous problem is chosen such that the mean reflection coefficient modulus of the clustered humps matches with the reflection coefficient modulus of a single scatterer in the discrete problem, i.e.

$$\mathbf{E}[|R_i|] = \frac{|\eta|}{1 - |\eta|}. \tag{4.25b}$$

The individual attenuation coefficient for the continuous problem is constant since no positional disorder appears in this problem. We consider the non-dimensional correlation lengths $\bar{k}l_{\mathrm{G}} = 0.7$ (left-hand panels), which gives maximum attenuation, and $\bar{k}l_{\mathrm{G}} = 2.5$ (right-hand panels).

We can see in Fig. 4.18 for both cases, $\eta = 0.14/\mathrm{i}$ and $\eta = 0.26/\mathrm{i}$, that the scaled individual attenuation coefficients of the discrete problem show the same qualitative and quantitative behaviour with increasing positional disorder as we could observe in Fig. 4.15, reaching the Berry–Klein limit for the positional disorder threshold. The scaled attenuation coefficients for the continuous problem are significantly smaller than the Berry–Klein limit for the considered cases and for the larger scattering strength, $\mathrm{i}\eta = 0.26$, it is observably smaller than for $\eta = 0.14/\mathrm{i}$. The cases $\mathrm{i}\eta = 0.14$ and $\mathrm{i}\eta = 0.26$ suggest that the attenuation coefficients of both the continuous and the discrete problem intersect at $\log_{10}(\nu k d/\pi) \approx -0.3$. This positional disorder value, for which the attenuation of continuous and discrete problem yield the same attenuation, is studied next.

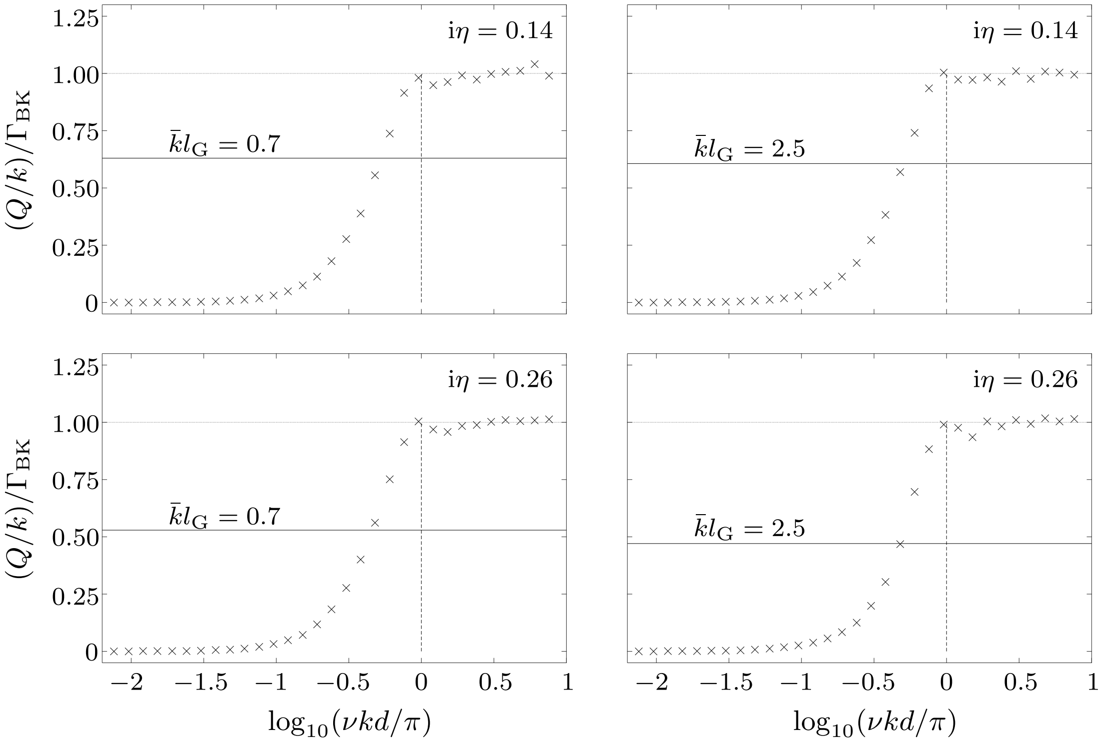

Figure 4.18: Scaled individual attenuation coefficients for continuous non-homogeneous string problem (solid line) and beaded-string problem (×) as functions of scaled non-dimensional positional disorder for $\mathrm{i}\eta = 0.14$ (top panels) and $\mathrm{i}\eta = 0.26$ (bottom panels), for non-dimensional correlation lengths $\bar{k}l_{\mathrm{G}} = 0.7$ (left-hand panels) and $\bar{k}l_{\mathrm{G}} = 2.5$ (right-hand panels). Berry–Klein limit and its positional disorder threshold (horizontal dotted and vertical dashed line, respectively) are shown for comparison.

Fig. 4.19 shows the required positional disorder values for the discrete problem to obtain at least the same attenuation as in the continuous problem as functions of the scattering strength, for the non-dimensional correlation lengths $\bar{k}l_{\mathrm{G}} = 0.7$ and 2.5.

It can be observed in Fig. 4.19 that the required positional disorder to obtain the same attenuation in the discrete and continuous problem for correlation length $\bar{k}l_{\mathrm{G}} = 0.7$ is situated in the small range $\log_{10} \nu kd/\pi \in (-0.3, -0.2)$ for scattering strengths $\mathrm{i}\eta \leq 0.3$. For $\mathrm{i}\eta > 0.3$, the required positional disorder decreases to approximately $\log_{10} \nu kd/\pi \approx -0.4$. The observable decrease in the required positional disorder is due to the loss of proportionality of the individual attenuation coefficients in the continuous problem with the roughness amplitude squared for large roughness amplitudes (corresponding to large scattering strength), which we have seen in Fig. 4.3. This is confirmed for the larger correlation length under consideration, $\bar{k}l_{\mathrm{G}} = 2.5$. As we noticed in Fig. 4.3, the scaled individual attenuation coefficients in the continuous problem for $\bar{k}l_{\mathrm{G}} = 2.5$ show an increase for $\log_{10} \epsilon \in (-1, -0.4)$ (whereas the attenuation coefficients for the discrete problem remain proportional to $\mathrm{i}\eta$), hence less positional disorder is required to obtain the same attenua-

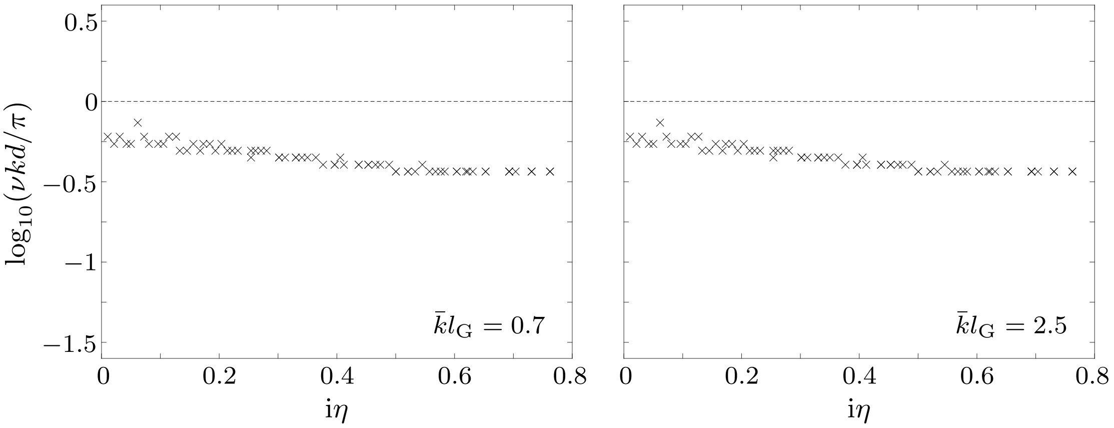

Figure 4.19: Required scaled positional disorder (×) for beaded-string problem to obtain at least same attenuation as in continuous non-homogeneous string problem as function of scattering strength for non-dimensional correlation lengths $\bar{k}l_{\mathrm{G}} = 0.7$ (left-hand panel) and $\bar{k}l_{\mathrm{G}} = 2.5$ (right-hand panel). Positional disorder threshold (dashed line) is shown for comparison.

tion. This can be observed in the right-hand panel of Fig. 4.19 for $\mathrm{i}\eta < 0.2$, for which the required positional disorder increases slightly with the scattering strength. For $\mathrm{i}\eta \geq 0.2$, the required positional disorder then decreases with the scattering strength (similar to the case $\bar{k}l_{\mathrm{G}} = 0.7$), which is backed up by the decrease of the individual attenuation coefficients in the continuous problem for $\log_{10}\epsilon \geq -0.4$.

Before we connect the continuous and the discrete problem, we turn our attention solely to the properties of the clustered humps in Sec. 4.3.1. This investigation is crucial for understanding the clustering process and the effects of the underlying continuous profile characteristics, i.e. roughness amplitude and correlation length, on the clustered humps.

4.3.1 Clustering humps

For the first comparison of the continuous and the discrete problem shown in Fig. 4.18, we already used the approach of clustering the continuous roughness profile into humps in order to retrieve a quantification of the characteristic, i.e. mean, hump. In the following, we analyse the statistical properties of the clustered humps, which are extracted from roughness profile realisations with length $L = 40000 \times l_{\mathrm{G}}$ giving approximately 14000 to 16000 humps per realisation. Fig. 4.20 illustrates the clustering of an extract from a continuous roughness profile realisation into humps schematically. The clustering is completed via a numerical scheme splitting the domain by finding the local minima of the roughness profile and identifying each patch between two minima as a single hump. The total reflection coefficient of a single hump is then calculated by merging all respective scattering matrices appearing in the step approximation of the single hump. We refer to the total reflection coefficient of a single hump as the clustered reflection coefficient.

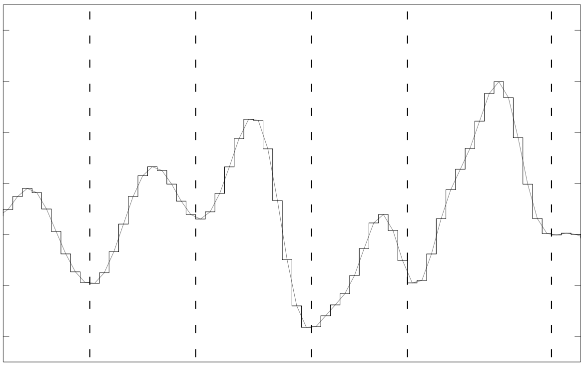

Figure 4.20: Schemata of clustering

The reflection (as well as the transmission) coefficients are complex numbers. Writing the reflection coefficient R in polar form gives $R = |R|\mathrm{e}^{\mathrm{i}\phi_R}$, where $|R|$ is the modulus and ϕ_R the argument of the reflection coefficient R. The key quantities arising from the clustering process are the moduli and the arguments of the clustered reflection coefficients. To study the attenuation behaviour, we firstly turn our attention to the clustered reflection coefficient moduli of clustered humps and the influence of the two main parameters in the continuous problem (roughness amplitude and correlation length) on them.

Fig. 4.21 shows the mean clustered reflection coefficient moduli scaled by the roughness amplitude ϵ as functions of the correlation length for the roughness amplitude $\epsilon = 1.0 \times 10^{-1}$ (left-hand panel) and the mean clustered reflection coefficient moduli as functions of the roughness amplitude ϵ for the non-dimensional correlation length $\bar{k}l_{\mathrm{G}} = 0.7$ (right-hand panel).

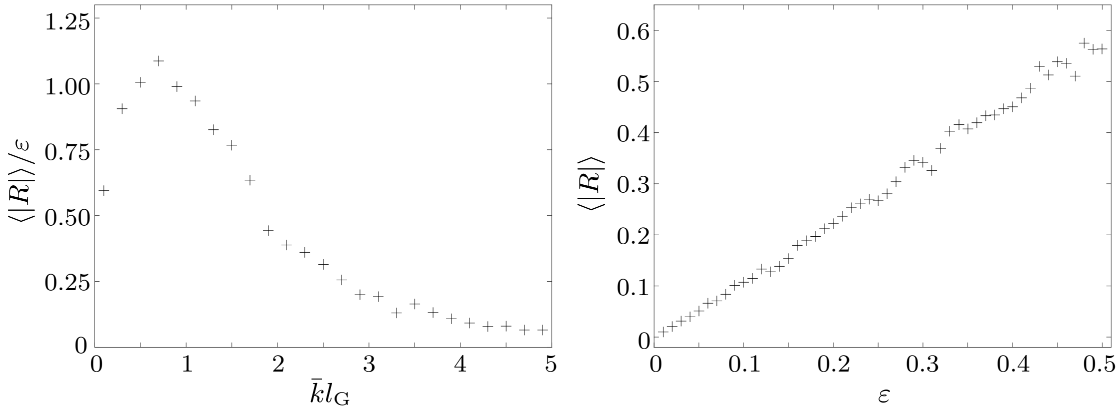

Figure 4.21: Left-hand panel: Mean reflection coefficient moduli of clustered humps (extracted from realisation with non-dimensional length $L = 40000 \times l_{\mathrm{G}}$) as functions of correlation length, for roughness amplitude $\epsilon = 1.0 \times 10^{-1}$. Right-hand panel: Mean reflection coefficient moduli of clustered humps as functions of roughness amplitude, for non-dimensional correlation length $\bar{k}l_{\mathrm{G}} = 0.7$.

We can see in the left-hand panel of Fig. 4.21 that the non-dimensional correlation length $\bar{k}l_{\mathrm{G}} = 0.7$ produces the maximum mean clustered reflection coefficient modulus. Especially in the small correlation length regime $\bar{k}l_{\mathrm{G}} < 2.0$, clustered humps exhibit large reflection coefficient moduli, which become smaller for $\bar{k}l_{\mathrm{G}} \geq 2.0$. In the large correlation length regime, the clustered reflection coefficient moduli get very small and tend to zero. This behaviour is similar to the deterministic hump analysis for the in-vacou beam problem in Sec. 2.3, where humps of intermediate length provided the largest reflection coefficient moduli. The reflection coefficient behaviour in dependence of the underlying correlation length is consistent with the attenuation behaviour of individual wave fields. It could be observed in Fig. 4.2 that the individual attenuation coefficients are only non-zero in the small correlation length regime and are negligible for $\bar{k}l_{\mathrm{G}} \geq 2.0$.

We can observe in the right-hand panel of Fig. 4.21 that the mean clustered reflection coefficient moduli scale with the roughness amplitude for the non-dimensional correlation length $\bar{k}l_{\mathrm{G}} = 0.7$ in the regime $\epsilon \leq 0.4$. Slight deviations from the linear scaling can be observed for $\epsilon \approx 0.3$ and roughness amplitudes larger than 0.4. Overall, the correlation length is a key parameter for wave field attenuation since it is decisive for the reflection ability of the humps appearing in roughness profiles with the same roughness amplitudes.

Before we analyse the second important quantity in the clustering process, the argument of the clustered reflection coefficients, we analyse the reflection coefficient moduli distributions. Fig. 4.22 shows histograms of the clustered reflection coefficient moduli, scaled with ϵ, for non-dimensional correlation lengths $\bar{k}l_{\mathrm{G}} = 0.1$ (top-left panel), 0.7 (top-right panel), 1.5 (bottom-left panel) and 2.5 (bottom-right panel), for the roughness amplitude $\epsilon = 1.0 \times 10^{-1}$. The histograms approximate the distributions of the reflection coefficient moduli of clustered humps.

The histograms exhibit a very similar behaviour of clustered reflection coefficient moduli for all correlation lengths considered, $\bar{k}l_{\mathrm{G}} = 0.1$, 0.7, 1.5 and 2.5. We can deduce that the clustered reflection coefficient modulus distributions are asymmetric and skewed to the right, which is due to the small magnitudes of the (non-negative) described quantities. Although the histogram shapes are very much alike, their widths differ significantly. The clustered reflection coefficient moduli attain larger values for the non-dimensional correlation length $\bar{k}l_{\mathrm{G}} = 0.7$ than for the other correlation lengths and are spread wider. While the (scaled) clustered reflection coefficient moduli for $\bar{k}l_{\mathrm{G}} = 0.7$ reach values up to 4.0, the maximum values for $\bar{k}l_{\mathrm{G}} = 0.1$ and 1.5 are smaller than 2.5 and only approximately 1.0 for $\bar{k}l_{\mathrm{G}} = 2.5$. A more detailed distribution analysis for $\bar{k}l_{\mathrm{G}} = 0.7$ is given below.

Fig. 4.23 displays the statistical distribution of the scaled clustered reflection coefficient moduli for roughness amplitudes $\epsilon = 5.0 \times 10^{-3}$, 1.0×10^{-2}, 5.0×10^{-2}, 1.0×10^{-1}, 2.0×10^{-1} and 5.0×10^{-1} in a box-and-whisker plot, where the non-dimensional correlation length is chosen to be $\bar{k}l_{\mathrm{G}} = 0.7$, which yields maximum clustered reflection coefficient moduli. The boxes and whiskers represent the same statistical quantities as in Fig. 2.15. For better visibility, points regarded as outliers are shown as pluses here.

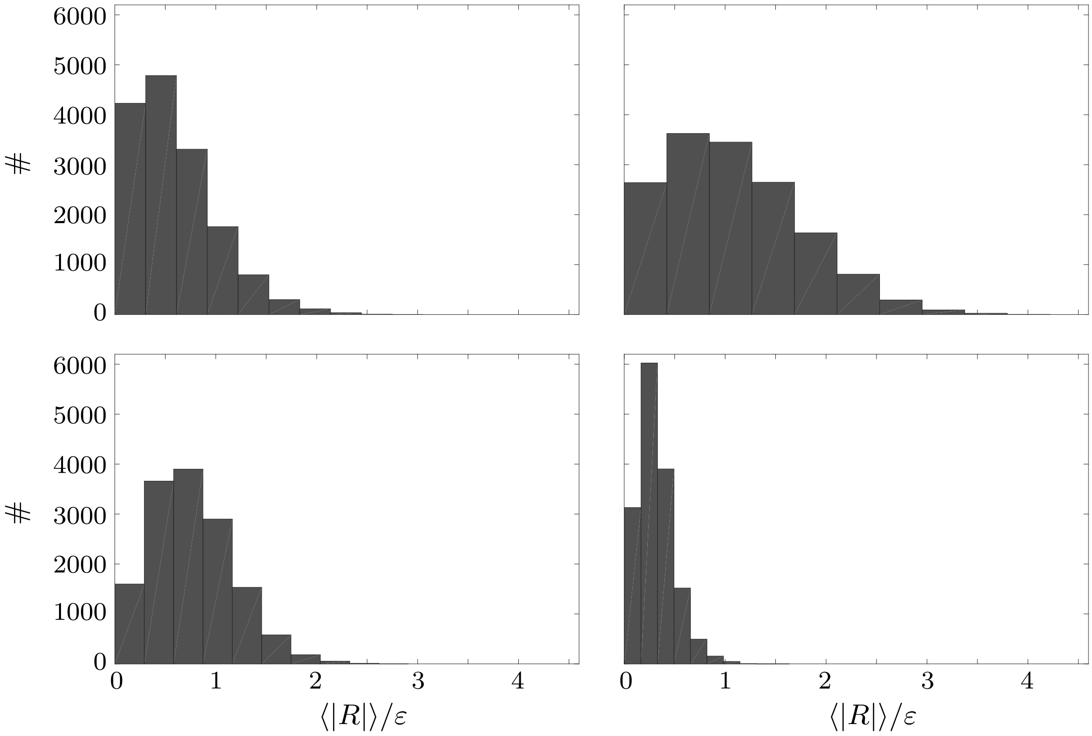

Figure 4.22: Histograms of reflection coefficient moduli of clustered humps, for roughness amplitude $\epsilon = 1.0 \times 10^{-1}$ and non-dimensional correlation lengths $\bar{k}l_{\mathrm{G}} = 0.1$ (top-left panel), $\bar{k}l_{\mathrm{G}} = 0.7$ (top-right panel), $\bar{k}l_{\mathrm{G}} = 1.5$ (bottom-left panel) and $\bar{k}l_{\mathrm{G}} = 2.5$ (bottom-right panel)

The results in Fig. 4.23 suggest that the mean clustered reflection coefficient moduli for the non-dimensional correlation length $\bar{k}l_{\mathrm{G}} = 0.7$ scale with the roughness amplitude. The medians of the clustered reflection coefficient moduli scaled by the roughness amplitude are of similar magnitude for all roughness amplitudes considered. The remaining features (quantiles, skewness towards larger clustered reflection coefficients indicated by the whiskers and outliers) characterising the distribution of the clustered reflection coefficient moduli for the different roughness amplitudes show a very similar behaviour up to $\epsilon = 2.0 \times 10^{-1}$ as well. For $\epsilon = 5.0 \times 10^{-1}$, no outliers appear for the respective clustered reflection coefficient moduli. This is due to the numerical scheme cutting off very small and negative wavenumbers. Although the existence of very large clustered reflection coefficient moduli is impeded as a result of the numerical cut-off, the 25% quantile remains similar to the statistics for smaller roughness amplitudes. However, the assimilated clustered reflection coefficient moduli lead to an increase of the mean and 75% quantile, which are slightly larger than the statistics for smaller roughness amplitudes. Even though the underlying distribution is asymmetric, using the mean reflection coefficient moduli of the clustered humps as typical reflection coefficient of a single hump to calculate the corresponding scattering strength in the discrete problem via Eqn. (4.25a) is still reasonable, since the outliers are not located far off the quantiles, and therefore, the mean includes these large

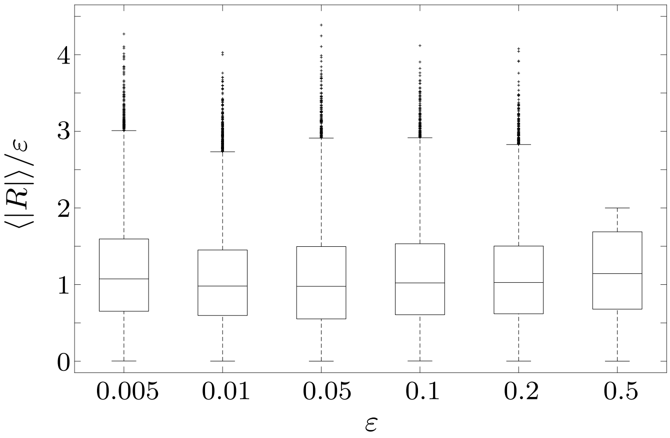

Figure 4.23: Box-and-whisker plot of scaled reflection coefficient moduli of clustered humps for roughness amplitudes $\epsilon = 0.005$, 0.01, 0.05, 0.1, 0.2 and 0.5, for non-dimensional correlation length $\bar{k}l_{\mathrm{G}} = 0.7$

values in a sensible way.

After we have studied the influence of the correlation length and the roughness amplitude on the reflection coefficient moduli of clustered humps, we want to investigate their impact on the reflection coefficient arguments of clustered humps now. The arguments of the clustered reflection coefficients correspond to a phase shift in the solution and hence specify the phases in wave interactions of adjacent humps. Fig. 4.24 shows the clustered reflection coefficient arguments in an angle histogram plot for the roughness amplitude $\epsilon = 1.0 \times 10^{-1}$ and non-dimensional correlation lengths $\bar{k}l_{\mathrm{G}} = 0.3$, 0.5, 0.7, 0.9, 1.1, 1.5, 2.5 and 4.1.

We can see in Fig. 4.24 that the mean clustered reflection coefficient argument is slightly below π for the non-dimensional correlation length $\bar{k}l_{\mathrm{G}} = 0.3$ and increases with increasing, but small correlation lengths. It reaches its maximum (value closest to π) for the non-dimensional correlation length $\bar{k}l_{\mathrm{G}} = 0.7$, which leads to the largest clustered reflection coefficient modulus and the largest individual attenuation coefficient for the continuous problem. From $\bar{k}l_{\mathrm{G}} = 0.7$ on, the mean clustered reflection coefficient arguments diminish for increasing correlation lengths. Beyond that, the clustered phase change spread is obviously smaller for $\bar{k}l_{\mathrm{G}} \leq 1.5$ than for the larger correlation lengths and is widest for the largest correlation length considered, $\bar{k}l_{\mathrm{G}} = 4.1$.

The mean reflection coefficient arguments of clustered humps are illustrated quantitatively as functions of correlation length for $\epsilon = 1.0 \times 10^{-1}$ in Fig. 4.25. For comparison, the reflection coefficient arguments of single discrete scatterers, which have scattering strengths corresponding to a typical hump in the continuous problem with the respective correlation length for $\epsilon = 1.0 \times 10^{-1}$, are shown as well. The reflection coefficient arguments for the discrete problem are already given by the constraint that the scattering strength has to be

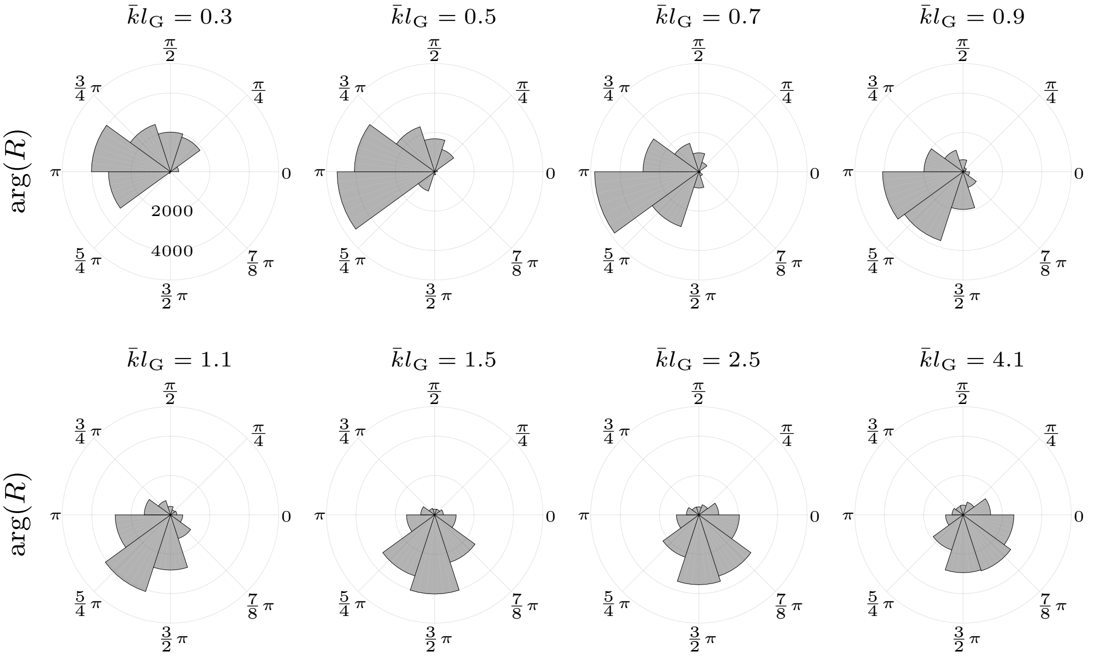

Figure 4.24: Angle histogram plot of reflection coefficient arguments of clustered humps, for roughness amplitude $\epsilon = 1.0 \times 10^{-1}$ and non-dimensional correlation lengths $\bar{k}l_G = 0.3$, 0.5, 0.7, 0.9, 1.1, 1.5, 2.5 and 4.1 (from left to right, top to bottom panel)

purely imaginary. Fig. 4.25 shows them for both choices, positive and negative imaginary part.

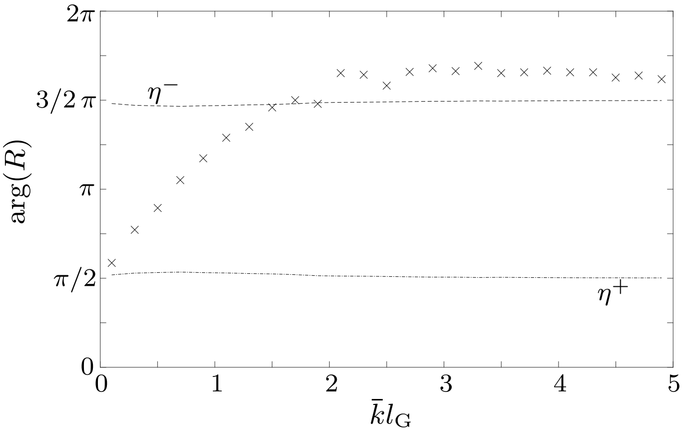

Figure 4.25: Mean arguments of reflection coefficients of clustered humps as functions of correlation length, for $\epsilon = 1.0 \times 10^{-1}$ (×). Arguments of reflection coefficients for single discrete scatterers with corresponding scattering strength with positive (dash-dotted line) and negative (dashed line) imaginary part, respectively, are shown for comparison.

The results in Fig. 4.25 confirm the findings from Fig. 4.24. The mean reflection coefficient arguments increase with increasing correlation lengths for $\bar{k}l_G \leq 2$. They increase more rapidly in the small correlation length regime before they level off and remain at about $7/4\,\pi$ for $\bar{k}l_\mathrm{G} > 2$. The maximum phase change of π is attained between $\bar{k}l_\mathrm{G} = 0.5$ and 0.7. Both reflection coefficient arguments of single discrete scatterers (with positive and negative imaginary part of scattering strength, respectively) exhibit the same distance to the maximum phase change π and do not show significant variability throughout the correlation length regime considered. While discrete scatterers with purely imaginary positive scattering strength have reflection coefficient arguments slightly larger than $\pi/2$, their equivalents with purely imaginary negative scattering strength have reflection coefficient arguments slightly smaller than $3/2\,\pi$ (or $-\pi/2$, respectively).

Although the results for the discrete scatterers with purely imaginary negative scattering strength might suggest a certain similarity between the continuous and the discrete problem, this choice of negative imaginary parts of the scattering strength is not substantial and discrete scatterers with purely imaginary positive scattering strength could be used alternatively (as long as a passband state in the underlying periodic setting is ensured for the purpose of our study). The important quantity is the positional disorder, which leads to wave interactions between adjacent scatterers with different phases in the perturbed setting. The great impact of positional disorder and the distribution inducing it becomes clear throughout the next section, where representative attenuation between the continuous and the discrete problem will be obtained.

4.3.2 Representative attenuation

As we can observe in Fig. 4.24, the distributions of clustered phase changes for the continuous problem are skewed for the non-dimensional correlation lengths $\bar{k}l_\mathrm{G} = 0.3$ and 0.5, and are shaped close to a bell curve for the larger correlation lengths. The derivation of the Berry–Klein limit is based on the assumption of uniformly distributed phase changes between adjacent scatterers. This assumption is fulfilled for the first comparison shown in Fig. 4.18 (and all numerical results in Sec. 4.2.3), where the positional disorder for all N discrete scatterers is realised by the uniformly distributed random variables $\nu_n, n = 1, \ldots, N$. To assimilate the continuous and the discrete problem, we adjust the distribution of the random variables ν_n to match with the clustered phase change distribution in the continuous problem. For this, our focus is on the continuous problem with non-dimensional correlation length $\bar{k}l_\mathrm{G} = 0.7$, which gives maximum attenuation. A non-parametric probability density function is fitted numerically using a kernel density estimator with a normal kernel smoothing function to the distribution of clustered reflection coefficient arguments for this case, see e.g. Silverman 1986. We refer to this probability density function for ν_n as kernel distribution from now on.

Fig. 4.26 shows the kernel distribution, which is scaled to fit to the histogram of clustered reflection coefficient arguments, for the roughness amplitude $\epsilon = 1.0 \times 10^{-1}$ and non-dimensional correlation length $\bar{k}l_\mathrm{G} = 0.7$ (left-hand panel). We also show the results for the non-dimensional correlation length $\bar{k}l_\mathrm{G} = 2.5$ (right-hand panel).

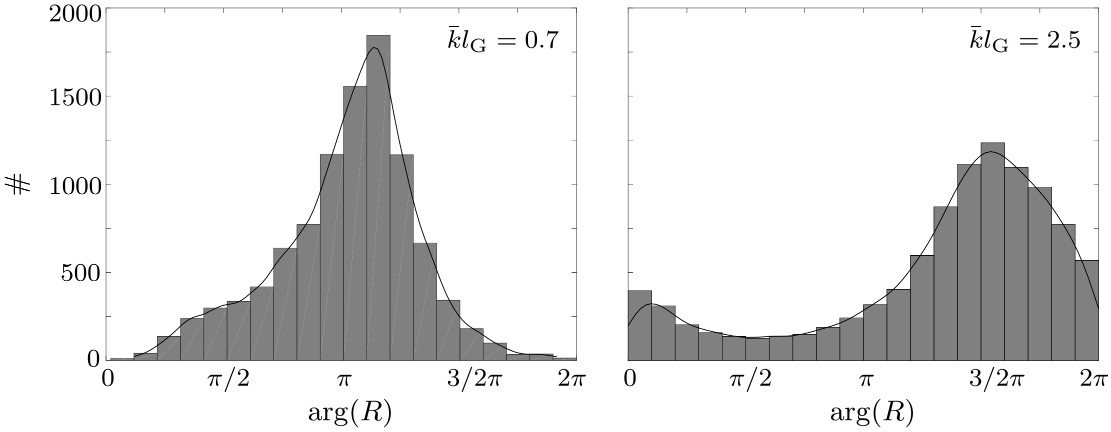

Figure 4.26: Scaled kernel distribution of reflection coefficient arguments of clustered humps, for roughness amplitude $\epsilon = 1.0 \times 10^{-1}$ and non-dimensional correlation lengths $\bar{k}l_{\mathrm{G}} = 0.7$ (left-hand panel) and $\bar{k}l_{\mathrm{G}} = 2.5$ (right-hand panel). Histogram plots of clustered reflection coefficient arguments are shown for comparison.

We can see in Fig. 4.26 that the scaled kernel distribution for the non-dimensional correlation length $\bar{k}l_{\mathrm{G}} = 0.7$ slightly deviates from a bell-shaped curve with its mode just above 1.1π. The curve is skewed to positive phase changes between 0.3π and 0.8π with very light tails, which indicates that significant phase changes occur throughout the whole rough interval. For the larger non-dimensional correlation length, $\bar{k}l_{\mathrm{G}} = 2.5$, the mode of the kernel distribution moves to approximately $3/2\,\pi$ and the distribution is broader compared to $\bar{k}l_{\mathrm{G}} = 0.7$. The clustered reflection coefficient arguments are more spread and the tails are significantly heavier, i.e. all phases are included in wave interactions between adjacent humps for $\bar{k}l_{\mathrm{G}} = 2.5$, even though the vast majority of phase changes still appear around the distribution's mode. In both cases it is better to avoid parametric distribution functions to describe the phase changes for the purpose of a good fit. We can observe that the kernel distributions constitute a good fit to the histograms (shown in Fig. 4.24 as polar histograms) and are representative for the phase changes.

Instead of choosing ν_n from $\mathcal{U}(-\nu/2,\nu/2)$ with $\nu \in [0,1)$, positional disorder of the N discrete scatterers from the underlying periodic setting is now introduced with ν_n being selected from the respective kernel distribution for the corresponding correlation length. The parameter ν is chosen to be the positional disorder threshold, $\nu = \pi/kd$, which ensures that all phases are included in the wave interaction between two adjacent scatterers.

Fig. 4.27 shows the individual attenuation coefficients for the discrete problem as functions of the scattering strength with positional disorder distributed according to the kernel distribution and uniformly, for non-dimensional correlation lengths $\bar{k}l_{\mathrm{G}} = 0.5$ (top-left panel), 0.7 (top-right panel), 1.1 (bottom-left panel) and 2.5 (bottom-right panel). Furthermore, the individual attenuation coefficients for the continuous problem and the Berry–Klein limit are shown for comparison. For the sake of brevity, we refer throughout the remainder of this section to the individual attenuation coefficients of the continuous problem and the individual attenuation coefficients of the discrete problem as continuous and discrete attenuation coefficients, respectively. Also, the constant wavenumber for non-dimensionalisation of the attenuation coefficients is denoted with $\bar{k}$ for both the discrete and continuous problem now.

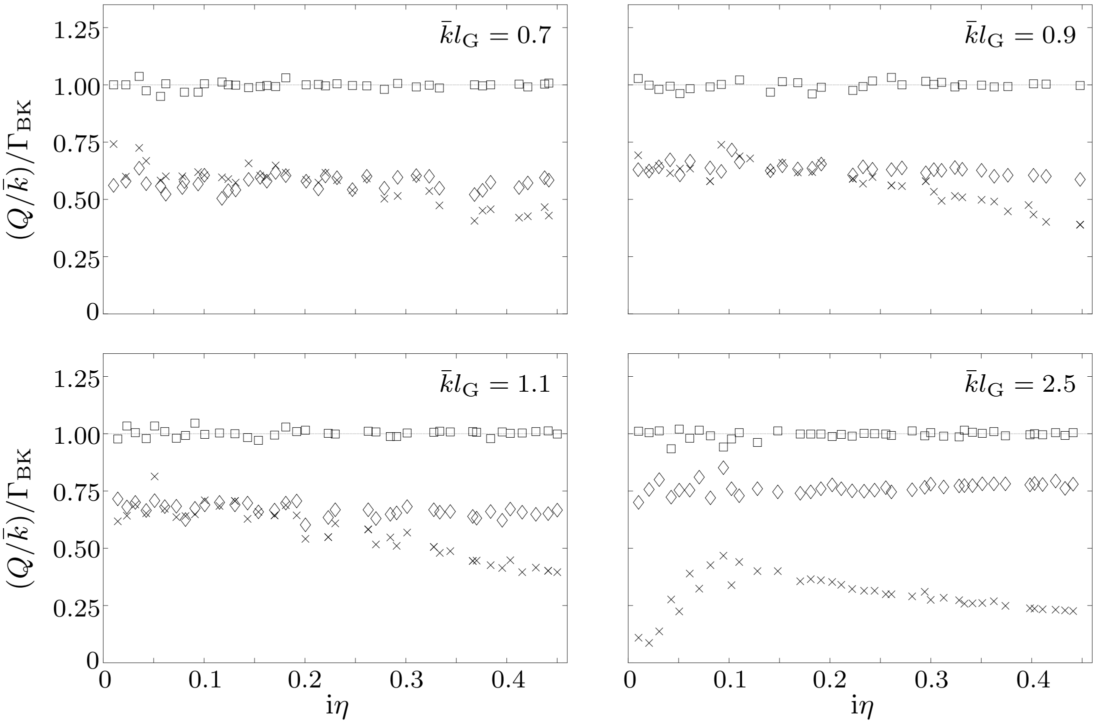

Figure 4.27: Scaled individual attenuation coefficients for continuous non-homogeneous string problem (×) and for beaded-string problem as functions of scattering strength for $\nu = \pi/kd$, with positional disorder distributed uniformly (□) and with kernel distribution (◇), for non-dimensional correlation lengths $\bar{k}l_\mathrm{G} = 0.7$ (top-left panel), $\bar{k}l_\mathrm{G} = 0.9$ (top-right panel), $\bar{k}l_\mathrm{G} = 1.1$ (bottom-left panel) and $\bar{k}l_\mathrm{G} = 2.5$ (bottom-right panel). Berry–Klein limit (dotted line) is shown for comparison.

We can see in Fig. 4.27 that the continuous attenuation coefficients are clearly smaller than the discrete attenuation coefficients with uniformly distributed positional disorder for all scattering strengths and correlation lengths considered. The discrete attenuation coefficients with uniformly distributed positional disorder coincide with the Berry–Klein limit. The continuous attenuation coefficients are proportional to the Berry–Klein limit for scattering strengths up to i$\eta \approx 0.3$ for $\bar{k}l_\mathrm{G} = 0.7$ and 0.9, before they level off for large moduli of η compared to the Berry–Klein limit. This is induced by the falling tendency of the continuous attenuation coefficients scaled by ϵ^2 for large ϵ (visible in Fig. 4.3), whereas the clustered reflection coefficient moduli show no deviation from the scaling with the roughness amplitude for large ϵ (see Fig. 4.23).

The most remarkable result in Fig. 4.27 is given by the discrete attenuation coefficients for the positional disorder distributed with the respective kernel distribution. The discrete attenuation coefficients are of the same magnitude as the continuous attenuation coefficients in the small correlation length cases, $\bar{k}l_{\mathrm{G}} = 0.5$, 0.7 and 1.1. For the large correlation length, $\bar{k}l_{\mathrm{G}} = 2.5$, the continuous attenuation coefficients are significantly smaller than for the smaller correlation length cases, while the discrete attenuation coefficients increase compared to the other cases, and the agreement between these attenuation coefficients ceases. The (continuous) rough profiles for this large correlation length are comparably smooth and lead to smaller attenuation coefficients than less correlated profiles with humps of similar reflection coefficient moduli, which is due to the different phase-change distributions. It is the broader phase-change distribution for $\bar{k}l_{\mathrm{G}} = 2.5$, which leads to larger discrete attenuation coefficients. Also note that in contrast to the continuous attenuation coefficients, the discrete attenuation coefficients for the kernel distribution do not level off for large η and are scaled with the discrete attenuation coefficients for uniform distribution (and hence the Berry–Klein limit) for all cases considered.

The results for the comparison between the continuous and discrete problem in Fig. 4.27 are only shown for a selection of correlation lengths. To show the effect of using the same phase-change distribution in both problems throughout the whole correlation length regime (and hence a great variety of different phase-change distributions), we compare the results for the continuous problem from Figs. 4.1 and 4.2 with the attenuation in the discrete problem with corresponding scattering strengths and assimilated phase-change distributions.

Fig. 4.28 shows the attenuation coefficients as functions of correlation length for the continuous problem and the discrete problem with positional disorder distributed both uniformly and with kernel distribution, for roughness amplitudes $\epsilon = 1.0 \times 10^{-2}$ (left-hand panel) and 1.0×10^{-1} (right-hand panel).

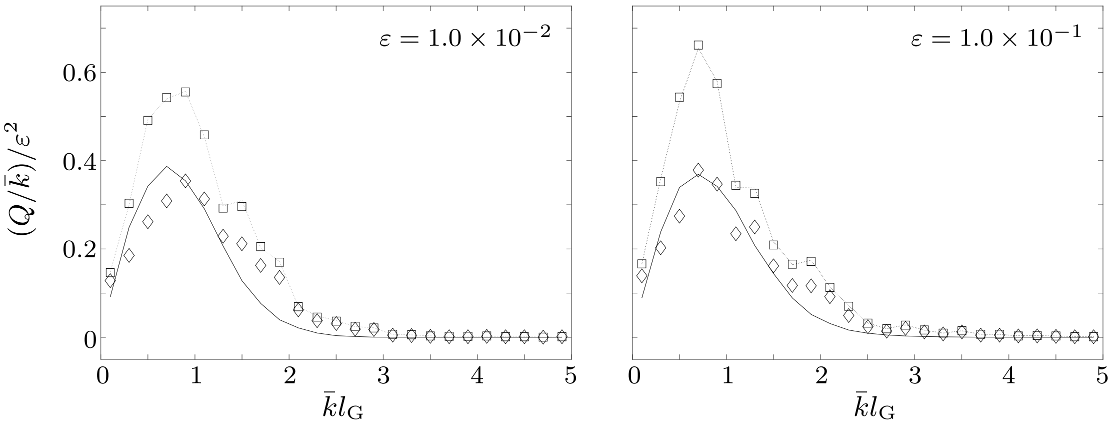

Figure 4.28: Scaled individual attenuation coefficients for continuous non-homogeneous string problem (black solid line) and for beaded-string problem as functions of underlying correlation length for $\nu = \frac{\pi}{kd}$, with positional disorder distributed uniformly (□) and with kernel distribution (◇), for roughness amplitudes $\epsilon = 1.0 \times 10^{-2}$ (left-hand panel) and $\epsilon = 1.0 \times 10^{-1}$ (right-hand panel). Berry–Klein limit (grey dotted line) is shown for comparison.

We can see in Fig. 4.28 the important influence of the phase-change distribution on the comparability of the continuous and discrete problem. For the discrete problem with uniformly distributed positional disorder, the attenuation coefficients show a hump behaviour for increasing correlation lengths, which is qualitatively similar to the attenuation coefficient curve for the continuous problem, but exceed these values significantly throughout the correlation length regime $\bar{k}l_{\mathrm{G}} \leq 2$, for which significant attenuation is observable.

Adjusting the positional-disorder distribution using the kernel distribution, which describes the phase-change distribution in the continuous problem, results in discrete attenuation coefficients, which leave the Berry–Klein limit and approach the continuous attenuation coefficients. For both roughness amplitudes, $\epsilon = 1.0 \times 10^{-2}$ and 1.0×10^{-1}, the attenuation coefficients of the continuous and adjusted discrete problem share the same qualitative and quantitative features and we get attenuation of the same magnitude. For the smaller roughness amplitude, $\epsilon = 1.0 \times 10^{-2}$, the hump of the adjusted discrete problem is slightly shifted towards the larger correlation lengths. In the intermediate correlation length regime, the attenuation coefficients for the discrete problem with adjusted positional disorder exceed the continuous attenuation coefficients and are (due to the broad phase-change distributions) close to the Berry–Klein limit again. For large correlation lengths, the discrepancy between continuous and discrete attenuation coefficients is not visible anymore, since the attenuation coefficients tend to zero for the small clustered reflection coefficient moduli. Altogether, Fig. 4.28 confirms the finding from Fig. 4.27 that the phase-change-adjustment approach only leads to representative attenuation for the continuous and discrete problem in the small correlation length regime, for which the phase-change distribution is not too broad.

In conclusion, assimilating the scattering strength and the phase-change distribution for the (continuous) non-homogeneous string problem and the (discrete) beaded-string problem yields similar attenuation for the cases of narrow phase-change distributions around π. The phase-change distribution is decisive for the agreement of the attenuation coefficients for both problems. This finding leads to the conclusion that, apart from the scattering strength, the phases included in wave interactions of adjacent scatterers play the key role for attenuation. With the phase-change assimilation, we obtained a regime for which discrete and continuous scatterers are representative for each other.

4.4 Summary and discussion

After introducing the problems of waves travelling along an inhomogeneous string with a continuous roughness profile, the step approximation and random-sampling method were applied to solve the problem in the same way as the in-vacuo beam and floating plate problems. A numerical cut-off scheme ensured for large roughness amplitudes that the problem did not become unphysical and allowed larger roughness amplitudes than in the solution procedure for the previous problems. The transition to large roughness amplitudes lead to agreement of individual and effective attenuation coefficients, which enhanced our understanding of the problem, in particular individual and effective wave fields can be representative for each other even for continuous scattering problems if the scattering is strong enough. It should be noted that due to the strong scattering, the effective wave field is subject to statistical artefacts in the large roughness amplitude regime, since the wave fields are fully attenuated over the interval under consideration. We circumvented this by introducing a quantile approach to remove non-representative individual wave fields, i.e. wave fields which attenuate much slower than the other wave fields and subsequently dominate the corresponding effective wave field. However, the statistical characteristics of the random process are lost in the large roughness regime by introducing the numerical cut-off scheme and the analytical multiple-scale method is not applicable anymore.

Before investigating the connection between wave propagation along strings with continuous and discrete inhomogeneities, we studied the discrete problem in the setting of a string beaded with point scatterers. To study the influence of disorder on the attenuation of waves travelling along a beaded string, we focused on disordering the position of the beads only and started in passbands for the underlying periodic beads configuration. The numerical method used for the continuous problem was modified such that it could be used for solving the discrete problem for given point scatterer configurations. Again, an averaging routine was used to calculate the effective wave field as average of individual wave fields for randomly generated point scatterer configurations. We could observe that in this problem setting, individual and effective wave fields correspond throughout a large regime of scattering strengths and their attenuation coefficients coincide with the Berry–Klein limit for sufficiently large positional disorder. For small scattering strengths, effective wave fields attenuate faster due to wave-cancellation effects (which were responsible for the discrepancy between the effective and individual wave fields for the continuous problems).

To connect the continuous and discrete string problems, a numerical routine was used to cluster continuous roughness profiles into single humps and we studied their statistics. We have seen that the phase-change distribution is important for the attenuation magnitude in the discrete problem. The maximum attenuation in the discrete problem occurs for phase changes distributed around π. We used the phase-change distribution for the continuous problem to fit a non-parametric distribution. This distribution was employed to describe the positional disorder in the discrete problem (mean scattering strength was obtained from clustered humps) and we compared the results with the underlying continuous problem. The key finding was that the phase-change distribution is decisive. For phase-change distributions in the correlation-length regime producing maximum attenuation for the continuous problem, agreement between the attenuation in the continuous and discrete problem was reached.

Appendix

4.A Multiple-scale method

In the following, we derive the multiple-scale method, which was used in Figs. 4.1–4.3. In analogy to the multiple-scale methods for the in-vacuo beam and floating plate problems in Chs. 2 and 3, the coordinates x and x_2 denote the coordinates on the local and observation scales, respectively. Using the multiple-scale expansion from Eqn. (2.82) for the wave field, u, describing the string deflection in Eqn. (4.1), and the derivative expansion from Eqn. (2.83), we obtain the equations, which have to be satisfied by the u_j, $j = 0{,}1{,}2$, by separating the terms with respect to orders of ϵ. Here, the representation of the varying wavenumber from Sec. 4.1, $k(x) = \bar{k}(1 + \epsilon\kappa(x))$, is used.

Order ϵ^0

The governing equation for the leading-order wave field, u_0, is the spatial Helmholtz equation for the constant wavenumber $\bar{k}$,

$$\partial_x^2 u(x{,}x_2) + \bar{k}^2 u(x{,}x_2) = 0, \qquad x \in (-\infty{,}\infty), \tag{4.A.1}$$

which describes the propagation of a wave along an uniform string.

To be consistent with the right incident wave for the finite roughness interval problem in Sec. 4.1 and in analogy the multiple-scale approximations for the in-vacuo beam and floating plate problems, we only consider a right-travelling wave at leading order and neglect the left-travelling wave. This gives the wave field at leading order,

$$u_0(x{,}x_2) = A(x_2)\, \mathrm{e}^{\mathrm{i}\bar{k}x}. \tag{4.A.2}$$

To determine the complex-valued amplitude A, the higher-order equations have to be solved.

Order ϵ^1

The order ϵ terms give the governing equation for u_1 to be

$$\partial_x^2 u_1(x{,}x_2) + \bar{k}^2 u_1(x{,}x_2) = -2\bar{k}^2\kappa(x) u_0(x{,}x_2). \tag{4.A.3}$$

To solve Eqn. (4.A.3), the force on the first-order wave field, u_1, described by the product of the leading-order wave field, u_0, and the random fluctuation, κ, is replaced by a point load with the Dirac delta distribution at the source point $\check{x}$, i.e.

$$\partial_x^2 G(|x-\check{x}|) + \bar{k}^2 G(|x-\check{x}|) = \delta(x-\check{x}), \quad x \in (-\infty,\infty). \tag{4.A.4}$$

The Green's function solving Eqn. (4.A.4) can easily be derived to be

$$G(|x-\check{x}|) = \frac{\mathrm{i}}{2\bar{k}} \mathrm{e}^{\mathrm{i}\bar{k}|x-\check{x}|}. \tag{4.A.5}$$

Fig. 4.A.1 shows the Green's function (left-hand panel) from Eqn. (4.A.5) and its first derivative (right-hand panel), for the constant wavenumber $\bar{k}$ scaled to unity.

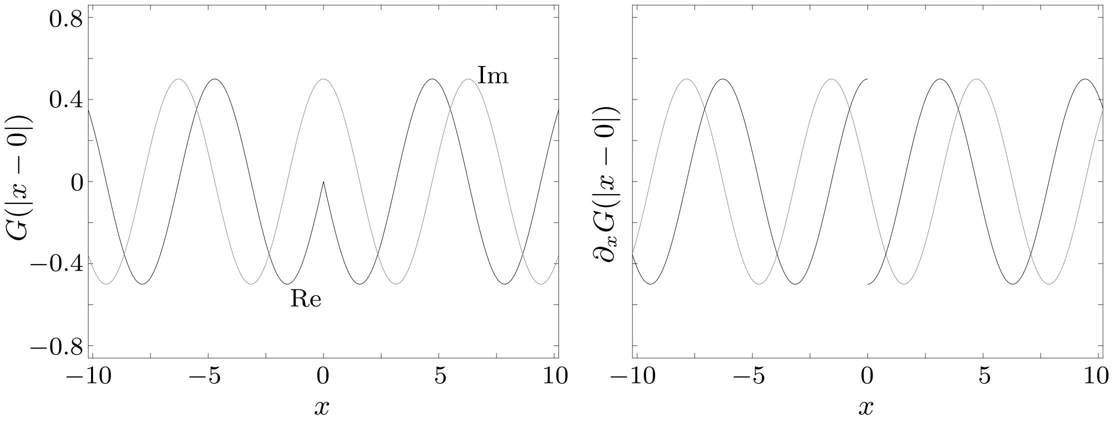

Figure 4.A.1: Green's function (left-hand panel) and its first derivative (right-hand panel) for Helmholtz equation with point load at source point $\check{x} = 0$, for $\bar{k}$ scaled to unity

The approach with Green's function leads to the solution of Eqn. (4.A.3) for a given κ to be

$$u_1(x,x_2) = -2\bar{k}^2 \int_{-\infty}^{\infty} G(|x-\check{x}|)\kappa(\check{x})u_0(\check{x},x_2)\,\mathrm{d}\check{x}. \tag{4.A.6}$$

Order ϵ^2

Collecting the terms at order ϵ^2 gives for $x \in (-\infty,\infty)$

$$\partial_x^2 u_2(x,x_2) + \bar{k}^2 u_2(x,x_2) = -2\bar{k}^2(\kappa(x))^2 u_0(x,x_2) - 2\partial_x\partial_{x_2}u_0 - 2\bar{k}^2\kappa(x)u_1(x,x_2), \tag{4.A.7}$$

which is the governing equation for the second-order wave field, u_2. Taking the ensemble average of Eqn. (4.A.7) leads to

$$\partial_x^2\langle u_2(x,x_2)\rangle + \bar{k}^2\langle u_2(x,x_2)\rangle = -2\bar{k}^2\langle(\kappa(x))^2 u_0(x,x_2)\rangle - 2\langle\partial_x\partial_{x_2}u_0\rangle - 2\bar{k}^2\langle\kappa(x)u_1(x,x_2)\rangle. \tag{4.A.8}$$

The averaged solution $\langle u_2 \rangle$ can be found by employing the ansatz $\langle \phi_2 \rangle = F(x_2)\mathrm{e}^{\mathrm{i}\bar{k}x}$. The left-hand side of Eqn. (4.A.8) vanishes, hence Eqn. (4.A.8) can be written as

$$-\bar{k}^2\mathrm{e}^{\mathrm{i}\bar{k}x}\langle A(x_2)\kappa(x)\kappa(x)\rangle - 2\mathrm{i}\bar{k}\mathrm{e}^{\mathrm{i}\bar{k}x}\langle \partial_{x_2}A(x_2)\rangle + 4\bar{k}^4\mathrm{e}^{\mathrm{i}\bar{k}x}\int\limits_{-\infty}^{\infty}\langle \kappa(x)\kappa(\check{x})A(x_2)\rangle G(|x-\check{x}|)\,\mathrm{d}\check{x} = 0. \tag{4.A.9}$$

Under the assumption of independence of the leading-order wave amplitude, $A(x_2)$, from $\kappa(x)\kappa(\check{x})$ appearing on the local scale, i.e. $\langle A(x_2)\kappa(x)\kappa(\check{x})\rangle = \langle A(x_2)\rangle\langle\kappa(x)\kappa(\check{x})\rangle$, the correlation length representation from Eqn. (2.70) for κ can be used to simplify Eqns. (4.A.8) and (4.A.9) to

$$\langle \partial_{x_2}A(x_2)\rangle = \mathrm{i}\underbrace{\left(\frac{\bar{k}}{2} + 2\bar{k}^3\hat{\zeta}\right)}_{=:\zeta}A(x_2), \tag{4.A.10}$$

where the complex constant $\hat{\zeta}$ is given by

$$\hat{\zeta} = \int_{-\infty}^{\infty} G(|\xi|)\mathrm{e}^{\mathrm{i}\bar{k}\xi}\rho(|\xi|)\,\mathrm{d}\xi. \tag{4.A.11}$$

For the calculation of $\hat{\zeta}$, the integral is calculated numerically using an adaptive quadrature scheme. The solution of the ordinary differential equation describing the averaged leading-order wave amplitude in Eqn. (4.A.10) is

$$\langle A(x_2)\rangle = A_0\,\mathrm{e}^{\mathrm{i}\zeta x_2}, \tag{4.A.12}$$

where A_0 is a constant and the complex constant ζ is defined in Eqn. (4.A.10). Hence, the effective attenuation coefficient, Q_{eff}, is given by

$$Q_{\text{eff}} = \epsilon^2\mathrm{Im}(\zeta). \tag{4.A.13}$$

4.B Direct numerical scheme

In Maurel et al. 2010, a direct numerical scheme is presented to calculate the wave field $u(x)$ along a string with a finite number of discrete scatterers of the same scattering strength. We apply this approach to our problem of N discrete scatterers of scattering strength η, positioned at $x = x_n, n = 1, \dots, N$, and an incident right-travelling wave of unit amplitude. Replacing the amplitude of the left-travelling waves in the wave field representation in Eqn. (4.8) by $b_n = a_n Z_n$, the wave field between adjacent scatterers can be written as

$$u(x) = a_n \left(\mathrm{e}^{\mathrm{i}k(x-x_n)} + Z_n \mathrm{e}^{-\mathrm{i}k(x-x_n)} \right), \quad x_{n-1} \le x \le x_n. \tag{4.B.1}$$

To derive a recurrence relation for Z_n, a ghost scatterer is appended at the position of the last scatterer, $x_{N+1} = x_N$. It follows that Z_{N+1} has to be zero to meet the radiation condition for $x \to \infty$. Applying the continuity of deflection and continuity of force conditions (4.9), the (backwards) recurrence relation for Z_n is

$$Z_n = -\frac{\eta \mathrm{e}^{-\mathrm{i}k(x_{n+1}-x_n)} + (1+\eta)\, \mathrm{e}^{\mathrm{i}k(x_{n+1}-x_n)} Z_{n+1}}{(\eta - 1)\, e^{-\mathrm{i}k(x_{n+1}-x_n)} + \eta \mathrm{e}^{\mathrm{i}k(x_{n+1}-x_n)} Z_{n+1}}, \quad n = N, \dots, 0, \tag{4.B.2}$$

where $Z_{N+1} = 0$. Starting with $a_0 = \mathrm{e}^{\mathrm{i}kx}$, which describes the incident wave of unit amplitude, the recurrence relation in Eqn. (4.B.2) allows to calculate the wave amplitudes of the right-travelling waves,

$$a_{n+1} = (\eta Z_n + \eta + 1)\, \mathrm{e}^{-\mathrm{i}k(x_{n+1}-x_n)} a_n, \quad n = 1, \dots, N, \tag{4.B.3}$$

and the full wave field is determined. Comparisons between this direct numerical scheme and the discrete iterative scheme, we used throughout Ch. 4, are presented in Fig. 4.6.

4.C Coherent potential approximation

The coherent potential approximation (CPA) is a widely used method in describing effective wave propagation in random media, see Sheng 2006. It is based on the assumption that a cell, which is embedded in the effective medium, is transparent to the propagating wave if the cell has the same properties as the effective medium. A CPA method to describe the effective wave propagation along an one-dimensional perturbed periodic structure was developed by Maurel et al. (2010). In the following, we introduce this method without firstly dealing with the perfectly periodic case (as done in Maurel et al. 2010). Therefore, we focus on the derivation of the CPA for the perturbed periodic setting from the beginning on.

We assume that the cell $[(n-1)d+z, nd+z]$, which contains the $(n+1)$-th scatterer at $x_n = (n+\nu_{n+1})d$, is embedded in the effective medium. The effective medium is obtained by averaging over all realisations of the scatterers but the scatterer in the isolated cell. The location of the embedded cell is specified with the parameter z, which can be varied as long as it contains the $(n+1)$-th scatterer in the inside, i.e. $\nu_{n+1}d < z < d - \nu_{n+1}d$. The parameter z can be set to any value in this interval without the problem to be changed. The perturbation of the single scatterer in the embedded cell from the underlying periodic position leads to reflection and transmission at the cell interfaces. (Note that $\nu_{n+1} = 0$ gives no reflection or transmission at the interfaces since the cell is then equivalent to the effective medium and hence transparent for the incident wave.) In the effective medium, right- and left-going waves appear propagating as $g_\nu(y)\mathrm{e}^{\mathrm{i}\tilde{Q}x}$ and $f_\nu(y)\mathrm{e}^{-\mathrm{i}\tilde{Q}x}$, respectively. In the case of $\tilde{\nu}_n := \nu_{n+1} \neq 0$, the wave field $\nu(x)$ is

$$\nu(x) = \begin{cases} g_\nu(y)\mathrm{e}^{\mathrm{i}Kx} + R_\nu(\tilde{\nu}_n)f_\nu(y)\mathrm{e}^{-\mathrm{i}Kx}, & x < (n-1)d+z, \\ a_1\mathrm{e}^{\mathrm{i}kx} + b_1\mathrm{e}^{-\mathrm{i}kx}, & (n-1)d+z \le x < (n+\tilde{\nu}_n)d, \\ a_2\mathrm{e}^{\mathrm{i}kx} + b_2\mathrm{e}^{-\mathrm{i}kx}, & (n+\tilde{\nu}_n)d \le x < nd+z, \\ T_\nu(\tilde{\nu}_n)g_\nu(y)\mathrm{e}^{\mathrm{i}Kx}, & x \ge nd+z, \end{cases} \tag{4.C.1}$$

where K is the wavenumber in the effective medium. Using the continuity of $\nu(x)$ and $\partial_x\nu(x)$ at the cell interfaces $x = (n-1)d+z$ and $x = nd+z$ as well as the continuity of $\nu(x)$ and force conditions at the scatterer position $x_n = (n+\tilde{\nu}_n)d$, we obtain

$$\left[(1-\eta)\,A_\nu - \eta B_\nu\mathrm{e}^{-2\mathrm{i}\tilde{\nu}_n kd}\right] T_\nu(\tilde{\nu}_n) - B_\nu\mathrm{e}^{-2\mathrm{i}Knd}R_\nu(\tilde{\nu}_n) = A_\nu\mathrm{e}^{\mathrm{i}(k-K)d}, \tag{4.C.2a}$$

$$\left[\eta A_\nu\mathrm{e}^{2\mathrm{i}\tilde{\nu}_n kd} + (1+\eta)\,B_\nu\right] T_\nu(\tilde{\nu}_n) - A_\nu\mathrm{e}^{-2\mathrm{i}Knd}R_\nu(\tilde{\nu}_n) = B_\nu\mathrm{e}^{-\mathrm{i}(k-K)d} \tag{4.C.2b}$$

with

$$g_\nu(y) = A_\nu\mathrm{e}^{\mathrm{i}(k-K)y} + B_\nu\mathrm{e}^{-\mathrm{i}(k-K)y}, \tag{4.C.3a}$$

$$f_\nu(y) = g_\nu(d-y) \tag{4.C.3b}$$

and

$$a_1 = T_\nu(\tilde{\nu}_n)\mathrm{e}^{\mathrm{i}(K-k)nd}\left[(1-\eta)\,A_\nu - \eta B_\nu \mathrm{e}^{-2\mathrm{i}\tilde{\nu}_n kd}\right], \qquad a_2 = A_\nu T_\nu(\tilde{\nu}_n)\mathrm{e}^{\mathrm{i}(K-k)nd}, \tag{4.C.3c}$$

$$b_1 = T_\nu(\tilde{\nu}_n)\mathrm{e}^{\mathrm{i}(K+k)nd}\left[\eta A_\nu \mathrm{e}^{2\mathrm{i}\tilde{\nu}_n kd} + (1+\eta)\,B_\nu\right], \qquad b_2 = B_\nu T_\nu(\tilde{\nu}_n)\mathrm{e}^{\mathrm{i}(K+k)nd}. \tag{4.C.3d}$$

To determine the effective wavenumber K from Eqns. (4.C.2), we have to apply the CPA assumption now, which was not used in the derivation of Eqns. (4.C.2) yet. The CPA idea here is that the embedded cell is transparent in the effective medium, if the scatterer position inside the cell is averaged with respect to all realisations, i.e.

$$\langle R_\nu \rangle = 0, \tag{4.C.4a}$$

$$\langle T_\nu \rangle = 1, \tag{4.C.4b}$$

where the average with respect to all scatterer positions is $\langle\cdot\rangle = 2/\nu\int_{-\nu}^{\nu}\cdot\,\mathrm{d}\tilde{\nu}_n$. Taking the average of Eqns. (4.C.2) and comparisons with the solution for the d-periodic host medium result in

$$\left(1-\eta-\mathrm{e}^{\mathrm{i}(k-K)d}\right)A_\nu - \eta\,\mathrm{sinc}(\nu kd)B_\nu = 0, \tag{4.C.5a}$$

$$\eta\,\mathrm{sinc}(kd\nu)A_\nu + \left(1+\eta-\mathrm{e}^{-\mathrm{i}(k+K)d}\right)B_\nu = 0. \tag{4.C.5b}$$

Eqns. (4.C.5) can be solved for K using the dispersion relation for the wavenumber of the Floquet mode, Eqn. (4.22a). Hence, the dispersion relation for the effective wavenumber is

$$\cos(Kd) = \cos(\tilde{Q}d) + \frac{1}{2}\eta^2\mathrm{e}^{\mathrm{i}Kd}\left(1-\mathrm{sinc}^2(\nu kd)\right). \tag{4.C.6}$$

For a detailed derivation of the dispersion relation for the effective wavenumber, we refer to Maurel et al. 2010.

CHAPTER 5

Localisation of waves in the audible frequency range travelling along a beam with discrete notches

We focused on beams in vacuo with continuous profile variations in Ch. 2 and established a connection between continuous and discrete scattering for inhomogeneous string problems in Ch. 4. We have seen that discrete scatterers consistently lead to attenuation, if their positions, which ensure passband states in the periodic configuration, are disordered. Now, we change over to a beam in vacuo again. Instead of dealing with continuous profile variations, we deal with discrete scatterers, which are realised by discrete notches cut into the beam. The length of the notches shall be of the order of the waves travelling along the beam and we focus on a beam with several notches (of uniform depth) located periodically, such that the distance between adjacent notches is the same as the (uniform) notch length. It is well known that this geometry yields a pass- and stopband behaviour for uniform notch depth of all notches, see Langley 1995. Our goal in this study is to achieve localisation of the travelling wave by notch depth variations. This corresponds to scattering strength variations in an underlying periodic structure, for which in the string problem only enhanced scattering and no localisation is observed, see Ottarsson and Pierre 1997 for the study of bead-mass disorder in a beaded string.

After introducing the problem setting in Sec. 5.1, we will show the pass- and stopband behaviour for the periodic problem in Sec. 5.2. The beam is modelled in analogy to Ch. 2 as an Euler–Bernoulli beam. The numerical calculations to obtain the wave fields and the scattering characteristics are performed with the step-approximation method from Sec. 2.2. After this preliminary study, we will introduce disorder into the notch depths and investigate the effect of disorder in the notch depths on the wave propagation along the beam.

Comparisons with results from computationally expensive finite element (FE) simulations performed with Abaqus FEA, a software suite for computer-aided design, engineering and finite element analysis, motivate the transition from the Euler–Bernoulli beam model to a Timoshenko beam model in Sec. 5.4. This transition is due to the frequency range of the waves in the audible kHz-regime, which we consider in our problem setting and for which the Timoshenko beam theory yields more accurate results than the Euler–Bernoulli beam theory. We will investigate the pass- and stopband behaviour in the periodic setting for the Timoshenko beam then as well as the effect of disordered notch depths. To lay the theoretical foundation of experiments in order to confirm the localisation of waves in the audible frequency range travelling along the beam with discrete notches, we extend the problem formulation to be time-dependent. For this, we use the Fourier transform to allow incoming waves with a frequency spectrum and use our numerical method for the analysis. Finally, a summary and discussion of the results are given in Sec. 5.5.

5.1 Problem formulation

For the localisation investigations in this chapter, we consider a non-uniform beam. Unlike in the studies of the beam in vacuo in Ch. 2, the non-uniformity is not induced by continuous variations in the material properties or its geometry, but by discrete thickness variations. A long Aluminium beam with a small, rectangular cross-section serves as a model, and we choose the constant beam width to be $w = 12\,\mathrm{mm}$ and the beam thickness for the uniform beam to be $h = 6\,\mathrm{mm}$. The cross-sectional area of the beam, $A(x)$, and the moment of inertia of the beam cross section, $I(x)$, are then given by Eqns. (2.120), i.e.

$$\begin{aligned} A(x) &= w\,h(x), \\ I(x) &= \frac{w\,h(x)^3}{12}. \end{aligned}$$

The Aluminium beam has a Young's modulus of $E = 69.5\,\mathrm{GPa} = 69.5 \times 10^9\,\mathrm{N/m^2}$ and density $\rho = 2.7 \times 10^3\,\mathrm{kg/m^3} = 2.7\,\mathrm{g/cm^3}$, see e.g. Ostermann 2014. These material properties shall be uniform along the beam. The beam mass per unit length, $g(x)$, is then given by the product of mass density and cross-sectional area, and the beam rigidity, $b(x)$, is the product of Young's modulus and the moment of inertia of the beam cross section, see Eqns. (2.7).

The discrete thickness variations are included by notches over the whole beam width, which are cut vertically into beam, reducing the beam thickness h. A finite number of notches, N, is used and each notch shall be of a constant notch depth. The depth of the nth notch is denoted with d_n. We restrict ourselves to notches of constant length l and constant distance between adjacent notches, which is chosen to be of the same length, l. The coordinate of the left end of the nth notch is denoted with x_n, $n = 1, \ldots, N$. Fig. 5.1 shows a section of the beam with discrete notches schematically.

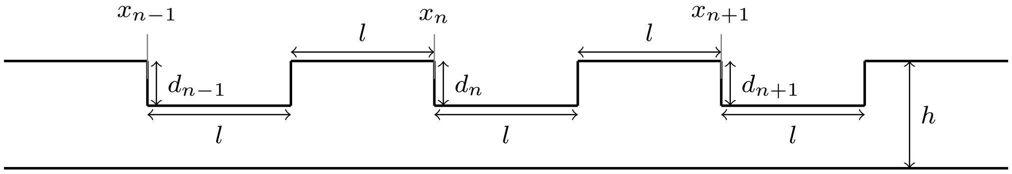

Figure 5.1: Schematical section of beam model with discrete notches

We consider two problems in the following. Firstly, we have a periodic notch configuration, which means that all N notches are of the same depth d_0, i.e. $d_n = d_0$, $n = 1, \ldots, N$. This periodic configuration helps us to understand the influence of the notch geometry on the wave propagation along the beam and the pass- and stopband behaviour for the frequency spectrum. It also serves as a starting point for our studies of the impact of deviations from the periodic configuration with notch depth variations. For practical feasibility with experiments, we only consider deviations leading to increasing notch depths. The notch depth disorder is introduced with random variables ϵ_n, $n = 1, \ldots, N$, which describe the relative increase of the nth notch depth from the underlying periodic configuration, i.e.

$$d_n = (1 + \epsilon_n)\, d_0, \quad n = 1, \ldots, N. \tag{5.1}$$

The random variables ϵ_n, $n = 1, \ldots, N$, are randomly chosen from the uniform distribution, $\epsilon_n \in \mathcal{U}(0,\epsilon)$. (Note that the choice $\epsilon_n = 0, n = 1, \ldots, N$, gives the periodic problem.) The initial depth in the periodic configuration, d_0, is restricted not to be larger than 2.5 mm for this randomisation scheme, which ensures that the beam thickness does not get smaller than 1 mm at any point for $\epsilon = 1$.

5.2 Time-harmonic setting with Euler–Bernoulli beam

We start the investigation of the posed problem with the Euler–Bernoulli beam model, which we studied thoroughly in Ch. 2. Since we assume to have a long beam with a finite number of notches placed far away from the ends of the beam, we can use, similarly to the previous problems, an infinite beam, for which we do not have to deal with interferences by the beam boundaries. We can use the step-approximation method for the in-vacuo beam problem, which was introduced in Sec. 2.2, to perform the numerical calculations to obtain the wave fields and the scattering characteristics. This method is computationally very efficient, since we do not have to approximate the stepped thickness profile and use a resolution as high as in the continuous problem. Each interval length in the numerical method is determined by the respective notch length, since only each jump in the beam thickness corresponds to a scattering interface.

5.2.1 Periodic notch configuration

Firstly, we study the pass- and stopband behaviour of the notched beam problem. For this, we analyse the eigenvalues of the transfer matrix $\mathbf{P}$. The transfer matrix for the in-vacuo beam problem is defined in Eqns. (2.27) and (2.28). To take the periodicity into account, we analyse the transfer matrix, which describes the propagation of a wave along one notch and the subsequent beam section of length l separating adjacent notches. This arrangement defines the periodic structure of the underlying problem with the periodic notch configuration.

Fig. 5.2 shows the eigenvalues of the transfer matrix, λ, for $d_0 = 1.0$ mm (left-hand panel) and 2.0 (right-hand panel) for frequencies $f \in (0, 50\,\mathrm{kHz})$. The ordinary frequency f is associated with the angular frequency ω via

$$f = \frac{\omega}{2\pi}. \tag{5.2}$$

Until specified again, the notch length is set to $l = 3.0\,\mathrm{cm}$.

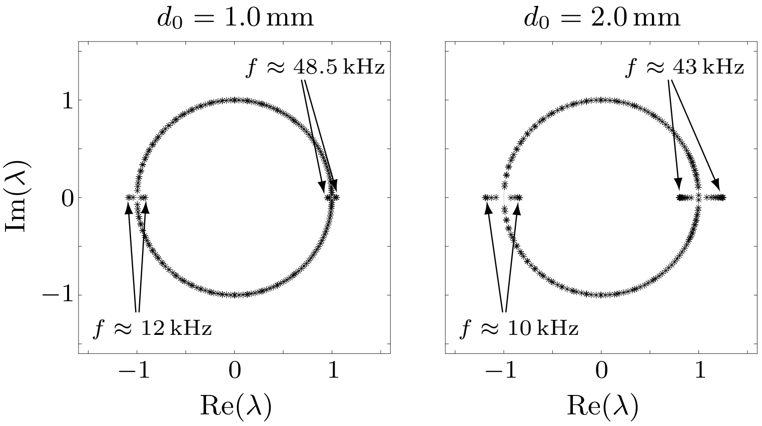

Figure 5.2: Eigenvalues of transfer matrix for $d_0 = 1.0\,\mathrm{mm}$ (left-hand panel) and $d_0 = 2.0\,\mathrm{mm}$ (right-hand panel), for frequencies $f \in (0\,\mathrm{kHz}, 50\,\mathrm{kHz})$

We can observe in Fig. 5.2 that the eigenvalues pass along the unit circle, form conjugate pairs and leave the unit circle, appearing as (real) reciprocal pairs, as the eigenvalues get close to the real axis, for both periodic notch depths, $d_0 = 1.0\,\mathrm{mm}$ and $2.0\,\mathrm{mm}$. We could already observe this behaviour for the beaded-string problem in Fig. 4.8. For $d_0 = 1.0\,\mathrm{mm}$, the eigenvalues depart around the frequencies $f \approx 12\,\mathrm{kHz}$ and $48\,\mathrm{kHz}$, suggesting the existence of stopbands around these frequencies, see Sec. 4.2. It is interesting to note and novel compared to the beaded-string problem that the maximum deviation from the unit circle depends on the frequency regime. The reciprocal pairs for $f \approx 12\,\mathrm{kHz}$ depart farther away from the unit circle than for $f \approx 48.5\,\mathrm{kHz}$. The larger moduli of the reciprocal pairs for $f \approx 12\,\mathrm{kHz}$ deviate from the unit circle by about 0.1 and for $f \approx 48.5\,\mathrm{kHz}$ by about 0.05 only.

For $d_0 = 2.0\,\mathrm{mm}$, the maximum deviation from the unit circle is attained for slightly smaller frequencies, $f \approx 10\,\mathrm{kHz}$ and $f \approx 43\,\mathrm{kHz}$ for the negative and positive real axis, respectively. We can see that the larger notch depth does not only lead to an increase of deviation of the eigenvalues with the larger modulus from the unit circle close to the real axis, but the eigenvalues for $f \approx 43\,\mathrm{kHz}$ deviate farther from the unit circle than those for $f \approx 10\,\mathrm{kHz}$ now (with maximum deviations of 0.25 and 0.19, respectively). To give us a better understanding of this phenomenon, the left-hand panel of Fig. 5.3 shows the moduli of the eigenvalues of the transfer matrix, which lie within the unit circle, as functions of the frequency f, for notch depths $d_0 = 1.0\,\mathrm{mm}$, $2.0\,\mathrm{mm}$ and $3.0\,\mathrm{mm}$. The right-hand panel of Fig. 5.3 shows the same moduli of the eigenvalues of the transfer matrix as functions of the frequency $K = 2kl/\pi$, which is used to characterise Bragg resonances, also for notch depths $d_0 = 1.0\,\mathrm{mm}$, $2.0\,\mathrm{mm}$ and $3.0\,\mathrm{mm}$.

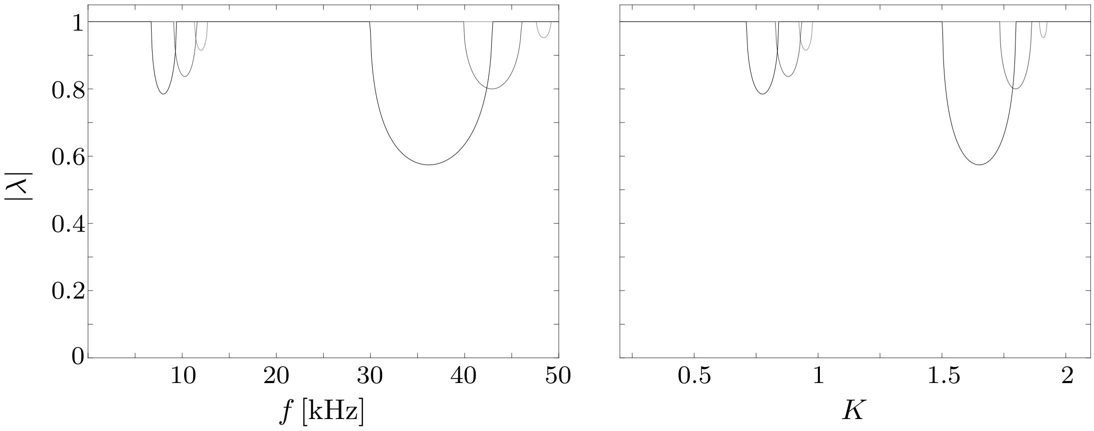

Figure 5.3: Left-hand panel: Eigenvalues of transfer matrix as functions of frequency, for $d_0 = 1.0\,\mathrm{mm}$ (light grey), $d_0 = 2.0\,\mathrm{mm}$ (dark grey) and $d_0 = 3.0\,\mathrm{mm}$ (black). Left-hand panel: Eigenvalues of transfer matrix as functions of Bragg's value, for $d_0 = 1.0\,\mathrm{mm}$ (light grey), $d_0 = 2.0\,\mathrm{mm}$ (dark grey) and $d_0 = 3.0\,\mathrm{mm}$ (black).

We can observe in the left-hand panel of Fig. 5.3 that the eigenvalue moduli shown are unity for most of the frequency regime, for $d_0 = 1.0\,\mathrm{mm}$, i.e. we have a passband there. The eigenvalues only depart from unity for $f \approx 12\,\mathrm{kHz}$ and slightly less for $f \approx 48\,\mathrm{kHz}$, which could already be observed in Fig. 5.2, defining the stopband in this regime. For increasing notch depth, the deviation from unity increases and the frequency bands, for which this is evident, become broader and travel towards the lower end of the frequency regime. In particular for $d_0 = 3.0\,\mathrm{mm}$, the considered eigenvalue moduli are only 0.8 and 0.6, respectively, and they depart from unity for $f \in (7\,\mathrm{kHz}, 12\,\mathrm{kHz})$ and $f \in (30\,\mathrm{kHz}, 43\,\mathrm{kHz})$, respectively, which define the stopbands. The minima are attained for $f \approx 9\,\mathrm{kHz}$ and $f \approx 36\,\mathrm{kHz}$, indicating that the attenuation is strongest for these values. It is clear that this behaviour is confirmed in the right-hand panel of Fig. 5.3, since the same eigenvalue moduli are shown, only as functions of K. For $d_0 = 1.0\,\mathrm{mm}$, the eigenvalue moduli shown depart from unity for values of K around the integers 1 and 2, which are the Bragg resonances, see Sec. 4.2.1. The Bragg resonances are generated by the underlying periodic structure with moderate scattering strength. For increasing d_0, the resonances move to the left of the values, known as Bragg resonances. Whereas the second Bragg resonance leads to smaller deviation of the eigenvalue moduli from unity than the first Bragg resonance for the smallest periodic notch depth under consideration, $d_0 = 1.0\,\mathrm{mm}$, it is clearly visible that the second Bragg resonance leads to more deviation than the first one for increasing notch depth, such that the deviation is twice as much as for the first resonance for $d_0 = 3.0\,\mathrm{mm}$. In particular, the eigenvalues in the stopbands are not of the same magnitude suggesting that the maximum attenuation differs for the two stopbands.

In addition to the studies in Ch. 4, we do not only start with passband states and analyse the behaviour when introducing disorder, but we also take stopbands into account for our analysis. The audible range with the frequency spectrum $f \leq 25\,\mathrm{kHz}$ provides us with two large passbands, which are separated by a stopband, and we use this frequency spectrum for the following analysis. Before we get to the results for disordered notch depths, we use our numerical method to get quantitative results for the periodic problem. Fig. 5.4 shows the moduli of the total reflection coefficients (reflection over whole domain with notches) and the attenuation coefficients, Q (measuring the exponential decay via the least-squares minimisation routine and Eqn. (2.77b) over the domain with notches), of the wave fields as functions of the frequency in the audible range, for notch depths $d_0 = 1.0\,\mathrm{mm}$, $1.5\,\mathrm{mm}$, $2.0\,\mathrm{mm}$ and $2.5\,\mathrm{mm}$. The number of notches is set to 24, which is sufficiently large for capturing the pass- and stopbands accurately, hence the notches (with length $l = 3.0\,\mathrm{cm}$) occupy a domain of 141 cm in total.

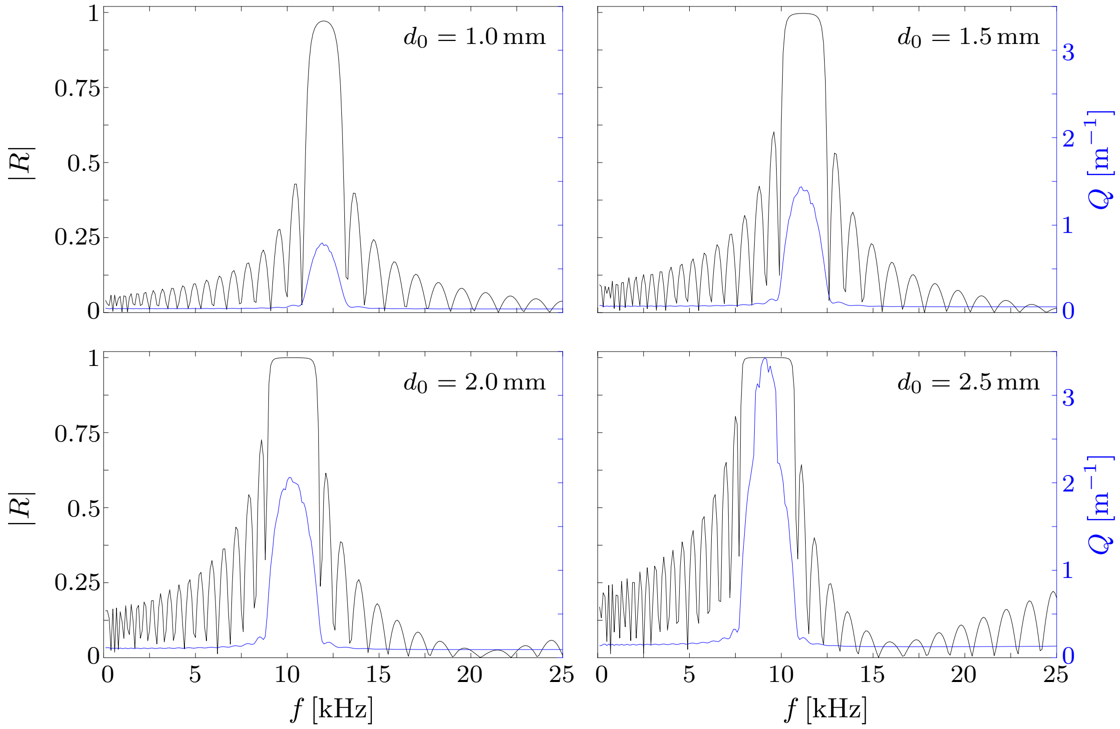

Figure 5.4: Total reflection coefficient moduli (black) and attenuation coefficients (blue) as functions of frequency for periodic notch configuration, for notch depths $d_0 = 1.0\,\mathrm{mm}$ (top-left panel), $d_0 = 1.5\,\mathrm{mm}$ (top-right panel), $d_0 = 2.0\,\mathrm{mm}$ (bottom-left panel) and $d_0 = 2.5\,\mathrm{mm}$ (bottom-right panel)

We can observe in Fig. 5.4 that the stopbands for $d_0 = 1.0\,\mathrm{mm}$ and $2.0\,\mathrm{mm}$ (characterised by full reflection) exist for the same values as suggested by the non-unity eigenvalues of the transfer matrix in Fig. 5.3. As seen previously, the stopbands move towards smaller frequencies for increasing notch depth and become broader. The oscillatory resonances, which are visible for the total reflection coefficient moduli, correspond to resonating harmonics of lower frequencies. These can be found in a variety of problems, e.g. in plate-fluid interactions, see Montiel et al. 2012. The attenuation coefficients, which are shown for comparison, reproduce the stopbands predicted by the eigenvalues of the transfer matrix for $d_0 = 1.0\,\mathrm{mm}$ and $2.0\,\mathrm{mm}$, showing maximum attenuation for exactly the frequencies as predicted by the eigenvalues. The attenuation coefficients provide a good measurement since they are less sensitive to the resonating harmonics, which lead to only small attenuation over the whole domain with notches.

5.2.2 Random variations

After the detailed investigation of the pass- and stopband behaviour for the periodic notch configuration, we now come to the main topic of this study. By introducing disorder into the notch configurations, we seek for disappearing passbands, i.e. minimising transmitted wave energy, and localisation of the incoming waves. As explained in Sec. 5.1, disorder will be induced by the uniformly distributed random variables ϵ_n, $n = 1, \ldots, N$, leading to relative increases of the notch depths from the underlying periodic configuration (see Eqn. (5.1)).

For the first result, we investigate the effect of different magnitudes of notch depth variations for underlying periodic notch configurations with different periodic notch depths d_0. Fig. 5.5 shows total reflection coefficient moduli as functions of the frequency in the audible range for increasing ϵ and underlying periodic notch depths $d_0 = 1.0\,\mathrm{mm}$ (top-left panel), $1.5\,\mathrm{mm}$ (top-right panel), $2.0\,\mathrm{mm}$ (bottom-left panel) and $2.5\,\mathrm{mm}$ (bottom-right panel). Results are shown using 100 different notch depth configurations from the underlying periodic configuration ($\epsilon = 0$) and only the notch depths are increased for increasing ϵ, i.e. we use 100 different realisations of standard uniformly distributed random variables and only scale them with ϵ for each case of ϵ shown. We then take the median of the calculated total reflection coefficient moduli to visualise the results. Due to possibly very strong scattering at single notches, attenuation coefficients describing the exponential decay of wave energy might be inaccurate and are therefore not shown for comparison anymore.

We can observe in Fig. 5.5 that in the case of the underlying periodic notch configuration with the smallest notch depth, $d_0 = 1.0\,\mathrm{mm}$, introducing notch depth disorder does not lead to significantly different results. Whilst the notch depth disorder does only produce slightly larger total reflection in the passbands for frequencies smaller than in the stopband, they shift the appearing resonating harmonics in the second passband slightly to the left. This shift is also noticeable for the stopband, which slightly moves towards the smaller frequencies for increasing notch depth disorder.

For $d_0 = 1.5\,\mathrm{mm}$, we can observe that the largest notch depth variation already leads to a significant increase of the reflection. For $f = 25\,\mathrm{kHz}$ the full reflection coefficient increases to approximately 0.6, but nevertheless, still most of the wave energy can travel along the beam for frequencies in the original passbands away from the stopband. In comparison to the first case, the stopband shift to the left for large notch depth variations is larger. It is remarkable that for higher frequencies in the original stopband, the stopband feature does not exist anymore and waves can travel along the beam, although they are partly reflected. Note that $\epsilon = 1.0$ here already might lead to configurations, for which notches are as deep as half of the beam thickness. However, this is still not sufficient to yield full reflection in the original passbands. But this is achieved for $d_0 = 2.0\,\mathrm{mm}$.

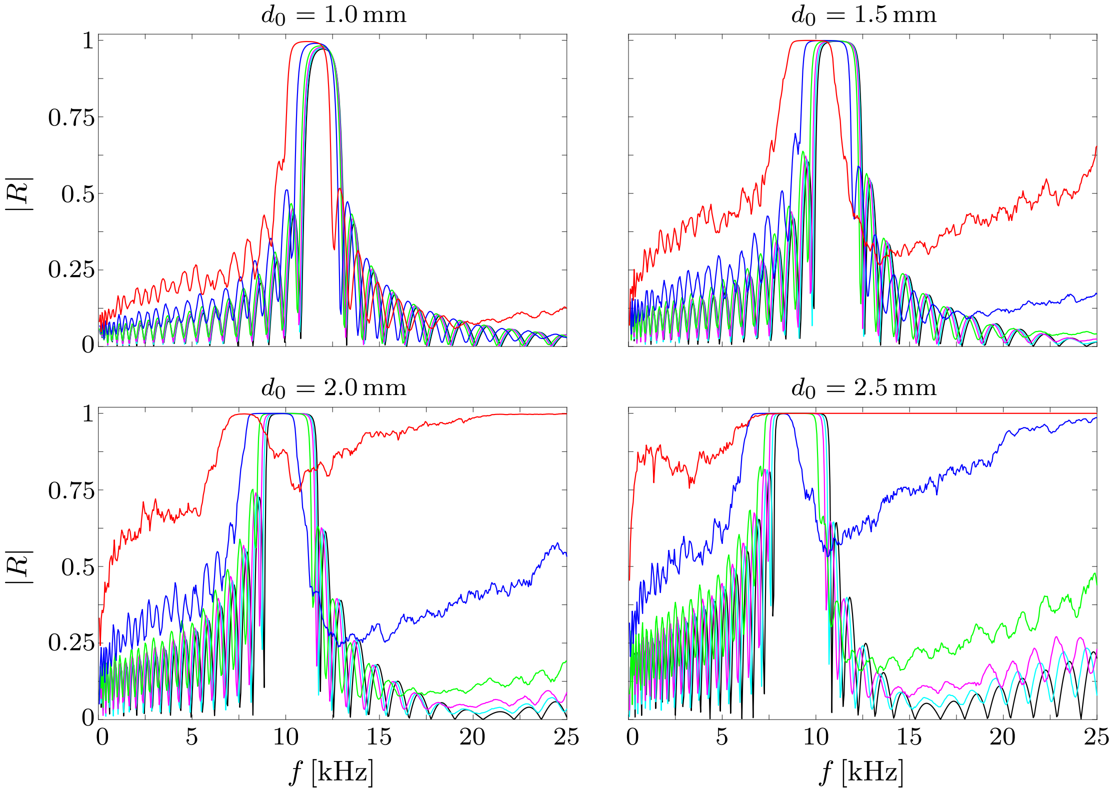

Figure 5.5: Total reflection coefficient moduli as functions of frequency for $\epsilon = 0$ (black), $\epsilon = 0.05$ (cyan), $\epsilon = 0.1$ (magenta), $\epsilon = 0.2$ (green), $\epsilon = 0.5$ (blue) and $\epsilon = 1.0$ (red), for underlying periodic notch depths $d_0 = 1.0\,\mathrm{mm}$ (top-left panel), $d_0 = 1.5\,\mathrm{mm}$ (top-right panel), $d_0 = 2.0\,\mathrm{mm}$ (bottom-left panel) and $d_0 = 2.5\,\mathrm{mm}$ (bottom-right panel)

In the large frequency regime, $\epsilon = 1.0$ provides enough disorder that incoming waves are fully reflected for $d_0 = 2.0\,\mathrm{mm}$. In contrast to this observation, for small frequencies the reflection is indeed larger than in the underlying periodic configuration, but the reflection coefficient moduli only reach up to 0.7 and diminish rapidly for frequencies smaller than 1 kHz. Interestingly, the original stopband fully vanishes, but for frequencies in the original stopband only a small proportion of the incoming waves is transmitted for $\epsilon = 1.0$. But we also note that $\epsilon = 0.5$ is far away from achieving full reflection in the original passbands and leads to reflection of the same magnitude as $\epsilon = 1.0$ for $d_0 = 1.5\,\mathrm{mm}$.

For $d_0 = 2.5\,\mathrm{mm}$, $\epsilon = 0.5$ is already sufficient to lead to full reflection for high frequencies, $f \geq 20\,\mathrm{kHz}$. For smaller frequencies, this values of disorder leads to full reflection only for frequencies from the shifted original stopband. But we can see that increasing the disorder to $\epsilon = 1.0$ yields full reflection for frequencies larger than $f > 5\,\mathrm{kHz}$.

We want to study the influence of the notch depth disorder magnitude, ϵ, more thoroughly in the following. For this, we focus on beams with an underlying periodic notch configuration with notch depths $d_0 = 2.0\,\mathrm{mm}$, since they provide full reflection of the original passband in the high frequency regime for $\epsilon \leq 1.0$.Fig. 5.6 shows the statistical distribution of the total reflection coefficient moduli as functions of the notch depth disorder magnitude ϵ in a box-and-whisker plot, for $d_0 = 2.0\,\mathrm{mm}$. Results are shown for $f = 5\,\mathrm{kHz}$ (top-left panel), 10 kHz (top-right panel), 15 kHz (bottom-left panel) and 20 kHz (bottom-right panel). This yields frequencies from the first passband (5 kHz), the stopband (10 kHz) and the second passband (15 kHz and 20 kHz) in the underlying periodic configuration. In analogy to the previous box-and-whisker plots, the boxes indicate the intervals containing the central 50% of the data (25% to 75% quantiles), and the horizontal lines within them denote the median values (50% quantiles), which were used in Fig. 5.5 to visualise the results. The whiskers indicate the remaining sampled data lying in the range of 1.5 times the height of the central box next to the quantiles. Data points outside this range are considered to be outliers and are shown as pluses.

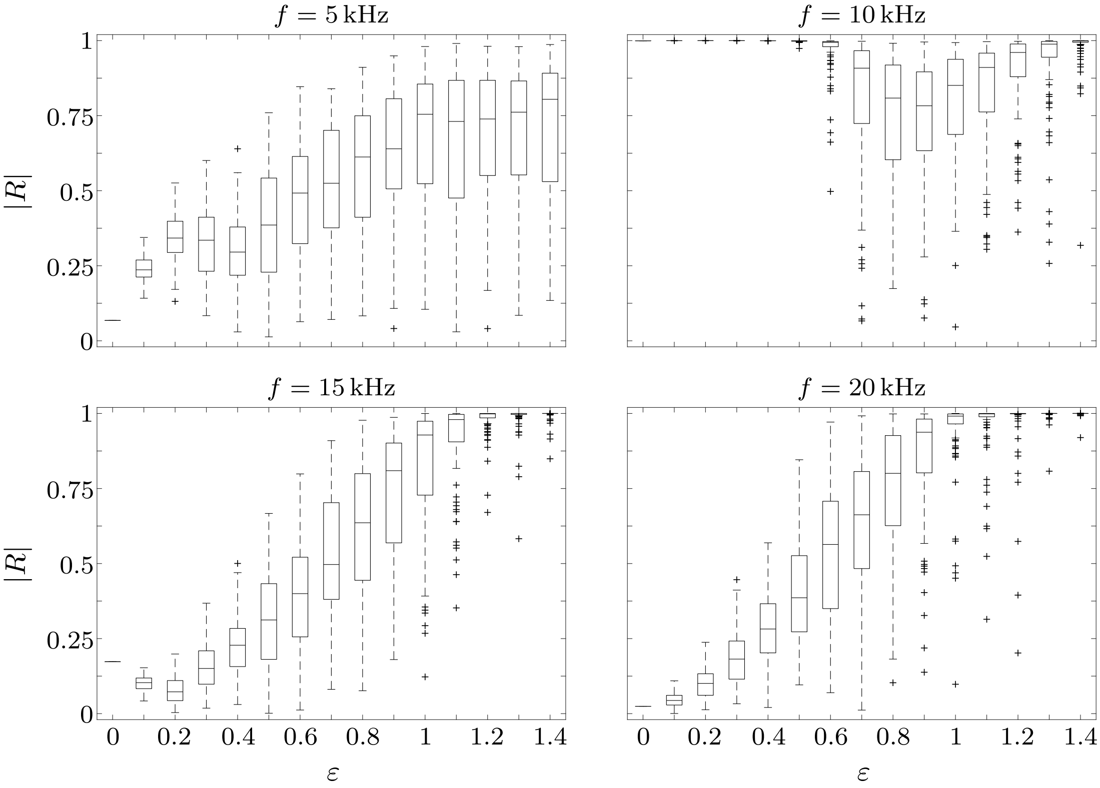

Figure 5.6: Box-and-whisker plot of total reflection coefficient moduli as functions of notch depth disorder magnitude for $d_0 = 2.0\,\mathrm{mm}$ and $f = 5\,\mathrm{kHz}$ (top-left panel), $f = 10\,\mathrm{kHz}$ (top-right panel), $f = 15\,\mathrm{kHz}$ (bottom-left panel) and $f = 20\,\mathrm{kHz}$ (bottom-right panel)

Fig. 5.6 gives a good impression of the effects of introducing disorder on the first and second passband as well as the stopband. The top-left panel shows the total reflection coefficient moduli for $\epsilon = 0, 0.1, \ldots, 1.4$ for $f = 5\,\mathrm{kHz}$. For the underlying periodic configuration, $\epsilon = 0$, the reflection coefficient moduli are close to zero, hence we are in a passband. When increasing the disorder magnitude, the reflection coefficient moduli increase. For $\epsilon \approx 0.7$, the first notch depth configurations exist, for which $|R|$ reaches up to 0.9 and for $\epsilon \geq 1.0$, full reflection occurs. However, the distributions of the reflection coefficient moduli are broad for $f = 5\,\mathrm{kHz}$, which lies in the first passband, and the median value does not exceed 0.8, not even for the largest disorder magnitude under consideration, $\epsilon = 1.4$, and a non-negligible number of configurations exist, for which barely any attenuation is apparent.

For $f = 10\,\mathrm{kHz}$, we are in a stopband. This state in the stopband is robust with respect to small disorder magnitudes and the reflection coefficient moduli remain one for $\epsilon \leq 0.5$. For $\epsilon = 0.6$, the first configurations exist, for which the full reflection over the notched domain is lost, and increasing the disorder further, the characteristic configuration (yielding the median total reflection) gives $|R| \approx 0.8$ for $\epsilon = 0.8$ and 0.9. In this medium disorder magnitude regime, the disorder provides notch depth configurations, for which most of the wave energy travels along the whole notched domain, see the whisker for $\epsilon = 0.8$ reaching down to $|R| \approx 0.2$ and the outliers for $\epsilon \leq 1.3$. On average, disorder magnitudes larger than one lead to configurations, which fully reflect the incoming waves on average again, and for $\epsilon \geq 1.3$, we obtain fully reflected waves for all configurations up to few outliers.

For $f = 15\,\mathrm{kHz}$ and $20\,\mathrm{kHz}$, we are in the second passband. Although for the small disorder magnitudes $\epsilon \leq 0.6$ the median reflection coefficient moduli are smaller than for $f = 5\,\mathrm{kHz}$, which is located in the first passband, the behaviour for larger disorder is significantly different. In contrast to $f = 5\,\mathrm{kHz}$, the reflection coefficient moduli for $f = 15\,\mathrm{kHz}$ and $20\,\mathrm{kHz}$ do not reach a saturated state, but they increase until full reflection is reached on average for $\epsilon \geq 1.2$ and 1.1, respectively. Increasing the disorder magnitude even further leads to the quantiles moving closer together, which indicates that fewer configurations exist, which allow waves of the respective frequency to pass the notched domain (partly).

After we have seen again that the second passband provides frequencies in the audible range, for which waves with those frequencies fully attenuate in contrast to waves with frequencies from the first passband, we finally merge the results shown in Figs. 5.5 and 5.6. Fig. 5.7 shows heatmaps of the total reflection coefficient moduli in dependence of the frequency in the audible range and the notch depth disorder magnitude for underlying periodic notch configurations of depth $d_0 = 1.0\,\mathrm{mm}$ (top-left panel), $1.5\,\mathrm{mm}$ (top-right panel), $2.0\,\mathrm{mm}$ (bottom-left panel) and $2.5\,\mathrm{mm}$ (bottom-right panel). This also gives a good insight into the behaviour of the stopband for large disorder, which was omitted for the beaded-string problem in Sec. 4.2, where we put our focus on underlying passbands only.

We can see the reflection coefficient moduli for starting notch depths $d_0 = 1.0\,\mathrm{mm}$, $1.5\,\mathrm{mm}$, $2.0\,\mathrm{mm}$ and $2.5\,\mathrm{mm}$ side by side in Fig. 5.7. As we observed previously, the stopband in the audible frequency range extents from $11\,\mathrm{kHz}$ to $13\,\mathrm{kHz}$ for the periodic configuration with the smallest notch depths, $d_0 = 1.0\,\mathrm{mm}$. It broadens and slightly moves towards the smaller frequencies for increasing notch depths in the periodic configuration, and it contains frequencies between $7\,\mathrm{kHz}$ and $11\,\mathrm{kHz}$ for $d_0 = 2.5\,\mathrm{mm}$. For the smallest notch depths, $d_0 = 1.0\,\mathrm{mm}$, introducing notch depth disorder up to notches, which are twice as large as in the underlying periodic configuration ($\epsilon = 1.0$), does not produce remarkable attenuation for the frequencies in the passband and the stopband moves towards the lower frequencies

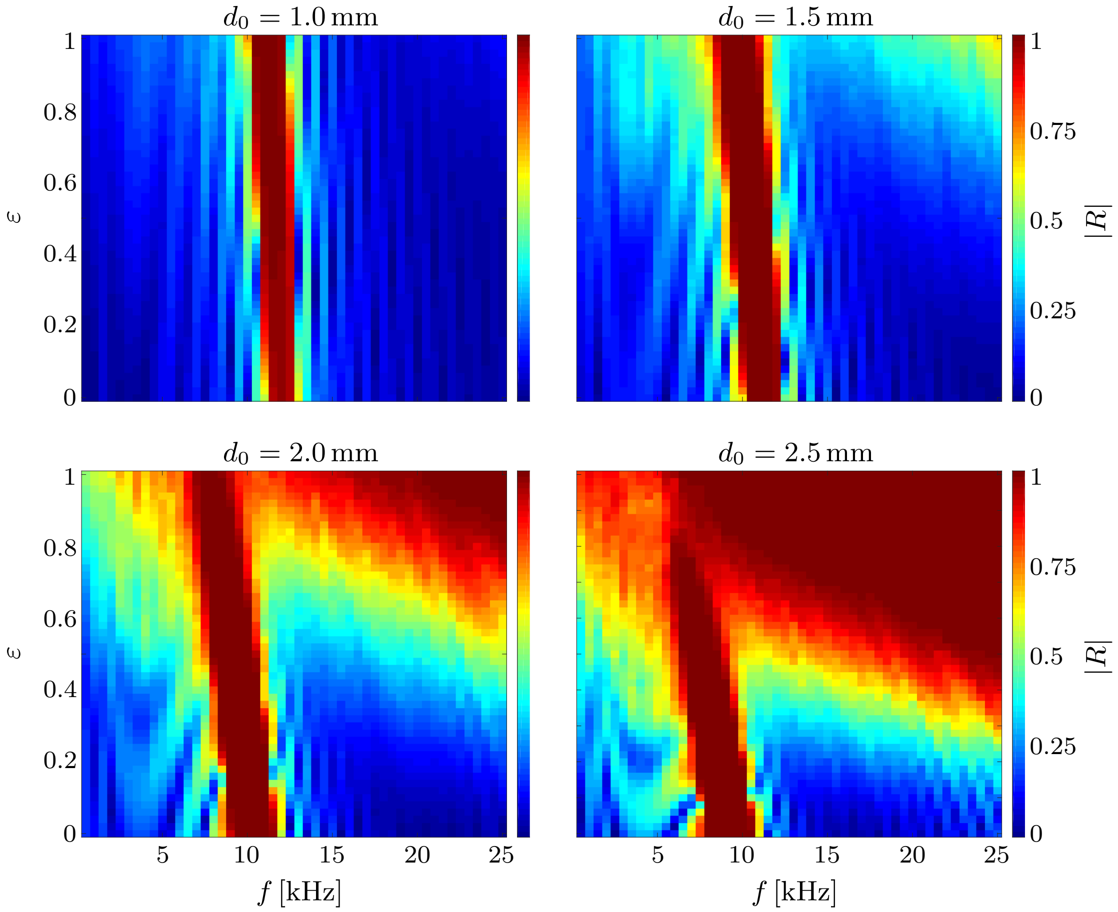

Figure 5.7: Heatmaps of total reflection coefficient moduli as functions of frequency and notch depth disorder magnitude, for $d_0 = 1.0\,\mathrm{mm}$ (top-left panel), $d_0 = 1.5\,\mathrm{mm}$ (top-right panel), $d_0 = 2.0\,\mathrm{mm}$ (bottom-left panel) and $d_0 = 2.5\,\mathrm{mm}$ (bottom-right panel)

only slightly. This shift gets already a bit more obvious for $d_0 = 1.5\,\mathrm{mm}$, but still, the reflection coefficient moduli are small in the original passbands and significant attenuation in those is only attained for the largest frequency under consideration, $f = 25\,\mathrm{kHz}$, for the largest disorder magnitude. We can clearly see that full reflection in original passbands for $\epsilon \leq 1$ needs a starting notch depth in the underlying periodic configuration of $d_0 = 2.0\,\mathrm{mm}$. Large disorder magnitudes yield full reflection in the second passband for $f \geq 15\,\mathrm{kHz}$. However, the first passband exhibits increasing reflection coefficient moduli for large disorder magnitude, but full reflection is not nearly reached. For $d_0 = 2.0\,\mathrm{mm}$, we can also identify the original stopband clearly throughout the whole disorder regime, as it is shifted to the left. It defines the boundary between the two original passbands. On the other hand for $d_0 = 2.5\,\mathrm{mm}$, the shifted stopband blurs for $\epsilon \geq 0.8$, and the significant difference between the two passbands emerges in the large disorder magnitude regime. Even for very large notch depth disorder, the first passband does not lead to full attenuation. This is contrast to the second passband, for which in the large frequency regime disorder magnitudes of only 0.5 are already sufficient to obtain full reflection. The heatmap visualises nicely the decreasing disorder magnitude, which is necessary for full attenuation.

5.3 Towards model validation

We would like to validate the qualitative results, which we obtained with our numerical method, by experiments to establish the finding from the previous section that localisation of waves travelling a long beam with discrete notches occurs. An experimental setup-up for this might be a beam, which is excited purely in vertical direction at one end and a laser vibrometer is used to measure the vibrations of the beam at several locations, while the excited signal travels along the beam. Signals in frequency dependent experiments and measurements are often excited as a toneburst with an excitation frequency to achieve high accuracy, see e.g. Liang et al. 1986. We generate a (Hanning-windowed) sinusoidal toneburst at $x = 0$ via

$$\mathcal{U}(0,t) = \frac{A_0}{2}\left(1 - \cos\left(\frac{2\pi f_\mathrm{c} t}{N_\mathrm{c}}\right)\right)\cos(2\pi f_\mathrm{c} t), \tag{5.3}$$

where A_0 is the amplitude of the pulse, N_c is the number of cycles, t is the time and f_c is the central frequency of the pulse. The toneburst defined in Eqn. (5.3) is used to excite the anti-symmetrical $A0$ Lamb wave, i.e. the zeroth mode of the anti-symmetrical motion with respect to the xy-plane. A schemata of the beam cross section is given in Fig. 2.32. Due to its perpendicular-to-the-plane motion characteristic, this mode is also called the flexural mode, see Achenbach 1984. Lamb waves are often used in non-destructive structural health monitoring since they can travel long distances without much attenuation and allow measurements with high accuracy, see e.g. Bao 2003 and Sause 2016.

Fig 5.8 shows the toneburst pulses of unit amplitude for $f_\mathrm{c} = 5\,\mathrm{kHz}$, $10\,\mathrm{kHz}$ and $15\,\mathrm{kHz}$ (top panels) in the time-domain. The number of cycles is set to $N_\mathrm{c} = 5$, which ensures good responses of the zeroth anti-symmetrical mode for the small central frequencies in the low ultrasonic frequency regime, see Michaels et al. 2011. The bottom panels display the respective spectral distributions of the signals, obtained via Fourier transformations (which will be explained shortly).

We can see in Fig. 5.8 that it takes about 1.0 ms to excite the toneburst for $f_\mathrm{c} = 5\,\mathrm{kHz}$ and it evolves symmetrically. The pulses for $f_\mathrm{c} = 10\,\mathrm{kHz}$ and $15\,\mathrm{kHz}$ are of exactly the same shape, but they only cover approximately 50 ms and 35 ms, respectively. We can also see the spectral distribution of those pulses in the bottom panels. The spectral distributions are symmetrically centred around the central frequency f_c for all three choices of f_c. While the distribution for $f_\mathrm{c} = 5\,\mathrm{kHz}$ yields non-zero values in the regime between 0 and 10 kHz, only, the distributions are more spread out for the pulses with higher central frequencies and the distribution magnitudes decrease.

We now have to solve the (time-dependent) dynamic Euler–Bernoulli beam Eqn. (2.6), for

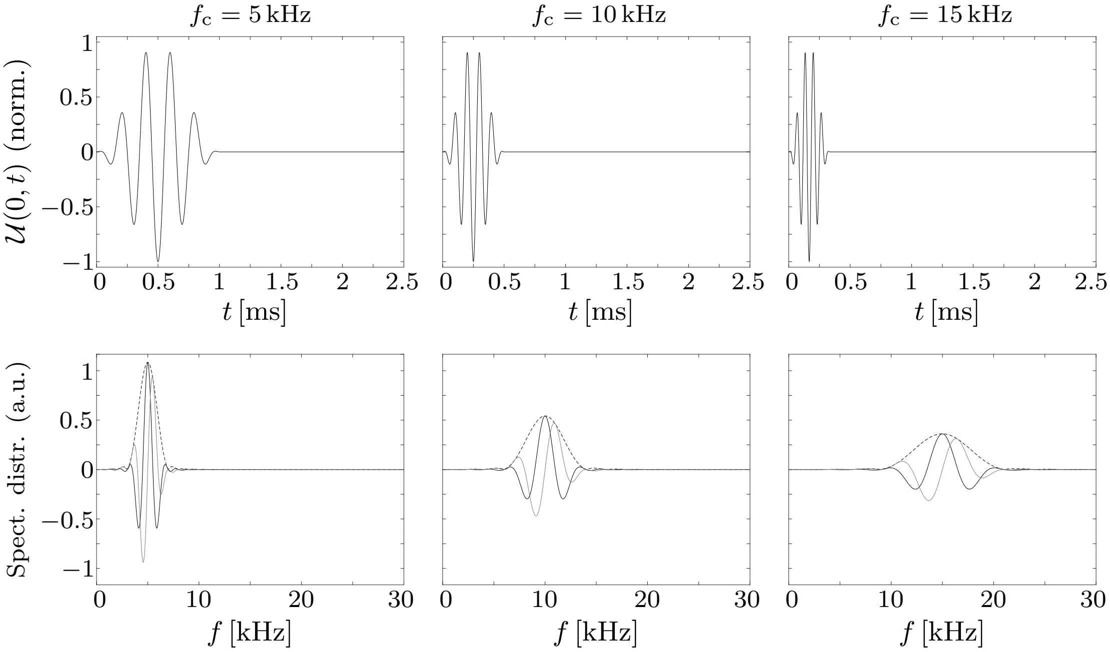

Figure 5.8: Top panels: Toneburst pulses of unit-amplitude in the time-domain for $f_c = 5\,\text{kHz}$ (top-left panel), $f_c = 10\,\text{kHz}$ (top-middle panel) and $f_c = 15\,\text{kHz}$ (top-right panel) and 5 number of cycles. Bottom panels: Respective spectral distribution of toneburst pulses for $f_c = 5\,\text{kHz}$ (bottom-left panel), $f_c = 10\,\text{kHz}$ (bottom-middle panel) and $f_c = 15\,\text{kHz}$ (bottom-right panel), split into real (black solid line) and imaginary part (grey solid line). The absolute value is shown for comparison (black dashed line).

which the toneburst might be induced with the external force at $x = 0$. Solution methods for the problem in the time-domain have been studied extensively in the last two centuries of the last decade for the design and dynamic behaviour of railway tracks and bridges and various methods can be found in the literature. A solution method for a beam under a dynamic moving force using a double Laplace transformation can be found in Hamada 1981. Similar problems including dynamic moving loads were solved on the basis of finite element formulations and the following integrations in time accomplished with implicit direct integration and Runge–Kutta integration methods, see e.g. Hino et al. 1985 and Kin and Trethewey 1990. Modal superposition methods to transform the dynamic problem into a set of ordinary differential equations can be found e.g. in Lee 1996a,b and Law and Chan 1997. Gutierrez and Laura (1997) studied vibrations of a beam of non-uniform cross section, which is traversed by a dynamic force and used the Galerkin–Kantorovich method to solve this problem. A good overview over dynamic and static behaviour of solids and structures under loads is given by Frýba (1999). We want to determine the temporal evolution of the signal by performing the calculations in the frequency-domain, i.e. for time-harmonic excitations. This allows us to use the numerical method we used in the previous section. We want to map the frequency- and the time-domain into each other by standard Fourier transformations, which is e.g. used in Montiel et al. 2012 for floating plates excited by a wavemaker. The solution in the time-domain is obtained by transforming the excitation signal into the frequency-domain, solving the time-harmonic problem for the involved frequencies with our numerical method and mapping the solutions for the time-harmonic problem back into the time-domain with the inverse Fourier transformation.

In our solution procedure for the response of the beam to a toneburst, we use the fast Fourier transform algorithm, which computes the discrete Fourier transformation of a signal and its inverse, see Brigham 1988. In particular, the fast Fourier transformation converts the toneburst pulse from the time-domain into the frequency-domain. The fast Fourier transformation was already used in Fig. 5.8 to show the spectral distributions of the toneburst pulses. Hence, the spectral distribution describes the toneburst in the frequency-domain and we can use our numerical method to calculate the time-harmonic solution for each of the frequencies characterising the toneburst pulse in the spectral distribution together with their corresponding amplitudes. Since the toneburst signal is real, we know that the second half of the transformed values are the complex conjugates of the first half of transformed values. This comes from the phenomenon that M real points can be transformed into $M/2$ complex points without losing any information. This implies that for the sampling frequency f_{sampl} only half of the frequency range provides useful information, i.e.

$$f_{\mathrm{Nyquist}} = \frac{f_{\mathrm{sampl}}}{2}, \tag{5.4}$$

which is the so-called Nyquist frequency, see e.g. Doyle 1997. The sampling frequency f_{sampl} describes the number of samples obtained in one second (samples per second), i.e.

$$f_{\mathrm{sampl}} = \frac{1}{\mathit{\Delta} T}, \tag{5.5}$$

where $\mathit{\Delta} T$ denotes the sampling time, see e.g. Haykin and Veen 2002. To achieve high accuracy in the time-domain, $\mathit{\Delta} T$ has to be small. To take this into account, the sampling frequency shall be ten times higher than the largest non-negligible frequency in the toneburst for central frequency $f_{\mathrm{c}} = 25\,\mathrm{kHz}$, which is about $48\,\mathrm{kHz}$, i.e. we set the sampling frequency to be $f_{\mathrm{sampl}} = 480\,\mathrm{kHz}$. Hence, the Nyquist frequency is $f_{\mathrm{Nyquist}} = 240\,\mathrm{kHz}$, and it is clearly ensured that all occurring frequencies are smaller than f_{Nyquist}. The high sampling frequency guarantees to capture interactions with the appearing ultrasonic frequencies and tests were run to ensure that the used sampling frequency provides accurate results.

For validation of the results obtained with our numerical method for the Euler–Bernoulli beam (short EBBM method in the following), we first want to compare the wave speed along the homogeneous beam without notches for our model and FE simulations. The FE simulations are performed with Abaqus FEA using a solid element formulation. The formulation of the elements involves rotations and strains. In our problem with small beam deflections, the strain is defined via the Lagrangian strain tensor, $\mathbf{E}$, which is the symmetric part of the spatial gradient of the wave field, i.e.

$$\mathbf{E} = \frac{1}{2}\left(\nabla_{\mathbf{X}}\mathbf{u} + (\nabla_{\mathbf{X}}\mathbf{u})^{\mathrm{T}} + (\nabla_{\mathbf{X}}\mathbf{u})^{\mathrm{T}}\nabla_{\mathbf{X}}\mathbf{u}\right) \approx \frac{1}{2}\left(\nabla_{\mathbf{X}}\mathbf{u} + (\nabla_{\mathbf{X}}\mathbf{u})^{\mathrm{T}}\right), \tag{5.6}$$

where $\mathbf{X}$ is the spatial position of the considered point in the original configuration and $\mathbf{u}$ is the total displacement, see Hibbitt et al. 2015. The second-order terms are neglected in the linearised finite strain tensor, which holds for small strains and rotations. The strain definition can be found e.g. in Slaughter 2002. It would go beyond the scope of this thesis to go into details of the solid element formulation and we refer the reader to the extensive literature on this topic, see e.g. Oñate 2009, 2013 and Zienkiewicz and Taylor 2013.

The Aluminium beam in the FE simulations has the same cross-section dimensions as in our model in the EBBM method with constant beam width $w = 12\,\mathrm{mm}$ and beam thickness $h = 6\,\mathrm{mm}$ in the uniform case. We choose the beam length to be $L = 2.0\,\mathrm{m}$, which is sufficiently long to incorporate the desired number of notches for the full analysis in the beam model without having to place a notch too close to the beam ends. The beam mesh, which is used for the FE simulations, is chosen very fine for accurate results. The beam width is divided into 30 sub-intervals of length 0.4 mm and the beam height into 15 sub-intervals of length 0.4 mm, hence 450 elements are generated along the beam cross section in our very fine mesh. The beam length is divided into 5000 sub-intervals of length 0.4 mm, which gives us in total more than two million rectangular elements in our solid element formulation. A convergence analysis was performed to ensure that the grid is fine enough and we obtain accurate simulation results. For our simulations, eight nodes per element and three degrees of freedom per node are used.

To extract the speed of waves travelling along the homogeneous beam from both the EBBM method and FE simulations, we use an envelope around the wave packet, observed at various locations. Since the flexural waves travelling along the beam are dispersive and the envelopes around the waves level off, we choose the first and second observation point, $x = 30.0\,\mathrm{cm}$ and $52.0\,\mathrm{cm}$, respectively, to calculate the wave speed as distance travelled (22.0 cm) per time. The travelling time is determined by the time, which lies between the envelope maxima passing the first and second observation point. Fig. 5.9 shows the signal, which is excited by the toneburst pulse with central frequency $f_{\mathrm{c}} = 15\,\mathrm{kHz}$ at $x = 0$, in the simulation for the EBBM method at the first and second observation point. The envelope is calculated using the Hilbert transform, see Ulrich 2006.

An elementary difference between the EBBM method (for the one-dimensional beam model) and the solid element formulation (for the three-dimensional beam model) in the present problem is the beam length. While the cross-section is equivalent in both formulations, we neglect the finite length of the beam in the EBBM method, i.e. we have no boundary conditions, we only have conditions in the far-field, and the toneburst is excited as an occurring pulse at $x = 0$. This could be interpreted as an incoming wave from $x \to -\infty$, which is of the form of the toneburst at $x = 0$. As opposed to this, the beam in the FE simulations is indeed of finite dimension with length $L = 2.0\,\mathrm{m}$. The beam shall not be clamped and

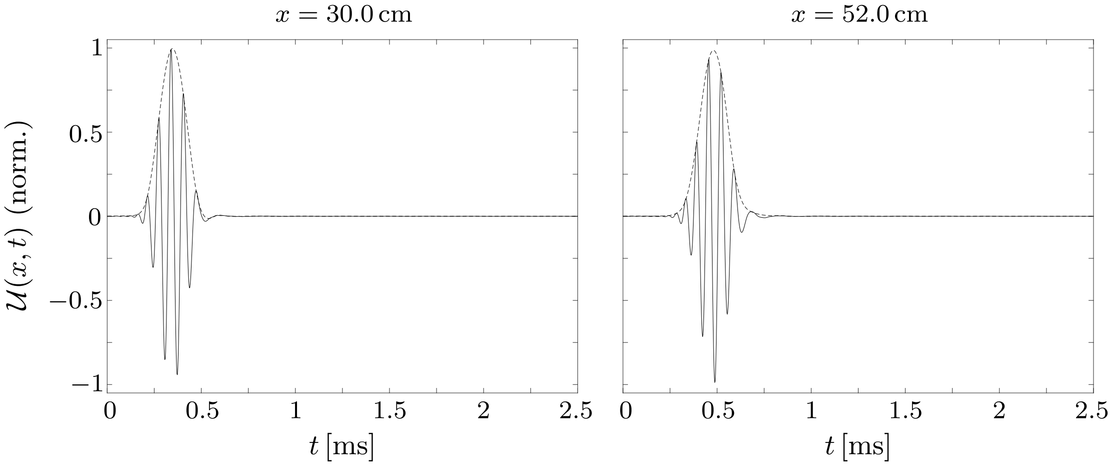

Figure 5.9: Simulated signal (solid line) excited by toneburst pulse with $f_\mathrm{c} = 15\,\mathrm{kHz}$ in homogeneous beam and wave packet envelope (dashed line), measured at first (left-hand panel) and second observation point (right-hand panel)

the ends shall be free, which gives free-end boundary conditions. This can be achieved in experimental setups by placing the beam on foam support, see e.g. Ernst and Dual 2014. In an experimental setup, the pulse could be excited by a piezoelectric transducer, which is applied to the left end of the beam at $x = 0$. Piezoelectric material undergoes mechanical strain when an electric field is applied, hence a piezoelectric transducer can convert an electric current into a pressure field, see e.g. *COMSOL Multiphysics 5.2 User's Guide (Acoustics Module Application Library)* 2015. Piezoelectric transducers have a wide range of applications including structural health monitoring and bioimaging. Elaborate FE models exist for piezoelectric transducers, see e.g. Abboud et al. 1998 and Kocbach 2000, but to simplify matters, we do not include the piezoelectric transducer in the FE simulations and only imitate it by applying nodal deformation in the vertical direction at $x = 0$, exciting flexural waves with the toneburst pulse. The FE beam model was created under the guidance of Dr. Ching-Tai Ng.

After this short introduction into the FE beam model, we want to compare the wave speeds from the EBBM method with those from the FE beam model. This shall serve as a first step of validation of the EBBM method. Fig. 5.10 shows the comparison of wave speeds of the signals in the homogeneous beam, which are excited by toneburst pulses with central frequency f_c, as functions of f_c, for the EBBM method and the FE method. To extract the speed of the wave packets from the FE simulations, the envelope of the wave packet is also calculated via the Hilbert transform and the travelling time between the same two observations points as for the EBBM method ($x = 30.0\,\mathrm{cm}$ and $52.0\,\mathrm{cm}$) is measured.

We can observe in Fig. 5.10 that a large discrepancy exists between the speed of the wave packets for the EBBM method and the FE simulations. For the smallest central frequency under consideration in the FE model, $f_\mathrm{c} = 5.0\,\mathrm{kHz}$, the wave travels with approximately $1.0\,\mathrm{m/ms}$ in the FE model. This is overestimated by the EBBM method significantly, where

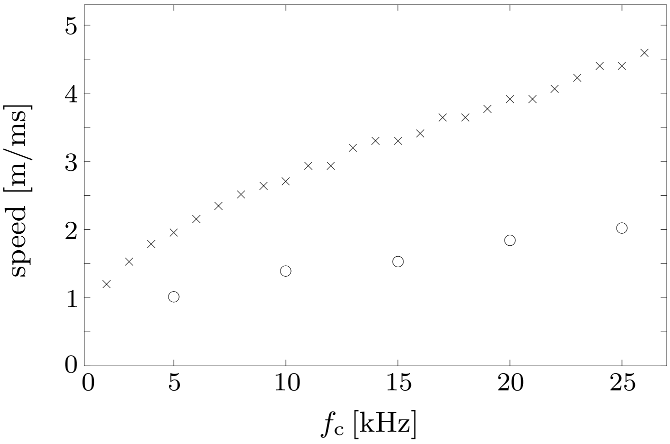

Figure 5.10: Comparison of wave speeds in homogeneous beam as functions of central frequency f_c of tone burst pulse, for numerical method for Euler–Bernoulli beam model (+) and FE method (∘)

the wave travels nearly twice as fast. The wave speeds get larger for increasing frequencies in both models, but the slope of increase is clearly larger for our Euler–Bernoulli beam model. Hence, for larger frequencies, the deviation between the two models becomes even larger. Good agreement between FE simulations and the behaviour of beams with similar dimensions in experiments was shown e.g. by He and Ng (2017), so it seems likely that the EBBM method is inadequate to solve the problem.

5.4 Transition to Timoshenko beam model

By using the Euler–Bernoulli beam theory, we not only assumed small and transverse deflection, but we neglected shear deformation, even though we assumed that a transverse shear force exists, see e.g. Doyle 1997. Neglecting the shear deformation is of negligible consequence for small frequencies under the assumption of small and transverse deflection, but it becomes an issue in the frequency regime we consider here. To take this effect into account for our model, we have to modify the Euler–Bernoulli beam theory, for which wave speed is unbounded with increasing frequencies, see Bilbao 2004. For example Ernst and Dual (2014) considered in their studies of acoustic emission localization in beams frequencies larger than 10 kHz and showed good agreement of phase speeds for the Timoshenko beam theory and experiments. The agreement motivates us to adopt our numerical method to Timoshenko beams. We derive the governing equations for the Timoshenko beam theory in the following in analogy to Doyle (1997). The derivation of the Timoshenko beam model complements the derivation of the Euler–Bernoulli beam model from Sec. 2.1.

5.4.1 Timoshenko beam model

By neglecting the shear deformation in the Euler–Bernoulli beam theory, the horizontal (longitudinal) deflection, which we denote with $\tilde{\mathfrak{U}}_{\mathrm{lon}}(x,z,t)$, could directly be expressed with the vertical (flexural) deflection, which we denote with $\tilde{\mathcal{U}}_{\text{fle}}(x,z,t)$ now. Both deflections are now linearised by using a Taylor expansion about their mid-plane deflections, $\mathcal{U}_{\text{fle}}(x,t) = \tilde{\mathcal{U}}_{\text{fle}}(x,0,t)$ and $\mathcal{U}_{\text{lon}}(x,t) = \tilde{\mathcal{U}}_{\text{lon}}(x,0,t)$, respectively, up to the first order,

$$\tilde{\mathcal{U}}_{\text{fle}}(x,z,t) \approx \mathcal{U}_{\text{fle}}(x,t) + z\,\frac{\partial \tilde{\mathcal{U}}_{\text{fle}}}{\partial z}\bigg|_{z=0} + \mathcal{O}(z^2), \tag{5.7a}$$

$$\tilde{\mathcal{U}}_{\text{lon}}(x,z,t) \approx \mathcal{U}_{\text{lon}}(x,t) + z\,\frac{\partial \tilde{\mathcal{U}}_{\text{lon}}}{\partial z}\bigg|_{z=0} + \mathcal{O}(z^2). \tag{5.7b}$$

To simplify the notation, we write

$$\mathcal{V}_{\text{fle}}(x,t) := \frac{\partial \tilde{\mathcal{U}}_{\text{fle}}}{\partial z}\bigg|_{z=0} \quad \text{and} \quad \mathcal{V}_{\text{lon}}(x,t) := \frac{\partial \tilde{\mathcal{U}}_{\text{lon}}}{\partial z}\bigg|_{z=0}.$$

Since we excite the beam in our problem formulation in a way that only flexural waves appear, we can neglect the horizontal deflection around the mid-plane, i.e. we can set $\mathcal{U}_{\text{lon}}(x,t) = 0$. Under the assumption that the horizontal deflection is linear and the vertical deflection is vertical only, the deflections from Eqns. (5.7) simplify to

$$\tilde{\mathcal{U}}_{\text{fle}}(x,z,t) \approx \mathcal{U}_{\text{fle}}(x,t), \tag{5.8a}$$

$$\tilde{\mathcal{U}}_{\text{lon}}(x,z,t) \approx -z\mathcal{V}_{\text{lon}}(x,t). \tag{5.8b}$$

Using the simplified representation of both deflections, we can write the axial strains, ϵ_{xx} and ϵ_{zz}, and the shear strain, γ_{xz}, as

$$\epsilon_{xx} = \frac{\partial \tilde{\mathcal{U}}_{\text{lon}}}{\partial x} = -z\frac{\partial \mathcal{V}_{\text{lon}}}{\partial x}, \tag{5.9a}$$

$$\epsilon_{zz} = \frac{\partial \tilde{\mathcal{U}}_{\text{fle}}}{\partial z} = 0, \tag{5.9b}$$

$$\gamma_{xz} = \frac{\partial \tilde{\mathcal{U}}_{\text{lon}}}{\partial z} + \frac{\partial \tilde{\mathcal{U}}_{\text{fle}}}{\partial x} = \left(-\mathcal{V}_{\text{lon}} + \frac{\partial \mathcal{U}_{\text{fle}}}{\partial x}\right). \tag{5.9c}$$

In our problem formulation of flexural waves travelling along a thin beam, we can neglect the stress in z-direction, i.e. $\sigma_{zz} = 0$, and following Hooke's law, the axial stress is $\sigma_{xx} = E\epsilon_{xx}$ and the shear stress is $\sigma_{xz} = G\gamma_{xz}$. G is the shear modulus, which characterises the response of the material to shear stress, see e.g. Crandall et al. 1999. The stresses can then be written as

$$\sigma_{xx} = -zE\frac{\partial \mathcal{V}_{\text{lon}}}{\partial x}, \tag{5.10a}$$

$$\sigma_{xz} = G\left(-\mathcal{V}_{\text{lon}} + \frac{\partial \mathcal{U}_{\text{fle}}}{\partial x}\right). \tag{5.10b}$$

At this point we can go into the difference of the Timoshenko beam theory to the Euler–Bernoulli beam theory. In the Euler–Bernoulli beam theory, it is assumed that no shear deformation occurs, i.e. $\mathcal{V}_{\text{lon}} = \partial_x \mathcal{U}_{\text{fle}}$. This implies in particular that the shear strain, γ_{xz}, and the shear stress, σ_{xz}, vanish, hence the only non-zero strains and stresses are ϵ_{xx} and σ_{xx}, respectively, in which $\mathcal{V}_{\text{lon}}$ can be replaced by $\partial_x \mathcal{U}_{\text{fle}}$. The bending moment can then directly be obtained by integrating σ_{xx} and be used in Eqns. (2.3) to derive the governing beam equation.

To derive the system of equations for the Timoshenko beam, we have to apply a variational principle, the so-called Hamilton's principle, which gives us the variational form of the problem. Hamilton's principle says that, see Doyle 1997,

> *"Among all motions that will carry a conservative system from a given configuration at time t_1 to a second given configuration at time t_2, that which actually occurs provides a stationary value of the integral*
>
> $$\int_{t_1}^{t_2} (T_{\text{tot}} - (S_{\text{tot}} + V_{\text{load}}))\, \mathrm{d}t.\text{"} \tag{5.11}$$

T_{tot} is the total kinetic energy in the beam, S_{tot} is the total strain energy and V_{load} is the potential of the loads. Hamilton's principle can be written as

$$\delta \int_{t_1}^{t_2} (T_{\text{tot}} - (S_{\text{tot}} + V_{\text{load}}))\, \mathrm{d}t = 0, \tag{5.12}$$

where δ is the variation.

The kinetic energy for a point object is well-known from classical mechanics as half of the mass of an object times its velocity squared, and we can extend this to the kinetic energy of the whole beam as

$$\begin{aligned} T_{\text{tot}} &= \frac{1}{2}\int_0^L \int_A \rho \left((\partial_t \mathcal{U}_{\text{lon}}(x,t))^2 + (\partial_t \mathcal{U}_{\text{fle}}(x,t))^2 \right) \mathrm{d}A \, \mathrm{d}x \\ &= \frac{1}{2}\int_0^L \int_A \rho K_2 \left(z^2 (\partial_t \mathcal{V}_{\text{lon}}(x,t))^2 + (\partial_t \mathcal{U}_{\text{fle}}(x,t))^2 \right) \mathrm{d}A \, \mathrm{d}x \\ &= \frac{1}{2}\int_0^L \rho I K_2 (\partial_t \mathcal{V}_{\text{lon}}(x,t))^2 + \rho A (\partial_t \mathcal{U}_{\text{fle}}(x,t))^2 \, \mathrm{d}x. \end{aligned} \tag{5.13}$$

The parameter K_2 is introduced to take into account that the horizontal deflection distribution was approximated only. We assumed the horizontal deflection to be linear, but this only holds approximately. For the exact deflection distributions, we refer the reader to Doyle 1997. The variational principle allows us to include the parameter K_2, since it will we be incorporated correctly.

The total strain energy, S_{tot}, describes the stored energy in the elastically deformed beam for small strains. It can be calculated as the integral of the scalar product of the stresses and strains over the whole beam, i.e. for our problem we obtain

$$\begin{aligned} S_{\text{tot}} &= \frac{1}{2}\int_0^L \int_A \sigma_{xx}\epsilon_{xx} + \sigma_{xz}\gamma_{xz} \, \mathrm{d}A \, \mathrm{d}x \\ &= \frac{1}{2}\int_0^L \int_A E\epsilon_{xx}^2 + G\gamma_{xz}^2 \, \mathrm{d}A \, \mathrm{d}x. \end{aligned} \tag{5.14}$$

Since the shear strain and shear stress are subject to the approximation of the horizontal deflection distribution (and the second term in Eqn. (5.14) is similarly to the total kinetic energy case quadratically as well), we modify the associated term in the total strain energy by adding the adjustable parameter K_1. With the parameter K_1 and the strains from Eqns. (5.9), we now get the total strain energy in terms of the deflections,

$$\begin{aligned} S_{\text{tot}} &= \frac{1}{2}\int_0^L \int_{-h/2}^{h/2} \left(Ez^2 \left(\frac{\partial \mathcal{V}_{\text{lon}}}{\partial x} \right)^2 + GK_1 \left(\mathcal{V}_{\text{lon}} - \frac{\partial \mathcal{U}_{\text{fle}}}{\partial x} \right)^2 \right) w \, \mathrm{d}z \, \mathrm{d}x \\ &= \frac{1}{2}\int_0^L EI \left(\frac{\partial \mathcal{V}_{\text{lon}}}{\partial x} \right)^2 + GAK_1 \left(\mathcal{V}_{\text{lon}} - \frac{\partial \mathcal{U}_{\text{fle}}}{\partial x} \right)^2 \mathrm{d}x. \end{aligned} \tag{5.15}$$

The potential of the loads, V_{load}, which takes the bending moments, M, and shear forces, V, from Sec. 2.1 at the beam ends into account as well as the external force f, is given by

$$V_{\text{load}} = -\int_0^L f(x,t)\mathcal{U}_{\text{fle}} \, \mathrm{d}x - M(L,t)\mathcal{V}_{\text{lon}}(L,t) + M(0,t)\mathcal{V}_{\text{lon}}(0,t) \tag{5.16}$$

$$\begin{aligned} &+ V(L,t)\mathcal{U}_{\text{fle}}(L,t) - V(0,t)\mathcal{U}_{\text{fle}}(0,t) \\ &= -\int_0^L f(x,t)\mathcal{U}_{\text{fle}} \, \mathrm{d}x - \left[M(x,t)\mathcal{V}_{\text{lon}}(x,t)\right]_{x=0}^L + \left[V(x,t)\mathcal{U}_{\text{fle}}(x,t)\right]_{x=0}^L . \end{aligned} \tag{5.17}$$

Now, applying Hamilton's principle and integrating by parts yields the variational Timoshenko beam formulation,

$$\begin{aligned} \int_{t_1}^{t_2} \Bigg\{ &\int_0^L \left(GAK_1 \left(\frac{\partial \mathcal{U}_{\text{fle}}}{\partial x} - \mathcal{V}_{\text{lon}} \right) + EI \frac{\partial^2 \mathcal{V}_{\text{lon}}}{\partial x^2} - \rho I K_2 \partial_t^2 \mathcal{V}_{\text{lon}} \right) \delta \mathcal{V}_{\text{lon}} \, \mathrm{d}x \\ &+ \int_0^L \left(GAK_1 \frac{\partial}{\partial x} \left(\frac{\partial \mathcal{U}_{\text{fle}}}{\partial x} - \mathcal{V}_{\text{lon}} \right) - \rho A \partial_t^2 \mathcal{U}_{\text{fle}} + f \right) \delta \mathcal{U}_{\text{fle}} \, \mathrm{d}x \\ &+ \left[\left(EI \frac{\partial \mathcal{V}_{\text{lon}}}{\partial x} - M \right) \delta \mathcal{V}_{\text{lon}} \right]_{x=0}^L + \left[\left(GAK_1 \left(\frac{\partial \mathcal{U}_{\text{fle}}}{\partial x} - \mathcal{V}_{\text{lon}} \right) + V \right) \delta \mathcal{U}_{\text{fle}} \right]_{x=0}^L \Bigg\} \mathrm{d}t = 0. \end{aligned} \tag{5.18}$$

Since this has to hold for all t_1 and t_2 as well as variations $\delta\mathcal{U}_{\text{fle}}$ and $\delta\mathcal{V}_{\text{lon}}$, the integrands have to be zero. This gives us the system of equations for the Timoshenko beam,

$$GAK_1 \frac{\partial}{\partial x}\left(\frac{\partial \mathcal{U}_{\text{fle}}}{\partial x} - \mathcal{V}_{\text{lon}}\right) = \rho A \partial_t^2 \mathcal{U}_{\text{fle}} - f, \tag{5.19a}$$

$$EI \frac{\partial^2 \mathcal{V}_{\text{lon}}}{\partial x^2} + GAK_1 \left(\frac{\partial \mathcal{U}_{\text{fle}}}{\partial x} - \mathcal{V}_{\text{lon}}\right) = \rho I K_2 \partial_t^2 \mathcal{V}_{\text{lon}}. \tag{5.19b}$$

The variational formulation also provides us with the boundary conditions at both beam ends (which have to be imposed separately in the classical form of the problem), which can directly be derived from Eqn. (5.18). Since we assume to have an infinite beam in our model again, we only have to impose the well-known far-field conditions. It is also clear from our problem formulation that the external force, f, is set to zero.

There exists an extensive literature about the determination of the Timoshenko shear coefficients K_1 and K_2. A first investigation can be found in Cowper 1966. This study was extended to arbitrary cross-section shapes by Gruttmann and Wagner (2001) and an alternative variational principle was employed by Hutchinson (2001) to derive new expressions for the Timoshenko shear coefficients. But these studies are mainly based on analytical considerations, less on experimental results. In preparation of possible experiments backing up this study, we intend to use parameters close to values, which have been determined in experiments. For this we refer to the work of He and Ng (2015), who used the Timoshenko shear coefficient $K_1 = 0.922$ in their parametric investigations. The second Timoshenko shear coefficient can then be obtained via $K_2 = 12K_1/\pi^2$, see Doyle 1997. The shear modulus G is given by

$$G = \frac{E}{2(1+\nu)}, \tag{5.20}$$

see e.g. Crandall et al. 1999, where we set Poisson's ratio to be $\nu = 0.33$. (Note that the dynamic Euler–Bernoulli beam Eqn. (2.6) can be recovered from the dynamic Timoshenko beam Eqns. (5.19) by taking the limits $GAK_1 \to \infty$, i.e. neglecting shear deformations, and $\rho I K_2 \to 0$, i.e. neglecting rotational inertia.)

For our numerical method it is essential to obtain the wavenumbers in each sub-interval. For the Euler–Bernoulli beam, the wavenumbers were given by Eqn. (2.10). This implied in particular that the evanescent wave modes in each sub-interval were already characterised by the travelling wave modes. This changes for the Timoshenko beam and we have to derive the characteristic equation to obtain the wavenumbers. With constant beam properties in each sub-interval, we assume the flexural deflection and rotation to be of the form

$$\mathcal{U}_{\text{fle}} = u_0 \mathrm{e}^{\mathrm{i}(kx+\omega t)}, \tag{5.21a}$$

$$\mathcal{V}_{\text{lon}} = v_0 \mathrm{e}^{\mathrm{i}(kx+\omega t)}, \tag{5.21b}$$

which yield the following system of equations, when substituting them into Eqns. (5.19),

$$\begin{pmatrix} GAK_1k^2 - \rho A\omega^2 & -ikGAK_1 \\ ikGAK_1 & EIk^2 + GAK_1 - \rho IK_2\omega^2 \end{pmatrix} \begin{pmatrix} u_0 \\ v_0 \end{pmatrix} = \mathbf{0}. \tag{5.22}$$

The characteristic equation is then given by

$$GAK_1EIk^4 - \left(GAK_1\rho IK_2\omega^2 + EI\rho A\omega^2\right)k^2 + \left(\rho IK_2\omega^2 - GAK_1\right)\rho A\omega^2 = 0, \tag{5.23}$$

which is quadratic in k^2 and we can easily obtain the four roots describing the right- and left-going travelling and evanescent wave modes in each sub-interval. Since the characteristic Eqn. (5.23) is quadratic in k^2, it is clear that we have two sets of mode pairs and the left-going wave modes are the negative right-going wave modes. Fig. 5.11 shows the wavenumbers in the homogeneous Timoshenko beam model with $h = 6.0\,\mathrm{mm}$ as functions of frequency. The wavenumbers are calculated by solving the characteristic Eqn. (5.23).

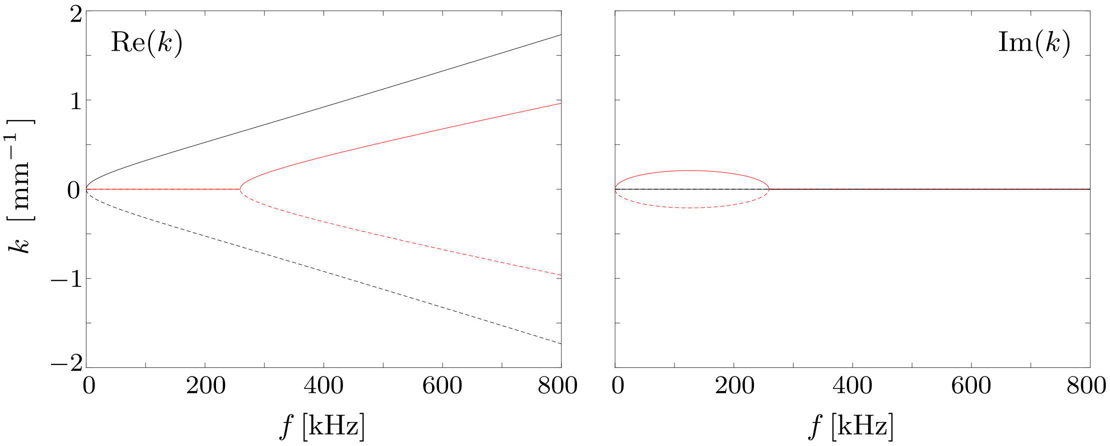

Figure 5.11: Left-hand panel: Real part of wavenumbers in Timoshenko beam model for homogeneous beam as functions of frequency. Right-hand panel: Imaginary part of wavenumbers in Timoshenko beam model for homogeneous beam as functions of frequency (same line and color scheme as in left-hand panel).

We can see that the four wavenumbers in Fig. 5.11 form two sets of pairs. The wavenumbers in each pair differ by the sign only. The first pair, which is coloured black, is real and starts at the origin, increasing superlinearly for small frequencies until approximately $f \approx 50\,\mathrm{kHz}$, from where on it increases linearly. However, the second pair of wavenumbers shows a behaviour, we could not observe in the Euler–Bernoulli beam theory, where the non-real pair of wavenumbers is purely imaginary and of the same modulus as the real pair of wavenumbers. The second pair in the Timoshenko setting is purely imaginary (again, the wavenumbers in the pair differ by sign solely) only up to $f \approx 260\,\mathrm{kHz}$, which is called the critical frequency. Up to the critical frequency, the imaginary wavenumbers form a semi-ellipse, increasing for small frequencies and decreasing from approximately 130 kHz again. When the critical frequency is reached, the imaginary part vanishes completely, and the wavenumbers become real and show from there on a qualitatively similar behaviour as the first pair of wavenumbers, although their slope is slightly smaller. Hence, the evanescent wave modes disappear for large frequencies and give place for a second pair of propagating wave modes. Note that the critical frequency depends on the beam properties of course and in the transition to the Euler–Bernoulli beam ($GAK_1 \to \infty$ and $\rho I K_1 \to 0$), the critical frequency moves to infinity.

The comparison of the wavenumbers in the Timoshenko and Euler–Bernoulli beam model is shown in the left-hand panel of Fig. 5.12, where the real, positive wavenumber in the Timoshenko beam model is shown as black, solid line and the imaginary, positive wavenumber is shown as black, dashed line. The real, positive (and imaginary, positive) wavenumber in the Euler–Bernoulli beam model is shown for comparison as grey solid line. The right-hand panel of Fig. 5.12 shows the respective phase speeds of the Timoshenko and Euler–Bernoulli beam model (black and grey solid line, respectively), which can be calculated as the angular frequency over the real, positive wavenumber, i.e. ω/k.

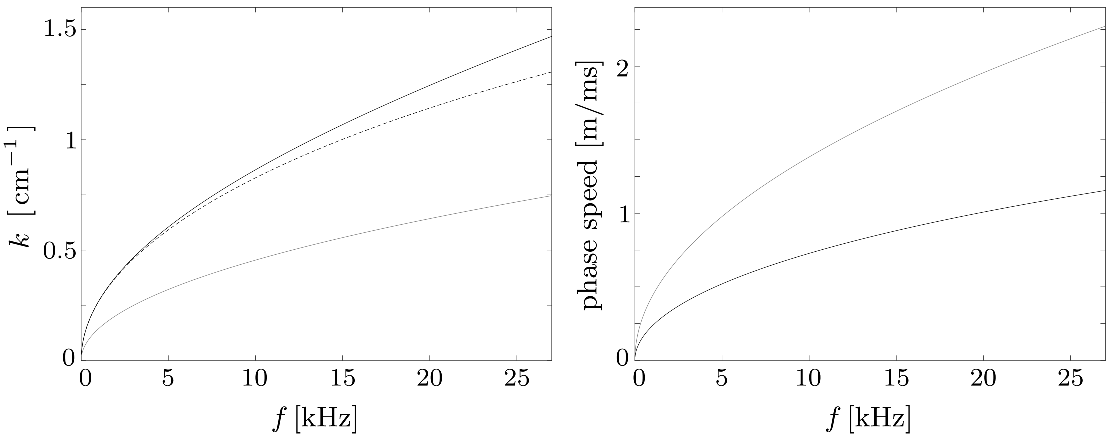

Figure 5.12: Left-hand panel: Comparison of wavenumbers in Timoshenko beam model (travelling mode as solid black line and evanescent mode as dashed black line) and Euler–Bernoulli beam model (grey line) as functions of frequency. Right-hand panel: Comparison of phase speeds in Timoshenko beam model (black) and Euler–Bernoulli beam model (grey line) as functions of frequency.

We can see in the left-hand panel of Fig. 5.12 that for the lower frequencies in the audible range, the real and purely imaginary wavenumbers in the Timoshenko beam theory have the same modulus (which holds in the Euler–Bernoulli beam theory for all frequencies). For $f \geq 5\,\text{kHz}$, they start to deviate and the real wavenumber is larger than the modulus of the imaginary wavenumber, which was already suggested in Fig. 5.11. The wavenumbers for both the Timoshenko and Euler–Bernoulli beam theory tend to zero for very small frequencies, but in comparison with the Euler–Bernoulli beam, the real wavenumber for the Timoshenko beam is significantly larger throughout the rest of the frequency regime and nearly twice as large in the high end of the audible range. This discrepancy is also reflected in the resulting phase speeds, where the real wavenumber appears as an inverse.

Hence, the phase speed in the Euler–Bernoulli model exceeds the phase speed in the Timoshenko beam model significantly. While phase speeds in both models tend to zero for $f \to 0\,\mathrm{kHz}$, they increase with increasing frequency qualitatively similarly to the increase of the wavenumbers, and phase speeds in the Timoshenko beam model are only half of the corresponding phase speeds in the Euler–Bernoulli beam model for large frequencies in the audible range.

5.4.2 Validation with finite element simulations

Before focusing on the wave speeds in our numerical method for the Timoshenko beam model (short TBM method in the following) and the FE simulations, we first compare the propagation of the excited signals in both methods. Fig. 5.13 shows the signals, which are excited by toneburst pulses with central frequencies $f_\mathrm{c} = 5\,\mathrm{kHz}$ (top panels) and $f_\mathrm{c} = 15\,\mathrm{kHz}$ (bottom panels) at $x = 0$ in the homogeneous beam calculated with the TBM method and the FE method, measured at the observations points at $x = 52.0\,\mathrm{cm}$ (left-hand panels) and $x = 106.0\,\mathrm{cm}$ (right-hand panels). The pulses are normalised with respect to their maximum value.

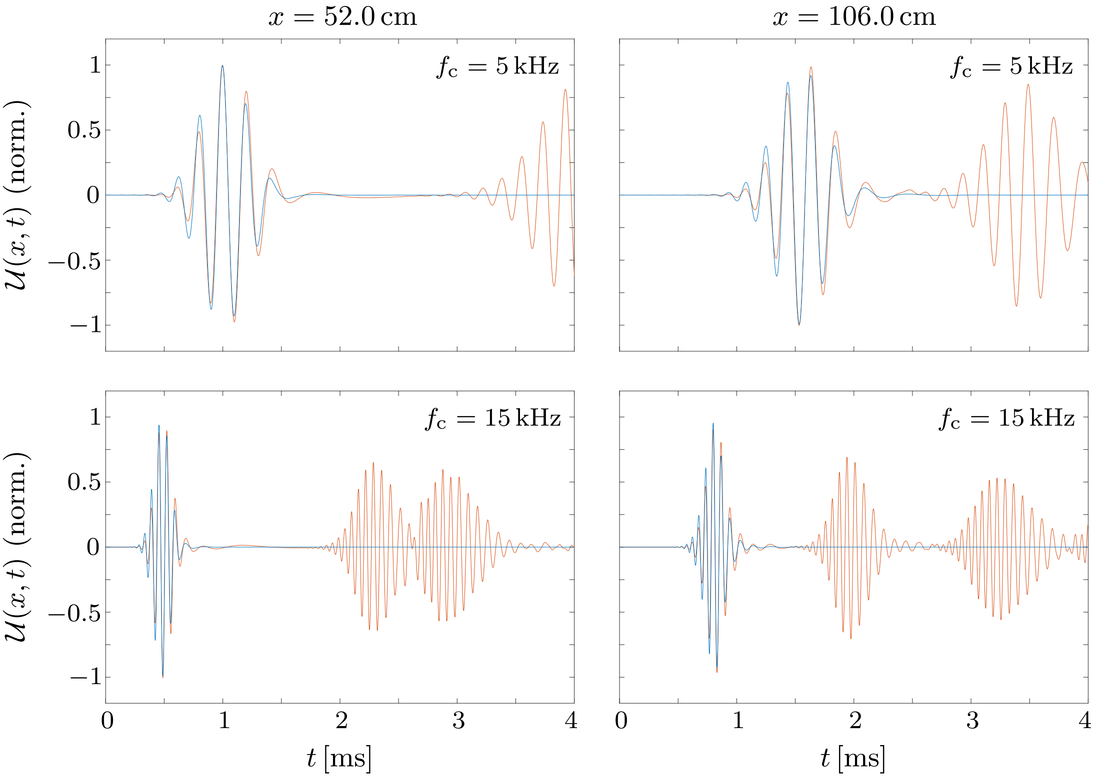

Figure 5.13: Simulated signal excited by toneburst pulse with $f_\mathrm{c} = 5\,\mathrm{kHz}$ (top panels) and $f_\mathrm{c} = 15\,\mathrm{kHz}$ (bottom panels) in homogeneous beam with numerical method for Timoshenko beam model (blue) and FE method (red), measured at $x = 52.0\,\mathrm{cm}$ (left-hand panels) and $x = 106.0\,\mathrm{cm}$ (right-hand panels)

We can observe in Fig. 5.13 a good agreement between the simulated signal with the TBM method and the FE method for both toneburst pulses. For $f_\mathrm{c} = 5\,\mathrm{kHz}$, we can see the good agreement in the deflections obtained by both methods and measured at $x = 52.0\,\mathrm{cm}$ in the first wave packet, where only small differences appear towards the edges of the pulse. The first wave packet, which is measured at $x = 52.0\,\mathrm{cm}$, is the right-going wave along the beam and passes this observation point between $0.5\,\mathrm{ms}$ and $1.7\,\mathrm{ms}$ after begin of the toneburst pulse excitation. The second wave packet, which is observable at both observations points, characterises the wave, which is reflected at the right-end of the beam. Naturally, the reflected wave is only observable in the FE simulations. (The beam in our numerical method is assumed to be of infinite horizontal extent to neglect the boundary interactions in our localisation study.) Moreover, the shape of the toneburst is clearly apparent at both observation points, since the dispersive effect is still small for this comparably small frequency over the distance between the two observation points. For $f_\mathrm{c} = 15\,\mathrm{kHz}$, the good agreement between the TBM method and the FE method holds, which can be observed at the first (right-going) wave packet. Additionally, two further wave packets passing the two observations points can be detected during the same time interval as for $f_\mathrm{c} = 5\,\mathrm{kHz}$. This is due to the higher wave speed for $f_\mathrm{c} = 15\,\mathrm{kHz}$. The second wave packet identifies the wave (again), which is reflected at the right-end of the beam, and the third wave packet characterises the wave, which is reflected at the left-end of the beam and right-going again, after it was already reflected at the right-end of the beam, i.e. we can see the wave, which was reflected at each end of the beam. The dispersive effect becomes visible most obviously at this third wave packet, which is of smaller amplitude than the other wave packets and broader than the excited toneburst pulse.

We observed in Fig. 5.13 good agreement of the simulated signals in the homogeneous beam with the TBM method and the FE method for $f = 5\,\mathrm{kHz}$ and $15\,\mathrm{kHz}$ at two different observations points. This suggests that the wave speeds in the cases of both central frequencies agree between the two methods. We want to validate this by comparing the wave speeds using the envelope of the wave packets, which is also calculated via the Hilbert transform, at the two observations points $x = 30.0\,\mathrm{cm}$ and $52.0\,\mathrm{cm}$ again. For this, we expand Fig. 5.10 by the wave speeds in the homogeneous beam, obtained with the TBM method. Fig. 5.14 shows the comparison of wave speeds of the signals, which are excited by toneburst pulses with central frequency f_c, in the homogeneous beam as functions of f_c for the TBM method and the FE method. Results with the EBBM method are shown for comparison.

We can observe in Fig. 5.14 that the wave speeds in the TBM method and the FE method (for central frequencies $f_\mathrm{c} = 5\,\mathrm{kHz}$, $10\,\mathrm{kHz}$, $15\,\mathrm{kHz}$, $20\,\mathrm{kHz}$ and $25\,\mathrm{kHz}$) nearly coincide. The wave speeds for the Timoshenko beam model are much smaller than for the Euler–Bernoulli beam model and the discrepancy between the results in the EBBM method and the FE method does not exist anymore. Hence, Fig. 5.14 provides the quantitative evidence that using the Timoshenko beam model in our numerical method is much more suitable for this study with frequencies in the audible range than the Euler–Bernoulli beam model. However, in the limit for small frequencies, the wavenumbers for the Timoshenko and the Euler–Bernoulli beam model agree (so do the wave speeds) and the Euler–Bernoulli beam theory remains as well as our results in Chs. 2 and 3 valid.

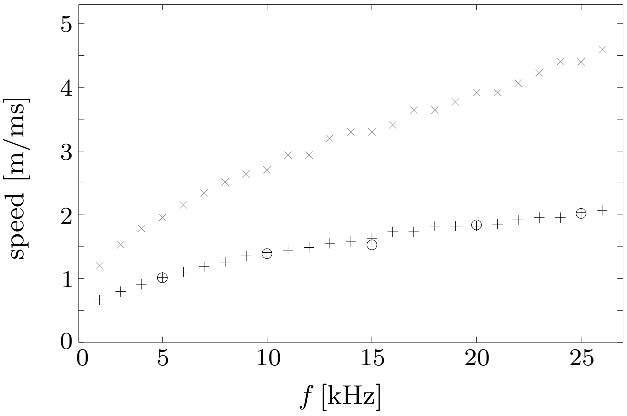

Figure 5.14: Comparison of wave speeds in homogeneous beam as functions of central frequency f_c of tone burst pulse for numerical method for Timoshenko beam model (+) and FE method (○). Results for Euler–Bernoulli beam model (×) are shown for comparison.

Before we study the localisation behaviour in the TBM method, we validate the TBM method with the help of the FE method for a beam with two notches. Note that, whereas for the Euler–Bernoulli beam only the deflection is the basic unknown, we either have the deflection, $\mathcal{U}_{\text{fle}}$, or the rotation, $\mathcal{V}_{\text{lon}}$, as basic unknown for the TBM method. We can solve for one and the other can directly be derived from Eqn. (5.22). To remain consistent with our numerical method, we use the deflection as our basic unknown again and use the continuity conditions from Eqns. (2.15) at each scattering interface, i.e. we neglect shear deformation and rotational inertia in the continuity conditions in the TBM method. This means in particular that the rotation can be obtained from the the beam deflection via $\mathcal{V}_{\text{lon}} = \partial_x \mathcal{U}_{\text{fle}}$. For the following comparison between the TBM method and the FE method, the beam shall have two notches of depth 2.0 mm and respective length 2.25 mm, located between 90.00 mm and 96.75 mm. In the beam model in Abaqus FEA, the notch is modelled to be symmetric with respect to the mid-plane of the beam, which ensures that we only have to deal with pure flexural waves in the FE simulations. For asymmetric notches, mode conversion effects occur for both reflected and transmitted waves, and the anti-symmetrical $A0$ Lamb wave is (partly) converted into the symmetrical $S0$ Lamb wave, which propagates much faster, see Behzad et al. 2013. Fig. 5.15 shows the schematic model of the dual-notched beam with $d_0 = 2.0$ mm, modelled in Abaqus FEA, illustrating the dimension of the beam and the notches.

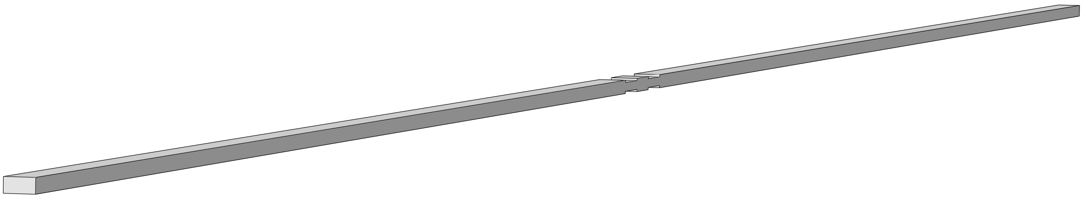

Figure 5.15: Schematic model of dual-notched beam in Abaqus FEA illustrating dimension of beam and notches

Fig. 5.16 shows the signals, which are excited by toneburst pulses with central frequencies $f_c = 5\,\mathrm{kHz}$ (top panels) and $f_c = 15\,\mathrm{kHz}$ (bottom panels) at $x = 0$ in the dual-notched beam, calculated with the TBM method and the FE method, measured at the observations points at $x = 52.0\,\mathrm{cm}$ (left-hand panels) and $x = 106.0\,\mathrm{cm}$ (right-hand panels).

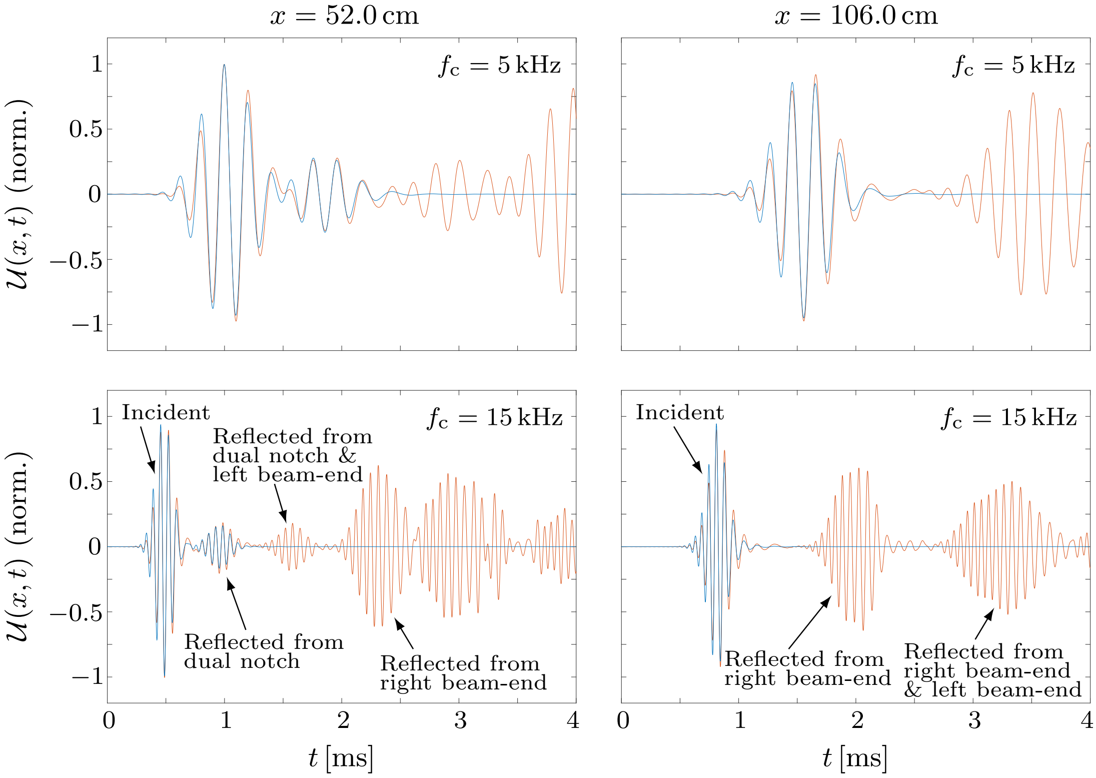

Figure 5.16: Simulated signal excited by toneburst pulse with $f_c = 5\,\mathrm{kHz}$ (top panels) and $f_c = 15\,\mathrm{kHz}$ (bottom panels) in dual-notched beam with numerical method for Timoshenko beam model (blue) and FE method (red), measured at $x = 52.0\,\mathrm{cm}$ (left-hand panels) and $x = 106.0\,\mathrm{cm}$ (right-hand panels)

The good agreement between the TBM method and the FE method, which we noticed in Fig. 5.13 for the homogeneous beam, can also be observed in the dual-notch problem. For $f_c = 5\,\mathrm{kHz}$, the excited wave and the wave reflected at the notches merge into each other at the first observation point, $x = 52.0\,\mathrm{cm}$. Slight deviations between the signals from both methods are visible in the transition zone (of the right-travelling excited wave and the wave, which was reflected at the notches) at $t \approx 1.5\,\mathrm{ms}$. After the transition between the two waves only the wave reflected at the notches can be seen and the TBM method reproduces it nearly perfectly. The oscillations in the FE simulations afterwards correspond to the waves, which are first reflected at the notches and afterwards at the left-end of the beam travelling towards the notches as well as the wave, which propagates through the notches and is subsequently reflected at the right-end of the beam. At the second observation point, which is located after the two notches, no additional pulses can be observed in the TBM method and the additional wave in the FE simulations corresponds to the first wave packet, which was reflected at the right end of the beam. We also notice that for the right-going wave pulse at the second observation point slight deviations between the two methods appear. For $f_\mathrm{c} = 15\,\mathrm{kHz}$, the wave is fast enough that the excited pulse and the wave, which is reflected at the notches, can be distinguished at the observation point at $x = 52.0\,\mathrm{cm}$. Most important, both methods yield very similar results again, not only for the excited pulse, but also for the reflected wave. Several additional pulses can be observed in the FE simulations, which arise due to the reflections at the notches and the beam ends. At the second observation point, $x = 106.0\,\mathrm{cm}$, the deflections show only small deviations again between the two solution methods.

In all cases, the amplitudes of the excited waves and waves reflected at the notches as well as the arrival times at the observation points show a very good agreement between the TBM method and the FE method. Altogether, the results produced with both methods show a very good agreement for this dual-notch problem, in particular the waves, which are reflected at the notches and hence of high importance for our study, are reproduced in a reliable manner. The results indicate that the TBM method can simulate wave propagation along a notched beam. The positive validation of the TBM method with the FE simulations, which reflect experiments in a realistic way, makes us confident that the following results on the localisation behaviour of waves in the audible frequency range with our numerical method on basis of the Timoshenko beam model can be established experimentally.

5.4.3 Numerical results for localisation along a Timoshenko beam

Before we study the localisation behaviour for disordered notch depths, we analyse the pass- and stopbands for the periodic Timoshenko beam model in the time-harmonic setting. This shall serve as the basis for our following studies in the frequency-domain and afterwards for the time-dependent problem. We possibly want to change the notch configurations to obtain an expedient experimental setup. Fig. 5.17 shows the moduli of the total reflection coefficients and the attenuation coefficients of the wave fields as functions of the frequency in the audible range, for notch lengths $l = 3.00\,\mathrm{cm}$ (left-hand panel) and $2.25\,\mathrm{cm}$ (right-hand panel). The notch depths are chosen to be $d_0 = 2.0\,\mathrm{mm}$ and the number of notches is set to be 24 in both cases.

We can observe in Fig. 5.17 that for $l = 3.00\,\mathrm{cm}$ in addition to the pass- and stopband configuration in Fig. 5.4 an additional stopband appears here for the Timoshenko beam model. The original stopband around $f = 10\,\mathrm{kHz}$ moved in this setting towards the lower end of the audible range and is now located between $2.5\,\mathrm{kHz}$ and $3.5\,\mathrm{kHz}$. The second stopband appears between $11\,\mathrm{kHz}$ and $12.5\,\mathrm{kHz}$, which leads to larger attenuation. This is the stopband, which was visible in Fig. 5.3 and was originally located above the audible range. Since the Timoshenko theory leads to larger wavenumbers for the same beam geometry, it was expected that the pass- and stopbands move towards the smaller frequencies for the Timoshenko beam model. We also notice that the frequencies in the first stopband for the Timoshenko beam model lead to the same attenuation as those in the respective stopband in the Euler–Bernoulli beam model.

We keep $d_0 = 2.0\,\mathrm{mm}$ as the underlying notch depth in our periodic configuration, from

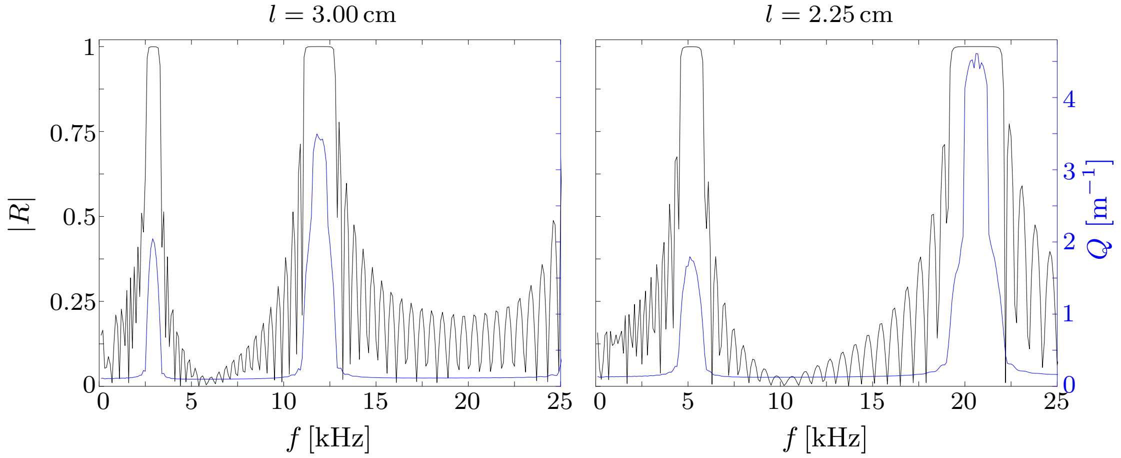

Figure 5.17: Total reflection coefficient moduli (black) and attenuation coefficients (blue) as functions of frequency for periodic notch configuration for Timoshenko beam model, for notch lengths $l = 3.00\,\mathrm{cm}$ (left-hand panel) and $l = 2.25\,\mathrm{cm}$ (right-hand panel) with respective notch depths $d_0 = 2.0\,\mathrm{mm}$

where on notch depth disorder is introduced, since it produces reasonably large attenuation and clear pass- and stopband behaviour is provided. Also, the passbands are completely turned into stopbands for positional disorder magnitudes of $\epsilon \approx 1$, which corresponds to beams, whose notches are not deeper than 4.0 mm and consequently the beam thickness does not have to come below 2.0 mm. We learnt that deeper notches only broaden stopbands and leave us less freedom to increase notches, hence we choose $d_0 = 2.0\,\mathrm{mm}$ as the underlying notch depth in our periodic configuration. Because experiments might be difficult to be conducted for frequencies of 5 kHz and smaller due to the restricted beam lengths, we are interested in an underlying periodic configuration, for which a large passband exists in the audible range above 5 kHz. We notice the perfect passband for $l = 3.00\,\mathrm{cm}$ between the two stopbands. By decreasing the notch length l, the Bragg value is naturally decreased, too, and hence, the stopbands move towards higher frequencies.

For $l = 2.25\,\mathrm{cm}$, the first stopband is located around 5 kHz now and the second stopband moved towards the upper end of the audible range and is located around 20 kHz. This configuration provides us with a large passband in the audible range between 7 kHz and 17 kHz. The two stopbands at the edges of the frequency regime, for which simulations and experiments with time-dependent signals such as toneburst pulses are possible (also possible for frequencies larger than 20 kHz, which are, however, not in the audible range anymore then), will provide us with qualitatively different behaviours in the disordered problem. Note that the second stopband is significantly stronger than the first one, i.e. the attenuation coefficient is approximately three times larger. In the configuration with notch lengths $l = 2.25\,\mathrm{cm}$, the first of the 24 notches is located between 45.00 cm and 47.25 cm and the last notch is located between 148.50 cm and 150.75 cm, occupying in total 105.75 cm of the 2 m-beam with at least 45.0 cm uniform beam adjacent to the beam ends. This shall minimise confounding effects with waves reflected at the beam ends (and the number of notches along the beam is sufficiently large to provide the possibility of localisation).

Next, we leave the periodic problem and turn our attention to the disordered problem. For this, we remain in the Timoshenko beam setting with 24 notches of length $l = 2.25\,\mathrm{cm}$ and notch depth $d_0 = 2.0\,\mathrm{mm}$ in the underlying periodic configuration. This configuration is chosen to be standard for the remaining investigations in this chapter. Now, we study the effect of different magnitudes of notch depth variations for our problem configuration. Fig. 5.18 shows the total reflection coefficient moduli medians for an ensemble of 100 realisations as functions of frequencies in the audible range for increasing ϵ.

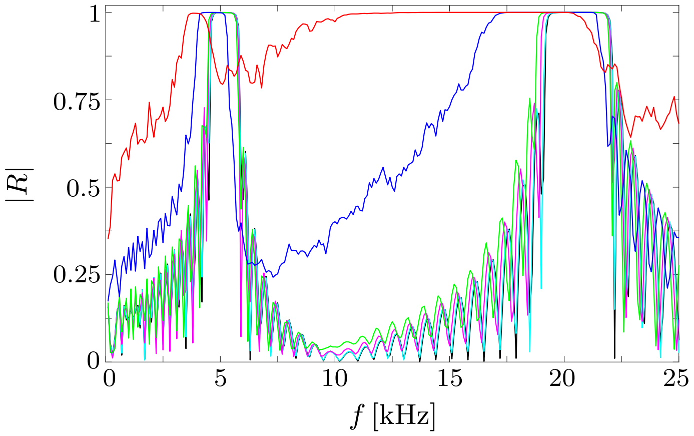

Figure 5.18: Medians of total reflection coefficient moduli for Timoshenko beam model as functions of frequencies for $\epsilon = 0$ (black), $\epsilon = 0.05$ (cyan), $\epsilon = 0.1$ (magenta), $\epsilon = 0.2$ (green), $\epsilon = 0.5$ (blue) and $\epsilon = 1.0$ (red), for notch length $l = 2.25\,\mathrm{cm}$ and underlying periodic notch depth $d_0 = 2.0\,\mathrm{mm}$

We can observe in Fig. 5.18 that for $\epsilon \leq 0.2$, only a small increase in the reflection coefficient moduli compared to the underlying periodic configuration is visible. This changes when the notch depth disorder magnitude is increased further and for $\epsilon = 0.5$, the first stopband moves slightly to the left, such that the original stopband is lost at the edge towards higher frequencies. This loss at the edge towards higher frequencies can be observed for the second stopband, which is significantly broader now, reaching from 17 kHz to 21 kHz. The original passband between the two stopbands is also lost, but the disorder is not strong enough to lead to full reflection for these frequencies. However, the total reflection is significantly increased in this frequency regime. It needs the largest magnitude of notch depth disorder under consideration, $\epsilon = 1.0$, for full reflection in the audible range $f \geq 10\,\mathrm{kHz}$. For smaller frequencies, which are still larger than in the first stopband, i.e. for frequencies between 4 kHz and 10 kHz, a very large reflection is achieved (with the reflection coefficient moduli larger than 0.8). Left of the first stopband and for frequencies larger than 21 kHz, this does not hold anymore and the reflection is smaller.

To get a quantitative insight into the influence of the notch depth disorder magnitude on the localisation behaviour in the two stopbands (for $f = 5\,\mathrm{kHz}$ and $20\,\mathrm{kHz}$) and for two frequencies in the passband between the two stopbands ($f = 10\,\mathrm{kHz}$ and $15\,\mathrm{kHz}$), we have a look on the statistical distribution of the total reflection. Fig. 5.19 shows box-and-whisker plots of the total reflection coefficient moduli as functions of the notch depth disorder magnitude ϵ. The box-and-whisker plot is depicted in the same way as in Fig. 5.6. Again, results are shown using 100 different notch depth configurations from the underlying periodic configuration ($\epsilon = 0$) and only the notch depths are increased for increasing ϵ without generating new realisations.

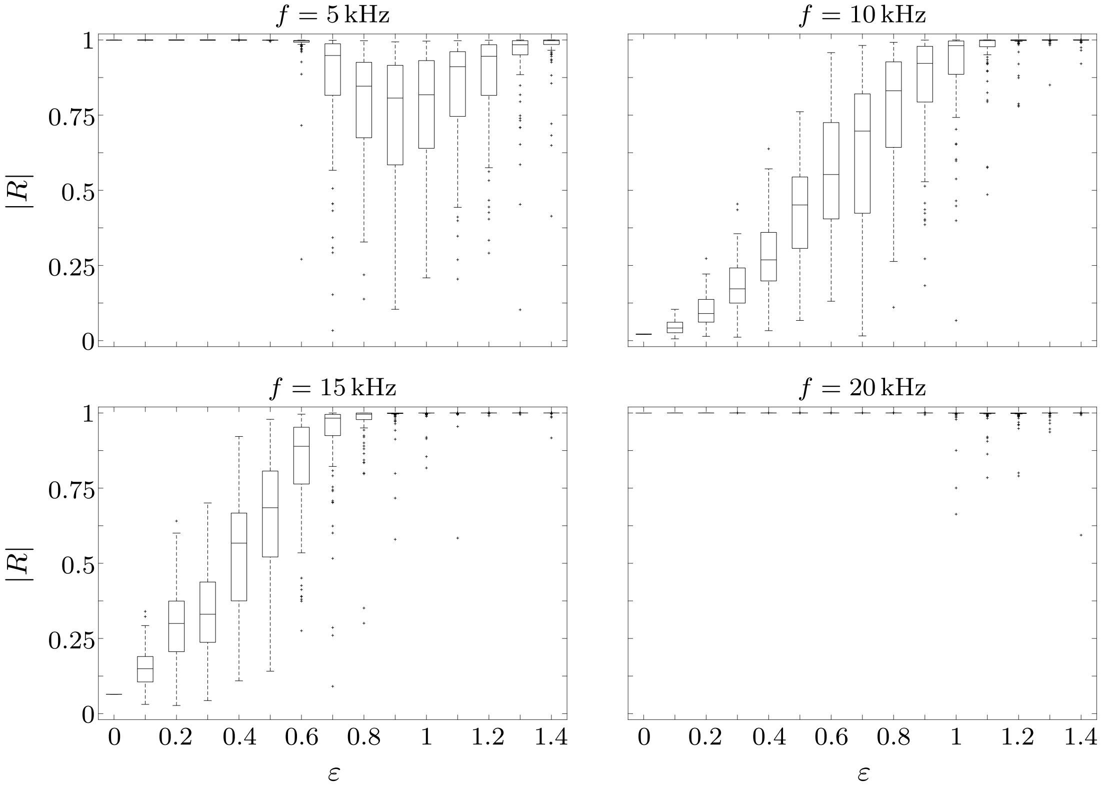

Figure 5.19: Box-and-whisker plot of total reflection coefficient moduli for Timoshenko beam model as functions of notch depth disorder magnitude for $f = 5\,\mathrm{kHz}$ (top-left panel), $f = 10\,\mathrm{kHz}$ (top-right panel), $f = 15\,\mathrm{kHz}$ (bottom-left panel) and $f = 20\,\mathrm{kHz}$ (bottom-right panel)

Fig. 5.19 shows the behaviour on the two stopbands as well as the passband, when disorder is introduced. For $f = 5\,\mathrm{kHz}$ (top-left panel), we are in the first stopband, which is robust with respect to disorder magnitudes for $\epsilon \leq 0.5$, for which full reflection is maintained. When ϵ is increased beyond this value, the stopband is lost and the median of reflection coefficient moduli decreases to approximately 0.8 for $\epsilon = 0.9$, which is approximately the same value as for the respective stopband in the Euler–Bernoulli beam model. For this disorder magnitude, configurations exist, for which $|R|$ is only 0.1 and most of the wave energy travels along the whole notched domain. This changes again for $\epsilon \geq 1.3$, for which in most realisations full reflection of the incoming wave is attained again.

For $f = 10\,\mathrm{kHz}$ and $15\,\mathrm{kHz}$, we are in the passband between the two stopbands and for the underlying periodic configuration, $\epsilon = 0$, the reflection coefficient moduli are close to zero. Increasing the disorder magnitude leads to an increase of the total reflection. For the smaller frequency in the passband, $f = 10\,\mathrm{kHz}$, a disorder magnitude of $\epsilon \geq 1.1$ is necessary to achieve full reflection for (nearly) all disorder configurations. However, disorder configurations exist, for which $\epsilon \approx 0.7$ is already sufficient for no transmission along the notched beam. For the second frequency under consideration in the passband, $f = 15\,\mathrm{kHz}$, the increase of the reflection with increasing disorder magnitude is larger and transmission is basically already prevented for $\epsilon \approx 0.8$. The smaller distance to the more dominant second stopband leads to more attenuation in this case.

For $f = 20\,\mathrm{kHz}$, we are in the second stopband, for which larger attenuation could be observed in Fig. 5.17 than for the first stopband in the periodic configuration. This stopband exhibits a different behaviour than the first stopband. For $\epsilon < 0.9$, no configuration exists, for which wave energy is transmitted. Only for larger disorder magnitudes, very few outliers, i.e. configurations, which allow a small proportion of wave energy to travel along the notched beam, exist.

Concluding our investigations in the time-harmonic setting, the results shown in Figs. 5.18 and 5.19 are combined. Fig. 5.20 shows the heatmap of the total reflection coefficient moduli in dependence of the frequency in the audible range and the notch depth disorder magnitude.

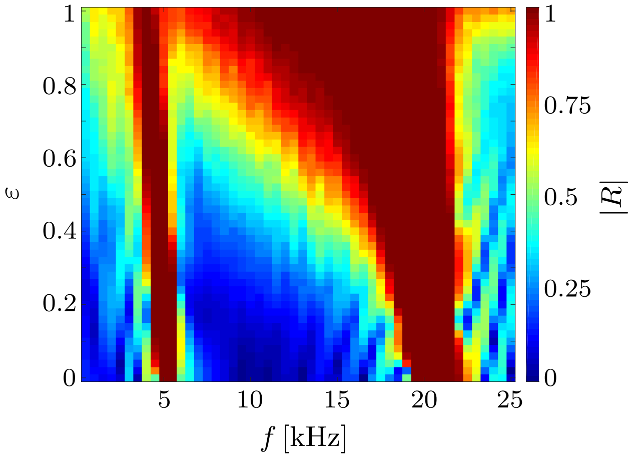

Figure 5.20: Heatmap of total reflection coefficient moduli for Timoshenko beam model as functions of frequency and notch depth disorder magnitude

We clearly notice the two stopbands in Fig. 5.20, which yield full reflection in the periodic notch configuration, i.e. $\epsilon = 0$. The first stopband is comparably small and located around $5\,\mathrm{kHz}$, the second stopband reaches from $19\,\mathrm{kHz}$ to $22\,\mathrm{kHz}$. They differ qualitatively significantly. The first stopband moves slightly towards the small frequency regime for increasing disorder magnitude, hence the original stopband is lost for large ϵ. In contrast to this, the second stopband does not move to the left as a whole, it rather broadens for increasing ϵ.

However, we can also note that for the edge of the second stopband towards the higher frequencies, full reflection is ultimately lost and small transmission allowed. This does not happen with the edge of the second stopband towards the smaller frequencies, which moves with increasing ϵ much more significantly towards the smaller frequencies, until the two stopbands nearly merge for $\epsilon = 1.0$. These characteristics serve as the basis for our final work, the study of localisation in the audible range for the time-dependent problem.

As final result for our investigations, we consider the problem of pulses travelling along the notched beam. The transition from time-harmonic to time-dependent waves in the TBM method is important for possible experimental validation of the obtained results. The waves travelling along the beam shall be excited by sinusoidal toneburst (Eqn. (5.3)), which yield good agreement of the TBM method with FE simulations for homogeneous and dual-notched beams, see Sec. 5.4.2. For our study of the localisation behaviour for (time-dependent) waves, we maintain our model of a Timoshenko beam with 24 notches of lengths $l = 2.25\,\mathrm{cm}$ and notch depth $d_0 = 2.0\,\mathrm{mm}$ in the underlying periodic configuration, for which disorder is induced by notch depth variations again. Fig. 5.21 shows transmitted energy ratios as functions of the central frequency of the excited toneburst pulses for $\epsilon = 0.0$, 0.2, 0.5, 0.8, 1.0 and $\epsilon = 1.2$. The transmitted energy ratio is the ratio of energy passing $x_{\mathrm{end}} = 2.0\,\mathrm{m}$ for the respective configuration compared to the wave energy passing the same location for the homogeneous beam. The transmitted wave energy is calculated via the square of the wave amplitude at x_{end}, i.e.

$$E_{\mathrm{transm}} = \int_0^T \mathcal{U}(x_{\mathrm{end}},t)^2 \,\mathrm{d}t, \tag{5.24}$$

where T is chosen to be sufficiently large to capture all waves passing x_{end}. The results are shown for an example notch depth configuration and increasing ϵ leads to an increase of the notch depths in this specific configuration.

We can observe in Fig. 5.21 for the periodic configuration ($\epsilon = 0.0$) that the pass- and stopbands are not defined as clearly as for the time-harmonic problem, since the toneburst pulses with central frequency f_{c} contain surrounding frequencies, see the spectral distributions of the toneburst pulses in Fig. 5.8. Hence, close to the edges of the passband, frequencies from the adjacent stopband can be found, leading to a decrease in the transmitted energy, and vice versa, close to the edges of the stopbands, frequencies from the passband can be found, leading to some transmission. However, the pass- and stopbands remain visible in Fig. 5.21. Since the stopbands for the time-harmonic problem are much narrower than the respective passband in-between, transmission occurs in both cases due to the existence of frequencies from the passband in the toneburst pulses. As we could observe in Fig. 5.8, the spectral distributions widen for increasing central frequencies, which implies in particular that the pass- and stopband characteristics blur more for large frequencies. This can be noticed for the two stopbands under consideration, located around 5 kHz and 20 kHz. The first stopband is comparably narrow and the transmitted energy ratio decreases to approximately 0.2. For the second stopband, which is inherently about twice as broad as the first one, the transmitted energy ratio decreases only to approximately 0.5 and the

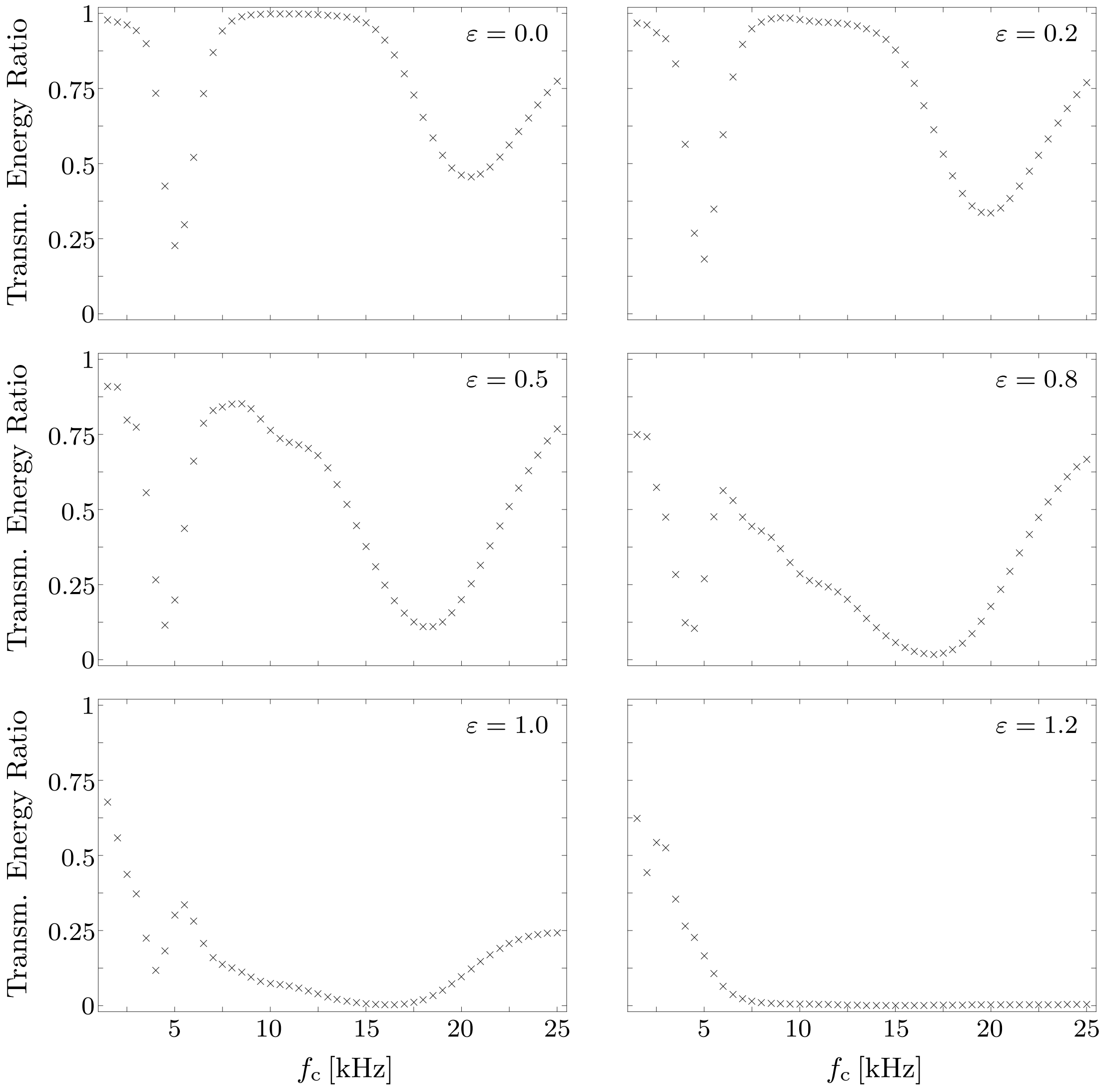

Figure 5.21: Transmitted energy ratios for Timoshenko beam model with example notch depth configuration as functions of central frequency of excited toneburst pulses for $\epsilon = 0.0$ (top-left panel), $\epsilon = 0.2$ (top-right panel), $\epsilon = 0.5$ (middle-left panel), $\epsilon = 0.8$ (middle-right panel), $\epsilon = 1.0$ (bottom-left panel) and $\epsilon = 1.2$ (bottom-right panel)

passband is already left for $f_c \geq 15\,\mathrm{kHz}$, hence for a significantly smaller frequency than for the time-harmonic problem. Nevertheless, for central frequencies between 8 kHz and 15 kHz, the original passband is preserved and we have full transmission in this frequency regime. This passband is of our main interest and we hope to achieve localisation in this passband in the audible range by introducing disorder into the underlying periodic problem.

As expected, for the smallest notch depth disorder magnitude, $\epsilon = 0.2$, only a small downshift of the transmitted energy ratio can be observed for the stopbands and for the passband edge towards higher frequencies. The passband edge towards the first stopband remains unchanged, though. This changes for $\epsilon = 0.5$, for which no complete transmission in the former passband occurs anymore, but it takes a disorder magnitude of $\epsilon = 0.8$ to achieve full reflection in the former second stopband for $f_\mathrm{c} \approx 17.5\,\mathrm{kHz}$. Full reflection is also almost attained for the former first stopband for $\epsilon = 0.8$, but the frequencies in the original passband close to the first stopband still lead to a significant transmitted energy ratio of 0.6.

For the time-harmonic problem, a disorder magnitude of 1.0 is necessary to prevent transmission between 10 kHz and 20 kHz. Here, for the time-dependent problem with excited pulses in this specific notch depth configuration, this almost holds and the transmitted energy ratio does not exceed 0.1 in this frequency regime. However, for larger central frequencies, a significant transmission can be observed, as well as for frequencies in the original first stopband and below. Increasing the notches further, this feature is conserved for central frequencies smaller than 7 kHz and the transmission increases the longer the waves become (decreasing frequency). But most important, for frequencies larger than 7 kHz full reflection is obtained and the excited pulses do not pass the notches.

5.5 Summary and discussion

After formulating the problem of waves travelling along a notched beam with notches of the same length, we showed that stopbands exist around Bragg's values in the periodic notch configuration, for which all notches are of the same depth. We have also seen that the stopbands move towards the smaller frequencies and the attenuation increases for increasing notch depths. Furthermore, we could observe harmonics of lower frequencies in the passbands, especially for frequencies smaller than in the first stopband. After that, we introduced disorder into the notch depths to investigate the effect of disorder in the notch depths on the wave propagation along the beam. We set the number of notches as 24, which yields a clear pass- and stopband behaviour and this number can be placed on a beam of 2 m length, without having to place the notches too close towards the beam ends, which might lead to difficulties in the analysis. We observed that the notch depths have to be at least 2.0 mm in the underlying periodic configuration in order to obtain localisation for notch depth disorder magnitudes of 1.0, which corresponds to doubling the notch depths at most. For larger notch depths in the underlying periodic configuration, the localisation effect for disorder magnitude 1.0 is even stronger, but the problem becomes unpractical due to the very small remaining beam thickness, though. All these calculations were performed with the numerical method, which was introduced for the in-vacuo beam problem, without having to use step approximations to approximate the profile now, since the profile is already piece-wise constant in the present problem. The numerical method is for this discrete problem computationally very efficient, since scattering matrices only appear at the scattering interfaces, which are the notch edges.

After this preliminary analysis, we used Abaqus FEA to perform simulations to validate our numerical method for the Euler–Bernoulli beam model in the present problem setting. For realistic simulations, a (finite) 2 m-beam was simulated with toneburst pulses excited at the left end of the beam. To allow comparisons with our numerical method for the Euler–Bernoulli beam model, which we used for time-harmonic problems so far only, the Fourier transform is applied to translate the time-dependent problem into the frequency-domain, where our numerical method solves the respective problem, and to translate the obtained results back into the time-domain again. In a first step of validation, the wave speeds of signals excited by toneburst pulses were compared between our numerical method for the Euler–Bernoulli beam model and the FE method. We observed that our method for the Euler–Bernoulli beam model overestimates the wave speeds clearly. This motivated the transition in our numerical method from the Euler–Bernoulli beam model to a Timoshenko beam model, which takes shear deformations and rotational inertia into account.

The Timoshenko beam model is an extension to the Euler–Bernoulli beam model and after its derivation, we examined the occurring wavenumbers and ensured that in our problem formulation, the second wave mode remains evanescent for frequencies in the audible range. We noticed that the phase speeds in the Timoshenko beam model are approximately only half of the phase speeds in the Euler–Bernoulli beam model in this frequency regime. After that, we compared signals excited by toneburst pulses for the homogeneous beam, simulated with our numerical method for the Timoshenko beam model and the FE method, which yields good agreement with experimental results for beams with similar dimensions. The comparisons showed very good agreement, which we then extended to multiple frequencies in the audible range and observed very good agreement for the wave speeds as well. Motivated by these observations, a beam with two notches was considered and the signal excited by toneburst pulses simulated with our numerical method for the Timoshenko beam model and the FE method. The agreement between both methods was striking and indicated that the Timoshenko beam model is adequate to describe the wave propagation along the beam and possible localisation effects.

As preparatory work towards final results for the time-dependent problem, we focussed on the time-harmonic problem first and formulated a setting for our final investigations and in particular for possible experimental setups. Since the Timoshenko beam model gives larger wavenumbers than the corresponding Euler–Bernoulli beam model, the pass- and stopbands move towards the smaller frequencies and we chose the notch lengths, which make significant contributions to the Bragg's values and hence to the locations of pass- and stopbands, in a way such that the stopbands are located at the lower and upper ends of our frequency regime of interest. The passband between both stopbands was then of our main interest to find localisation when introducing disorder. We observed that for large disorder, transmission of waves along the notched beam was prevented in the time-harmonic problem. This prevention comes from the original second stopband, which extends to the left for increasing disorder magnitude to merge with the first stopband finally. However, the first stopband does not extend and moves towards smaller frequencies only slightly and no transmission in the original stopbands can be observed, such as in the work of Poddubny et al. (2012), who transformed stopbands into passbands by introducing disorder for one-dimensional photonic crystals.

With the understanding of the time-harmonic problem, we finally considered toneburst pulses interacting with notches of a single example notch depth configuration for increasing notch depths, which is a realistic and feasible experimental setup. In the time-dependent problem, the pass- and stopbands merge into each other at their respective edges due to the toneburst pulses, which contain a significant frequency spectrum around the central frequencies. This does not affect the results for large disorder magnitudes and transmission is finally prevented and localisation achieved in the audible range for frequencies larger than 5 kHz.

CHAPTER 6

Summary and Future Work

The main aim of this thesis has been to study the behaviour of waves along solids with inhomogeneities. We dealt with various problems and developed a framework for semi-analytical approaches to describe the attenuation behaviour of effective wave fields travelling along beams and floating plates with small-scale continuous property and thickness variations over long distances. We briefly review the content of each chapter in the following and summarise the key outcomes. A detailed summary of the results for the various problems is given at the end of the each chapter, respectively. Due to the fundamental nature of this project, there is much future work to be done surrounding the respective problems discussed in this thesis, and we give an outlook on future work.

In Ch. 2, we studied wave propagation along rough Euler–Bernoulli beams, whose roughnesses were incorporated by continuous beam property variations and thickness variations. Beam property variations include varying densities and a varying Young's modulus along the beam, which leads to varying mass and varying rigidity, respectively. Before we investigated the attenuation behaviour over long distances, we validated our numerical method, which is based on a step approximation of the underlying continuous roughness profile. To validate the numerical method, we considered beams with deterministically varying mass and rigidity profiles. This allowed us to describe wave propagation along those beams with integral equations, which were solved with a collocation method. This approach lead us to the correct discretisation scheme for varying rigidity problems in the numerical method based on the step approximation and we could validate our numerical method, which can be used for general continuous roughness profiles. Due to the superposition principle, we could restrict ourselves to time-harmonic waves in our investigations.

Our primary focus was put on the effective waves along rough thin-elastic beams over long distances. The beam roughness was modelled via random variations in its mass, rigidity or thickness using a Gaussian autocorrelated random process, for which only the amplitude and the correlation length had to be prescribed. The effective wave fields were obtained as the ensemble average of individual wave fields for randomly generated roughness realisations for a given amplitude and correlation length, whereby the step-approximation method was used to calculate the individual wave fields. This approach was used to validate the semi-analytical approach, which was sought and derived to describe the propagation of the effective wave field more efficiently. To obtain sufficiently accurate effective wave fields, a very large ensemble of individual wave fields was needed. Hence, for the computations of the effective wave field via the numerical method, a high-performance computing cluster was used to reduce the computing time hugely, compared to standard and high specification PC systems. The semi-analytical approach was based on a multiple-scale expansion of the effective beam deflection and yielded the phase changes and attenuation coefficients of the effective wave fields, on the assumption that the roughness amplitude was small. The phase changes and attenuation coefficients for the problems of varying mass, varying rigidity and varying thickness, predicted by the multiple-scale method and obtained by the numerical method, were compared over a range of correlation lengths and roughness amplitudes, and individual wave fields could be compared with the corresponding effective wave fields using the numerical method. The key findings were as follows:

a. The varying mass and varying rigidity produce identical attenuation coefficients, and identical phase changes up to the addition of a constant.

b. For varying mass, the effective wavelength is longer than the wavelength of the corresponding uniform beam, but it is shorter for the varying rigidity.

c. In the limit that the correlation length tends to zero, the varying mass produces no phase change, but the varying rigidity does produce a phase change.

d. Varying thickness leads to significantly larger attenuation coefficients than varying mass and varying rigidity, only.

e. The effective wavelength in the case of varying thickness is shorter than the wavelength of the corresponding uniform beam.

f. The phase changes and attenuation coefficients predicted by the numerical method and the multiple-scale method agree up to $\epsilon \approx 0.1$.

g. The effective wave fields differ from the individual wave fields, particularly in the large-correlation-length regime.

We have seen that the multiple-scale method yielded accurate phase changes as well as attenuation coefficients for the varying mass, varying rigidity and varying thickness problems in the small roughness-amplitude regime. The roughness in the material properties and beam thickness lead to a random left-travelling wave component, which cannot be neglected anymore for large roughness amplitudes. To take this into account in the large roughness-amplitude regime, a left-travelling wave could be included at leading order in the multiple-scale method. The spatial structure of the waves along the rough beam, in particular the intrinsic left-travelling wave components, could be analysed and solutions studied using dynamical system tools. Moreover, further autocorrelation functions could easily be used for the numerical and semi-analytical methods and their impact be analysed. In particular, our numerical method is capable of calculating the (individual as well as effective) wave fields for more generic and complicated beams incorporated with other random processes. Taking care of more general random processes describing the beam properties and thickness would require more detailed modelling sophistication of the statistics though. More extensive modifications of our model would result from the consideration of different kinds of non-linearity, which might reveal numerous effects not occurring in our linear problem, and the enhancement to thick beams, for which compressibility, rotational inertia, shear deformation and dissipation could be taken into account, see e.g. Balmforth and Craster 1999.

In Ch. 3, the problem formulation was extended to wave propagation along rough plates floating on water. This problem formulation for long plates typically has applications in the construction of very large floating structures and in modelling the interaction of ocean waves with very large ice floes in the marginal ice zone. We focused in our investigations on the sea-ice model for very large ice floes, which help to prevent the continuous ice from being broken by the long ocean waves travelling unimpeded through the marginal ice zone. Since the amplitudes of the incoming ocean waves in the marginal ice zone are comparable small to their wavelengths, linear water wave theory could be applied, and since the very large ice floes are of comparable small thickness and highly flexible, they could be modelled as Euler–Bernoulli plates. At the interface between the water and the floating plate, a dynamic and a kinematic boundary condition were applied to couple the equation of motion for the floating plate with the potential equation of the water. This lead us to a system of equations for the velocity potential of the water and the plate deflection, consisting of an equation for the velocity potential in the water domain, an impermeability condition at the sea-floor and the coupled condition for the floating plate. We modelled the plate roughness similarly to the in-vacuo beam problem as a continuous, Gaussian autocorrelated random process with roughness profile variations being uniform along the y-axis, which made the model two-dimensional. The numerical method based on the step approximation of the continuous roughness profile, which was presented for the in-vacuo beam problem, had to be extended for the floating plate problem, since the full-linear solution of the velocity potential contains an infinite number of wave modes in each sub-interval. For numerical computations, the full-linear solution in each sub-interval had to be approximated with a finite number of wave modes. To obtain the effective wave field for the floating plate problem via the numerical method, the computing time increased compared to the in-vacuo beam problem, which was already computationally very expensive. For this reason, a semi-analytical method is derived to describe the attenuation of the effective wave field in presence of continuous thickness and plate property variations. This multiple-scale method is based on the assumption again that the roughness amplitude of the plate variations is small. The attenuation coefficients for the problems of varying mass, varying rigidity and varying thickness, predicted by the multiple-scale method and obtained by the numerical method, were compared over a range of correlation lengths and roughness amplitudes. The key findings were as follows:

a. The attenuation coefficients predicted by the numerical method and the multiple-scale method agree up to $\epsilon \approx 0.1$.

b. The attenuation coefficients show the same qualitative behaviour as for the in-vacuo beam problem.

c. Varying thickness leads to significantly larger attenuation coefficients than varying mass and varying rigidity only.

d. The attenuation for varying rigidity dominates the attenuation for varying mass.
e. The effective wave fields differ from the individual wave fields, particularly in the large-correlation-length regime.

The approaches to characterise the dynamic behaviour in the marginal ice zone are numerous. For this reason, we restrict our outlook for the future work on approaches, which can directly be pursued from our work. Although we have been interested in the attenuation for the floating plate problem, it would be obvious to characterise the phase change as well. However, to give the phase change for this problem, the discontinuities of the higher-order derivatives of the corresponding Green's function have to be taken into account, which result from the impulse at the source point. We want to emphasize the simplifying character of this study and that ocean wave interactions with large ice floes have to be characterised more sophistically. A first step towards a more realistic model would be to include cracks, pressure ridges and extending the model to discrete ice floes, for which additional boundary conditions (between plates and open water, corner conditions for cracks, ...) and no flow conditions from open water through submerged part of plate edge (see e.g. Squire 2010) have to be applied.

The multiple-scale method represents a very efficient method to capture the attenuation for the present problem. However, it describes the attenuation of the effective wave field only. To find the transmission and reflection of flexural waves across a patch of random inhomogeneities such as mass and/or rigidity in a floating plate, numerical methods such as our step-approximation method could be used, but it takes a long computing time, when the patch is long. Efficient computational methods could possibly be found to describe the transmission and reflection in such problems by using Fourier transform methods in 1D and 2D to find the plate deflection, which avoids the discretisation of the roughness profile. Unfortunately, due to the ignorance of mankind, sea-ice is condemned to vanish. For consequences of the loss of sea-ice in polar regions on areas across the planet, we refer to Wadhams 2016.

In Ch. 4, we studied wave propagation along strings with continuous and discrete inhomogeneities. To start with, we investigated an inhomogeneous string with a continuous roughness profile, which exhibited the same roughness characteristics (for the string density) as the in-vacuo beam and floating beam problems. The problem for a string with continuous roughness profile was of second order only, which was easier to deal with than the beam and plate problems (and a simplified version of the step-approximation method could be used) and primarily served as a simpler model to gain a deeper understanding of scattering at continuous roughness profiles. A numerical modification allowed larger roughness amplitudes in our investigations than for the previous problems. This modification caused the statistical characteristics of the random process to be lost in the large roughness-amplitude regime, for which, in addition, the limits of validity of analytical approximations such as multiple-scale expansions are exceeded. However, the transition to large roughness amplitudes lead to convergence of individual and effective attenuation coefficients, i.e. for strong enough scattering, the wave cancellation effect diminished, and individual and effective wave fields can be representative for each other.

Our aim in this chapter was to establish a connection between the scattering and attenuation behaviour of strings with continuous and discrete inhomogeneities. After we had studied the continuous problem, it was pending and necessary for the subsequent work to investigate and understand the discrete problem. To compute wave propagation along a string beaded with point scatterers, our numerical method for the continuous problem had to be modified to be applied for general point scatterer profiles. For our attenuation investigations, we started in passbands for the underlying periodic beads configuration and studied the effect of disordering the beads' positions on the wave attenuation. An averaging routine allowed us to calculate the effective wave field and we could observe that individual and effective wave fields correspond throughout a large regime of scattering strengths, and their attenuation coincided with the value predicted by the Berry–Klein limit for sufficiently large positional disorder. It was also interesting to note that wave-cancellation effects occurred in this setting for small scattering strengths, and effective wave fields were attenuated slightly faster than individual wave fields, which complemented our understanding of this phenomenon.

The separate analysis of the continuous and discrete problem, and the acquired understanding of the respective problems made it possible to change our focus over to connecting both problems. A numerical routine was then used to cluster continuous roughness profiles into single humps and we studied their statistics. We used the phase-change distribution for the continuous problem to fit a non-parametric distribution. This distribution was employed to describe the positional disorder in the discrete problem (mean scattering strength was obtained from clustered humps) and we compared the results with the underlying continuous problem. The key findings were as follows:

a. The attenuation in the discrete problem dominates the attenuation in the continuous problem with equivalent scattering strengths for uniformly distributed phase changes.

b. The phase-change distribution is important for the attenuation magnitude in the discrete problem.

c. The maximum attenuation in the discrete problem occurs for phase changes distributed around π.

d. Agreement between the attenuation in the continuous and discrete problem for the same phase-change distributions is reached in the correlation-length regime producing maximum attenuation.

The importance of the phase-change distribution explains the comparably weak attenuation for continuous roughness profiles (for rough beam and plates as well). The underlying (Gaussian autocorrelated) process gives a hump profile with humps of very similar length and the missing deviation in the hump lengths results in only similar phase changes of waves interacting between adjacent hump. A hump-length disorder might numerically be introduced into the continuous random profile to include all phase changes. To obtain similar attenuation as for disordered discrete problems, it has to be taken into account that increasing hump lengths might lead to humps, which are too smooth then to attenuate the propagating waves. This could possibly be compensated by adjusting the roughness amplitudes for these scaled humps. We could observe that wave fields exist for large roughness amplitudes and scattering strengths, which attenuate much slower than the remaining wave fields and subsequently dominate the corresponding effective wave field, which we eluded by introducing the quantile approach in our investigations. This has to be studied carefully in the future. Preliminary investigations for the in-vacuo beam problem suggested that a significant increase in the roughness amplitude gives rise to a converging behaviour of individual and effective wave fields to each other for maximum-attenuation-producing correlation lengths as well. Moreover, the connection between the continuous and discrete string problems can be specified more accurately by identifying the scattering strength and phase change of each clustered hump in the continuous problem and transferring it to the corresponding point scatterer in the discrete problem instead of assigning the mean scattering strength of all clustered humps and the corresponding phase change distribution to the point scatterers. The more elaborate ansatz of individual scattering strengths corresponds to compositional disorder of discrete scatterers, which is less influential on the attenuation behaviour than positional disorder, see e.g. Maurel and Martin 2013.

In Ch. 5, we studied waves with frequencies in the audible range travelling along beams with discrete, periodically located notches. Our aim was to find and investigate localisation behaviour in this setting by introducing notch depth variations. We started with showing the pass- and stopband behaviour for the periodic configuration, for which the notch depth is uniform for all notches along the beam. This allowed us to analyse the fundamental influence of the notch-configuration geometry for time-harmonic waves. The number of notches was chosen to be sufficiently large for providing a clear pass- and stopband behaviour, but not too large to avoid difficulties in the analysis of possible experiments, which might occur, when notches are placed too close towards the beam ends. However, these difficulties do not arise with our efficient numerical method, introduced for the in-vacuo beam problem in Ch. 2, for which the interactions at the beam ends are neglected. After a preliminary investigation of the effect of disordering notch depths for the Euler–Bernoulli beam model, we used FE simulations in order to validate our numerical method for the Euler–Bernoulli beam model. For this purpose, a 2 m-beam was simulated with toneburst pulses excited at the left end of the beam. To use our numerical method for time-dependent problems, a Fourier transform was applied, which made it possible to apply the numerical method in the frequency-domain and yield the results in the time-domain. The observed discrepancy of wave speeds for a homogeneous beam between our numerical method for the Euler–Bernoulli beam model and the FE simulations motivated a transition from the Euler–Bernoulli beam model to the Timoshenko beam model for our numerical method. The Timoshenko beam model was an extension to the Euler–Bernoulli beam model taking shear deformations and rotational inertia into account and showed very good agreement with the wave speed obtained by the FE simulations for frequencies in the audible range. The Timoshenko beam model gave larger wavenumbers than the corresponding Euler–Bernoulli beam model, which is why the pass- and stopbands move towards the smaller frequencies compared to the Euler–Bernoulli beam model. We chose the notch lengths in a way such that the stopbands are located at the lower and upper ends of the audible frequency regime of interest. The passband between these two stopbands was then of our main interest to find localisation when introducing disorder. The key findings were as follows:

a. Good agreement between our numerical method for the Timoshenko beam model and FE simulations for a toneburst pulse travelling along a beam with two notches can be observed.

b. For notch depths of 2.0 mm in the underlying periodic configuration, their depths have to be randomly doubled to obtain clear localisation in the time-harmonic setting.

c. Transmission of waves along the notched beam is prevented by the original second stopband, which extends towards first stopband for large disorder magnitudes.

d. No transmission in the original stopbands can be observed.

e. The localisation effect in the original passband becomes stronger when the notch depth disorder magnitude is increased beyond doubling notch depths.

f. The pass- and stopbands merge into each other at their respective edges in the time-dependent problem (because of the frequency spectrum of the toneburst pulses).

g. Localisation is achieved in the audible range for frequencies larger than 5 kHz in the time-dependent problem by disordering notch depths.

This study was intended as preparatory work for experimental validation, for which the experiments still have to be conducted. Our setting was chosen with those in view to yield good experimental results. For the analysis of toneburst signals after the notched domain, it is required that they are isolated and reflections at the beam ends do not distort amplitude measurements. This might be circumvented for our localisation investigations by damping the right-end of the beam to absorb the signals there and prevent wave reflection. Also, to design efficient experiments, frequency bands might be considered instead of toneburst pulses to see which frequencies are localised along the notched beam. Moreover, comparisons with wave propagation along notched beams with asymmetric notches, i.e. the notches are not modelled to be symmetric with respect to the mid-plane of the beam anymore, would be informative for physical problems as well. The asymmetric notches give rise to mode conversion of the anti-symmetric propagating Lamb waves (which our numerical method cannot capture). The resulting symmetric Lamb waves have different wave speeds and stresses through the beam thickness, see e.g. Bao 2003, and their influence on the localisation behaviour has to be studied. We have investigated notch-depth configurations for increasing notch depths, which is a realistic and feasible experimental setup, to obtain localisation. This corresponds to compositional disorder for the beaded-string problem, for which less attenuation is observed compared to positional disorder, see Maurel and Martin 2013. This could be studied in the setting of notched beams as well by comparing our results with those for notch position variations. The notch position variations could be incorporated by describing the notch lengths and the distance between adjacent notches via random distributions.

In this work, we showed efficient computational methods to describe effective wave fields in beam and floating plate problems with continuous roughness profiles. This research contributed to the fundamental analysis of effective and individual waves, and their interaction with continuous inhomogeneities along rough thin-elastic solids. In addition, we studied wave propagation along solids with discrete scatterers and investigated their connection to continuous inhomogeneities for strings. The findings in this thesis lay out the groundwork for future work and might be applied on more complex inhomogeneous solid structures.

APPENDIX A

Random process in rough profile generation

The following paragraphs are based on the study by Shinozuka (1971) to show that the random process in Eqn. (2.73) has mean zero and (on average) the same autocorrelation and mean-square spectral density function as the target random process ψ_0, and is ergodic in the autocorrelation. According to the central limit theorem, the random process ψ is Gaussian for sufficiently large N, and we can use the ensemble average

$$\langle \cos(r_n x + \varphi_n) \rangle = \frac{1}{2\pi} \int_{-\infty}^{\infty} \int_0^{2\pi} \cos(r_n x + \varphi_n) f(r_n) \, \mathrm{d}\varphi_n \, \mathrm{d}r_n \tag{A.1}$$

and the independent choice of the random variables r_n and φ_n, $n = 1, \ldots, N$, to obtain

$$\begin{aligned} \langle \psi(x) \rangle &= \left\langle \sigma \sqrt{\frac{2}{N}} \sum_{n=1}^{N} \cos(r_n x + \varphi_n) \right\rangle = \sigma \sqrt{\frac{2}{N}} \sum_{n=1}^{N} \langle \cos(r_n x + \varphi_n) \rangle \\ &= \sigma \frac{\sqrt{2N}}{2\pi} \int_{-\infty}^{\infty} \int_0^{2\pi} \cos(rx + \varphi) f(r) \, \mathrm{d}\varphi \, \mathrm{d}r = \sigma \frac{\sqrt{2N}}{2\pi} \int_{-\infty}^{\infty} [\sin(rx + \varphi) f(r)]_0^{2\pi} \, \mathrm{d}r \\ &= 0. \end{aligned} \tag{A.2}$$

Hence, the ensemble average of $\psi(x)$ vanishes as expected.

To show the other properties, i.e. same autocorrelation and mean-square spectral density as the target random process, the autocorrelation function of $\psi(x)$, ρ, is written as

$$\begin{aligned} \rho(x,x+\xi) &= \langle \psi(x) \, \psi(x+\xi) \rangle = \frac{2\sigma^2}{N} \sum_{m=1}^{N} \sum_{n=1}^{N} \langle \cos(r_m x + \varphi_m) \cos(r_n(x+\xi) + \varphi_n) \rangle \\ &= \frac{2\sigma^2}{N} \sum_{n=1}^{N} \langle \cos(r_n x + \varphi_n) \cos(r_n(x+\xi) + \varphi_n) \rangle \\ &= 2\sigma^2 \langle \cos(rx + \varphi) \cos(r(x+\xi) + \varphi) \rangle \, . \end{aligned} \tag{A.3}$$

Here, it was used that the 2π-periodicity of the trigonometric functions (similar argument as in Eqn. (A.2)) leads to

$$\langle \cos\left(r_m x + \varphi_m\right) \cos\left(r_n(x+\xi) + \varphi_n\right) \rangle = 0 \quad \text{for } m \neq n. \tag{A.4}$$

With the general addition theorem,

$$\cos(a)\,\cos(b) = \frac{1}{2}\left[\cos(a+b) + \cos(a-b)\right] \tag{A.5}$$

for real a and b, the expected value in Eqn. (A.3) for r being considered as a sample can be written as

$$\frac{1}{2\pi}\int_0^{2\pi} \cos\left(rx+\varphi\right)\cos\left(r(x+\xi)+\varphi\right) \mathrm{d}\varphi = \frac{1}{2}\cos\left(r\xi\right) \tag{A.6}$$

and Eqn. (A.3) simplifies with the representation of the probability density function f from Eqn. (2.74) to

$$\rho(\xi) = \rho(x{,}x+\xi) = \sigma^2 \int_{-\infty}^{\infty} f(r)\cos\left(r\xi\right) \mathrm{d}r = \int_{-\infty}^{\infty} S_0(r)\cos\left(r\xi\right) \mathrm{d}r. \tag{A.7}$$

Eqns. (A.2) and (A.7) imply that the random process ψ is stationary in a wide sense, i.e. the mean as well as the autocorrelation function ψ do not vary with respect to space. This is fulfilled, since the mean value is constant and the autocorrelation function only depends on the difference ξ between two points x and $x+\xi$. The wide-sense stationarity of ψ makes it possible to apply the Wiener–Khinchin theorem, which relates the autocorrelation function, ρ_0, and the spectral density function, S_0, via the Fourier transform and its inverse,

$$\rho_0(\xi) = \mathcal{F}[S_0(r)] := \int_{-\infty}^{\infty} S_0(r)\mathrm{e}^{\mathrm{i}r\xi}\,\mathrm{d}r = \int_{-\infty}^{\infty} S_0(r)\cos\left(r\xi\right)\mathrm{d}r \tag{A.8a}$$

$$S_0(r) = \mathcal{F}^{-1}[\rho_0(\xi)] := \frac{1}{2\pi}\int_{-\infty}^{\infty} \rho_0(\xi)\mathrm{e}^{-\mathrm{i}r\xi}\,\mathrm{d}\xi = \frac{1}{2\pi}\int_{-\infty}^{\infty} \rho(\xi)\cos\left(r\xi\right)\mathrm{d}\xi\,. \tag{A.8b}$$

It is used in Eqns. (A.8) that the autocorrelation function and the spectral density function are even functions, and the second identity in Eqn. (A.8b) follows from application of the inverse Fourier transform on Eqn. (A.7).

Recapitulating, we showed in Eqn. (A.2) that the first moment for both the random process ψ and the target random process ψ_0 coincide (on average and for N large enough). It follows from Eqns. (A.8) that (again considering the ensemble average and sufficiently large N) the autocorrelation function, ρ, and the mean-square spectral density, S, agree with the target autocorrelation function, ρ_0, and target mean-square spectral density, S_0, of the (target) random process ψ_0.

After we have considered the statistical properties of the random process with respect to ensemble averages above, we focus on individual realisations of the underlying process ψ, i.e. the statistical properties with respect to spatial averages, now. For the sake of notation simplicity, the spatial mean of an included quantity is denoted with **E**. First, it can be shown that the spatial mean vanishes,

$$\begin{aligned}|\mathbf{E}[\psi(x)]| &= \left|\lim_{L\to\infty}\frac{1}{L}\int_0^L \sigma\sqrt{\frac{2}{N}}\sum_{n=1}^{N}\cos\left(r_n x+\varphi_n\right)\,\mathrm{d}x\right| = \left|\lim_{L\to\infty}\frac{\sigma}{L}\sqrt{\frac{2}{N}}\sum_{n=1}^{N}\int_0^L\cos\left(r_n x+\varphi_n\right)\mathrm{d}x\right| \\ &\leq \lim_{L\to\infty}\frac{\sigma}{L}\sqrt{\frac{2}{N}}\sum_{n=1}^{N}\frac{1}{r_n}\left|\left[\sin\left(r_n x+\varphi_n\right)\right]_{x=0}^{L}\right| \leq \lim_{L\to\infty}\frac{2\sigma}{L}\sqrt{2N}\max_{n=1,\ldots,N}\frac{1}{r_n}=0. \end{aligned} \tag{A.9}$$

Hence, each realisation of the random process is expected to vary around its mean 0. It is important to keep in mind, when dealing with individual process realisations (as we do now considering spatial means, spatial autocorrelation, …), that r_n and φ_n, $n = 1,\ldots,N$, are not random variables anymore but sample values.

Next, the spatial autocorrelation function for the random process ψ is of interest. The spatial autocorrelation function is denoted with $\rho^*(\xi)$ and it simplifies to

$$\begin{aligned}\rho^*(\xi) &= \mathbf{E}[\psi(x)\,\psi(x+\xi)] \\ &= \lim_{L\to\infty}\frac{2\sigma^2}{LN}\sum_{m=1}^{N}\sum_{n=1}^{N}\int_0^L\cos\left(r_m x+\varphi_m\right)\cos\left(r_n(x+\xi)+\varphi_n\right)\mathrm{d}x \\ &= \lim_{L\to\infty}\frac{2\sigma^2}{LN}\sum_{n=1}^{N}\int_0^L\cos\left(r_n x+\varphi_n\right)\cos\left(r_n(x+\xi)+\varphi_n\right)\mathrm{d}x \\ &= \frac{\sigma^2}{N}\sum_{n=1}^{N}\cos\left(r_n\xi\right), \end{aligned} \tag{A.10}$$

where the following orthogonality result was used,

$$\frac{1}{L}\int_0^L\cos\left(r_m x+\varphi_m\right)\cos\left(r_n(x+\xi)+\varphi_n\right)\mathrm{d}x = \begin{cases}0 & \text{for } m\neq n,\\ \frac{1}{2}\cos\left(r_n\xi\right) & \text{for } m=n.\end{cases} \tag{A.11}$$

To obtain the corresponding mean-square spectral density function, S^*, from the autocorrelation function ρ^*, the Wiener–Khinchin theorem is applied in the same way as in Eqn. (A.8b),

$$S^*(r) = \frac{1}{2\pi}\int_{-\infty}^{\infty}\rho^*(\xi)\mathrm{e}^{-\mathrm{i}r\xi}\,\mathrm{d}\xi = \frac{\sigma^2}{2\pi N}\sum_{n=1}^{N}\int_{-\infty}^{\infty}\cos\left(r_n\xi\right)e^{-\mathrm{i}r\xi}\,\mathrm{d}\xi\,. \tag{A.12}$$

To simplify the expression for S^*, we make use of the following representations of the Dirac delta distribution,

$$\begin{aligned}\mathcal{F}^{-1}[\mathcal{F}[\delta(r-r_n)]] = \mathcal{F}^{-1}\Big[\int_{-\infty}^{\infty}\delta(r-r_n)\,\mathrm{e}^{\mathrm{i}r\xi}\,\mathrm{d}r\Big] = \mathcal{F}^{-1}\Big[\mathrm{e}^{\mathrm{i}r_n\xi}\Big] = \frac{1}{2\pi}\int_{-\infty}^{\infty}\mathrm{e}^{\mathrm{i}r_n\xi}\,\mathrm{e}^{-\mathrm{i}r\xi}\,\mathrm{d}\xi\\ = \frac{1}{2\pi}\int_{-\infty}^{\infty}\mathrm{e}^{-\mathrm{i}(r-r_n)\xi}\,\mathrm{d}\xi = \delta(r-r_n),\end{aligned}\tag{A.13a}$$

and similarly,

$$\mathcal{F}^{-1}[\mathcal{F}[\delta(r+r_n)]] = \frac{1}{2\pi}\int_{-\infty}^{\infty}\mathrm{e}^{\mathrm{i}(r+r_n)\xi}\,\mathrm{d}\xi = \delta(r+r_n).\tag{A.13b}$$

These representations lead to the following form of the (normalised) integral term in Eqn. (A.12),

$$\begin{aligned}\frac{1}{\pi}\int_{-\infty}^{\infty}\cos{(r_n\xi)}\mathrm{e}^{-\mathrm{i}r\xi}\,\mathrm{d}\xi &= \frac{1}{\pi}\int_{-\infty}^{\infty}\frac{\mathrm{e}^{-\mathrm{i}r_n\xi}+\mathrm{e}^{\mathrm{i}r_n\xi}}{2}\,\mathrm{e}^{\mathrm{i}r\xi}\,\mathrm{d}\xi\\ &= \frac{1}{2\pi}\int_{-\infty}^{\infty}\mathrm{e}^{\mathrm{i}(r-r_n)\xi}\,\mathrm{d}\xi + \frac{1}{2\pi}\int_{-\infty}^{\infty}\mathrm{e}^{\mathrm{i}(r+r_n)\xi}\,\mathrm{d}\xi\\ &= \delta(r-r_n)+\delta(r+r_n),\end{aligned}\tag{A.14}$$

so that we can rewrite the mean-square spectral density function from Eqn. (A.12) as

$$S^*(r) = \frac{\sigma^2}{2N}\sum_{n=1}^{N}\left[\delta(r-r_n)+\delta(r+r_n)\right].\tag{A.15}$$

To draw a comparison between the autocorrelation function in the ensembling case, ρ, and its spatial equivalent, ρ^*, it is expedient to construct the mean-square spectral distribution function, $\mathit{\Gamma}^*$, from the mean-square spectral density function, S^*,

$$\mathit{\Gamma}^*(r) = \int_{-\infty}^{r}S^*(\tilde{r})\,\mathrm{d}\tilde{r} = \frac{\sigma^2}{2N}\sum_{n=1}^{N}\int_{-\infty}^{r}\delta(r-r_n)+\delta(r+r_n)\,\mathrm{d}\tilde{r}.\tag{A.16}$$

To evaluate the corresponding integrals of the Dirac delta distributions in Eqn. (A.16), the cases $r \leq 0$ and $r \geq 0$ have to be analysed. For $r \leq 0$, we have

$$\int_{-\infty}^{r}\delta(\tilde{r}-r_n)+\delta(\tilde{r}+r_n)\,\mathrm{d}\tilde{r} = \begin{cases}1, & \text{if } r_n \leq r,\\ 1, & \text{if } r_n \geq -r,\\ 0, & \text{else,}\end{cases}\tag{A.17a}$$

whereas for $r \geq 0$, we have

$$\int_{-\infty}^{r} \delta(\tilde{r} - r_n) + \delta(\tilde{r} + r_n)\,\mathrm{d}\tilde{r} = \begin{cases} 2, & \text{if } |r_n| \leq r, \\ 1, & \text{if } r_n \leq -r, \\ 1, & \text{if } r_n \geq r. \end{cases} \tag{A.17b}$$

With these identities, the mean-square spectral distribution function, $\mathit{\Gamma}^*$, appearing in Eqn. (A.16) can be written as

$$\mathit{\Gamma}^*(r) = \int_{-\infty}^{r} S^*(\tilde{r})\,\mathrm{d}\tilde{r} = \frac{\sigma^2}{2N} N(r), \tag{A.18}$$

where $N(r)$ is the number of r_n in the sample of size N meeting the conditions in Eqns. (A.17) for $r \leq 0$ and $r \geq 0$, respectively, multiplied by the given coefficients. The representation of the mean-square spectral distribution function, $\mathit{\Gamma}^*$, from Eqn. (A.18) can now be used to characterise the random variable $\mathit{\Gamma}^*(r + \mathit{\Delta}r) - \mathit{\Gamma}^*(r)$ for positive r and $\mathit{\Delta}r$,

$$\mathit{\Gamma}^*(r + \mathit{\Delta}r) - \mathit{\Gamma}^*(r) = \frac{\sigma^2}{2N}\left[N(r + \mathit{\Delta}r) - N(r)\right] = \frac{\sigma^2}{2N} \sum_{n=1}^{N} I_{[r, r+\mathit{\Delta}r]}(r_n) \tag{A.19}$$

with the indicator function

$$I_{[r, r+\mathit{\Delta}r]}(r_n) = \begin{cases} 1, & \text{if } r \leq |r_n| \leq r + \mathit{\Delta}r, \\ 0, & \text{else}\,. \end{cases} \tag{A.20}$$

The determine the first as well as the second moment of $\mathit{\Gamma}^*(r + \mathit{\Delta}r) - \mathit{\Gamma}^*(r)$ (which obviously coincide), we consider the corresponding moments of $I_{[r, r+\mathit{\Delta}r]}(r_n)$,

$$\begin{aligned} &\mathbf{E}\left[(I_{[r, r+\mathit{\Delta}r]}(r_n))^2\right] = \mathbf{E}[I_{[r, r+\mathit{\Delta}r]}(r_n)] = \int_{-\infty}^{\infty} I_{[r, r+\mathit{\Delta}r]}(\tilde{r})\, f(\tilde{r})\,\mathrm{d}\tilde{r} \\ &= \int_{-r-\mathit{\Delta}r}^{-r} f(\tilde{r})\,\mathrm{d}\tilde{r} + \int_{r}^{r+\mathit{\Delta}r} f(\tilde{r})\,\mathrm{d}\tilde{r} = 2\int_{r}^{r+\mathit{\Delta}r} f(\tilde{r})\,\mathrm{d}\tilde{r} = 2f(r)\mathit{\Delta}r = \frac{2S_0(r)\mathit{\Delta}r}{\sigma^2}, \end{aligned} \tag{A.21}$$

which is valid for small $\mathit{\Delta}r$ and follows from the representation of f in Eqn. (2.74) together with the fact that S_0 is even. The expected value of $\mathit{\Gamma}^*(r + \mathit{\Delta}r) - \mathit{\Gamma}^*(r)$ is then given by

$$\mathbf{E}\left[\mathit{\Gamma}^*(r + \mathit{\Delta}r) - \mathit{\Gamma}^*(r)\right] = \frac{\sigma^2}{2N} \sum_{n=1}^{N} \mathbf{E}\left[I_{[r, r+\mathit{\Delta}r]}(r_n)\right] = S_0(r)\mathit{\Delta}r \tag{A.22}$$

and its second moment by

$$\begin{aligned}
\mathbf{E}\left[(\mathit{\Gamma}^*(r+\mathit{\Delta}r)-\mathit{\Gamma}^*(r))^2\right] &= \frac{\sigma^4}{4N^2}\sum_{m=1}^{N}\sum_{n=1}^{N}\mathbf{E}[I_{[r,r+\mathit{\Delta}r]}(r_m)\,I_{[r,r+\mathit{\Delta}r]}(r_n)] \\
&= \frac{\sigma^4}{4N^2}\left[\sum_{n=1}^{N}\mathbf{E}[(I_{[r,r+\mathit{\Delta}r]}(r_m))^2]+\sum_{m=1}^{N}\sum_{\substack{n=1\\n\neq m}}^{N}\mathbf{E}[I_{[r,r+\mathit{\Delta}r]}(r_m)]\,\mathbf{E}[I_{[r,r+\mathit{\Delta}r]}(r_n)]\right] \\
&= \frac{\sigma^4}{4N^2}\left[\frac{2NS_0(r)\mathit{\Delta}r}{\sigma^2}+N(N-1)\frac{4S_0^2(r)(\mathit{\Delta}r)^2}{\sigma^4}\right] \\
&= \frac{\sigma^2}{2N}S_0(r)\mathit{\Delta}r+\frac{1}{N}S_0^2(r)(\mathit{\Delta}r)^2, \qquad \text{(A.23)}
\end{aligned}$$

using the independence of $I_{[r,r+\mathit{\Delta}r]}(r_m)$ and $I_{[r,r+\mathit{\Delta}r]}(r_n)$ for $m \neq n$. Under the assumption of small $\mathit{\Delta}r$ (which was already used in Eqn. (A.21)), the square of the first moment of $\mathit{\Gamma}^*(r+\mathit{\Delta}r)-\mathit{\Gamma}^*(r)$ can be neglected and the limit of its variance for $N \to \infty$ becomes

$$\lim_{N\to\infty}\mathbf{Var}\left[\mathit{\Gamma}^*(r+\mathit{\Delta}r)-\mathit{\Gamma}^*(r)\right]=0. \qquad \text{(A.24)}$$

To investigate the convergence of $\mathit{\Gamma}^*(r+\mathit{\Delta}r)-\mathit{\Gamma}^*(r)$, the target mean-square spectral distribution function $\mathit{\Gamma}_0$, which is defined by

$$\mathit{\Gamma}_0(r)=\int_{-\infty}^{r}S_0(\tilde{r})\,\mathrm{d}\tilde{r}, \qquad \text{(A.25)}$$

is approximated on the basis of the Taylor series expansion as

$$\mathit{\Gamma}_0(r+\mathit{\Delta}r)=\mathit{\Gamma}_0(r)+S_0(r)\mathit{\Delta}r+\mathcal{O}((\mathit{\Delta}r)^2). \qquad \text{(A.26)}$$

Again under the assumption of small $\mathit{\Delta}r$, it is clear that $\mathit{\Gamma}_0(r+\mathit{\Delta}r)-\mathit{\Gamma}_0(r)$ equals $S_0(r)\mathit{\Delta}r$, and since $\mathit{\Gamma}_0(r+\mathit{\Delta}r)-\mathit{\Gamma}_0(r)$ is deterministic, its variance is zero, i.e. we have

$$\begin{aligned}
&\lim_{N\to\infty}\mathbf{E}\left[\,|(\mathit{\Gamma}^*(r+\mathit{\Delta}r)-\mathit{\Gamma}^*(r))-(\mathit{\Gamma}_0(r+\mathit{\Delta}r)-\mathit{\Gamma}_0(r))|^r\,\right] \\
&\quad=\lim_{N\to\infty}\left[\,|(\mathit{\Gamma}^*(r+\mathit{\Delta}r)-\mathit{\Gamma}^*(r))-(\mathit{\Gamma}_0(r+\mathit{\Delta}r)-\mathit{\Gamma}_0(r))|^r\,\right]=0 \quad \text{for } r=1,2. \qquad \text{(A.27)}
\end{aligned}$$

The case $r=2$ is the characterisation of convergence in mean square and already implies convergence in the mean (case $r=1$).

So it is shown now (based on the work of Shinozuka (1971)) that the random process ψ becomes mean-ergodic and ergodic in the mean-square spectral density, hence ergodic in the autocorrelation, for N approaching infinity, i.e. the mean as well as the autocorrelation yield the same results regardless whether the ensemble average or the spatial average is taken. As a consequence, these ensemble quantities can be deduced from one single, random sample of the process ψ over a sufficiently long interval. In addition, these properties of the simulated random process ψ are the same as for the corresponding target process ψ_0.

The target autocorrelation function, ρ_0, which describes the autocorrelation of the target random process ψ_0, was chosen in Sec. 2.4 to be a squared exponential (Gaussian) autocorrelation function with correlation length l_G (see Eqn. (2.75)). To simulate this target random process ψ_0, the probability density function f for the frequencies r in Eqn. (2.73) has to be specified. This can be done via the corresponding mean-square spectral density function S_0. Owing to the Wiener–Khinchin relationship in Eqn. (A.8b), the target mean-square spectral density function, S_0, can be obtained by applying the inverse Fourier transform to the target autocorrelation function, ρ_0,

$$S_0(r) = \mathcal{F}^{-1}[\rho_0(\xi)] = \frac{1}{2\pi}\int_{-\infty}^{\infty} \rho_0(\xi)\mathrm{e}^{-\mathrm{i}r\xi}\,\mathrm{d}\xi = \frac{1}{2\pi}\int_{-\infty}^{\infty} \mathrm{e}^{-\frac{\xi^2}{l_\mathrm{G}}}\,\mathrm{e}^{-\mathrm{i}r\xi}\,\mathrm{d}\xi = \frac{1}{\sqrt{2\pi\frac{2}{l_\mathrm{G}^2}}}\mathrm{e}^{-\frac{r^2}{2\cdot\frac{2}{l_\mathrm{G}^2}}}\,. \tag{A.28}$$

Since S_0 is already a probability density function in this case (Gaussian distribution with mean zero and variance equals $2/l_\mathrm{G}^2$), the choice $\rho_0 = \mathrm{e}^{-\xi^2/l_\mathrm{G}^2}$ ensures that the standard deviation σ is normalised to unity and hence

$$f(r) = \frac{1}{\sqrt{4\pi/l_\mathrm{G}^2}}\mathrm{e}^{-\frac{r^2}{4/l_\mathrm{G}^2}}\,. \tag{A.29}$$

With the previous results about the random process ψ we know that the autocorrelation function of ψ with respect to the ensemble average, ρ, and the spatial average, ρ^*, are identical with the target autocorrelation function, ρ_0, for N approaching infinity. Hence, the target random process satisfying the Gaussian autocorrelation condition Eqn. (2.75) in the limit $N \to \infty$ can be simulated with the series given in Eqn. (2.76).

We now want to convince ourselves numerically that the random process ψ from Eqn. (2.76) indeed has vanishing ensemble average and spatial mean, and it fulfils the ensemble and spatial autocorrelation condition ρ_0. Fig. A.1 shows the ensemble average of the random process, $\langle\psi\rangle$, over the spatial domain of $(0,L)$, where the domain length is set to be $L = 400 \times l_\mathrm{G}$, for increasing number of terms in the random process generation, $N = 100$ (top panel), 400 (second panel), 1000 (third panel) and 10000 (bottom panel). For each case of N, the ensemble averages calculated for ensemble sizes of 100, 1000 and 100000 are shown. The correlation length here is chosen to be $l_\mathrm{G} = 2.5$ and the random process is evaluated at the mid-point of each of the four sub-intervals, which divide each correlation length. This is in accordance with the step approximation, where the the roughness profile (beam mass, beam rigidity and beam thickness, respectively) is approximated by a piece-wise constant function on $M \gg 1$ sub-intervals, with $(-\infty, 0)$ and (L,∞) the 0th and $(M+1)$th sub-intervals, respectively. The resolution of four sub-intervals per correlation length corresponds in this case to $M = 1600$.

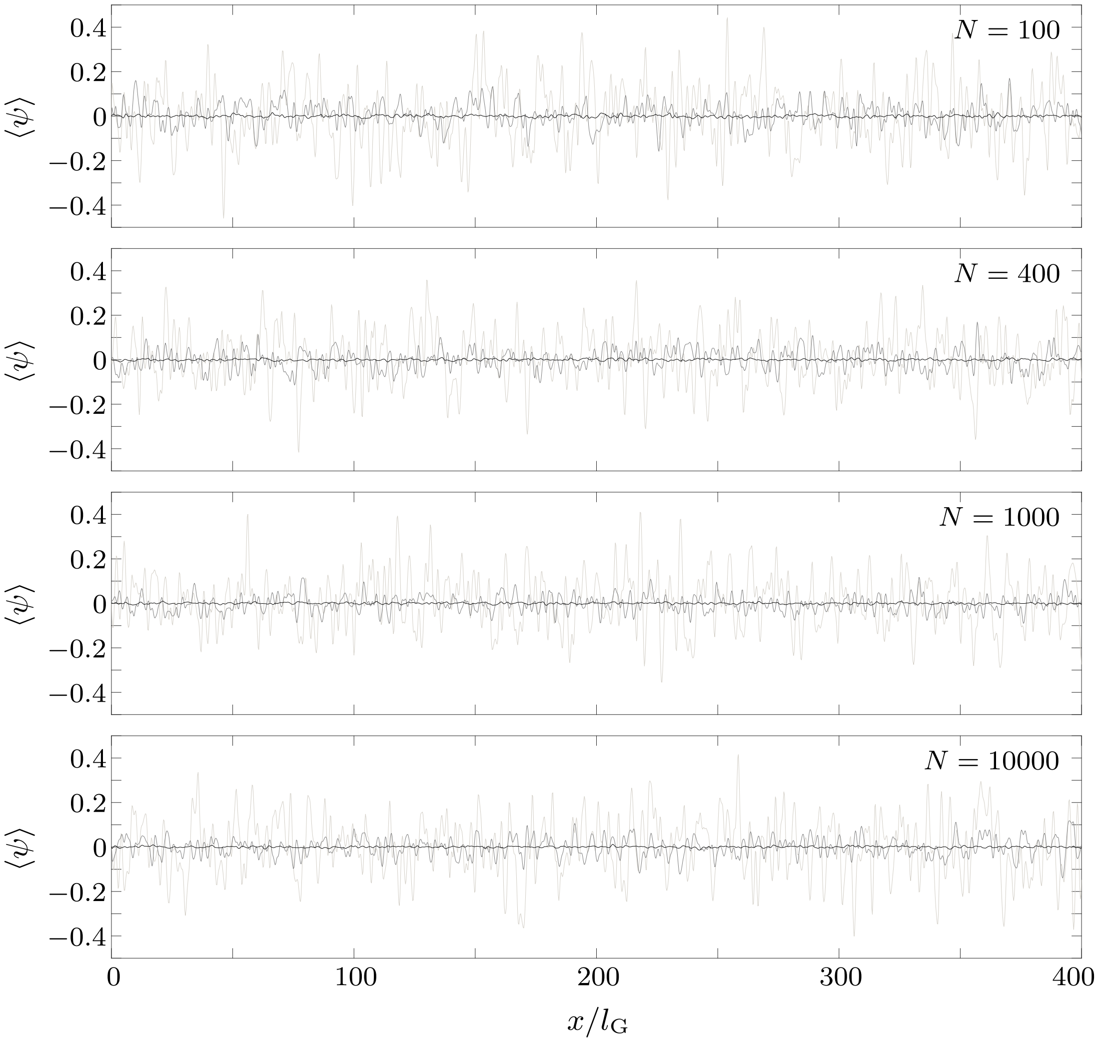

Figure A.1: Ensemble average of random process ψ over domain $(0,L)$ for $N = 100$ (top panel), $N = 400$ (second panel), $N = 1000$ (third panel) and $N = 10000$ (bottom panel). Ensemble averages are calculated using ensemble sizes of 100 (light grey), 1000 (dark grey) and 100000 (black).

We can observe in Fig. A.1 for $N = 100$ that the ensemble averages look noticeably different for the three ensemble sizes. For the smallest ensemble size in consideration, 100, the ensemble average essentially fluctuates around zero, but it deviates randomly along the domain significantly by magnitude 0.4 upwards and downwards. For the medium ensemble size, 1000, the number of outliers does not decrease, but their magnitudes do considerably. The ensemble average deviates in this case not more than 0.15 upwards and downwards henceforth. As expected, the largest ensemble size, 100000, yields the best result. Here, the ensemble average of the random process shows only very small deviations of magnitude 0.01 from the expected value zero. In the other cases, $N = 400$, 1000 and 10000, the ensemble averages look qualitatively very much the same with similar magnitude of deviations for the different ensemble sizes. This is consistent with the analytical calculation of the ensemble average, which is influenced by N, but the ensemble size has to be sufficiently large to calculate the expected value.

Next, we analyse the autocorrelation of the random process, ρ, and compare it with the target autocorrelation ρ_0, which is given by the squared exponential Gaussian function in Eqn. (2.75). Fig. A.2 shows the ensembled autocorrelation function ρ of the random process (as function of distance between points, ξ) for ensemble sizes 100 and 1000. Random processes are generated with $N = 100$ (top panels), 400 (middle panels) and 1000 (bottom panels) terms and results are shown for correlation lengths $l_\mathrm{G} = 0.9$, 2.5 and 4.1. The domain (0,L) is chosen to be of length $L = 400 \times l_\mathrm{G}$ again.

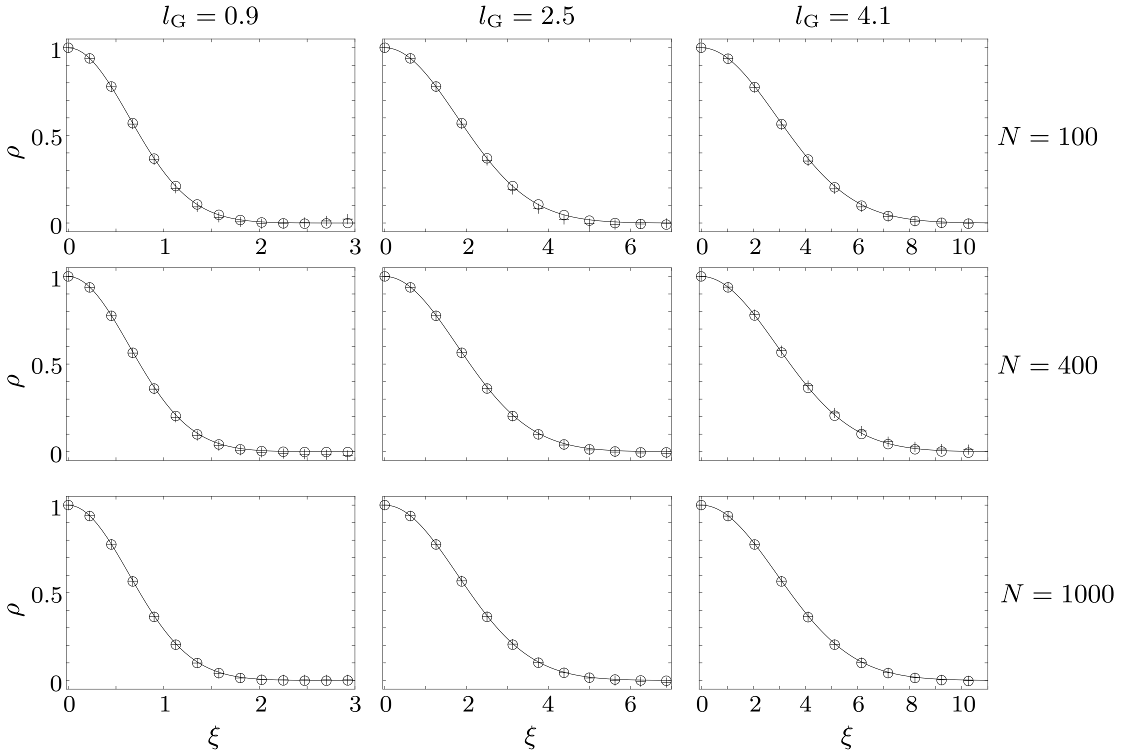

Figure A.2: Ensembled autocorrelation function of random process ψ for $N = 100$ (top panels), $N = 400$ (middle panels) and $N = 1000$ (bottom panels) and correlation lengths $l_\mathrm{G} = 0.9$ (left-hand panels), $l_\mathrm{G} = 2.5$ (middle panels) and $l_\mathrm{G} = 4.1$ (right-hand panels). Autocorrelation function is calculated for ensemble size 100 (+) and 1000 (∘). Target autocorrelation function is shown for comparison (solid grey curve).

We can see in Fig. A.2 that already the autocorrelation of the random process with only $N = 100$ shows good agreement with the target autocorrelation function for the larger ensemble size 1000, for all correlation lengths considered. Using a smaller ensemble size of only 100 leads to small deviations of the actual and the target autocorrelation function in the case of $l_\mathrm{G} = 0.9$ for (relatively) more distant points and to less correlated neighbouring points in the case of $l_{\mathrm{G}} = 2.5$. For $N = 400$, the results are similar, i.e. an ensemble size of 1000 yields accurate autocorrelation of the underlying random process and for the smaller ensemble size, 100, we can see small deviations, here for $l_{\mathrm{G}} = 0.9$ for large ξ and for $l_{\mathrm{G}} = 4.1$ in the middle regime of all ξ considered. For $N = 1000$ we can observe a slight improvement and only very small deviations in the case of the larger ensemble size for $l_{\mathrm{G}} = 2.5$. Similarly to the previous results, the ensembled autocorrelation function gives excellent agreement with the squared exponential Gaussian target autocorrelation function, hence the random process ψ fulfils the autocorrelation condition for sufficiently large ensemble size for all cases of N and l_{G} considered.

After confirming the derived properties of the ensemble mean and autocorrelation of the random process ψ numerically, we now study these characteristics taking the spatial average. The analysis for the spatial average in Appendix A is based on the assumption that $L \to \infty$. We use the same domain length as in the previous results, $L = 400 \times l_{\mathrm{G}}$, and study the mean and autocorrelation of single realisations of ψ for this long, but finite interval.

Fig. A.3 shows box-and-whisker plots of the spatial mean, for four different numbers of terms in the generation of the random process, $N = 100$, 400, 1000 and 10000, for the correlation lengths $l_{\mathrm{G}} = 0.9$ (left-hand panel), 2.5 (middle panel) and 4.1 (right-hand panel). For each N and l_{G}, the spatial mean over $(0,L)$ is calculated 100000 times, providing a large sample size. The boxes and whiskers represent the same statistical quantities as in Fig. 2.15. For better visibility, points regarded as outliers are shown as crosses here.

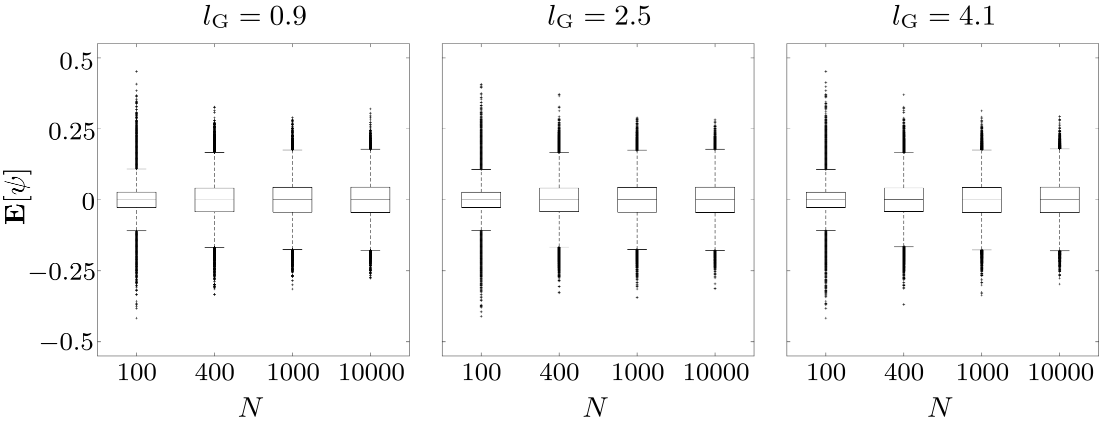

Figure A.3: Box-and-whisker plots of spatial mean for $N = 100$, $N = 400$, $N = 1000$ and $N = 10000$, for correlation lengths $l_{\mathrm{G}} = 0.9$ (left-hand panel), $l_{\mathrm{G}} = 2.5$ (middle panel) and $l_{\mathrm{G}} = 4.1$ (right-hand panel)

We can observe in Fig. A.3 that the median of the spatial mean (50% quantile) is zero for all correlation lengths considered, $l_{\mathrm{G}} = 0.9$, 2.5 and 4.1, and the reasonably symmetric data distributions indicate that the mean of the ensembled spatial mean is zero, too. $N = 100$ leads to more variation in the spatial mean, indicated by the spread outliers. Increasing the number of terms in the random profile generation to $N = 400$ significantly reduces the spread of the outliers for all l_{G}. It is interesting to note that as a consequence thereof, the

25% and 75% quantiles move slightly away from the mean. Further increase of N to 1000 and 10000 does not change the 25%, 50% and 75% quantiles anymore and the spread of the outliers is reduced only slightly. To obtain results with the 25% and 75% quantiles moved closer together, the domain length has to be increased.

To complete this section about the statistical analysis of the generated random process, which shall describe the beam's roughness profile, we study the autocorrelation of ψ taking the spatial average. Since the spatial average is already included in the results in Fig. A.2, we focus now on the spatial autocorrelation for single realisations of the random process for the large domain length $L = 400 \times l_\mathrm{G}$. Fig. A.4 shows the spatial autocorrelation ρ^* of single example process realisations for $N = 100$ (left-hand panel), 400 (middle panel) and 1000 (right-hand panel), for the correlation length $l_\mathrm{G} = 2.5$. Under the assumption of $L \to \infty$, the spatial autocorrelation function is given analytically by Eqn. (A.10). This curve is shown for comparison.

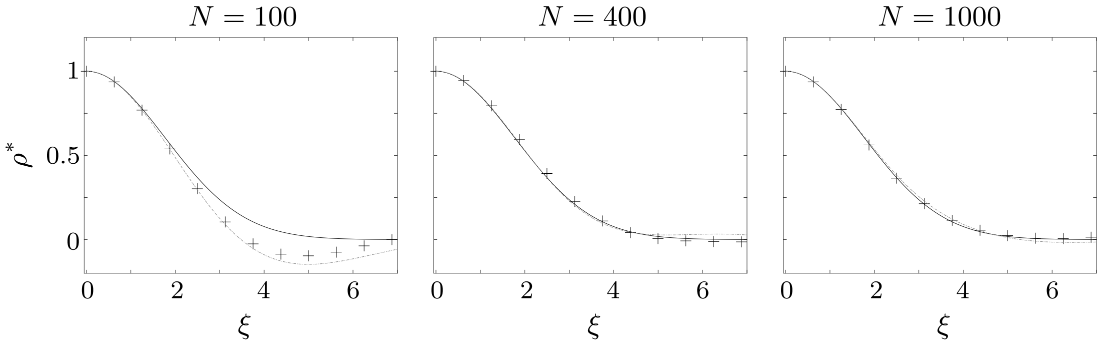

Figure A.4: Spatial autocorrelation function (+) of example realisation of random process ψ for $N = 100$ (left-hand panel), $N = 400$ (middle panel) and $N = 1000$ (right-hand panel), for correlation length $l_\mathrm{G} = 2.5$. Target autocorrelation function (solid grey curve) and analytical spatial autocorrelation function (dash-dotted grey curve) are shown for comparison.

We can observe in Fig. A.4 that the spatial autocorrelation function for the example realisation of the random process for $N = 100$ shows a significant deviation from the prescribed squared exponential Gaussian target autocorrelation function ρ_0 for $\xi \geq 2$, where the process realisation exhibits markedly less autocorrelation than given by ρ_0. However, it shows very similar behaviour as the analytical spatial autocorrelation function in the limit $L \to \infty$ given by Eqn. (A.10). For $N = 400$, the autocorrelation is much closer to the target autocorrelation function and for $N = 1000$, the spatial autocorrelation agrees with the target autocorrelation function. This confirms the findings from Fig. A.2 that $N = 100$ is not sufficient to obtain Gaussian autocorrelated realisations of the random process ψ, but $N = 400$ yields reliable results. In all the cases, the spatial autocorrelation is remarkably close to the suggested analytical values, for which the assumption $L \to \infty$ has to be made. Increasing L certainly gives agreement between them.

The representation in Eqn. (2.76) provides a much more efficient way to calculate Gaussian autocorrelated random processes than their widely used generation via Cholesky decomposition, which is computationally very expensive for generating roughness realisations over the long distances, which we are interested in. Gaussian random processes of this type can also be represented via the Karhunen–Loève expansion, a sum of eigenfunctions of the associated covariance operator weighted with the eigenvalues and independent, identically standard normal distributed random variables, see Stark and Woods 2011.

Bibliography

Abboud, N. N., G. L. Wojcik, D. K. Vaughan, J. Mould, D. J. Powell, and L. Nikodym (1998): 'Finite Element Modeling for Piezoelectric Ultrasonic Transducers'. *Proceedings to SPIE International Symposium on Medical Imaging.*

Achenbach, J. D. (1984): *Wave Propagation in Elastic Solids.* Elsevier.

Alexander, I. (2014): *Mechanical Engineering Analysis.* Lecture Notes. Case Western Reserve University, Cleveland (USA).

Amore, P. (2010): 'The string of variable density: Perturbative and non-perturbative results'. *Annals of Physics*, vol. 325: pp. 2679–2696.

Amore, P. (2011): 'The string of variable density: Further results'. *Annals of Physics*, vol. 326: pp. 2315–2355.

Anderson, P. W. (1958): 'Absence of Diffusion in Certain Random Lattices'. *Physical Review*, vol. 109(5): pp. 1492–1505.

Aristégui, C. and Y. C. Angel (2002): 'New results for isotropic point scatterers: Foldy revisited'. *Wave Motion*, vol. 36: pp. 383–399.

Ascher, U. M. and L. R. Petzold (1998): *Computer Methods for Ordinary Differential Equations and Differential-Algebraic Equations.* SIAM.

Ashby, M. F. and D. R. H. Jones (2011): *Engineering Materials 1: An Introduction to Properties, Applications and Design.* 4th ed. Butterworth–Heinemann.

Baldi, P. and M. Berti (2008): 'Forced vibrations of a nonhomogeneous string'. *SIAM Journal on Mathematical Analysis*, vol. 40(1): pp. 382–412.

Balmforth, N. J. and R. V. Craster (1999): 'Ocean Waves and ice sheets'. *Journal of Fluid Mechanics*, vol. 395: pp. 89–124.

Bao, J. (2003): 'Lamb Wave Generation and Detection with Piezoelectric Wafer Active Sensors'. PhD thesis. Department of Mechanical Engineering, University of South Carolina (USA).

Bardell, N. S., R. S. Langley, J. M. Dunsdon, and T. Klein (1996): 'The Effect of Period Asymmetry on Wave Propagation in Periodic Beams'. *Journal of Sound and Vibration*, vol. 197(4): pp. 427–445.

Barnwell, E. G. (2014): ‘One and two-dimensional propagation of waves in periodic heterogeneous media: transient effects and band gap tuning’. PhD thesis. School of Mathematics, University of Manchester (UK).

Batchelor, G. K. (2000): *An Introduction to Fluid Dynamics.* 2nd ed. Cambridge University Press.

Bauchau, O. A. and J. I. Craig (2009): *Structural Analysis: With Applications to Aerospace Structures.* Vol. 163. Solid Mechanics and Its Applications. Springer Netherlands.

Behzad, M., H. R. Mirdamadi, and A. Ghadami (2013): ‘Guided Wave Propagation in Stepped Beams’. *Proceedings of 21st Annual International Conference on Mechanical Engineering.*

Bennetts, L. G. (2007): ‘Wave Scattering by Ice Sheets of Varying Thickness’. PhD thesis. Department of Mathematics, University of Reading (UK).

Bennetts, L. G. and M. A. Peter (2012): ‘Approximations of wave propagation in one-dimensional multiple scattering problems with random characteristics’. *Proceedings of 27th International Workshop on Water Waves and Floating Bodies.*

Bennetts, L. G. and M. A. Peter (2013): ‘Spectral analysis of wave propagation through rows of scatterers via random sampling and a coherent potential approximation’. *SIAM Journal on Applied Mathematics*, vol. 73(4): pp. 1613–1633.

Bennetts, L. G. and V. A. Squire (2009): ‘Wave scattering by multiple rows of circular ice floes’. *Journal of Fluid Mechanics*, vol. 639: pp. 213–238.

Bennetts, L. G. and V. A. Squire (2012): ‘On the calculation of an attenuation coefficient for transects of ice-covered ocean’. *Proceedings of the Royal Society of London A*, vol. 468(2137): pp. 136–162.

Bennetts, L. G., N. R. T. Biggs, and D. Porter (2007): ‘A multi-mode approximation to wave scattering by ice sheets of varying thickness’. *Journal of Fluid Mechanics*, vol. 579: pp. 413–443.

Bennetts, L. G., M. A. Peter, and H. Chung (2015): ‘Absence of localisation in ocean wave interactions with a rough seabed in intermediate water depth’. *Quarterly Journal of Mechanics and Applied Mathematics*, vol. 68(1): pp. 97–113.

Beran, M. J. (1994): ‘Scattering of flexural waves by random density fluctuations in a plate’. *Waves in Random Media*, vol. 4(3): pp. 221–232.

Berry, M. V. and S. Klein (1997): ‘Transparent mirrors: rays, waves and localization’. *European Journal of Physics*, vol. 18: pp. 222–228.

Bilbao, S. (2004): *Wave and Scattering Methods for Numerical Simulation.* John Wiley & Sons, Inc.

Billingham, J. and A. C. King (2001): *Wave Motion.* Cambridge University Press.

Biondi, B. and S. Caddemi (2005): ‘Closed form solutions of Euler–Bernoulli beams with singularities’. *International Journal of Solids and Structures*, vol. 42(9–10): pp. 3027–3044.

Bobrovnitskii, Y. I. and V. P. Maslov (1966): ‘Propagation of flexural waves along a beam with periodic point loading’. *Soviet Physics-Acoustics*, vol. 12: pp. 150–154.

Boresi, A. P. and R. J. Schmidt (2002): *Advanced Mechanics of Materials*. 6th ed. John Wiley & Sons, Inc.

Brigham, E. O. (1988): *Fast Fourier Transform and Its Applications*. Pearson.

Bronstein, I. N., K. A. Semendjaew, G. Grosche, V. Ziegler, and D. Ziegler (2012): *Springer-Taschenbuch der Mathematik*. 3rd ed. Springer Vieweg.

Broström, G. and K. Christensen (2008): *Waves in sea ice*. Tech. rep. Norwegian Meteorological Institute.

Carrera, E., G. Giunta, and M. Petrolo (2015): *Beam Structures: Classical and Advanced Theories*. John Wiley & Sons, Inc.

Chamberlain, P. G. and D. Porter (1995): ‘Decomposition methods for wave scattering by topography with application to ripple beds’. *Wave Motion*, vol. 22: pp. 201–214.

Chaves, E. W. V., G. R. Fernandes, and W. S. Venturini (1999): ‘Plate bending boundary element formulation considering variable thickness’. *Engineering Analysis with Boundary Elements*, vol. 23(5–6): pp. 405–418.

Chung, H. (2002): ‘Mathematical studies of wave propagation in sea-ice’. PhD thesis. Department of Mathematics, University of Auckland (NZ).

COMSOL Multiphysics 5.2 User’s Guide (Acoustics Module Application Library) (2015). COMSOL Multiphysics.

Cowper, G. R. (1966): ‘The Shear Coefficient in Timoshenko’s Beam Theory’. *Journal of Applied Mechanics*, vol. 33: pp. 335–340.

Crandall, S. H., N. C. Dahl, and T. J. Lardner (1999): *An Introduction to the Mechanics of Solids*. 2nd ed. McGraw-Hill.

Dall’Agnol, F. F. (2011): ‘Wave propagation in a non-uniform string’. *Revista Brasileira de Ensino de Fisica*, vol. 33(4).

de L. Kronig, R. and W. G. Penney (1931): ‘Quantum Mechanics of Electrons in Crystal Lattices’. *Proceedings of the Royal Society A*, vol. 130: pp. 499–513.

Debnath, L. (2012): *Nonlinear Partial Differential Equations for Scientists and Engineers*. 3rd ed. Birkhäuser.

Dixon, T. W. and V. A. Squire (2000): ‘Energy transport velocity of flexural waves in a random medium’. *Waves Random Media*, vol. 10: pp. 83–102.

Doyle, J. F. (1997): *Wave Propagation in Structures: Spectral Analysis Using Fast Discrete Fourier Transforms*. 2nd ed. Mechanical Engineering Series. Springer-Verlag New York.

Ernst, R. and J. Dual (2014): ‘Acoustic emission localization in beams based on time reversed dispersion’. *Ultrasonics*, vol. 54(6): pp. 1522–1533.

Evans, D. V. and R. Porter (2003): ‘Wave scattering by narrow cracks in ice sheets floating on water of finite depth’. *Journal of Fluid Mechanics*, vol. 484: pp. 143–165.

Evans, D. V. and R. Porter (2007): ‘Penetration of flexural waves through a periodically constrained thin elastic plate in vacuo and floating on water’. *Journal of Engineering Mathematics*, vol. 58: pp. 317–337.

Failla, G. and A. Santini (2007): ‘On Euler–Bernoulli discontinuous beam solutions via uniform-beam Green’s functions’. *International Journal of Solids and Structures*, vol. 44: pp. 7666–7687.

Figotin, A. and A. Klein (1996): ‘Localization of Classical Waves I: Acoustic Waves’. *Communications in Mathematical Physics*, vol. 180(2): pp. 439–482.

Figotin, A. and P. Kuchment (1995a): ‘Band-Gap Structure of Spectra of Periodic Dielectric and Acoustic Media. I. Scalar Model’. *SIAM Journal on Applied Mathematics*, vol. 56(1): pp. 68–88.

Figotin, A. and P. Kuchment (1995b): ‘Band-Gap Structure of Spectra of Periodic Dielectric and Acoustic Media. Ii. Two-Dimensional Photonic Crystals’. *SIAM Journal on Applied Mathematics*, vol. 56(6): pp. 1561–1620.

Filippi, P. J. T. (2008): *Vibrations and Acoustic Radiation of Thin Structures: Physical Basis, Theoretical Analysis and Numerical Methods*. ISTE and John Wiley & Sons, Inc.

Fox, C. and V. A. Squire (1994): ‘On the oblique reflexion and transmission of ocean waves at shore fast sea ice’. *Philosophical Transactions of the Royal Society of London A*, vol. 347(1682): pp. 185–218.

Freitag, E. and R. Busam (2009): *Complex Analysis*. 2nd ed. Universitext. Springer-Verlag Berlin Heidelberg.

Frýba, L. (1999): *Vibration of Solids and Structures Under Moving Loads*. 3rd ed. Thomas Telford Ltd.

Ghavami, P. (2015): *Mechanics of Materials: An Introduction to Engineering Technology*. Springer International Publishing.

Gimbutas, Z. and L. Greengard (2013): ‘Fast multi-particle scattering : A hybrid solver for the Maxwell equations in microstructured materials’. *Journal of Computational Physics*, vol. 232: pp. 22–32.

Gladwell, G. M. L. (2005): *Inverse Problems in Vibration*. 2nd ed. Vol. 119. Solid Mechanics and Its Applications. Springer Netherlands.

Godin, Y. A., S. Molchanov, and B. Vainberg (2007): ‘Wave propagation in a one-dimensional randomly perturbed periodic medium’. *Waves in Random and Complex Media*, vol. 17(3): pp. 381–395.

Gómez, B. J., C. E. Repetto, C. R. Stia, and R. Welti (2007): ‘Oscillations of a string with concentrated masses’. *European Journal of Physics*, vol. 28(5): pp. 961–975.

Gospodinov, G. and D. Ljutskanov (1982): ‘The boundary element method applied to plates’. *Applied Mathematical Modelling*, vol. 6(4): pp. 237–244.

Goto, H. and K. Toki (1969): ‘Structural Response to Nonstationary Random Excitation’. *Proceedings of the 4th World Conference on Earthquake Engineering.*

Gruttmann, F. and W. Wagner (2001): ‘Shear correction factors in Timoshenko’s beam theory for arbitrary shaped cross-sections’. *Computational Mechanics*, vol. 27: pp. 199–207.

Gutierrez, R. H. and P. A. A. Laura (1997): ‘Vibrations of a Beam of Non-Uniform Cross-Section Traversed by a Time Varying Concentrated Force’. *Journal of Sound and Vibration*, vol. 207(3): pp. 419–425.

Hagedorn, P. and A. DasGupta (2007): *Vibrations and Waves in Continuous Mechanical Systems.* John Wiley & Sons, Inc.

Hamada, T. R. (1981): ‘Dynamic Analysis of a Beam Under a Moving Force: a Double Laplace Transformation Solution’. *Journal of Sound and Vibration*, vol. 74(2): pp. 221–233.

Haykin, S. and B. Van Veen (2002): *Signals and Systems.* 2nd ed. John Wiley & Sons, Inc.

He, S. and J. D. Maynard (1986): ‘Detailed Measurements of Inelastic Scattering in Anderson Localization’. *Physical Review Letters*, vol. 57: pp. 3171–3174.

He, S. and C.-T. Ng (2015): ‘Analysis of mode conversion and scattering of guided waves at cracks in isotropic beams using a time-domain spectral finite element method’. *Electronic Journal of Structural Engineering*, vol. 14: pp. 20–32.

He, S. and C.-T. Ng (2017): ‘Guided wave-based identification of multiple cracks in beams using a Bayesian approach’. *Mechanical Systems and Signal Processing*, vol. 84: pp. 324–345.

Hibbitt, D., B. Karlsson, and P. Sorensen (2015): *Abaqus Theory Manual (6.12).* Dassault Systèmes Simulia Corp.

Hino, J., T. Yoshimura, and N. Ananthanarayana (1985): ‘Vibration Analysis of Non-Linear Beams Subjected to a Moving Load Using the Finite Element Method’. *Journal of Sound and Vibration*, vol. 100(4): pp. 477–491.

Hodges, C. H. and J. Woodhouse (1983): ‘Vibration isolation from irregularity in a nearly periodic structure: Theory and measurements’. *Journal of the Acoustical Society of America*, vol. 74(3): pp. 894–905.

Hodges, C. H. and J. Woodhouse (1989a): ‘Confinement of vibration by one-dimensional disorder, I: theory of ensembling averaging’. *Journal of Sound and Vibration*, vol. 130: pp. 237–251.

Hodges, C. H. and J. Woodhouse (1989b): ‘Confinement of vibration by one-dimensional disorder, II: a numerical experiment of different ensemble averages’. *Journal of Sound and Vibration*, vol. 130: pp. 253–268.

Horgan, C. O. and A. M. Chan (1999): ‘Vibration of inhomogeneous strings, rods and membranes’. *Journal of Sound and Vibration*, vol. 225(3): pp. 503–513.

Hutchinson, J. R. (2001): ‘Shear Coefficients for Timoshenko Beam Theory’. *Journal of Applied Mechanics*, vol. 68: pp. 87–92.

Isaacson, E. and H. B. Keller (1994): *Analysis of Numerical Methods.* Dover Publications.

John, S. (1991): ‘Localization of Light’. *Physics Today*, vol. 44(5): pp. 32–40.

Kashiwagi, M. (2000): ‘Research on Hydroelastic Response of VLFS: Recent Progress and Future Work’. *International Journal of Offshore and Polar Engineering*, vol. 10(2): pp. 81–90.

Kawahara, T. (1976): ‘Effect of random inhomogeneities on nonlinear propagation of water waves’. *Journal of the Physical Society of Japan*, vol. 41(4): pp. 1402–1409.

Kin, Y. H. and M. W. Trethewey (1990): ‘Finite Element Analysis of Elastic Beams Subjected to Moving Dynamic Loads’. *Journal of Sound and Vibration*, vol. 136(2): pp. 323–342.

Kocbach, J. (2000): ‘Finite Element Modeling of Ultrasonic Piezoelectric Transducers’. PhD thesis. Department of Physics, University of Bergen (Norway).

Kohn, R. V. and M. Vogelius (1984): ‘A new model for thin plates with rapidly varying thickness’. *International Journal of Solids and Structures*, vol. 20: pp. 333–350.

Kümmel, W. (2007): *Technische Strömungsmechanik – Theorie und Praxis.* Teubner B.G.

Lamas-Pardo, M., G. Iglesias, and L. Carral (2015): ‘A review of Very Large Floating Structures (VLFS) for coastal and offshore uses’. *Ocean Engineering*, vol. 109: pp. 677–690.

Landau, L. D. and E. M. Lifshitz (1986): *Theory of Elasticity.* 3rd ed. Vol. 7. Butterworth–Heinemann.

Langley, R. S. (1995): ‘Wave Transmission Through One-Dimensional Near Periodic Structures: Optimum and To Random Disorder’. *Journal of Sound and Vibration*, vol. 188(5): pp. 717–743.

Law, S. S. and T. H. T. Chan (1997): ‘Moving Force Identification: a Time Domain Method’. *Journal of Sound and Vibration*, vol. 201(1): pp. 1–22.

Le Bas, P. and J. Conoir (2005): ‘Reflection and transmission by randomly spaced elastic cylinders in a fluid slab-like region’. *Journal of the Acoustical Society of America*, vol. 117(3): pp. 1088–1097.

Lee, H. P. (1996a): ‘Dynamic Response of a Beam with a Moving Mass’. *Journal of Sound and Vibration*, vol. 191(2): pp. 289–299.

Lee, H. P. (1996b): ‘The Dynamic Response of a Timoshenko Beam Subjected to a Moving Mass’. *Journal of Sound and Vibration*, vol. 198(2): pp. 248–256.

Liang, K. K., S. D. Bennett, and G. S. Kino (1986): ‘Precision phase measurement with short tone burst signals in acoustic microscopy’. *Review of Scientific Instruments*, vol. 57(3): pp. 446–452.

Limaco, J., H. R. Clark, and L. A. Medeiros (2008): ‘Vibrations of elastic string with nonhomogeneous material’. *Journal of Mathematical Analysis and Applications*, vol. 344(2): pp. 806–820.

Linton, C. M. and P. A. Martin (2005): ‘Multiple scattering by random configurations of circular cylinders: Second-order corrections for the effective wavenumber’. *Journal of the Acoustical Society of America*, vol. 117: pp. 3413–3423.

Lüthi, M. (2012): *Physics of Glaciers*. Lecture Notes. ETH Zürich (Switzerland).

Martin, P. A. (2014): ‘N masses on an infinite string and related one-dimensional scattering problems’. *Wave Motion*, vol. 51: pp. 296–307.

Martin, P. A., I. D. Abrahams, and W. J. Parnell (2015): ‘One-dimensional reflection by a semi-infinite periodic row of scatterers’. *Wave Motion*, vol. 58: pp. 1–12.

Masson, D. and P. H. LeBlond (1989): ‘Spectral evolution of wind-generated surface gravity waves in a dispersed ice field’. *Journal of Fluid Mechanics*, vol. 202: pp. 43–81.

Maurel, A. (2010): ‘Reflection and transmission by a slab with randomly distributed isotropic point scatterers’. *Journal of Computational and Applied Mathematics*, vol. 234: pp. 1842–1850.

Maurel, A. and P. A. Martin (2013): ‘Propagation in one-dimensional crystals with positional and compositional disorder’. *European Physical Journal B*, vol. 86: pp. 486–495.

Maurel, A. and V. Pagneux (2008): ‘Effective propagation in a perturbed periodic structure’. *Physical Review B*, vol. 78(5). id. 052301.

Maurel, A., P. A. Martin, and V. Pagneux (2010): ‘Effective propagation in a one-dimensional perturbed periodic structure: comparison of several approaches’. *Waves in Random and Complex Media*, vol. 20(4): pp. 634–655.

McPhedran, R. C., L. C. Botten, A. A. Asatryan, N. A. Nicorovici, P. A. Robinson, and C. M. de Sterke (1999): ‘Calculation of electromagnetic properties of regular and random arrays of metalic and dielectric cylinders’. *Physical Review E*, vol. 60(6): pp. 7614–7617.

Mei, C. C. and M. J. Hancock (2003): ‘Weakly nonlinear surface waves over a random bed’. *Journal of Fluid Mechanics*, vol. 475: pp. 247–268.

Mei, C. C., M. Stiassnie, and D. K.-P. Yue (2005): *Theory and Applications of Ocean Surface Waves. Part I: Linnear Aspects*. Vol. 23. Advanced Series on Ocean Engineering. World Scientific.

Meylan, M. H. (2002): ‘Wave response of an ice floe of arbitrary geometry’. *Journal of Geophysical Research*, vol. 107(C1): pp. 5–1–5–11.

Meylan, M. H. (2003): ‘Wave Scattering in the Marginal Ice Zone’. *Proceedings of 18th International Workshop on Water Waves and Floating Bodies.*

Meylan, M. H. and V. A. Squire (1996): ‘Response of a circular ice floe to ocean waves’. *Journal of Geophysical Research*, vol. 101(C4): pp. 8869–8884.

Meylan, M. H., L. G. Bennetts, and A. L. Kohout (2014): ‘In-situ measurements and analysis of ocean waves in the Antarctic marginal ice zone’. *Geophysical Research Letters*, vol. 14: pp. 5046–5051.

Michaels, J. E., S. J. Lee, J. S. Hall, and T. E. Michaels (2011): ‘Multi-mode and multi-frequency guided wave imaging via chirp excitations’. *Proceedings of SPIE Conference on Health Monitoring of Structural and Biological Systems.*

Miles, J. W. (1956): ‘Vibrations of Beams on Many Supports’. *Journal of the Engineering Mechanics Division*, vol. 82(1): pp. 1–9.

Mindlin, R. D. (1951): ‘Influence of Rotary Inertia and Shear on Flexural Motions of Isotropic Elastic Plates’. *Journal of Applied Mechanics*, vol. 18(31): pp. 31–38.

Montiel, F., L. G. Bennetts, and V. A. Squire (2012): ‘The transient response of floating elastic plates to wavemaker forcing in two dimensions’. *Journal of Fluids and Structures*, vol. 28: pp. 416–433.

Montiel, F., V. A. Squire, and L. G. Bennetts (2015): ‘Evolution of directional spectra through finite regular and randomly perturbed arrays of scatterers’. *SIAM Journal on Applied Mathematics*, vol. 75(2): pp. 630–651.

Morin, D. (2016): *Waves.* Tech. rep. Physics Department, Harvard University (USA).

Morse, P. M. (1948): *Vibration and Sound.* 2nd ed. International Series in Pure & Applied Physics. McGraw-Hill.

Olver, P. J. (2014): *Introduction to Partial Differential Equations.* Undergraduate Texts in Mathematics. Springer International Publishing.

Oñate, E. (2009): *Structural Analysis with the Finite Element Method. Linear Statics.* Vol. 1. Lecture Notes on Numerical Methods in Engineering and Sciences. Springer Netherlands.

Oñate, E. (2013): *Structural Analysis with the Finite Element Method. Linear Statics.* Vol. 2. Lecture Notes on Numerical Methods in Engineering and Sciences. Springer Netherlands.

Ostermann, F. (2014): *Anwendungstechnologie Aluminium.* 3rd ed. VDI-Buch. Springer Vieweg.

Ottarsson, G. and C. Pierre (1997): ‘Vibration and wave localization in a nearly periodic beaded string’. *Journal of the Acoustical Society of America*, vol. 101(6): pp. 3430–3442.

Parnell, W. J. and I. D. Abrahams (2008): *Multiple Scattering in Periodic and Random Media: An Overview.* Tech. rep. School of Mathematics, University of Manchester (UK).

Peter, M. A. and M. H. Meylan (2009): ‘Water-wave scattering by vast field of bodies’. *SIAM Journal on Applied Mathematics*, vol. 70(5): pp. 1567–1586.

Poddubny, A. N., M. V. Rybin, M.F. Limonov, and Y.S. Kivshar (2012): ‘Fano interference governs wave transport in disordered systems’. *Nature Communications*, vol. 3(4).

Porter, D. and R. Porter (2004): ‘Approximations to wave scattering by an ice sheet of variable thickness over undulating bed topography’. *Journal of Fluid Mechanics*, vol. 509: pp. 145–179.

Porter, R. and D. V. Evans (2006): ‘Scattering of flexural waves by multiple narrow cracks in ice sheets floating on water’. *Wave Motion*, vol. 43: pp. 425–443.

Rawitscher, G. and J. Liss (2011): ‘The vibrating inhomogeneous string’. *American Journal of Physics*, vol. 79(4).

Reddy, J. N. (2002): *Energy Principles and Variational Methods in Applied Mechanics*. 2nd ed. John Wiley & Sons, Inc.

Richoux, O. and V. Pagneux (2002): ‘Acoustic characterization of Hofstadter butterfly with resonant scatterers’. *Europhysics Letters*, vol. 59(1): pp. 34–40.

Richoux, O., V. Tournat, and T. Le Van Suu (2007): ‘Acoustic wave dispersion in a one-dimensional lattice of nonlinear resonant scatterers’. *Physical Review E*, vol. 75. id. 026615.

Richoux, O., A. Maurel, and V. Pagneux (2015): ‘Disorder persistent transparency within the bandgap of a periodic array of acoustic Helmholtz resonators’. *Journal of Applied Physics*, vol. 117(10): pp. 1–6.

Romack, G. M. and R. L. Weaver (1990): ‘Monte Carlo studies of multiple scattering of waves in one-dimensional random media’. *Journal of the Acoustical Society of America*, vol. 87(2): pp. 487–494.

Rose, J. L. (2014): *Ultrasonic Guided Waves in Solid Media*. Cambridge University Press.

Rupprecht, S. (2013): ‘Wasserwellen-Diffraktion an Eisschollen’. MA thesis. Institute of Mathematics, University of Augsburg (Germany).

Rupprecht, S., L. G. Bennetts, and M. A. Peter (2017): ‘Effective wave propagation along a rough thin-elastic beam’. *Wave Motion*, vol. 70: pp. 3–14.

Sarpkaya, T. and M. Isaacson (1981): *Mechanics of Wave Forces on Offshore Structures*. Van Nostrand Reinhold Company.

Sause, M. G. R. (2016): *In Situ Monitoring of Fiber-Reinforced Composites: Theory, Basic Concepts, Methods, and Applications*. Vol. 242. Springer Series in Materials Science. Springer International Publishing.

Senning, J. R. (2017): *Computing and Estimating the rate of convergence*. Tech. rep. Gordon College, Department of Mathematics and Computer Science, Wenham (USA).

Sheng, P. (2006): *Introduction to Wave Scattering, Localization and Mesoscopic Phenomena.* 2nd ed. Vol. 88. Springer Series in Materials Science. Springer-Verlag Berlin Heidelberg.

Shinozuka, M. (1971): 'Simulation of multivariate and multidimensional random processes'. *Journal of the Acoustical Society of America*, vol. 49: pp. 357–368.

Shinozuka, M. and T. Kobori (1972): 'Fatigue analysis of highway bridges'. *Proceedings of Japan Society of Civil Engineers.*

Silverman, B. W. (1986): *Density Estimation for Statistics and Data Analysis.* Chapman and Hall.

Slaughter, W. S. (2002): *The Linearised Theory of Elasticity.* Birkhäuser.

Sommerfeld, A. (1949): *Partial Differential Equations in Physics.* Academic Press.

Squire, V. A. (2007): 'Of ocean waves and sea-ice revisited'. *Cold Regions Science and Technology*, vol. 49: pp. 110–133.

Squire, V. A. (2008): 'Synergies between VLFS hydroelasticity and sea ice research'. *International Journal of Offshore and Polar Engineering*, vol. 18: pp. 1–13.

Squire, V. A. (2010): 'Contemporary Perspectives on Ocean Wave/Sea Ice Interaction'. *Proceedings to 20th IAHR International Symposium on Ice.*

Stark, H. and J. Woods (2011): *Probability, Statistics, and Random Processes for Engineers.* 4th ed. Pearson.

Thomas, T. R. (1999): *Rough Surfaces.* 2nd ed. World Scientific Publishing.

Timco, G. W. and W. F. Weeks (2010): 'A review of the engineering properties of sea ice'. *Cold Regions Science and Technology*, vol. 60(2): pp. 107–129.

Timoshenko, S. and S. Woinowsky-Krieger (1959): *Theory of plates and shells.* 2nd ed. McGraw-Hill.

Townsend, A. (2014): 'Computing with functions in two dimensions'. PhD thesis. St John's College, University of Oxford (UK).

Tsang, L., J. A. Kong, and K. Ding (2000): *Scattering of Electromagnetic Waves: Theories and Applications.* John Wiley & Sons, Inc.

Ulrich, T. J. (2006): *Envelope Calculation from the Hilbert Transform.* Tech. rep. Los Alamos National Laboratory (USA).

Vaughan, G. L. and V. A. Squire (2008): 'Ocean wave scattering by natural sea ice transects'. *Journal of Geophysical Research: Oceans*, vol. 113(10): pp. 1–18.

Wadhams, P. (2016): *A Farewell to Ice: A Report from the Arctic.* Allen Lane.

Wadhams, P., V. A. Squire, J. A. Ewing, and R. W. Pascal (1986): 'The effect of the marginal ice zone on the directional wave spectrum of the ocean'. *Journal of Physical Oceanography*, vol. 16(2): pp. 358–375.

Wang, C. D. (2004): ‘The linear wave response of a single and a periodic line-array of floating elastic plates’. PhD thesis. Massey University, Albany (NZ).

Wang, C. Y. and C. M. Wang (2013): *Structural Vibration: Exact Solutions for Strings, Membranes, Beams, and Plates.* CRC Press.

Watanabe, E., T. Utsunomiya, and C. M. Wang (2004): ‘Hydroelastic analysis of pontoon-type VLFS: a literature survey’. *Engineering Structures*, vol. 26(2): pp. 245–256.

Watanabe, K. (2014): *Integral Transform Techniques for Green’s Function.* Vol. 71. Lecture Notes in Applied and Computational Mechanics. Springer International Publishing.

Weaver, R. L. (1997): ‘Multiple-scattering theory for mean responses in a plate with sprung masses’. *Journal of the Acoustical Society of America*, vol. 101: pp. 3466–3474.

Weaver, R. L. (1998): ‘Mean-square responses in a plate with sprung masses, energy flow and diffusion’. *Journal of the Acoustical Society of America*, vol. 103: pp. 414–427.

Williams, T. D. (2006): ‘Reflections on Ice: Scattering of Flexural Gravity Waves by Irregularities in Arctic and Antarctic Ice Sheets’. PhD thesis. Department of Mathematics and Statistics, University of Otago, Dunedin (NZ).

Williams, T. D. and V. A. Squire (2008): ‘The effect of submergence on wave scattering across a transition between two floating flexible plates’. *Wave Motion*, vol. 45(3): pp. 361–379.

Wu, R. (1982): ‘Mean field attenuation and amplitude attenuation due to wave scattering’. *Wave Motion*, vol. 4: pp. 305–316.

Yavari, A., S. Sarkani, and J. N. Reddy (2001): ‘On nonuniform Euler–Bernoulli and Timoshenko beams with jump discontinuities: application of distribution theory’. *International Journal of Solids and Structures*, vol. 38: pp. 8389–8406.

Zienkiewicz, O. C. and R. L. Taylor (2013): *The Finite Element Method for Solid and Structural Mechanics.* Elsevier Science & Technology.

List of Figures